



PACIFIC EARTHQUAKE ENGINEERING RESEARCH CENTER

Experimental and Analytical Studies on the Seismic Response of Freestanding and Anchored Laboratory Equipment

Dimitrios Konstantinidis

Department of Civil and Environmental Engineering
University of California, Berkeley

Nicos Makris

Department of Civil Engineering
University of Patras, Greece



PACIFIC EARTHQUAKE ENGINEERING RESEARCH CENTER

Experimental and Analytical Studies on the Seismic Response of Freestanding and Anchored Laboratory Equipment

Dimitrios Konstantinidis

Department of Civil and Environmental Engineering
University of California, Berkeley

Nicos Makris

Department of Civil Engineering
University of Patras, Greece

Experimental and Analytical Studies on the Seismic Response of Freestanding and Anchored Laboratory Equipment

Dimitrios Konstantinidis

Graduate Student Researcher
Department of Civil and Environmental Engineering
University of California, Berkeley

and

Nicos Makris

Professor of Structures and Applied Mechanics
Department of Civil Engineering
University of Patras, Greece

PEER Report 2005/07
Pacific Earthquake Engineering Research Center
College of Engineering
University of California, Berkeley

January 2005

ABSTRACT

This report presents the results of a comprehensive experimental program investigating the seismic response of freestanding and anchored laboratory equipment. The study is part of a broader study on the UC Science Laboratory facility that implements the performance-based earthquake engineering (PBEE) methodology proposed by the PEER Center.

In this study, quasi-static experiments were conducted in order to examine the mechanical behavior of the contact interface between laboratory equipment and the floors on which the equipment is situated. Based on the results of these experiments, the report presents two idealized contact friction models that were constructed: (a) an elastoplastic model and (b) a classical Coulomb friction model.

The report presents shake table test results of freestanding equipment subjected to ground and floor motions with 50% and 10% in 50 years hazard levels. For the equipment tested, although some rocking was observed, sliding was the predominant mode of response, with sliding displacements reaching up to 2 ft. Numerical simulations with the elastoplastic model using *MATLAB* and with the Coulomb model using the software *Working Model 2D* were performed. When the friction coefficient values obtained from the quasi-static tests were used, the simulations yielded time-history results that were in fair agreement with the experimental data. The predicted responses were appreciably improved for both models when reduced values of the friction coefficients were used.

Following the PEER methodology, the report identifies a representative Intensity Measure, *IM*, and the associated Engineering Demand Parameter, *EDP*. The proposed lognormal distribution of the *EDP* is tested against the shake table experimental results, and simple linear relationships for the mean and standard deviation of the *EDP* in terms of the *IM* are offered. The report presents generated fragility curves and an example that illustrates how to use them.

Results of shake table tests done on wooden scale models of the equipment confirm *Working Model's* ability to capture the overturning potential of equipment and provide confidence in its use to analyze the seismic response of equipment. *Working Model* was used to compute the responses of equipment subjected to 2% in 50 years motions (which were not tested on the shake table due to its displacement limitations). The report presents these responses together with generated fragility curves.

The report finally presents results of shake table tests performed on anchored equipment which indicate that recorded peak equipment accelerations are significantly larger than those recorded during the freestanding equipment tests, on several occasions 7 or more times larger. Such high accelerations may pose a threat to the sensitive contents of laboratory equipment.

ACKNOWLEDGEMENTS

From the UC Science Laboratory Building, we would like to thank Barbara Duncan (Building Manager) and Todd Laverty (Research Associate) for providing the equipment that were used for the shake table experiments; Eddy Kwan (Associate Development Engineer) for providing us with invaluable information regarding the laboratory equipment and their in-situ boundary conditions in the building laboratories. From the Structural Research Laboratory at the Richmond Field Station where the shake table experiments were conducted, we greatly appreciate the technical assistance of Don Clyde (Lab Manager), Wes Neighbour, and David Maclam.

We would also like to thank our PEER colleagues for their collaboration. We are very grateful for their continual feedback throughout the course of this study.

This work was supported primarily by the Earthquake Engineering Research Centers Program of the National Science Foundation under award number EEC-9701568 through the Pacific Earthquake Engineering Research Center (PEER).

Any opinions, findings, and conclusions or recommendations expressed in this material are those of the authors and do not necessarily reflect those of the National Science Foundation.

CONTENTS

ABSTRACT.....	iii
ACKNOWLEDGEMENTS.....	v
CONTENTS.....	vii
LIST OF FIGURES	ix
LIST OF TABLES.....	xxiii
LIST OF SYMBOLS	xxv
1 INTRODUCTION.....	1
1.1 Motivation	1
1.2 Background and Testbed	1
1.2.1 Overview of the PEER Methodology	1
1.2.2 Testbed: The UC Science Research Facility	3
1.3 Objectives of the Research	5
2 SEISMIC HAZARD AND STRUCTURAL ANALYSIS.....	7
2.1 Seismic Hazard	7
2.2 Structural Analysis.....	7
3 LABORATORY EQUIPMENT AND FRICTION EXPERIMENTS.....	9
3.1 Slender Laboratory Equipment.....	9
3.2 Friction Tests	12
4 SHAKE TABLE TESTS OF FREESTANDING LABORATORY EQUIPMENT	21
5 REGRESSION ANALYSIS AND FRAGILITY CURVES FOR 50% IN 50 YEARS AND 10% IN 50 YEARS HAZARD MOTIONS.....	55
5.1 Sliding and Governing Parameters	55
5.2 Closed-Form Deterministic Approximation of Pulse-Type and Near-Source Earthquake Motions.....	56
5.3 Intensity Measure and Engineering Demand Parameter	60
5.3.1 Intensity Measure, <i>IM</i>	60
5.3.2 Engineering Demand Parameter, <i>EDP</i>	60
5.4 Fragility Analysis for 50% and 10% in 50 Years Hazard Level Motions.....	64

5.4.1	Regression of the Experimental Data	64
5.4.2	The <i>EDP</i> as a Lognormally Distributed Random Variable	67
5.4.3	Fragility Curves	71
6	RESPONSE ANALYSIS OF FREESTANDING EQUIPMENT AND VALIDATION OF EXISTING SOFTWARE	77
6.1	Dynamic Response of a Piece of Equipment.....	77
6.1.1	Pure, Planar Rocking Motion of a Rigid Block.....	78
6.1.2	Pure Sliding Motion of a Rigid Block	86
6.1.3	Planar Slide-Rocking Motion of a Rigid Block.....	88
6.2	Validation of Working Model Software	91
6.2.1	Pure-Rocking Response Analysis.....	93
6.2.2	Pure-Sliding Response Analysis.....	95
6.2.3	Slide-Rocking Response Analysis.....	97
7	SHAKE TABLE TESTS OF WOODEN BLOCKS	99
7.1	Wooden Block Models	99
7.2	Evaluation of the Friction Coefficient of the Wooden Blocks	99
7.3	Shake Table Experiments on Wooden Block Models	99
7.4	Simulation Studies on Equipment Prototypes	103
8	REGRESSION ANALYSIS AND FRAGILITY CURVES FOR 2% IN 50 YEARS HAZARD MOTIONS	133
8.1	Sliding Response due to 2% in 50 Years Hazard Motions.....	133
8.2	Fragility Analysis for 2% in 50 Years Hazard Level Motions	135
8.2.1	Regression of the Experimental Data	135
8.2.1	The <i>EDP</i> as a Lognormally Distributed Random Variable	135
8.2.2	Fragility Curves	139
9	SHAKE TABLE TESTS OF ANCHORED LABORATORY EQUIPMENT	141
9.1	Anchoring of Laboratory Equipment.....	141
9.2	Shake Table Tests of Anchored Equipment	144
10	CONCLUSIONS	163
	REFERENCES	165
	INDEX	169

LIST OF FIGURES

Figure 1.1	<i>Top</i> : Location of the UC Science Laboratory Building. The heavy dashed line traces the nearby Hayward fault. <i>Bottom</i> : Typical floor plan of the UC Science research facility (from Comerio 2005).	4
Figure 3.1	The three pieces of freestanding heavy laboratory equipment that were obtained from the UC Science research facility for the purposes of this study.	10
Figure 3.2	Schematic of a piece of equipment.....	13
Figure 3.3	Schematic diagram of the experimental setup for the quasi-static pull tests.....	14
Figure 3.4	Recorded load-displacement plots for the FORMA incubator obtained from the slow pull tests (wavy lines); the elastoplastic idealization with μ_k from the slow pull tests (dashed line); the elastoplastic idealization with μ_k from the best fit of the shake table test data (solid line); the Coulomb friction model calibrated to best fit data obtained from the shake table tests (heavy line).	15
Figure 3.5	Recorded load-displacement plots for the Kelvinator refrigerator obtained from the slow pull tests (wavy lines); the elastoplastic idealization with μ_k from the slow pull tests (dashed line); the elastoplastic idealization with μ_k from the best fit of the shake table test data (solid line); the Coulomb friction model calibrated to best fit data obtained from the shake table tests (heavy line).	16
Figure 3.6	Recorded load-displacement plots for the ASP refrigerator obtained from the slow pull tests (wavy lines); the elastoplastic idealization with μ_k from the slow pull tests (dashed line); the elastoplastic idealization with μ_k from the best fit of the shake table test data (solid line); the Coulomb friction model calibrated to best fit data obtained from the shake table tests (heavy line).	17
Figure 4.1	The FORMA incubator resting atop the shake table at the Richmond Field Station Earthquake Simulation Laboratory. The locations of the wire transducers are indicated with white lines, and the locations of the accelerometers are indicated with dark arrows.	22
Figure 4.2	Response of the FORMA incubator subjected to the OTE FP motion recorded during the 1995 Aigion, Greece, earthquake. The heavy grey lines on the bottom two graphs plot a Type-B trigonometric pulse that approximates the main pulse of the motion record.	26
Figure 4.3	Response of the FORMA incubator subjected to the Gilroy Array #6 motion recorded during the 1979 Coyote Lake, California, earthquake. The heavy grey lines on the bottom two graphs plot a Type-C ₁ trigonometric pulse that approximates the main pulse of the motion record.	27

Figure 4.4	Response of the FORMA incubator subjected to the Gilroy Array #6 ground motion (50% in 50 years) recorded during the 1979 Coyote Lake, California, earthquake. The heavy grey lines on the bottom two graphs plot a Type-C ₁ trigonometric pulse that approximates the main pulse of the motion record.	28
Figure 4.5	Response of the FORMA incubator subjected to the UC Science Building 6th floor motion of the Gilroy Array #6 (50% in 50 years) record of the 1979 Coyote Lake, California, earthquake. The heavy grey lines on the bottom two graphs plot a Type-C ₁ trigonometric pulse that approximates the main pulse of the motion record.	29
Figure 4.6	Response of the FORMA incubator subjected to the Gavilan College ground motion (10% in 50 years) recorded during the 1989 Loma Prieta, California, earthquake. The heavy grey lines on the bottom two graphs plot a Type-A trigonometric pulse that approximates the main pulse of the motion record.	30
Figure 4.7	Response of the Kelvinator refrigerator subjected to the OTE FP motion recorded during the 1995 Aigion, Greece, earthquake. The heavy grey lines on the bottom two graphs plot a Type-B trigonometric pulse that approximates the main pulse of the motion record.	31
Figure 4.8	Response of the Kelvinator refrigerator subjected to the Gilroy Array #6 motion recorded during the 1979 Coyote Lake, California, earthquake. The heavy grey lines on the bottom two graphs plot a Type-C ₁ trigonometric pulse that approximates the main pulse of the motion record.	32
Figure 4.9	Response of the Kelvinator refrigerator subjected to the Gilroy Array #6 ground motion (50% in 50 years) recorded during the 1979 Coyote Lake, California, earthquake. The heavy grey lines on the bottom two graphs plot a Type-C ₁ trigonometric pulse that approximates the main pulse of the motion record.	33
Figure 4.10	Response of the Kelvinator refrigerator subjected to the UC Science Building 6th floor motion of the Gilroy Array #6 (50% in 50 years) record of the 1979 Coyote Lake, California, earthquake. The heavy grey lines on the bottom two graphs plot a Type-C ₁ trigonometric pulse that approximates the main pulse of the motion record.	34
Figure 4.11	Response of the Kelvinator refrigerator subjected to the Gavilan College ground motion (10% in 50 years) recorded during the 1989 Loma Prieta, California, earthquake. The heavy grey lines on the bottom two graphs plot a Type-A trigonometric pulse that approximates the main pulse of the motion record.	35
Figure 4.12	Response of the Kelvinator refrigerator subjected to the UC Science Building 6th floor motion of the Gavilan College (10% in 50 years) record of the 1989 Loma Prieta, California, earthquake. The heavy grey lines on the bottom two	

graphs plot a Type-C ₁ trigonometric pulse that approximates the main pulse of the motion record.	36
Figure 4.13 Response of the Kelvinator refrigerator subjected to the UC Science Building 6th floor motion of the Kofu FN (10% in 50 years) record of the 2000 Tottori, Japan, earthquake. The heavy grey lines on the bottom two graphs plot a Type-C ₂ trigonometric pulse that approximates the main pulse of the motion record.	37
Figure 4.14 Response of the ASP refrigerator (face configuration) subjected to the OTE FP motion recorded during the 1995 Aigion, Greece, earthquake. The heavy grey lines on the bottom two graphs plot a Type-B trigonometric pulse that approximates the main pulse of the motion record.	38
Figure 4.15 Response of the ASP refrigerator (face configuration) subjected to the Gilroy Array #6 motion recorded during the 1979 Coyote Lake, California, earthquake. The heavy grey lines on the bottom two graphs plot a Type-C ₁ trigonometric pulse that approximates the main pulse of the motion record.	39
Figure 4.16 Response of the ASP refrigerator (face configuration) subjected to the Gilroy Array #6 ground motion (50% in 50 years) recorded during the 1979 Coyote Lake, California, earthquake. The heavy grey lines on the bottom two graphs plot a Type-C ₁ trigonometric pulse that approximates the main pulse of the motion record.	40
Figure 4.17 Response of the ASP refrigerator (face configuration) subjected to the UC Science Building 6th floor motion of the Gilroy Array #6 (50% in 50 years) record of the 1979 Coyote Lake, California, earthquake. The heavy grey lines on the bottom two graphs plot a Type-C ₁ trigonometric pulse that approximates the main pulse of the motion record.	41
Figure 4.18 Response of the ASP refrigerator (face configuration) subjected to the Gavilan College ground motion (10% in 50 years) recorded during the 1989 Loma Prieta, California, earthquake. The heavy grey lines on the bottom two graphs plot a Type-A trigonometric pulse that approximates the main pulse of the motion record.	42
Figure 4.19 Response of the ASP refrigerator (face configuration) subjected to the UC Science Building 6th floor motion of the Gavilan College (10% in 50 years) record of the 1989 Loma Prieta, California, earthquake. The heavy grey lines on the bottom two graphs plot a Type-C ₁ trigonometric pulse that approximates the main pulse of the motion record.	43
Figure 4.20 Response of the ASP refrigerator (face configuration) subjected to the Kofu FN motion (10% in 50 years) recorded during the 2000 Tottori, Japan, earthquake. The heavy grey lines on the bottom two graphs plot a Type-C ₂ trigonometric pulse that approximates the main pulse of the motion record.	44

Figure 4.21	Response of the ASP refrigerator (face configuration) subjected to the UC Science Building 6th floor motion of the Kofu FN (10% in 50 years) record of the 2000 Tottori, Japan, earthquake. The heavy grey lines on the bottom two graphs plot a Type-C ₂ trigonometric pulse that approximates the main pulse of the motion record.	45
Figure 4.22	Response of the ASP refrigerator (profile configuration) subjected to the OTE FP motion recorded during the 1995 Aigion, Greece, earthquake. The heavy grey lines on the bottom two graphs plot a Type-B trigonometric pulse that approximates the main pulse of the motion record.	46
Figure 4.23	Response of the ASP refrigerator (profile configuration) subjected to the Gilroy Array #6 motion recorded during the 1979 Coyote Lake, California, earthquake. The heavy grey lines on the bottom two graphs plot a Type-C ₁ trigonometric pulse that approximates the main pulse of the motion record.	47
Figure 4.24	Response of the ASP refrigerator (profile configuration) subjected to the Gilroy Array #6 ground motion (50% in 50 years) recorded during the 1979 Coyote Lake, California, earthquake. The heavy grey lines on the bottom two graphs plot a Type-C ₁ trigonometric pulse that approximates the main pulse of the motion record.	48
Figure 4.25	Response of the ASP refrigerator (profile configuration) subjected to the UC Science Building 6th floor motion of the Gilroy Array #6 (50% in 50 years) record of the 1979 Coyote Lake, California, earthquake. The heavy grey lines on the bottom two graphs plot a Type-C ₁ trigonometric pulse that approximates the main pulse of the motion record.	49
Figure 4.26	Response of the ASP refrigerator (profile configuration) subjected to the Gavilan College ground motion (10% in 50 years) recorded during the 1989 Loma Prieta, California, earthquake. The heavy grey lines on the bottom two graphs plot a Type-A trigonometric pulse that approximates the main pulse of the motion record.	50
Figure 4.27	Response of the ASP refrigerator (profile configuration) subjected to the UC Science Building 6th floor motion of the Gavilan College (10% in 50 years) record of the 1989 Loma Prieta, California, earthquake. The heavy grey lines on the bottom two graphs plot a Type-C ₁ trigonometric pulse that approximates the main pulse of the motion record.	51
Figure 4.28	Response of the ASP refrigerator (profile configuration) subjected to the Kofu FN motion (10% in 50 years) recorded during the 2000 Tottori, Japan, earthquake. The heavy grey lines on the bottom two graphs plot a Type-C ₂ trigonometric pulse that approximates the main pulse of the motion record.	52

Figure 4.29	Response of the ASP refrigerator (profile configuration) subjected to the UC Science Building 6th floor motion of the Kofu FN (10% in 50 years) record of the 2000 Tottori, Japan, earthquake. The heavy grey lines on the bottom two graphs plot a Type-C ₂ trigonometric pulse that approximates the main pulse of the motion record.	53
Figure 5.1	Dimensionless displacement Π_1 as a function of the dimensionless strength Π_2 for rigid-plastic system subjected to rectangular and Type-A acceleration pulses with amplitude a_p and duration $T_p=2\pi/\omega_p$. The response saturates into a single master curve for each pulse, indicating the physical similarity.	63
Figure 5.2	<i>Top</i> : The Engineering Demand Parameter $\Delta=U_{max}\omega_p^2/PTA$ as a function of the Intensity Measure $PTA/\mu g-1$ for the shake table tests performed on the three pieces of equipment. The value of μ is that obtained by the slow pull tests. <i>Bottom</i> : Standard deviation to the mean as a function of the Intensity Measure $PTA/\mu g-1$	65
Figure 5.3	<i>Top</i> : The Engineering Demand Parameter $\Delta=U_{max}\omega_p^2/PTA$ as a function of the Intensity Measure $PTA/\mu g-1$ for the shake table tests performed on the three pieces of equipment. The value of μ is obtained by best-fit of numerical simulation results to shake table test results. <i>Bottom</i> : Standard deviation to the mean as a function of the Intensity Measure $PTA/\mu g-1$	66
Figure 5.4	The empirical cumulative distribution function of the <i>EDP</i> Δ (50% and 10% hazard level motions) and the theoretical cumulative distribution function of its hypothesized lognormal distribution. The value of the friction coefficient μ that the random variable Δ depends on is that obtained from the slow pull tests.	70
Figure 5.5	The empirical cumulative distribution function of the <i>EDP</i> Δ (50% and 10% hazard level motions) and the theoretical cumulative distribution function of its hypothesized lognormal distribution. The value of the friction coefficient μ that the random variable Δ depends on is that obtained from best-fitting numerical simulation results to the results obtained from the shake table tests.	72
Figure 5.6	Fragility curves for $C=0.5$ (top) and $C=1.0$ (bottom). Two curves are plotted in each graph. The top curve corresponds to values of μ obtained by slow pull tests, while the bottom curve corresponds to values of μ obtained by best-fitting numerical simulation results to shake table experiment results.	73
Figure 5.7	Fragility curves for $C=2.0$ (top) and $C=3.0$ (bottom). Two curves are plotted in each graph. The top curve corresponds to values of μ obtained by slow pull tests, while the bottom curve corresponds to values of μ obtained by best-fitting numerical simulation results to shake table experiment results.	74

Figure 5.8	Fragility curve for $C=2.0$. With $PTA=1.4g$ and $\mu=0.5$, the Intensity Measure is $IM=PTA/\mu g-1=1.8$ and the probability that $U_{max}>18$ in. for $\omega_p=2\pi/0.8$ rad/sec is roughly $P(U_{max}\omega_p^2/PTA>2)=P(U_{max}>18 \text{ in.})\sim 0.4$	76
Figure 6.1	<i>Top</i> : Schematic of a rigid block in pure, planar rocking motion induced by base acceleration \ddot{u}_g . <i>Bottom</i> : Schematic of a rigid block in pure sliding motion induced by base acceleration \ddot{u}_g	79
Figure 6.2	Schematic diagram of a rocking block just before it impacts point O'	83
Figure 6.3	The <i>Working Model 2D</i> software environment.	92
Figure 6.4	Rotation and angular velocity of a rigid block with frequency parameter $p=1.25$ rad/sec and stockiness $\alpha=0.16$ rad subjected to two strong ground motions.	94
Figure 6.5	Overturning acceleration spectrum of a rigid block with frequency parameter $p=1.25$ rad/sec and stockiness $\alpha=0.16$ rad subjected to a one-sine (Type-A) pulse.	96
Figure 6.6	Sliding displacement of a freestanding rigid mass ($\mu=0.3$) subjected to three strong earthquakes. The response obtained with the software <i>Working Model</i> is in excellent agreement with the numerical solution obtained with <i>MATLAB</i>	98
Figure 7.1	Quarter-scale wooden block models of the full-scale prototype equipment (pictured in Fig. 3.1) resting on the shaking table at the Richmond Field Station Earthquake Simulation Laboratory, UC Berkeley. The excitation of the table is parallel to the more slender face of the models (labelled "SMALL α ").	100
Figure 7.2	Recorded load-displacement plots for the wooden block models obtained from quasi-static pull tests. The wood-concrete interface exhibits a nearly perfect rigid-plastic behavior.	101
Figure 7.3	<i>Left</i> : Outcome of the shake table experiment on the quarter-scale wooden block model together with the table acceleration and displacement of the compressed (by a factor of 2) motion to which the block was subjected. <i>Right</i> : Computed response by <i>Working Model</i> simulations on the full-scale equipment prototype subjected to the uncompressed motion. The simulations were done for three values of the friction coefficient μ	106
Figure 7.4	<i>Left</i> : Outcome of the shake table experiment on the quarter-scale wooden block model together with the table acceleration and displacement of the compressed (by a factor of 2) motion to which the block was subjected. <i>Right</i> : Computed response by <i>Working Model</i> simulations on the full-scale equipment prototype subjected to the uncompressed motion. The simulations were done for three values of the friction coefficient μ	107

Figure 7.5	<i>Left:</i> Outcome of the shake table experiment on the quarter-scale wooden block model together with the table acceleration and displacement of the compressed (by a factor of 2) motion to which the block was subjected. <i>Right:</i> Computed response by <i>Working Model</i> simulations on the full-scale equipment prototype subjected to the uncompressed motion. The simulations were done for three values of the friction coefficient μ .	108
Figure 7.6	<i>Left:</i> Outcome of the shake table experiment on the quarter-scale wooden block model together with the table acceleration and displacement of the compressed (by a factor of 2) motion to which the block was subjected. <i>Right:</i> Computed response by <i>Working Model</i> simulations on the full-scale equipment prototype subjected to the uncompressed motion. The simulations were done for three values of the friction coefficient μ .	109
Figure 7.7	<i>Left:</i> Outcome of the shake table experiment on the quarter-scale wooden block model together with the table acceleration and displacement of the compressed (by a factor of 2) motion to which the block was subjected. <i>Right:</i> Computed response by <i>Working Model</i> simulations on the full-scale equipment prototype subjected to the uncompressed motion. The simulations were done for three values of the friction coefficient μ .	110
Figure 7.8	<i>Left:</i> Outcome of the shake table experiment on the quarter-scale wooden block model together with the table acceleration and displacement of the compressed (by a factor of 2) motion to which the block was subjected. <i>Right:</i> Computed response by <i>Working Model</i> simulations on the full-scale equipment prototype subjected to the uncompressed motion. The simulations were done for three values of the friction coefficient μ .	111
Figure 7.9	<i>Left:</i> Outcome of the shake table experiment on the quarter-scale wooden block model together with the table acceleration and displacement of the compressed (by a factor of 2) motion to which the block was subjected. <i>Right:</i> Computed response by <i>Working Model</i> simulations on the full-scale equipment prototype subjected to the uncompressed motion. The simulations were done for three values of the friction coefficient μ .	112
Figure 7.10	<i>Left:</i> Outcome of the shake table experiment on the quarter-scale wooden block model together with the table acceleration and displacement of the compressed (by a factor of 2) motion to which the block was subjected. <i>Right:</i> Computed response by <i>Working Model</i> simulations on the full-scale equipment prototype subjected to the uncompressed motion. The simulations were done for three values of the friction coefficient μ .	113
Figure 7.11	<i>Left:</i> Outcome of the shake table experiment on the quarter-scale wooden block model together with the table acceleration and displacement of the compressed (by a factor of 2) motion to which the block was subjected. <i>Right:</i> Computed response by <i>Working Model</i> simulations on the full-scale equipment prototype	

	subjected to the uncompressed motion. The simulations were done for three values of the friction coefficient μ	114
Figure 7.12	<i>Left</i> : Outcome of the shake table experiment on the quarter-scale wooden block model together with the table acceleration and displacement of the compressed (by a factor of 2) motion to which the block was subjected. <i>Right</i> : Computed response by <i>Working Model</i> simulations on the full-scale equipment prototype subjected to the uncompressed motion. The simulations were done for three values of the friction coefficient μ	115
Figure 7.13	<i>Left</i> : Outcome of the shake table experiment on the quarter-scale wooden block model together with the table acceleration and displacement of the compressed (by a factor of 2) motion to which the block was subjected. <i>Right</i> : Computed response by <i>Working Model</i> simulations on the full-scale equipment prototype subjected to the uncompressed motion. The simulations were done for three values of the friction coefficient μ	116
Figure 7.14	<i>Left</i> : Outcome of the shake table experiment on the quarter-scale wooden block model together with the table acceleration and displacement of the compressed (by a factor of 2) motion to which the block was subjected. <i>Right</i> : Computed response by <i>Working Model</i> simulations on the full-scale equipment prototype subjected to the uncompressed motion. The simulations were done for three values of the friction coefficient μ	117
Figure 7.15	<i>Left</i> : Outcome of the shake table experiment on the quarter-scale wooden block model together with the table acceleration and displacement of the compressed (by a factor of 2) motion to which the block was subjected. <i>Right</i> : Computed response by <i>Working Model</i> simulations on the full-scale equipment prototype subjected to the uncompressed motion. The simulations were done for three values of the friction coefficient μ	118
Figure 7.16	<i>Left</i> : Outcome of the shake table experiment on the quarter-scale wooden block model together with the table acceleration and displacement of the compressed (by a factor of 2) motion to which the block was subjected. <i>Right</i> : Computed response by <i>Working Model</i> simulations on the full-scale equipment prototype subjected to the uncompressed motion. The simulations were done for three values of the friction coefficient μ	119
Figure 7.17	<i>Left</i> : Outcome of the shake table experiment on the quarter-scale wooden block model together with the table acceleration and displacement of the compressed (by a factor of 2) motion to which the block was subjected. <i>Right</i> : Computed response by <i>Working Model</i> simulations on the full-scale equipment prototype subjected to the uncompressed motion. The simulations were done for three values of the friction coefficient μ	120

Figure 7.18	<i>Left:</i> Outcome of the shake table experiment on the quarter-scale wooden block model together with the table acceleration and displacement of the compressed (by a factor of 2) motion to which the block was subjected. <i>Right:</i> Computed response by <i>Working Model</i> simulations on the full-scale equipment prototype subjected to the uncompressed motion. The simulations were done for three values of the friction coefficient μ .	121
Figure 7.19	<i>Left:</i> Outcome of the shake table experiment on the quarter-scale wooden block model together with the table acceleration and displacement of the compressed (by a factor of 2) motion to which the block was subjected. <i>Right:</i> Computed response by <i>Working Model</i> simulations on the full-scale equipment prototype subjected to the uncompressed motion. The simulations were done for three values of the friction coefficient μ .	122
Figure 7.20	<i>Left:</i> Outcome of the shake table experiment on the quarter-scale wooden block model together with the table acceleration and displacement of the compressed (by a factor of 2) motion to which the block was subjected. <i>Right:</i> Computed response by <i>Working Model</i> simulations on the full-scale equipment prototype subjected to the uncompressed motion. The simulations were done for three values of the friction coefficient μ .	123
Figure 7.21	<i>Left:</i> Outcome of the shake table experiment on the quarter-scale wooden block model together with the table acceleration and displacement of the compressed (by a factor of 2) motion to which the block was subjected. <i>Right:</i> Computed response by <i>Working Model</i> simulations on the full-scale equipment prototype subjected to the uncompressed motion. The simulations were done for three values of the friction coefficient μ .	124
Figure 7.22	<i>Left:</i> Outcome of the shake table experiment on the quarter-scale wooden block model together with the table acceleration and displacement of the compressed (by a factor of 2) motion to which the block was subjected. <i>Right:</i> Computed response by <i>Working Model</i> simulations on the full-scale equipment prototype subjected to the uncompressed motion. The simulations were done for three values of the friction coefficient μ .	125
Figure 7.23	<i>Left:</i> Outcome of the shake table experiment on the quarter-scale wooden block model together with the table acceleration and displacement of the compressed (by a factor of 2) motion to which the block was subjected. <i>Right:</i> Computed response by <i>Working Model</i> simulations on the full-scale equipment prototype subjected to the uncompressed motion. The simulations were done for three values of the friction coefficient μ .	126
Figure 7.24	<i>Left:</i> Outcome of the shake table experiment on the quarter-scale wooden block model together with the table acceleration and displacement of the compressed (by a factor of 2) motion to which the block was subjected. <i>Right:</i> Computed response by <i>Working Model</i> simulations on the full-scale equipment prototype	

	subjected to the uncompressed motion. The simulations were done for three values of the friction coefficient μ .	127
Figure 7.25	<i>Left</i> : Outcome of the shake table experiment on the quarter-scale wooden block model together with the table acceleration and displacement of the compressed (by a factor of 2) motion to which the block was subjected. <i>Right</i> : Computed response by <i>Working Model</i> simulations on the full-scale equipment prototype subjected to the uncompressed motion. The simulations were done for three values of the friction coefficient μ .	128
Figure 7.26	<i>Left</i> : Outcome of the shake table experiment on the quarter-scale wooden block model together with the table acceleration and displacement of the compressed (by a factor of 2) motion to which the block was subjected. <i>Right</i> : Computed response by <i>Working Model</i> simulations on the full-scale equipment prototype subjected to the uncompressed motion. The simulations were done for three values of the friction coefficient μ .	129
Figure 7.27	<i>Left</i> : Outcome of the shake table experiment on the quarter-scale wooden block model together with the table acceleration and displacement of the compressed (by a factor of 2) motion to which the block was subjected. <i>Right</i> : Computed response by <i>Working Model</i> simulations on the full-scale equipment prototype subjected to the uncompressed motion. The simulations were done for three values of the friction coefficient μ .	130
Figure 7.28	<i>Left</i> : Outcome of the shake table experiment on the quarter-scale wooden block model together with the table acceleration and displacement of the compressed (by a factor of 2) motion to which the block was subjected. <i>Right</i> : Computed response by <i>Working Model</i> simulations on the full-scale equipment prototype subjected to the uncompressed motion. The simulations were done for three values of the friction coefficient μ .	131
Figure 7.29	<i>Left</i> : Outcome of the shake table experiment on the quarter-scale wooden block model together with the table acceleration and displacement of the compressed (by a factor of 2) motion to which the block was subjected. <i>Right</i> : Computed response by <i>Working Model</i> simulations on the full-scale equipment prototype subjected to the uncompressed motion. The simulations were done for three values of the friction coefficient μ .	132
Figure 8.1	<i>Top</i> : The Engineering Demand Parameter $\Delta=U_{max}\omega_p^2/PTA$ as a function of the Intensity Measure $PTA/\mu g-1$ for the <i>Working Model</i> simulations on the three pieces of equipment. The value of μ is obtained by best-fit of numerical simulation results to shake table test results. <i>Bottom</i> : Standard deviation to the mean as a function of the Intensity Measure $PTA/\mu g-1$.	136
Figure 8.2	The empirical cumulative distribution function of the <i>EDP</i> Δ (50% and 10% hazard level motions) and the theoretical cumulative distribution function of its	

	hypothesized lognormal distribution. The value of the friction coefficient μ that the random variable Δ depends on is that obtained from the slow pull tests.	138
Figure 8.3	Fragility curves for various threshold limits, C . The curves are constructed based on the results obtained by <i>Working Model</i> simulations on the three pieces of equipment subjected to 2% in 50 years hazard level motions.	140
Figure 9.1	Photograph of the ASP refrigerator anchored to the mock non-structural wall that is nearly identical to those present at the UC Science laboratories.	142
Figure 9.2	The top photograph shows how the equipment is typically cross-chained to anchors that are screwed into the light steel framing of the wall. The bottom photograph shows the minor damage of the connection even under the very violent shaking induced by the UC Science Building 6th Floor Motion for the Cholome Array #8 record of the 1966 Parkfield, California, earthquake.	143
Figure 9.3	Comparison between recorded Peak Equipment Acceleration (<i>PEA</i>) for the Kelvinator and ASP refrigerator in freestanding and anchored configurations.	146
Figure 9.4	Shake table test results of the freestanding and anchored (cross-chained) Kelvinator refrigerator subjected to the OTE FP motion recorded during the 1995 Aigion, Greece, earthquake (left) and to the Gilroy Array #6 FN motion recorded during the 1979 Coyote Lake, California, earthquake (right).	148
Figure 9.5	Shake table test results of the freestanding and anchored (cross-chained) Kelvinator refrigerator subjected to the Cholome Array #8 FN (50% in 50 years) ground motion recorded during the 1966 Parkfield, California, earthquake (left) and to its corresponding UC Science Building 6th floor motion (right).	149
Figure 9.6	Shake table test results of the freestanding and anchored (cross-chained) Kelvinator refrigerator subjected to the Gilroy Array #6 FN (50% in 50 years) ground motion recorded during the 1979 Coyote Lake, California, earthquake (left) and to its corresponding UC Science Building 6th floor motion (right).	150
Figure 9.7	Shake table test results of the freestanding and anchored (cross-chained) Kelvinator refrigerator subjected to the Gavilan College FN (10% in 50 years) ground motion recorded during the 1989 Loma Prieta, California, earthquake (left) and to its corresponding UC Science Building 6th floor motion (right).	151
Figure 9.8	Shake table test results of the freestanding and anchored (cross-chained) Kelvinator refrigerator subjected to the Kofu FN (10% in 50 years) ground motion recorded during the 2000 Tottori, Japan, earthquake (left) and to its corresponding UC Science Building 6th floor motion (right).	152
Figure 9.9	Shake table test results of the freestanding and anchored (straight-chained) Kelvinator refrigerator subjected to OTE FP motion recorded during the 1995	

	Aigion, Greece, earthquake (left) and to the Gilroy Array #6 FN motion recorded during the 1979 Coyote Lake, California, earthquake (right).	153
Figure 9.10	Shake table test results of the freestanding and anchored (straight-chained) Kelvinator refrigerator subjected to the Cholome Array #8 FN (50% in 50 years) ground motion recorded during the 1966 Parkfield, California, earthquake (left) and to its corresponding UC Science Building 6th floor motion (right).	154
Figure 9.11	Shake table test results of the freestanding and anchored (straight-chained) Kelvinator refrigerator subjected to the Gilroy Array #6 FN (50% in 50 years) ground motion recorded during the 1979 Coyote Lake, California, earthquake (left) and to its corresponding UC Science Building 6th floor motion (right).	155
Figure 9.12	Shake table test results of the freestanding and anchored (straight-chained) Kelvinator refrigerator subjected to the Gavilan College FN (10% in 50 years) ground motion recorded during the 1989 Loma Prieta, California, earthquake (left) and to its corresponding UC Science Building 6th floor motion (right).	156
Figure 9.13	Shake table test results of the freestanding and anchored (straight-chained) Kelvinator refrigerator subjected to the Kofu FN (10% in 50 years) ground motion recorded during the 2000 Tottori, Japan, earthquake (left) and to its corresponding UC Science Building 6th floor motion (right).	157
Figure 9.14	Shake table test results of the freestanding and anchored (cross-chained) ASP refrigerator subjected to OTE FP motion recorded during the 1995 Aigion, Greece, earthquake (left) and to the Gilroy Array #6 FN motion recorded during the 1979 Coyote Lake, California, earthquake (right).	158
Figure 9.15	Shake table test results of the freestanding and anchored (cross-chained) ASP refrigerator subjected to the Cholome Array #8 FN (50% in 50 years) ground motion recorded during the 1966 Parkfield, California, earthquake (left) and to its corresponding UC Science Building 6th floor motion (right).	159
Figure 9.16	Shake table test results of the freestanding and anchored (cross-chained) ASP refrigerator subjected to the Gilroy Array #6 FN (50% in 50 years) ground motion recorded during the 1979 Coyote Lake, California, earthquake (left) and to its corresponding UC Science Building 6th floor motion (right).	160
Figure 9.17	Shake table test results of the freestanding and anchored (cross-chained) ASP refrigerator subjected to the Gavilan College FN (10% in 50 years) ground motion recorded during the 1989 Loma Prieta, California, earthquake (left) and to its corresponding UC Science Building 6th floor motion (right).	161
Figure 9.18	Shake table test results of the freestanding and anchored (cross-chained) ASP refrigerator subjected to the Kofu FN (10% in 50 years) ground motion record-	

ed during the 2000 Tottori, Japan, earthquake (left) and to its corresponding UC
Science Building 6th floor motion (right).162

LIST OF TABLES

Table 2.1	List of selected records.	8
Table 3.1	Geometric and physical characteristics of the equipment.	11
Table 3.2	Coefficients of friction and yield displacements obtained from slow pull tests and from best fitting numerical simulation results to experimental results from the shake table tests.	19
Table 4.1	Input motions for the shake table tests conducted on the three pieces of laboratory equipment. Recorded Peak Table Accelerations (<i>PTA</i>) and maximum sliding displacements (U_{max}) of the freestanding equipment.	23
Table 5.1	Kinematic characteristic of the 50% and 10% in 50 years hazard level earthquake motions used in this study. The motion <i>PTA</i> and pulse $\omega_p=2\pi/T_p$ together with the maximum recorded equipment sliding displacement U_{max} and interface friction coefficient μ produce the intensity measure <i>IM</i> and engineering demand parameter <i>EDP</i>	59
Table 7.1	Results of shake table tests on the wooden block models subjected to compressed 2% in 50 years earthquake motions. Listed are also the outcomes predicted by <i>Working Model</i> simulations on full-scale prototypes subjected to the corresponding uncompressed motions.	102
Table 8.1	Kinematic characteristic of the 2% in 50 years hazard level earthquake motions used in this study. Together with the maximum computed equipment sliding displacement U_{max} and interface friction coefficient μ , the motion <i>PTA</i> and pulse $\omega_p=2\pi/T_p$ produce the intensity measure <i>IM</i> and engineering demand parameter <i>EDP</i>	134
Table 9.1	Results of the static pull-out tests performed in order to determine the strength of the connection. Tabulated is the force on the chain required to fail the connection when the chain is (a) at a 15°-angle from the wall (cross-chained) and (b) perpendicular to the wall (straight-chained).	144
Table 9.2	Recorded Peak Equipment Acceleration (<i>PEA</i>) for the freestanding and anchored shake table tests on the Kelvinator and ASP refrigerators.	145

LIST OF SYMBOLS

α	stockiness of a piece of equipment in planar rocking (see Fig. 6.1)
α_D	stockiness of a piece of equipment along the plane of D (see Fig. 3.2)
α_W	stockiness of a piece of equipment along the plane of W (see Fig. 3.2)
β	dimensionless parameter that controls the shape of the hysteretic loop in the Bouc-Wen model
γ	dimensionless parameter that controls the shape of the hysteretic loop in the Bouc-Wen model
Δ	$= U_{max}\omega_p^2 / PTA$, dimensionless random variable used as the <i>EDP</i> in this study
$\bar{\Delta}$	mean of Δ
θ	uplift rotation
$\dot{\theta}_-$	angular velocity immediately before impact
$\dot{\theta}_+$	angular velocity immediately after impact
λ	mean of X
μ	coefficient of friction
μ_k	coefficient of kinetic friction
μ_s	coefficient of static friction
Π_1, Π_2	dimensionless products obtained by formal dimensional analysis
ρ	density
σ_Δ	standard deviation of $\Delta = U_{max}\omega_p^2 / PTA$
φ	phase angle of a Type- C_n pulse
ω	standard deviation of X
ω	angular velocity vector

ω_p	circular frequency of a trigonometric pulse that approximates the predominant distinguishable pulse of an earthquake excitation
a_p	amplitude of a rectangular acceleration pulse
B	rigid block
C	threshold value for the <i>EDP</i>
D	depth of a piece of equipment (distance between leg supports)
DM	Damage Measure
DV	Decision Variable
e	coefficient of restitution
e_{max}	maximum value of the coefficient of restitution for which a block will undergo rocking motion
$\{\mathbf{e}_1, \mathbf{e}_2, \mathbf{e}_3\}$	corotational basis
$\{\mathbf{E}_1, \mathbf{E}_2, \mathbf{E}_3\}$	Cartesian basis
<i>EDP</i>	Engineering Demand Parameter
f	time-derivative of x
f_Δ	probability density function of Δ
f_x	horizontal reaction force
f_y	vertical reaction force
F	force vector
F_Δ	cumulative distribution function of Δ
F_Δ^*	empirical cumulative distribution function of Δ
g	acceleration of gravity
$g[A B]$	occurrence frequency of A given B
H	height of a piece of equipment

$\mathbf{H}_{-}^{O'}$	angular momentum vector about point O' immediately before impact
$\mathbf{H}_{+}^{O'}$	angular momentum vector about point O' immediately after impact
IM	Intensity Measure
\mathbf{J}	inertia tensor about the center of mass
m	mass
\mathbf{M}	“mass matrix” in the ODE system for slide-rocking
$\bar{\mathbf{M}}$	moment about the center of mass
M_W	earthquake magnitude
n	parameter that controls the smoothness of the transition from the elastic to plastic region in the Bouc-Wen model
p	frequency parameter of a piece of equipment (in planar rocking)
$p[A B]$	probability density of A given B
p_D	frequency parameter of a piece of equipment along the plane of D
p_W	frequency parameter of a piece of equipment along the plane of W
P_f	fragility
PEA	Peak Equipment Acceleration
PGA	Peak Ground Acceleration
PGD	Peak Ground Displacement
POE	Probability of Exceedence
PTA	Peak Table Acceleration
Q	post-yield force
Q_θ	generalized force along coordinate θ
Q_x	generalized force along coordinate x
r	correlation coefficient (r^2 : determination coefficient)

$\bar{\mathbf{r}}$	position vector of the center of mass
\mathbf{r}_p	position vector of contact point P
R	distance from the pivot point to the axis parallel to \mathbf{e}_3 that passes through the center of mass (planar rocking) (see Fig. 6.1)
R_D	distance from the pivot point to the axis parallel to \mathbf{e}_1 that passes through the center of mass (see Fig. 3.2)
R_W	distance from the pivot point to the axis parallel to \mathbf{e}_3 that passes through the center of mass (see Fig. 3.2)
S	distance between F_Δ and F_Δ^*
S_a	design spectral acceleration
S_C	NEHRP soil-type classification
t	time
t^*	time when impact occurs
T	kinetic energy
\bar{T}	translational kinetic energy
T°	rotational kinetic energy
T_p	period of a trigonometric pulse that approximates the predominant distinguishable pulse of an earthquake excitation
u	relative displacement of sliding mass
\mathbf{u}	position vector of an infinitesimal mass element
u_g	ground displacement
u_y	yield displacement
U_{max}	equipment maximum sliding displacement
$\bar{\mathbf{v}}$	velocity vector of the center of mass
\mathbf{v}_-	velocity vector of an infinitesimal mass element immediately before impact

\mathbf{v}_+	velocity vector of an infinitesimal mass element immediately after impact
v_p	amplitude of a velocity pulse that approximates the predominant velocity pulse of an earthquake excitation
W	width of a piece of equipment (distance between leg supports)
x	\mathbf{E}_1 -component of the position vector of the pivot point O or O'
\mathbf{x}	state variable vector
\bar{x}	horizontal component of the position vector of the center of mass
x_-	the value of x immediately before impact
x_+	the value of x immediately after impact
X	normally distributed random variable so $X = \ln \Delta$
\bar{y}	vertical component of the position vector of the center of mass
z	dimensionless hysteretic variable in the Bouc-Wen model

1 Introduction

1.1 MOTIVATION

During strong earthquake shaking, heavy equipment located at various floor levels of hospitals, university laboratories, and other critical facilities may slide appreciably, slide-rock, rock, or even overturn. Rocking response is very sensitive to the geometry of the rocking object and the kinematic characteristics of the ground. Minor variations in the input can result in overturning—*catastrophe* (Yim et al. 1980; Makris and Roussos 2000; Makris and Konstantinidis 2003a). Therefore, rocking is in principle an undesirable response for the equipment because it is often the cause of mechanical damage or total loss in the event of overturning. Yet even if overturning does not occur, the high acceleration spikes that develop during impact of the rocking equipment are a major concern, since they can result in serious damage or loss of the vulnerable and precious equipment contents.

Of the possible modes of response, sliding is the most favorable. Nonetheless, *excessive* sliding displacements may block a path or doorway that services evacuation. Large displacements of sensitive/heavy equipment that result in impact with walls or neighboring equipment should be avoided, since the resulting acceleration spikes endanger the contents or even the equipment itself. In practice, excessive sliding is prevented by restraining the equipment—commonly by chaining it to the framing of the nearby wall. Although this may succeed in reducing sliding displacements, it substantially amplifies accelerations.

1.2 BACKGROUND AND TESTBED

1.2.1 Overview of the PEER Methodology

This research is part of a larger study that sets out to apply the PEER-proposed performance-based earthquake engineering (PBEE) methodology on a specific testbed: an actual science labo-

ratory building, herein referred to as *UC Science Building*. Performance-based earthquake engineering implies design, evaluation, and construction of engineered facilities whose performance under common and extreme loads responds to the diverse needs and objectives of owners-users and society (Comerio 2005).

The PEER PBEE methodology consists of four stages (Porter 2003):

- Hazard analysis. In this stage, the seismic environment of the facility site (e.g., fault distances, fault mechanisms, occurrence intervals, site soil conditions) is used to evaluate a seismic hazard considering various facility features (e.g., structural and architectural features). This includes the selection or generation of sets of ground-motion time histories whose *Intensity Measures, IM* (e.g., *Peak Ground Acceleration, PGA, Peak Ground Displacement, PGD*), characterize varying levels of seismic hazard (e.g., one set for events with *Probability of Exceedence, POE*, of 50% in 50 years, one with *POE* of 10% in 50 years, and one with *POE* of 2% in 50 years).
- Structural analysis. In this stage, a structural model of the facility is created, and nonlinear dynamic analyses are performed in order to compute the response of the facility to ground motions of a given *IM*. This produces *Engineering Demand Parameters, EDP* (e.g., floor accelerations, interstory drifts).
- Damage analysis. In this stage, the above-determined *EDP*'s are used as input to component fragility functions in order to determine *Damage Measures, DM*, to the facility components (e.g., beams, columns, building contents).
- Loss analysis. Given the determined *DM*, the performance of the facility is evaluated. This performance is parametrized by *Decision Variables, DV*, that are of greatest concern to the stakeholders (e.g., deaths, dollars, downtime).

Each relationship, from the facility features (location and design) to the *IM*, from the *IM* to the *EDP*, from the *EDP* to the *DM*, and from the *DM* to the *DV*, involves uncertainty and is therefore treated probabilistically. The PEER methodology can be summarized mathematically by

$$g[DV|D] = \int_{DM} \int_{EDP} \int_{IM} p[DV|DM, D] p[DM|EDP, D] p[EDP|IM, D] g[IM|D] dIM dEDP dDM \quad (1.1)$$

where $p[A|B]$ denotes the probability density of A conditioned on knowledge of B , and $g[A|B]$ is the occurrence frequency of A given B (Porter 2003).

1.2.2 Testbed: The UC Science Research Facility

There is a class of buildings, such as museums, high-tech fabrication facilities, hospitals, and research laboratories, in which the contents far outcost the structure itself (Comerio 2005). Oftentimes the contents can also pose a credible health hazard to the building occupants or even the general public. For instance, spillage or leakage of hazardous agents in a laboratory due to an earthquake can cause serious injuries or deaths. Research facilities, which often occupy a relatively large percentage of the campus space in universities, concentrate a significant portion of the university's research funding, valuable equipment, and ideas. The testbed for this study, the UC Science Building, is such a research facility.

The UC Science Building is located on the western part of the main UC Berkeley campus and is approximately 1 km west of the Hayward fault (Fig. 1.1 top). The building is six stories tall plus a basement. The basement is contained within the perimeter of the approximately 306-ft (north-south) by 105-ft (east-west) building (Fig. 1.1 bottom). It is a modern structure that was completed in 1988 in order to provide high-tech research laboratories. It is 203,800 sq ft overall, of which 122,000 sq ft are used for research laboratories, animal facilities, offices, and related support spaces (Comerio 2005).

The gravity load-carrying system of the structure consists of a reinforced concrete space frame. The floors consist of waffle slab systems with solid parts acting as integral beams between columns. The lateral force-resisting system consists of coupled shear walls in the east-west direction and perforated shear walls in the north-south direction. The building foundation is a 38-in.-thick mat. It is worth noting that the particular facility was chosen to apply the PEER PBEE methodology because the structural system is expected to perform well in earthquakes. In fact, the seismic performance of the building was rated above average: "operational" to "safe" for moderate (72-year return period) to extreme seismic events (2500-year return period) (UCB 1997; Comerio 2000). The attention of the research could therefore be concentrated on the performance of the valuable building contents and their contribution to losses, in particular downtime (Comerio 2005).

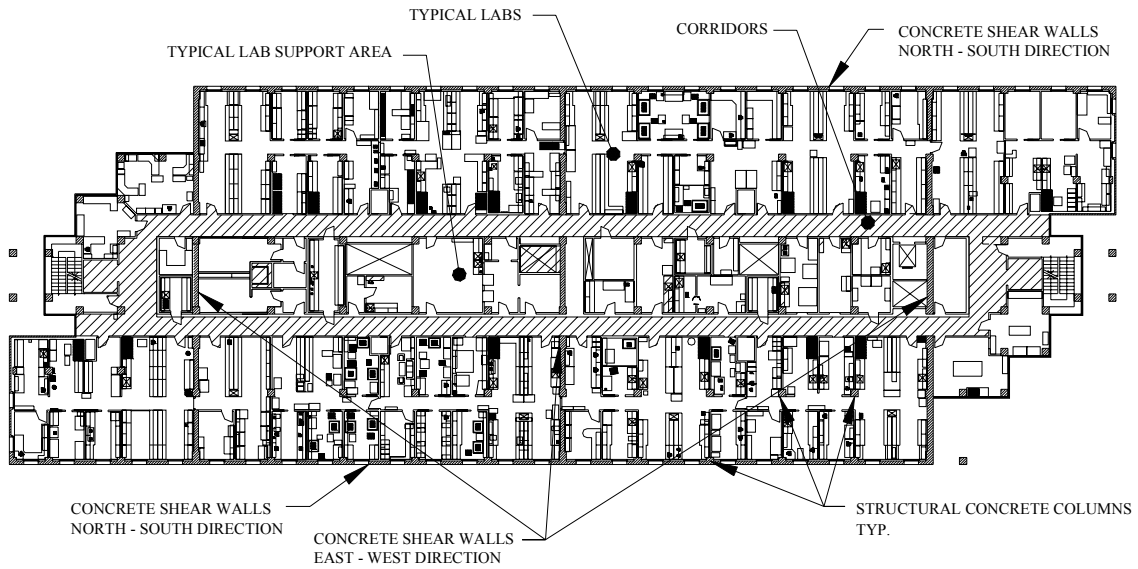


Figure 1.1 *Top*: Location of the UC Science Laboratory Building. The heavy dashed line traces the nearby Hayward fault. *Bottom*: Typical floor plan of the UC Science research facility (from Comerio 2005).

1.3 OBJECTIVES OF THE RESEARCH

In this project, experimental and analytical studies were undertaken to examine the seismic vulnerability of freestanding and restrained laboratory equipment located in the UC Science Building laboratories within several floor levels. The equipment of interest included low-temperature refrigerators, freezers, incubators, and other heavy equipment.

The dynamic behavior of either freestanding or restrained equipment is sensitive to many parameters, including the characteristics of the base input (mainly peak base acceleration and duration of the predominant acceleration pulse of the excitation), the frictional characteristics of the equipment-base interface, and the slenderness of the equipment. The results of the shake table tests were used to arrive at relationships that describe a meaningful dimensionless engineering demand parameter, *EDP*, as a function of intensity measure, *IM*, and mechanical properties of the equipment, *D*. Since uncertainties are inherent in all stages of the PEER methodology, a probabilistic approach was taken. Finally, an analysis was performed to generate *fragility curves*, which give the probability that the aforementioned *EDP* will exceed a specified limit as a function of the *IM* and *D*.

Due to displacement limitations of the shake table, experiments could only be performed for lower to intermediate hazard levels. The results obtained were used to validate/calibrate analytical tools which, in turn, were used to compute the response of heavy laboratory equipment to higher hazard levels. The results were used in the above recipe: construct a relationship between the *EDP* and the *IM* and *D*, and generate fragility curves for various limit values.

2 Seismic Hazard and Structural Analysis

The seismic hazard study for the UC Science testbed was performed by Somerville (2001), while the structural response analysis was performed by Lee and Mosalam (2005).

2.1 SEISMIC HAZARD

The seismic hazard on the Berkeley campus is dominated by potential ground motions generated from the Hayward fault, which is located approximately one kilometer east of the site. The Hayward fault is a strike-slip fault that has a potential to generate earthquakes having magnitudes as large as $M_W = 7.0$. The ground motions for the site were selected and scaled to correspond to three hazard levels: (1) events with Probability of Exceedence, *POE*, equal to 50% in 50 years, (2) events with *POE* 10% in 50 years, and (3) events with *POE* 2% in 50 years. For a hazard level equal to 50% in 50 years, the largest contributions come from earthquakes in the magnitude range of $M_W = 5.5$ to $M_W = 6.0$. For hazard level equal to 10% in 50 years and to 2% in 50 years, the largest contributions come from earthquakes in the magnitude range of $M_W = 6.5$ to $M_W = 7.0$. It is noteworthy that the higher 2% in 50% hazard levels do not reflect larger magnitudes (as the Hayward fault can generate earthquakes only up to $M_W = 7.0$) but rather stronger ground motions with the *same* magnitude (with larger standard deviation above the mean) (Somerville 2001).

The motions listed in Table 2.1 have been selected to satisfy (to the extent possible) the magnitude and distance combination from a strike-slip earthquake on NEHRP-classified S_C soil type.

2.2 STRUCTURAL ANALYSIS

The interest of the UC Berkeley administration in the seismic response of the UC Science Laboratory Building supported a comprehensive nonlinear dynamic analysis of the building. The task

Table 2.1 List of selected records.

Earthquake	Record	M_W	Distance [km]	Hazard Level
Aigion, Greece June 15, 1995	OTE, FP (ground)	6.2	5.0	-
Coyote Lake, California August 6, 1979	Gilroy Array #6, FN (ground)	5.7	3.0	-
Parkfield, California June 27, 1966	Cholome Array #6, FN (ground and 6th floor)	6.0	8.0	50% in 50 years
Coyote Lake, California August 6, 1979	Gilroy Array #6, FN (ground)	5.7	3.0	50% in 50 years
Loma Prieta, California October 17, 1989	Gavilan College, FN (ground and 6th floor)	7.0	9.5	10% in 50 years
Tottori, Japan October 6, 2000	Kofu, FN (ground and 6th floor)	6.6	10.0	10% in 50 years
Loma Prieta, California October 17, 1989	Los Gatos PC, FP (ground)	7.0	3.5	2% in 50 years
Loma Prieta, California October 17, 1989	Corralitos, FP (ground)	7.0	3.4	2% in 50 years
Loma Prieta, California October 17, 1989	Gilroy Historic Bldg., FN (ground and 6th floor)	7.0		2% in 50 years

was undertaken by Lee and Mosalam (2005) who developed an elaborate structural model of the UC Science research facility. The model was created in *OpenSees*, a PEER-sponsored software framework that simulates the performance of structural and geotechnical systems subjected to earthquakes (McKenna and Fenves 2001). Modeling and analysis in *OpenSees* incorporates recent model developments to improve on the accuracy of the computed seismic response.

Lee and Mosalam (2002) performed nonlinear time-history analyses of the structural model subjected to all the selected ground records. These analyses resulted in simulated floor motions. Floor motions are of unique interest in assessing the seismic response of building contents, since they differ appreciably from ground motions. Table 2.1 lists the recorded ground-acceleration motions and the simulated floor-acceleration motions that were used as input for the shake table experiments conducted in this study.

3 Laboratory Equipment and Friction Experiments

3.1 SLENDER LABORATORY EQUIPMENT

The equipment of interest included incubators, low-temperature freezers, refrigerators, and other heavy laboratory equipment of the UC Science Building at the UC Berkeley campus. In particular, three pieces of equipment were obtained from the building laboratories in order to examine their mechanical properties and to perform shake table tests. Figure 3.1 shows pictures of the equipment, while Table 3.1 lists their geometric and physical characteristics. Figure 3.2 is a schematic of a piece of equipment that shows the geometric quantities that are listed in Table 3.1. Each piece of equipment has two vertical faces, designated here by W for *width* and D for *depth*. The stockiness angles α_W and α_D of a piece of equipment are defined by

$$\alpha_W = \tan^{-1}\left(\frac{W}{H}\right) \quad \text{and} \quad \alpha_D = \tan^{-1}\left(\frac{D}{H}\right) \quad (3.1)$$

The stockiness of a block is an indicator of its disposition to enter rocking motion. The smaller the stockiness, the more likely for the equipment to uplift, enter rocking motion, and possibly overturn. The frequency parameters p_W and p_D are measures of the size of the equipment and are given by

$$p_W = \sqrt{\frac{3g}{4R_W}} \quad \text{and} \quad p_D = \sqrt{\frac{3g}{4R_D}} \quad (3.2)$$

where g is the acceleration of gravity and $R_W = \sqrt{H^2 + W^2} / 2$, $R_D = \sqrt{H^2 + D^2} / 2$ (Fig. 3.2). The larger the block (larger R), the smaller p . It is interesting to note that when two geometrically similar blocks (same stockiness angle α) of different size (different frequency parameter p) experience free vibrations with the same initial conditions, $\theta(0) = \theta_o$ and $\dot{\theta}(0) = 0$, each



FORMA Incubator



Kelvinator Refrigerator



ASP Refrigerator

Figure 3.1 The three pieces of freestanding heavy laboratory equipment that were obtained from the UC Science research facility for the purposes of this study.

Table 3.1 Geometric and physical characteristics of the equipment.

Equipment	<i>Weight</i> [lb.]	<i>H</i> [in]	<i>W</i> (<i>W_{out}</i>) [in]	<i>D</i> (<i>D_{out}</i>) [in]	<i>R_W</i> [in]	<i>R_D</i> [in]	α_W [rad]	α_D [rad]	<i>p_W</i> [rad/s]	<i>p_D</i> [rad/s]
<i>FORMA</i> Reach-In Incubator	850	90.0	36.5 (38.0)	24.5 (31.0)	48.6	46.6	0.39	0.27	2.44	2.49
<i>KELVINATOR</i> Refrigerator/Freezer	352	84.0	25.0 (33.0)	26.0 (32.5)	43.8	44.0	0.29	0.30	2.57	2.57
<i>AMERICAN SCIENTIFIC</i> Refrigerator	162	71.0	30.0 (32.0)	23.0 (26.5)	38.5	37.3	0.40	0.31	2.74	2.79

response cycle of the larger block (smaller p) is longer than the corresponding response cycle of the smaller block (larger p) (Housner 1963; Makris and Konstantinidis 2003a). Accordingly, the quantity p is a measure of the dynamic characteristics of the block. For planar pure rocking motion (no sliding), the frequency parameter p and the stockiness α of the block are the two parameters in the equation of motion.

Besides rocking, sliding and slide-rocking are possible modes of response for the laboratory equipment. The study of the interface between the equipment and the floor surfaces on which the equipment rests inside the UC Science laboratories was imperative.

3.2 FRICTION TESTS

The mechanical properties of the contact interface between the equipment and the laboratory floors were determined by conducting slow pull tests on the equipment. The floors throughout the UC Science Building are lined with vinyl tiles. In order to simulate the actual conditions, a 4-ft x 8-ft pressboard surface covered with identical vinyl tiles was constructed. Atop it rested the equipment specimens. Figure 3.3 shows a schematic of the experimental setup of the pull tests conducted on the equipment.

Figures 3.4 through 3.6 plot load-displacement curves recorded during the quasi-static pull tests on the three pieces of equipment shown in Figure 3.1. All three sets of curves shown in Figures 3.4 through 3.6 exhibit a peak value when sliding initiates and subsequently a relatively constant friction force, Q , while sliding occurs. The pre-yielding elasticity in the load-displacement curves originates from the flexure of the legs of the equipment prior to sliding. This pre-yielding elasticity of the legs and the friction force that develops along the vinyl surface combine to a yielding mechanism of the interface. A simple idealization of the yielding mechanism of the interface is the elastoplastic model shown with dashed lines in Figures 3.4 to 3.6. The model parameters that define the elastoplastic idealization are the yield displacement, u_y , and the normalized strength, $\mu_k = Q / mg$, where Q is the post-yield constant force. Another idealization of the contact interface is that of classical Coulomb friction where a static friction coefficient, μ_s , and a kinetic friction coefficient, μ_k , are used.

Simulation studies on the sliding response of the equipment using the elastoplastic model with the values of the friction coefficient μ_k extracted from the slow pull tests yielded results

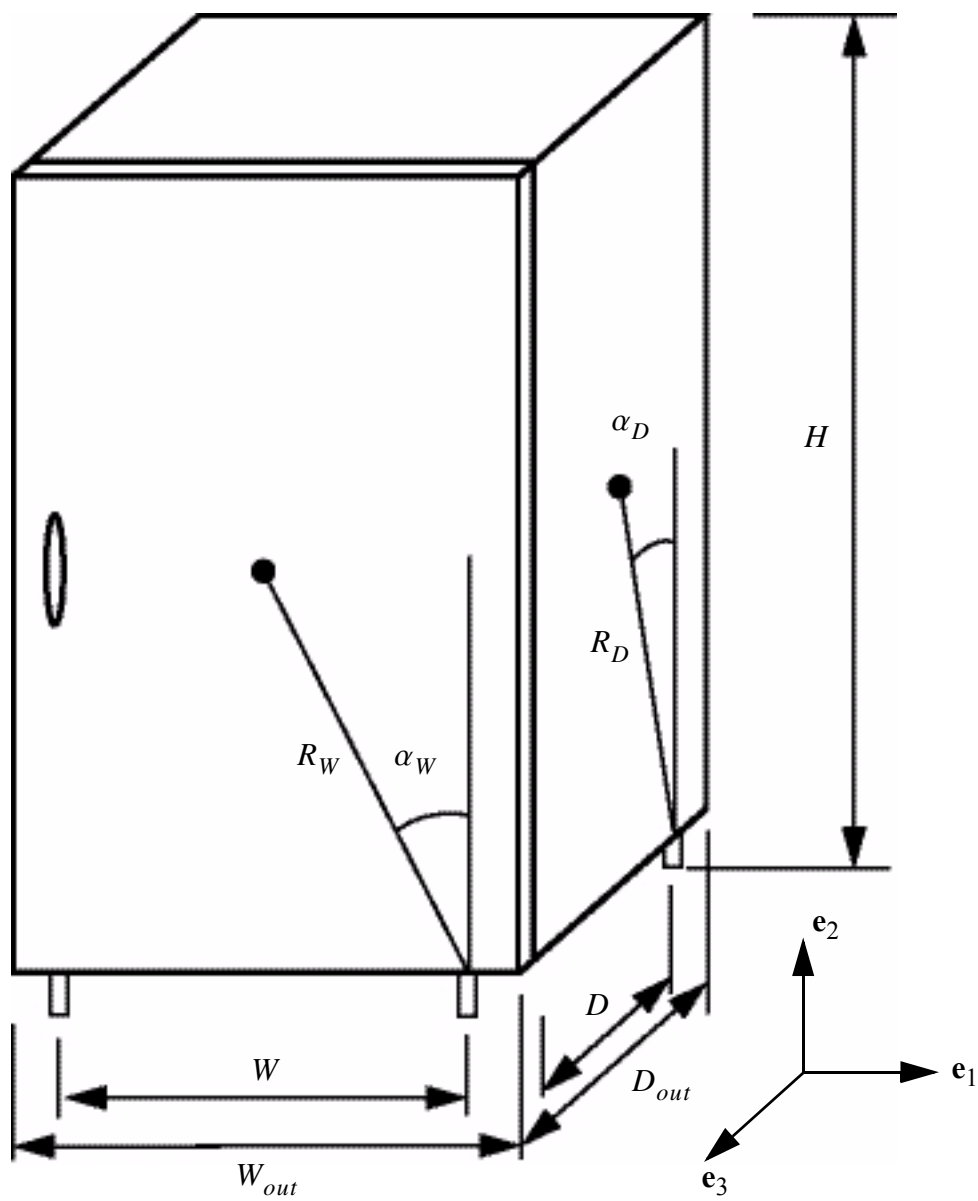


Figure 3.2 Schematic of a piece of equipment.

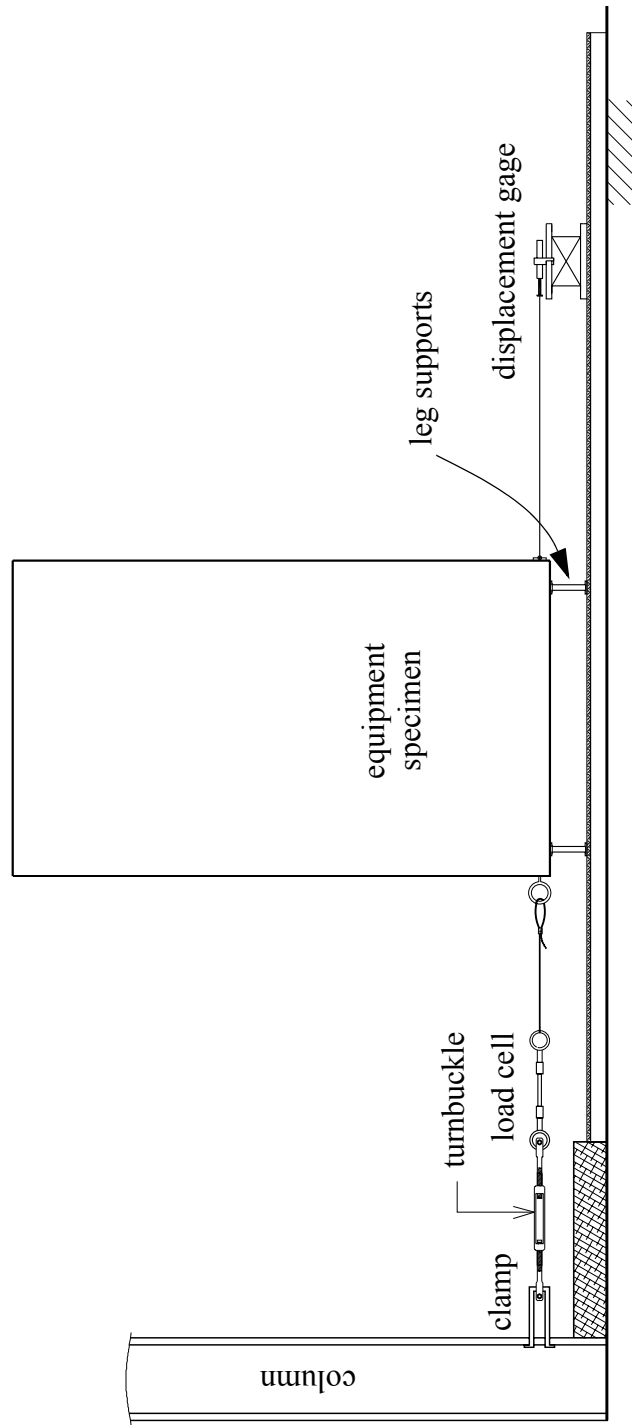


Figure 3.3 Schematic diagram of the experimental setup for the quasi-static pull tests.

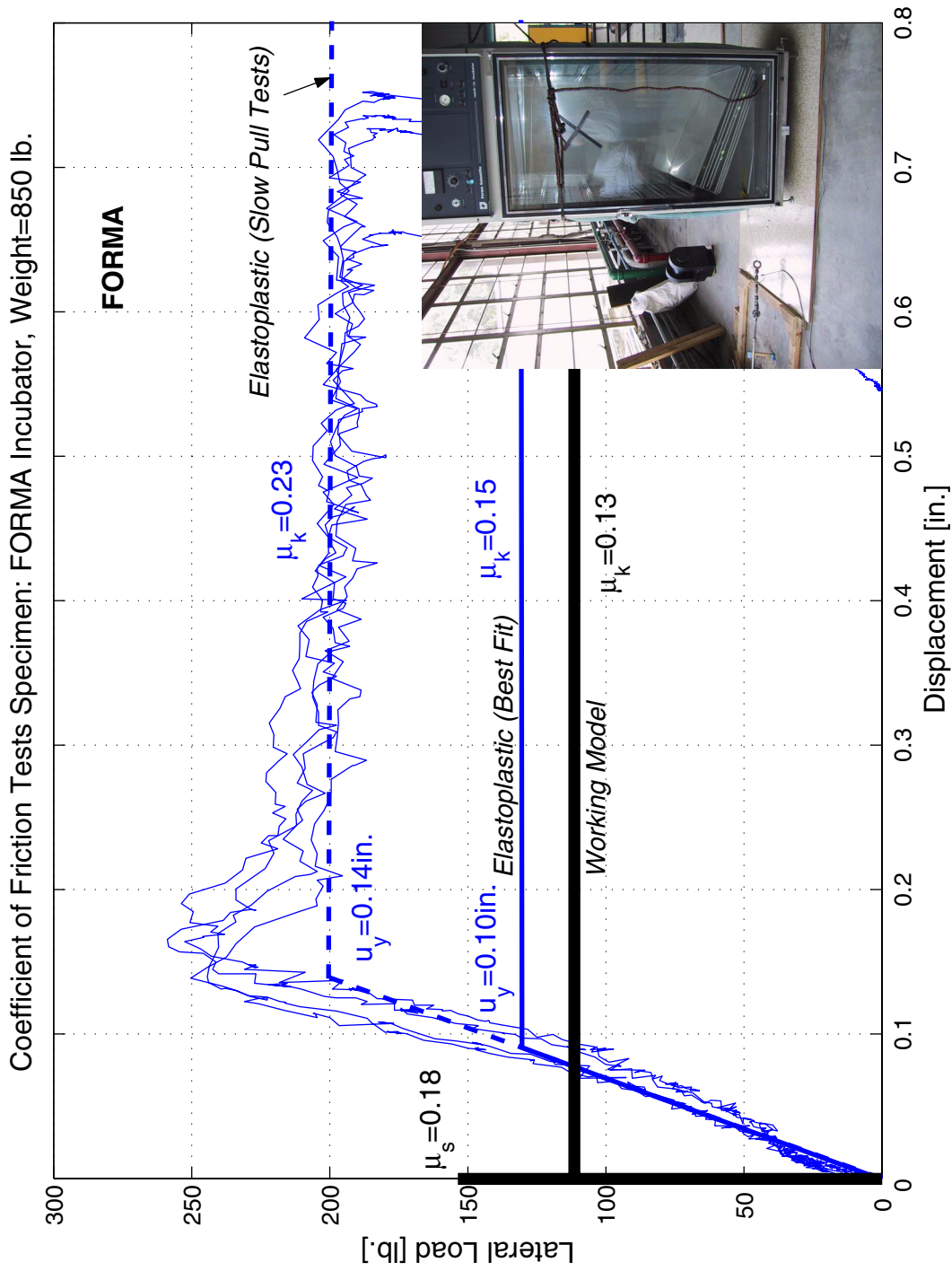


Figure 3.4 Recorded load-displacement plots for the FORMA incubator obtained from the slow pull tests (wavy lines); the elastoplastic idealization with μ_k from the slow pull tests (dashed line); the elastoplastic idealization with μ_k from the best fit of the shake table test data (solid line); the Coulomb friction model calibrated to best fit data obtained from the shake table tests (heavy line).

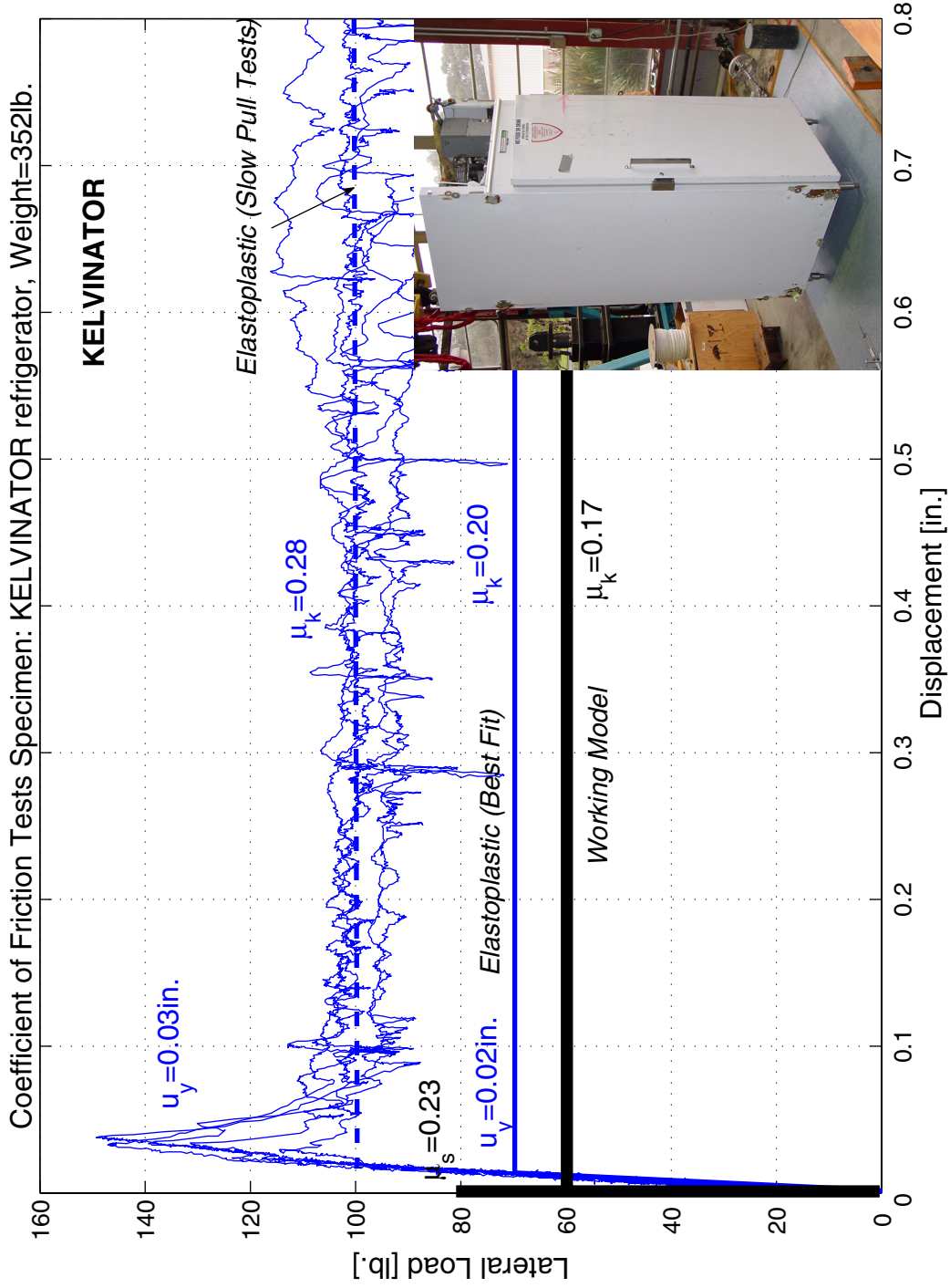


Figure 3.5 Recorded load-displacement plots for the Kelvinator refrigerator obtained from the slow pull tests (wavy lines); the elastoplastic idealization with μ_k from the slow pull tests (dashed line); the elastoplastic idealization with μ_k from the best fit of the shake table test data (solid line); the Coulomb friction model calibrated to best fit data obtained from the shake table tests (heavy line).

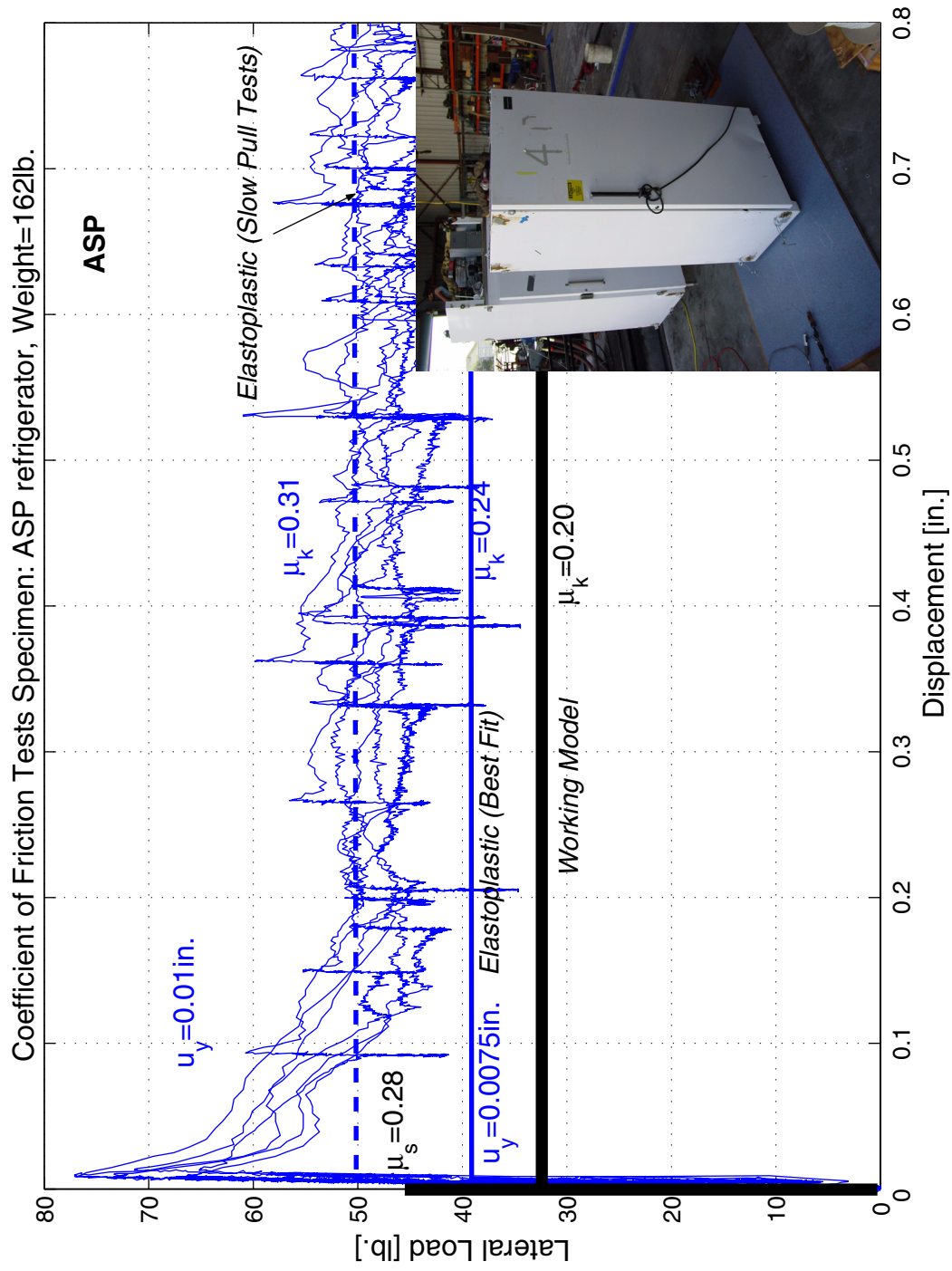


Figure 3.6 Recorded load-displacement plots for the ASP refrigerator obtained from the slow pull tests (wavy lines); the elastoplastic idealization with μ_k from the slow pull tests (dashed line); the elastoplastic idealization with μ_k from the best fit of the shake table test data (solid line); the Coulomb friction model calibrated to best fit data obtained from the shake table tests (heavy line).

which are in fair agreement with the experimental data. The predicted response of all three pieces of equipment was appreciably improved when lower values of their respective friction coefficients were used. The lower friction levels of the elastoplastic idealization of the contact-interface yielding mechanism are indicated in Figures 3.4 to 3.6 with solid lines. The heavy solid lines shown in Figures 3.4 to 3.6 correspond to the Coulomb model with reduced friction coefficients. The reduced values of the coefficients of static friction μ_s and coefficients of kinetic friction μ_k have been obtained by best-fitting results from numerical simulations using the commercially available software *Working Model* (2000) to results obtained from shake table experiments. Table 3.2 summarizes the values of friction coefficients and yield displacements that were obtained from the slow pull tests and from the best fit of the data obtained from shake table studies. The prediction of the recorded response using the values of the coefficients of friction shown in Figures 3.4 to 3.6 and Table 3.2 and a further discussion of the elastoplastic and the Coulomb models of the contact interface are offered in Chapters 5 and 6.

Table 3.2 Coefficients of friction and yield displacements obtained from slow pull tests and from best fitting numerical simulation results to experimental results from the shake table tests.

Equipment	Values from <i>Slow Pull Tests</i>		Values used to fit <i>Elastoplastic Model</i> simulation data to experimental data from the shake table tests		Values used to fit <i>Coulomb Friction Model</i> simulation data to experimental data from the shake table tests		
	μ_s	μ_k	u_y [in]	μ_k	u_y [in]	μ_s	μ_k
<i>FORMA</i> Incubator	0.30	0.23	0.14	0.15	0.10	0.18	0.13
<i>Kelvinator</i> Refrigerator	0.37	0.28	0.03	0.20	0.02	0.23	0.17
<i>ASP</i> Refrigerator	0.43	0.31	0.01	0.24	0.0075	0.28	0.20

4 Shake Table Tests of Freestanding Laboratory Equipment

The three pieces of equipment shown in Figure 3.1 were subjected to shake table tests at the Richmond Field Station Earthquake Simulator Laboratory, UC Berkeley. The same type of pressboard surface that was used as the base for the slow pull tests was positioned atop the shake table to support the equipment. Figure 4.1 shows a photograph of one of the freestanding equipment resting on the shake table.

The displacement of the shake table and the equipment were measured with wire transducers attached to a frame fixed on the laboratory floor. Figure 4.1 shows the locations of the wire transducers on the test specimen with heavy white lines. Accelerometers were also installed on the positions shown with black arrows in Figure 4.1 in order to capture horizontal and vertical accelerations.

The horizontal displacement capacity of the shake table at the Richmond Field Station is ± 6.0 in. Given this constraint, experiments at full scale were run only for the ground motions with hazard level equal to 50% in 50 years and 10% in 50 years. Shake table tests using the stronger ground motions with probability of exceedence equal to 2% in 50 years were conducted on scaled-down models by compressing the duration of the records. These shake table tests are discussed in Chapter 7 of this report.

Table 4.1 presents a list of the shake table tests conducted on the full-scale freestanding equipment that are shown in Figure 3.1. On all the tests listed in Table 4.1 the shake table excitation was one-directional. The motion of the equipment was mostly along the direction of the input excitation. However, in several occasions the equipment while shaken along the primary direction, exhibited rotations about its vertical axis. In some cases these plane rotations were as small as 0.005 rad, while in others as large as 0.33 rad, indicating that even when the excitation is one-directional, the response is in fact in three dimensions.



Figure 4.1 The FORMA incubator resting atop the shake table at the Richmond Field Station Earthquake Simulation Laboratory. The locations of the wire transducers are indicated with white lines, and the locations of the accelerometers are indicated with dark arrows.

Table 4.1 Input motions for the shake table tests conducted on the three pieces of laboratory equipment. Recorded Peak Table Accelerations (PTA) and maximum sliding displacements (U_{max}) of the freestanding equipment.

Earthquake	Record	Hazard Level	PGA [g]	Equipment							
				FORMA FACE		KELVIN FACE		ASP PROFILE			
				PTA [g]	U_{max} [in]	PTA [g]	U_{max} [in]	PTA [g]	U_{max} [in]		
Aigion, Greece 6/15/1995	OTE FP		0.50	0.75	6.9	0.76	6.0	0.86	3.2	0.73	2.4
Coyote Lake, California 8/6/1979	Gilroy Array #6 FN		0.47	0.68	2.6	0.69	2.1	0.73	1.6	0.70	1.0
Parkfield, California 6/27/1966	Cholome Array #8 FN	50% in 50 yrs	0.56	0.70	3.7	0.75	1.3	0.77	0.8	0.70	0.3
Parkfield, California 6/27/1966	Cholome Array #8 FN	50% in 50 yrs	0.71	1.61	13.5	1.66	8.9	1.70	22.8	1.68	23.7
Coyote Lake, California 6/8/1979	Gilroy Array #6 FN GROUND	50% in 50 yrs	0.47	0.75	3.1	0.74	3.3	0.76	3.6	0.75	3.7
Coyote Lake, California 6/8/1979	Gilroy Array #6 FN 6TH LEVEL	50% in 50 yrs	0.78	0.43	0.8	0.76	7.4	0.77	9.4	0.80	8.0
Loma Prieta, California 10/17/1989	Gavilan College FN GROUND	10% in 50 yrs	0.66	0.73	3.8	0.76	2.3	0.77	1.9	0.79	2.6
Loma Prieta, California 10/17/1989	Gavilan College FN 6TH LEVEL	10% in 50 yrs	0.75	leg failure		0.64	5.1	0.67	7.0	0.67	6.7
Tottori, Japan 10/6/2000	Kofu FN GROUND	10% in 50 yrs	0.69					1.07	13.9	1.07	16.6
Tottori, Japan 10/6/2000	Kofu FN 6TH LEVEL	10% in 50 yrs	0.54			0.81	5.2	1.08	13.9	0.85	8.0

Table 4.1 lists the earthquake records that were used to test the freestanding equipment. Also listed are the recorded Peak Table Acceleration, PTA , and the equipment peak sliding displacement, U_{max} . The PTA level of the records used in this experimental program ranged from 0.43g to 1.70 g and the U_{max} from 1 in. to as much as 24 in. The shake table tests indicated that the primary mode of response of the three pieces of equipment is sliding. In fact, the maximum recorded uplift rotation in all tests for the Kelvinator refrigerator was only 0.02 rad (0.069α) and only 0.005 rad (0.015α) for the ASP refrigerator. The maximum recorded uplift rotation for the FORMA incubator was 0.13 rad (0.489α). Although the FORMA incubator experienced larger uplift rotations than the other two specimens, these rotations were still within safe levels. Nonetheless, after about 20 tests one of the flimsy leg supports of the FORMA incubator failed due to low-cycle fatigue. The resulting instability caused overturning of the specimen.

Figure 4.2 (bottom window) plots the OTE FP ground acceleration history recorded during the 1995 Aigion, Greece, earthquake. The graph on the window above the acceleration record plots the resulting shake table displacement, and the third window from the top plots with a heavy solid line the recorded sliding displacement of the FORMA incubator. The recorded sliding displacement history shows the equipment suddenly sliding once a threshold table acceleration is exceeded (at about 3.8 sec). If the contact interface were characterized by a Coulomb friction model (and there were no uplift), then this threshold value would simply be $\mu_s g$. However, the real behavior is complicated by the fact that the contact interface exhibits a pre-yielding elasticity due to the flexibility of the equipment legs and by the possibility of uplift. The top two graphs in Figure 4.2 which plot with heavy solid lines the equipment uplift and the plane rotation (rotation about the vertical axis) show that the specimen does indeed uplift and twist just slightly even before the initiation of sliding (at about 3.65 sec).

In other cases, one mode of response does not seem to trigger the other, but rather both happen simultaneously. Figure 4.3, which plot the response of the FORMA incubator subject to the Gilroy Array #6 record of the 1979 Coyote Lake, California, earthquake, shows a sliding-uplifting-twisting coupling. Figures 4.4 to 4.6 plot the recorded response of the FORMA incubator to two 50%-in-50-years and one 10%-in-50-years hazard level earthquake motions.

The response mode coupling is less pronounced for the Kelvinator refrigerator which, although demonstrating a slightly larger coefficient of friction during the slow pull tests than the FORMA incubator ($\mu_s = 0.37$, versus $\mu_s = 0.30$), is stockier ($\alpha = 0.289$ versus $\alpha = 0.266$)

and therefore less susceptible to uplift. Figures 4.7 to 4.13 show that the Kelvinator refrigerator exhibits relatively small rotations, never exceeding 7% its stockiness angle α in any of the tests. Moreover, the Kelvinator refrigerator exhibits very small rotation about its vertical axis. The maximum recorded plane rotation in all tests performed on the Kelvinator refrigerator was 0.05 rad.

The ASP refrigerator is considerably stockier in one direction than in the other ($\alpha_W = 0.400$ versus $\alpha_D = 0.313$; see Table 3.1 and Fig. 3.2). This geometric characteristic prompted us to test this piece of equipment along both directions. When the table excitation is along the more stocky direction (W), the configuration is designated *Profile* whereas when the table excitation is along the more slender direction (D), the configuration is designated *Face*. Figures 4.14 to 4.21 plot the recorded response for all the shake table tests performed on the ASP refrigerator in the *Face* configuration, and Figures 4.22 to 4.29 plot the response in the *Profile* configuration. It is seen that the response is almost identical. Although the ASP refrigerator has the largest coefficient of friction ($\mu_s = 0.43$ evaluated from the slow pull tests), which suggests a propensity towards uplift rather than sliding, it is fairly stocky in each direction compared to the FORMA incubator and Kelvinator refrigerator. Figures 4.14 to 4.21 and 4.22 to 4.29 show that the recorded uplift rotations were in fact very small for both the *Face* and *Profile* directional tests. The maximum recorded uplift rotation did not exceed 0.005 rad (1.5% of α_D).

An interesting characteristic to note is the waviness of the heavy solid lines that plot the sliding displacement in Figures 4.2 to 4.29. In the experimental setup, the sliding displacement of the equipment was not measured exactly at the floor-equipment interface but rather right above the leg supports. Even when the equipment was not sliding, the flexibility of the supports caused the equipment to wobble. As expected, the wobbling is more pronounced for the FORMA incubator whose legs were very flexible (Fig. 3.4), less pronounced for the Kelvinator refrigerator whose legs are fairly stiff (Fig. 3.5), and almost non-existent for the ASP refrigerator whose legs are nearly rigid (Fig. 3.6).

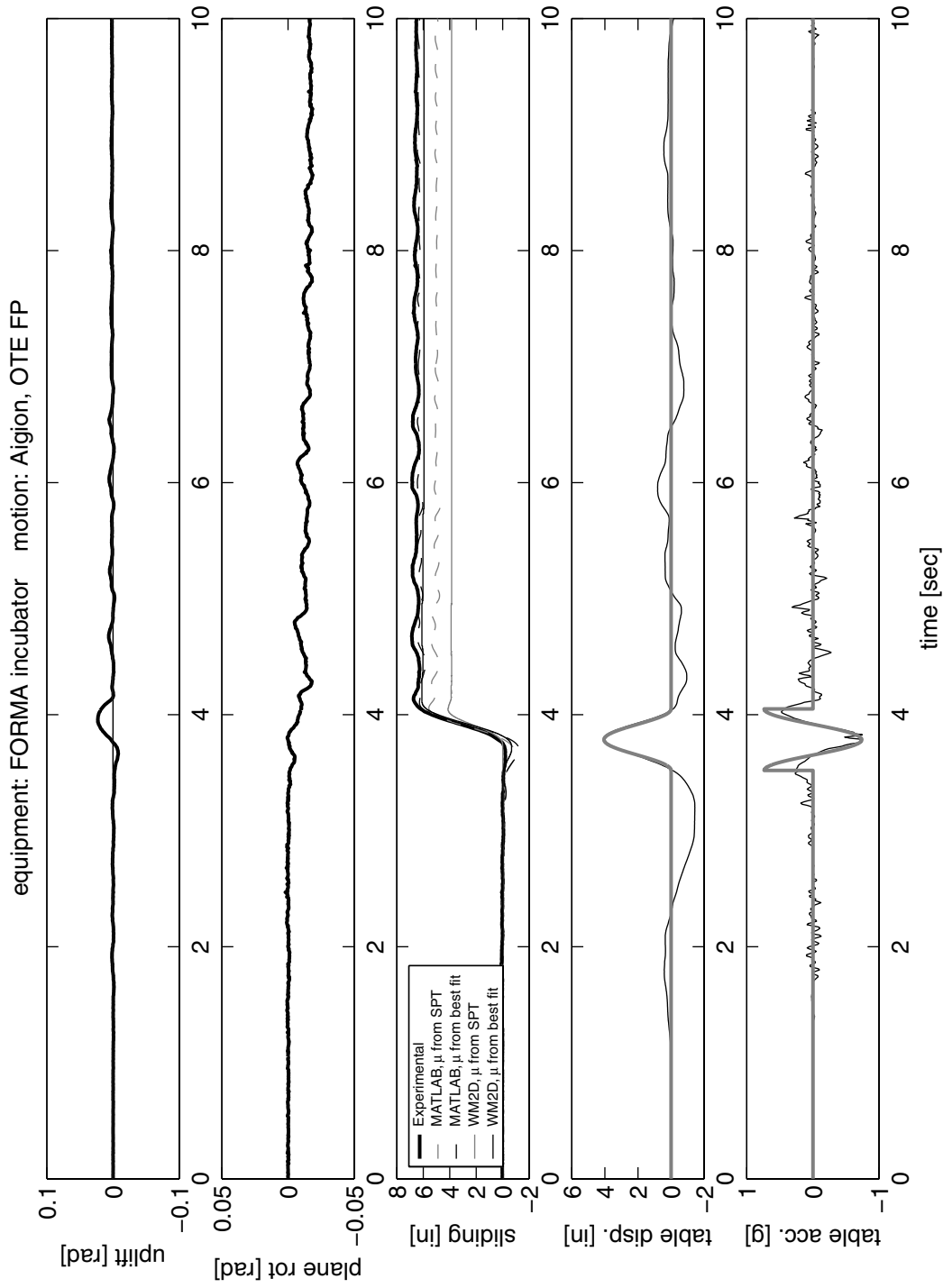


Figure 4.2 Response of the FORMA incubator subjected to the OTE FP motion recorded during the 1995 Aigion, Greece, earthquake. The heavy grey lines on the bottom two graphs plot a Type-B trigonometric pulse that approximates the main pulse of the motion record.

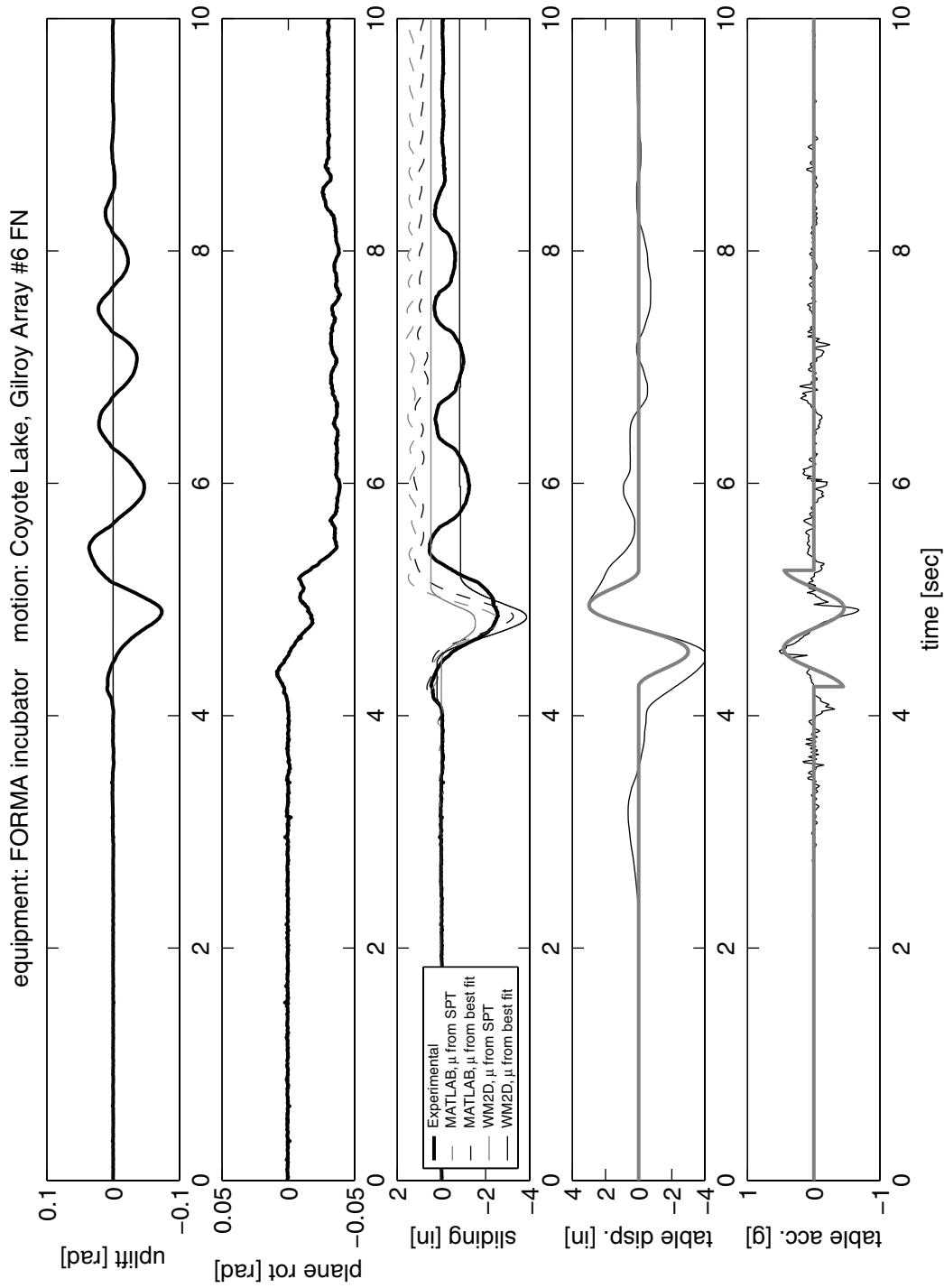


Figure 4.3 Response of the FORMA incubator subjected to the Gilroy Array #6 motion recorded during the 1979 Coyote Lake, California, earthquake. The heavy grey lines on the bottom two graphs plot a Type-C₁ trigonometric pulse that approximates the main pulse of the motion record.

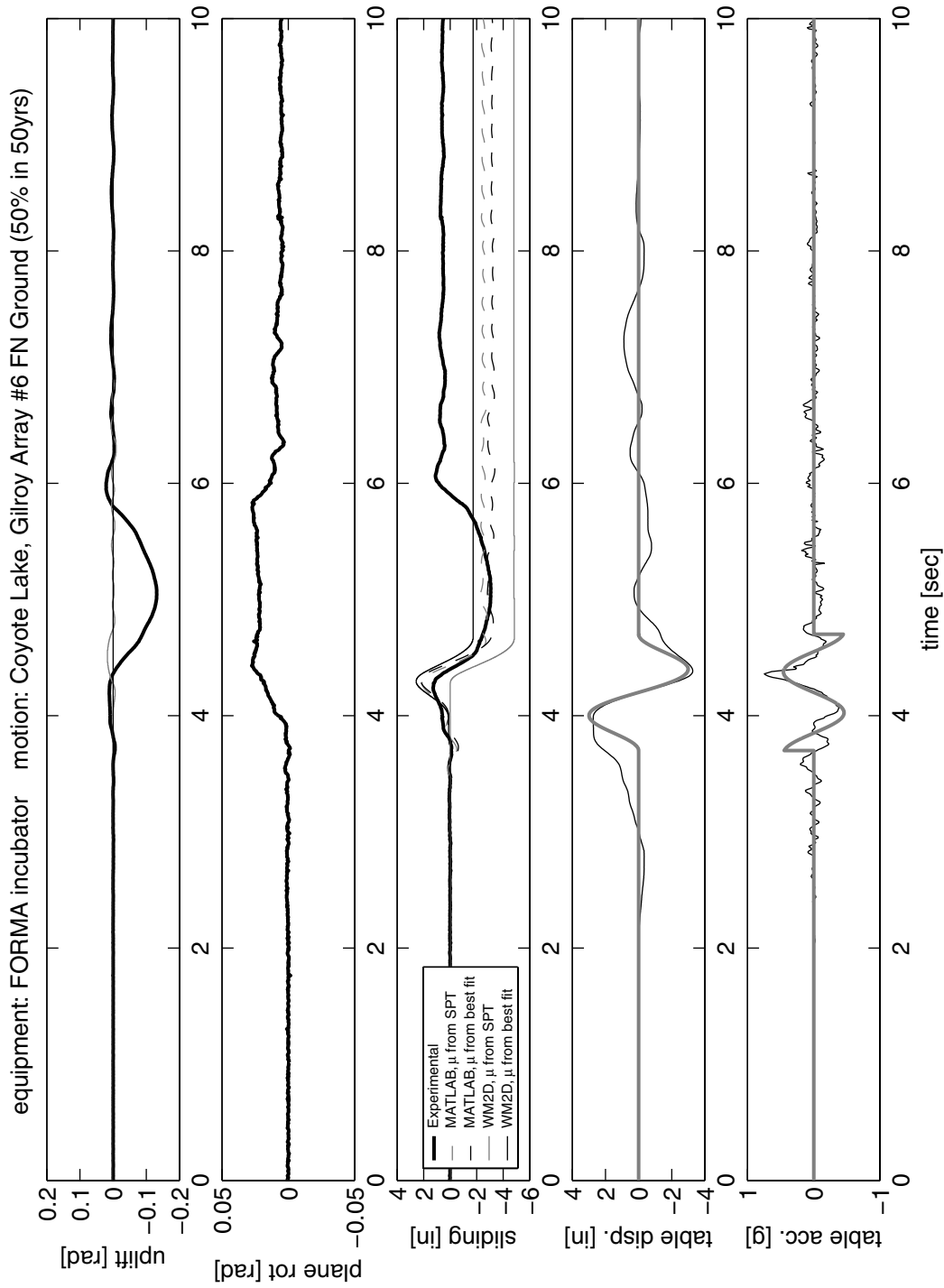


Figure 4.4 Response of the FORMA incubator subjected to the Gilroy Array #6 ground motion (50% in 50 years) recorded during the 1979 Coyote Lake, California, earthquake. The heavy grey lines on the bottom two graphs plot a Type- C_1 trigonometric pulse that approximates the main pulse of the motion record.

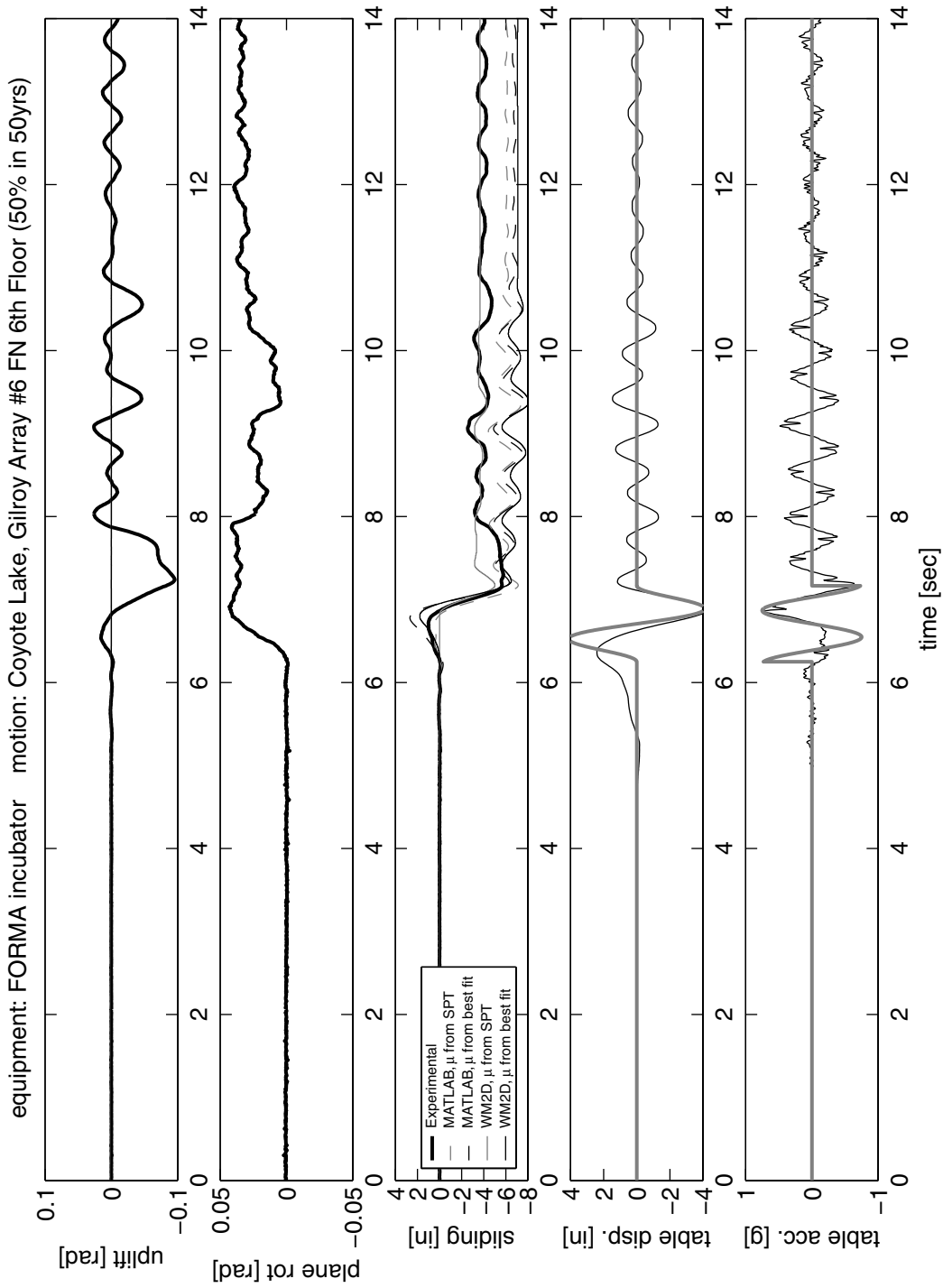


Figure 4.5 Response of the FORMA incubator subjected to the UC Science 6th floor motion of the Gilroy Array #6 (50% in 50 years) record of the 1979 Coyote Lake, California, earthquake. The heavy grey lines on the bottom two graphs plot a Type-C₁ trigonometric pulse that approximates the main pulse of the motion record.

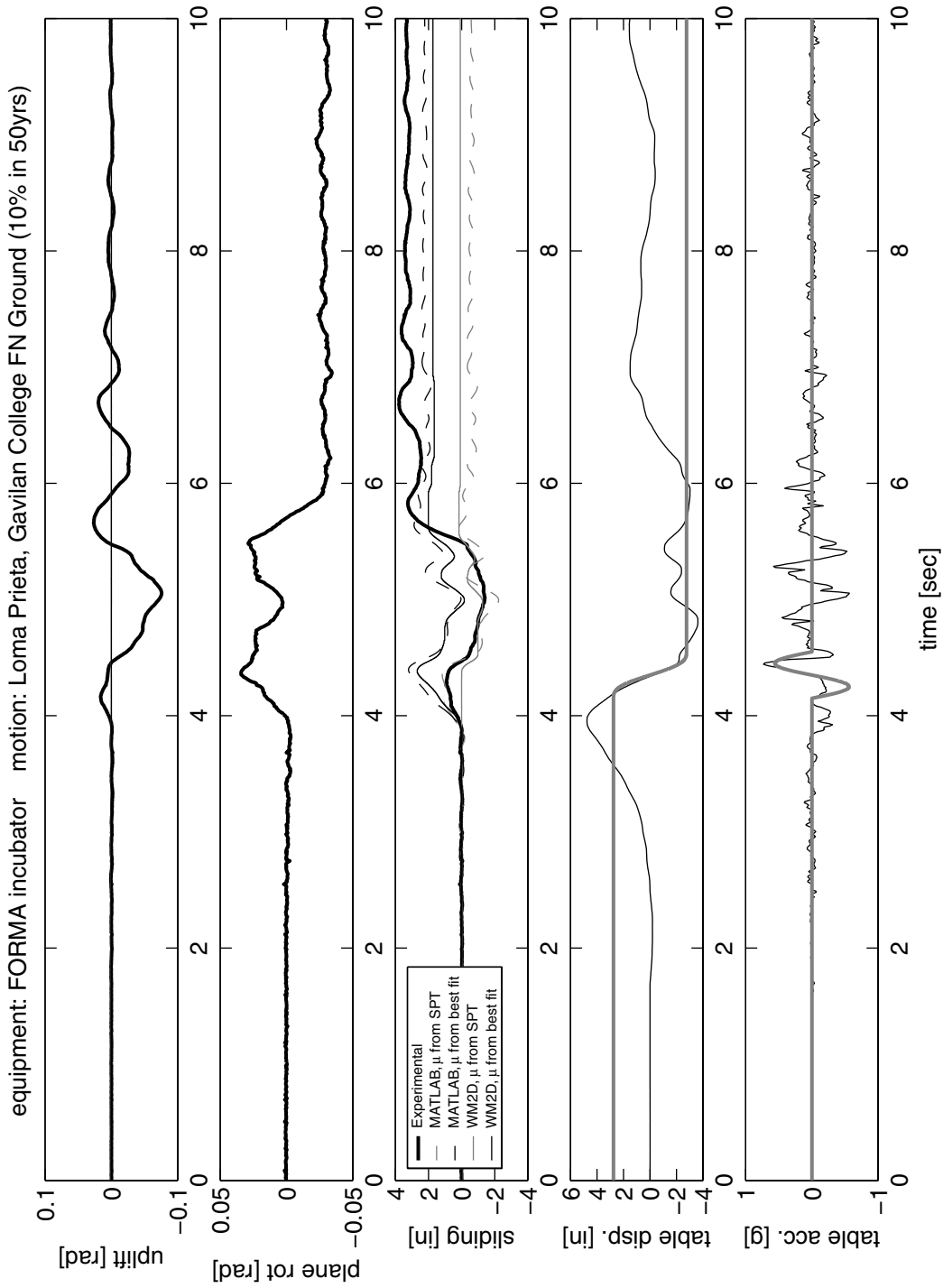


Figure 4.6 Response of the FORMMA incubator subjected to the Gavilan College ground motion (10% in 50 years) recorded during the 1989 Loma Prieta, California, earthquake. The heavy grey lines on the bottom two graphs plot a Type-A trigonometric pulse that approximates the main pulse of the motion record.

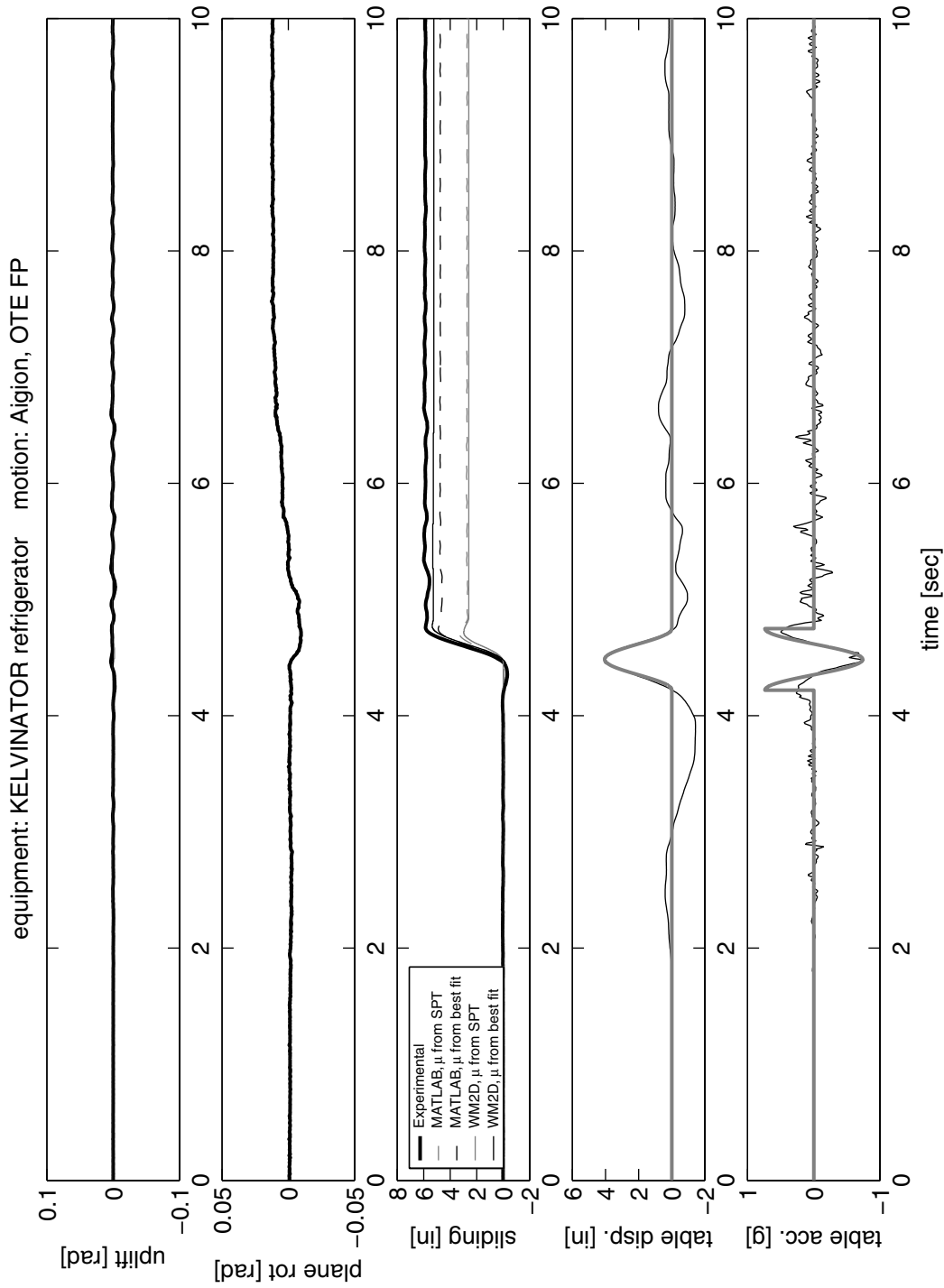


Figure 4.7 Response of the Kelvinator refrigerator subjected to the OTE FP motion recorded during the 1995 Aigion, Greece, earthquake. The heavy gray lines on the bottom two graphs plot a Type-B trigonometric pulse that approximates the main pulse of the motion record.

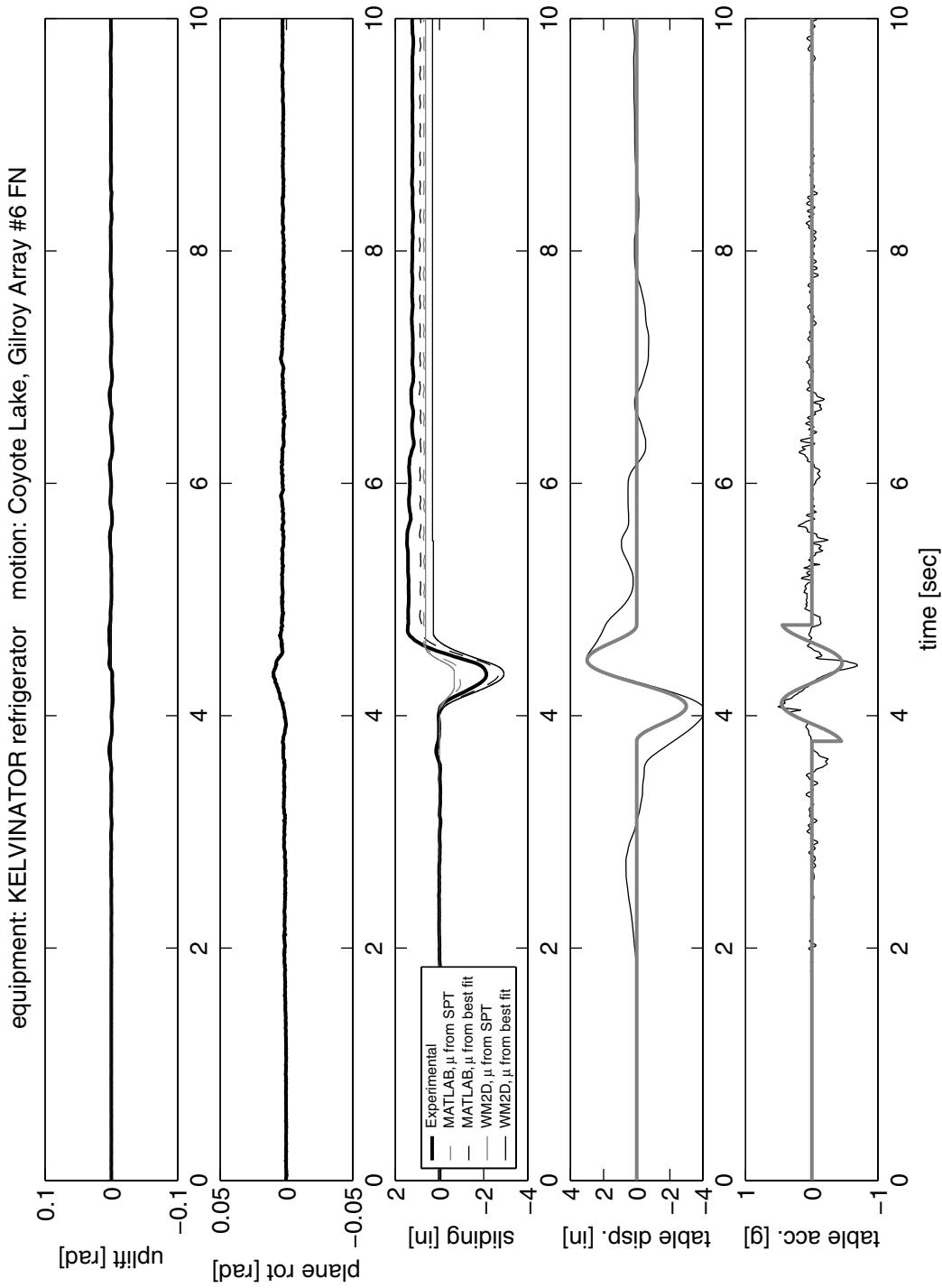


Figure 4.8 Response of the Kelvinator refrigerator subjected to the Gilroy Array #6 motion recorded during the 1979 Coyote Lake, California, earthquake. The heavy grey lines on the bottom two graphs plot a Type-C₁ trigonometric pulse that approximates the main pulse of the motion record.

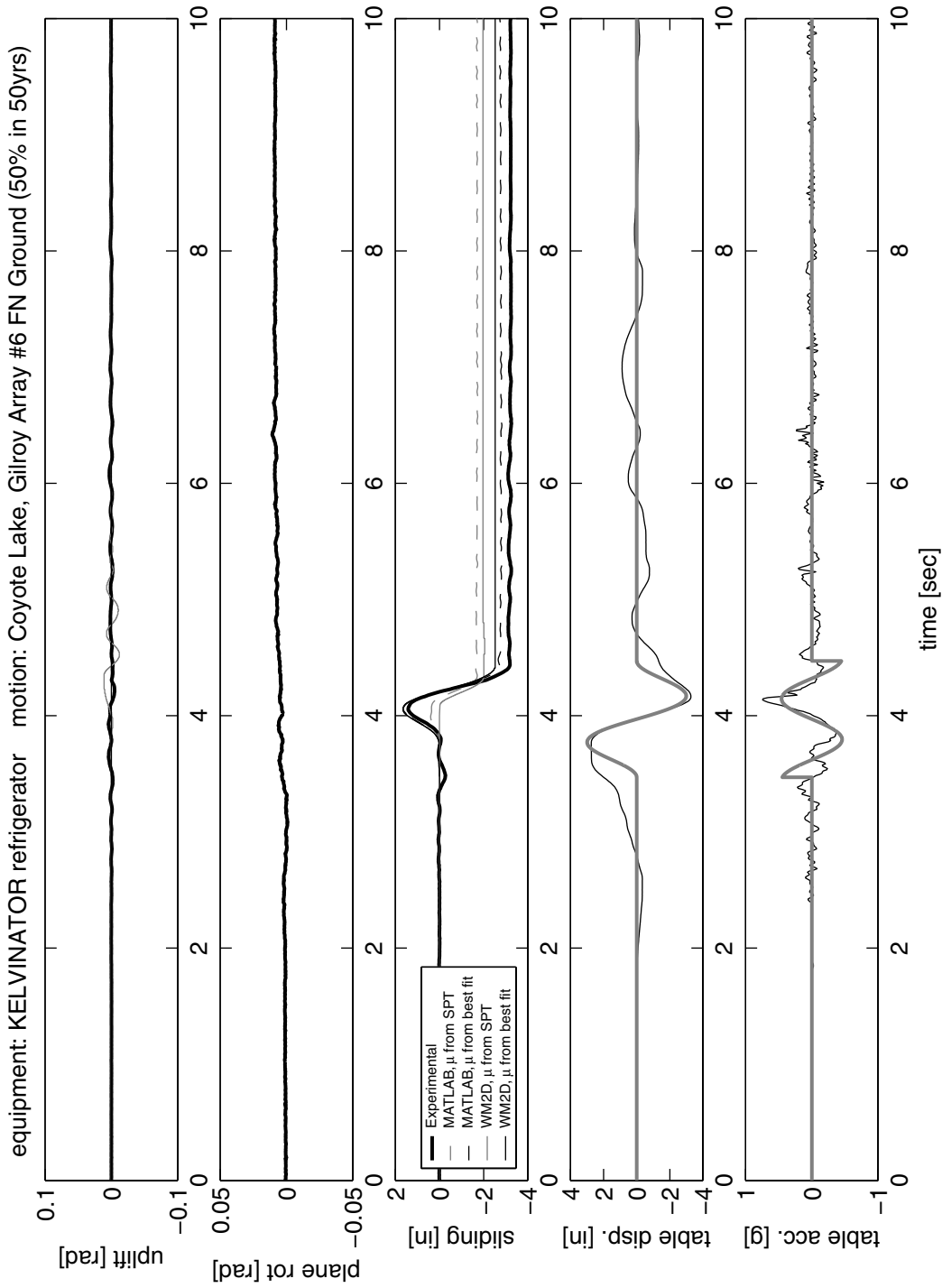


Figure 4.9 Response of the Kelvinator refrigerator subjected to the Gilroy Array #6 ground motion (50% in 50 years) recorded during the 1979 Coyote Lake, California, earthquake. The heavy grey lines on the bottom two graphs plot a Type-C₁ trigonometric pulse that approximates the main pulse of the motion record.

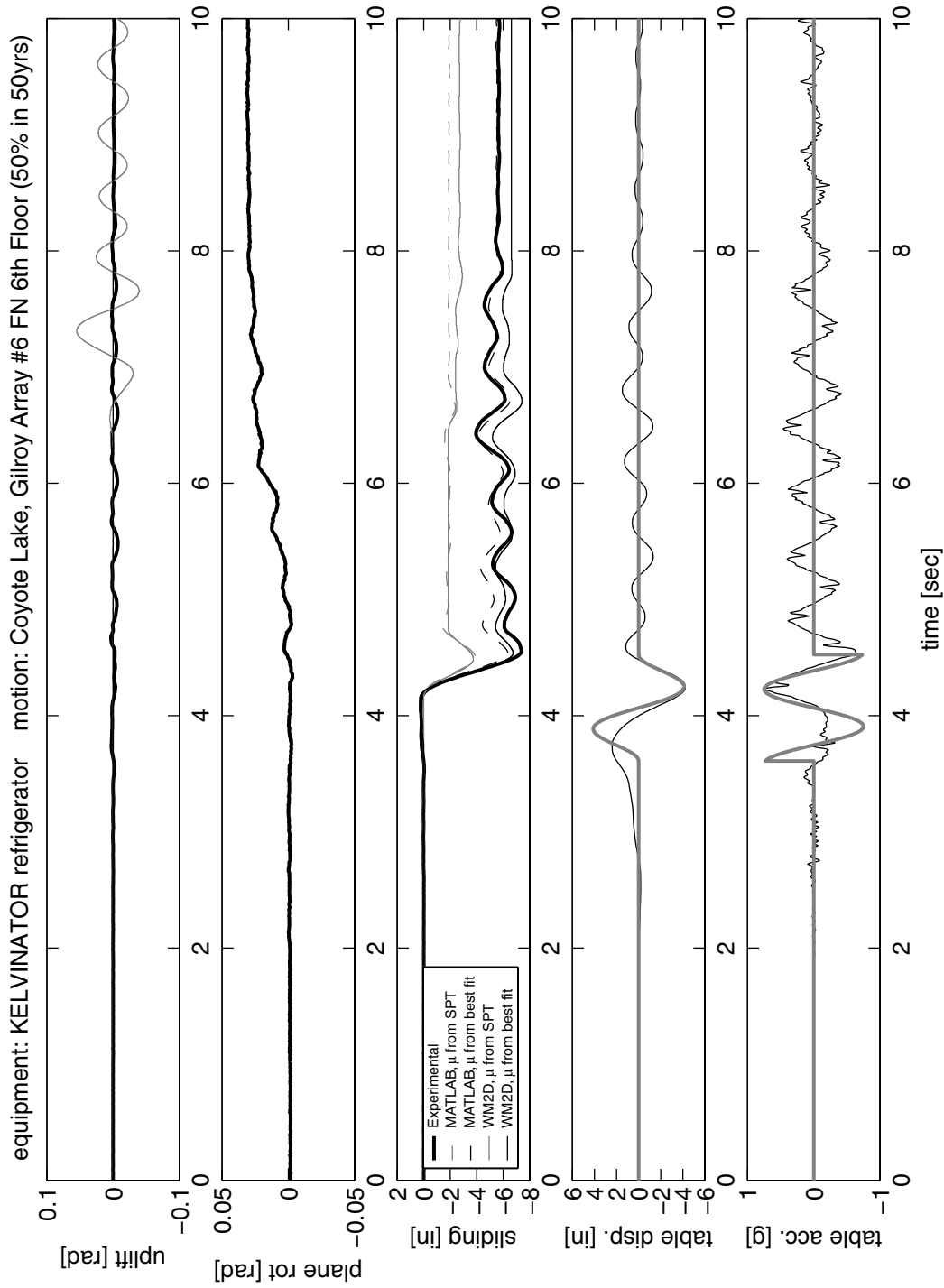


Figure 4.10 Response of the Kelvinator refrigerator subjected to the UC Science 6th floor motion of the Gilroy Array #6 (50% in 50 years) record of the 1979 Coyote Lake, California, earthquake. The heavy grey lines on the bottom two graphs plot a Type-C₁ trigonometric pulse that approximates the main pulse of the motion record.

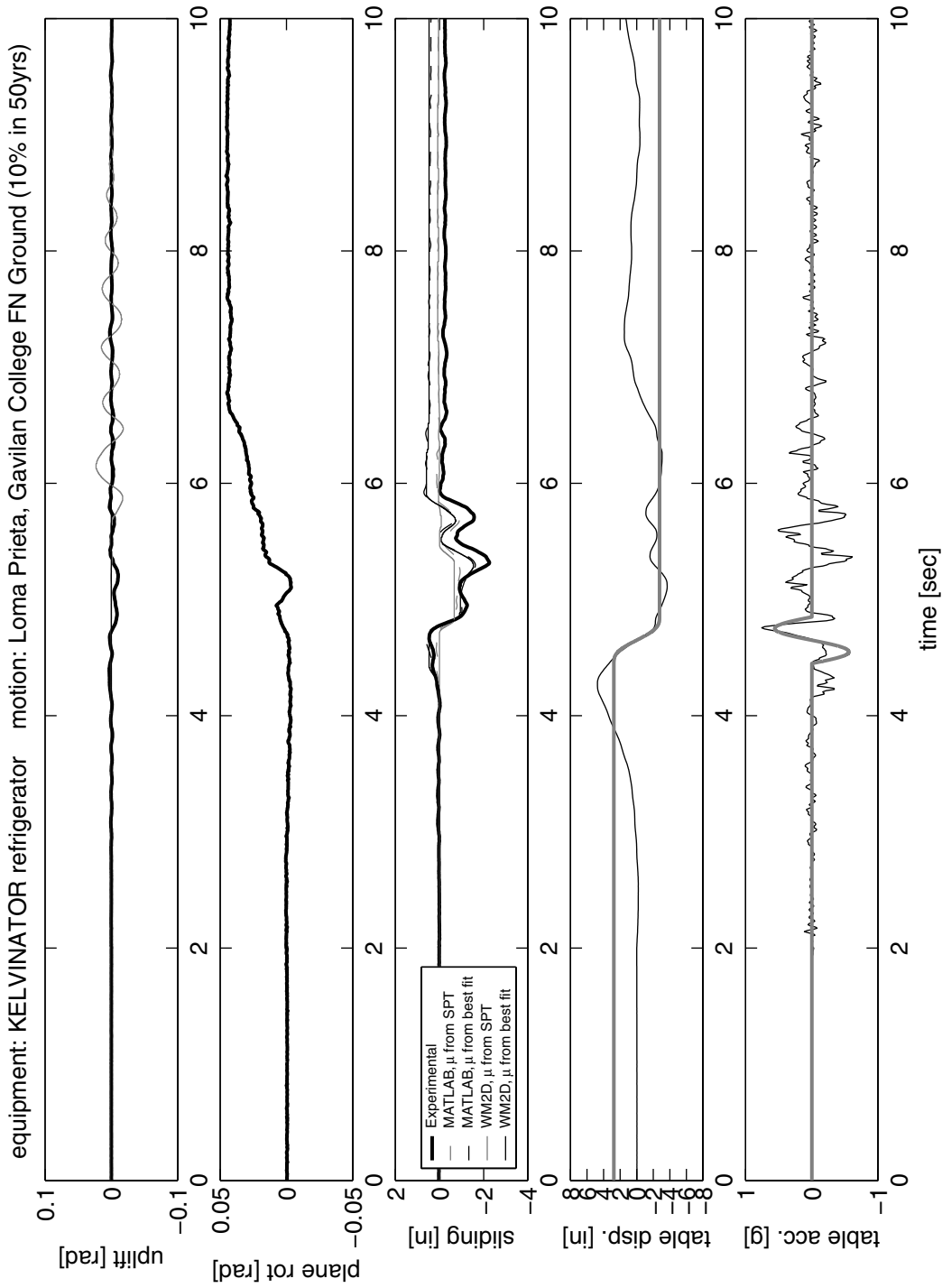


Figure 4.11 Response of the Kelvinator refrigerator subjected to the Gavilan College ground motion (10% in 50 years) recorded during the 1989 Loma Prieta, California, earthquake. The heavy grey lines on the bottom two graphs plot a Type-A trigonometric pulse that approximates the main pulse of the motion record.

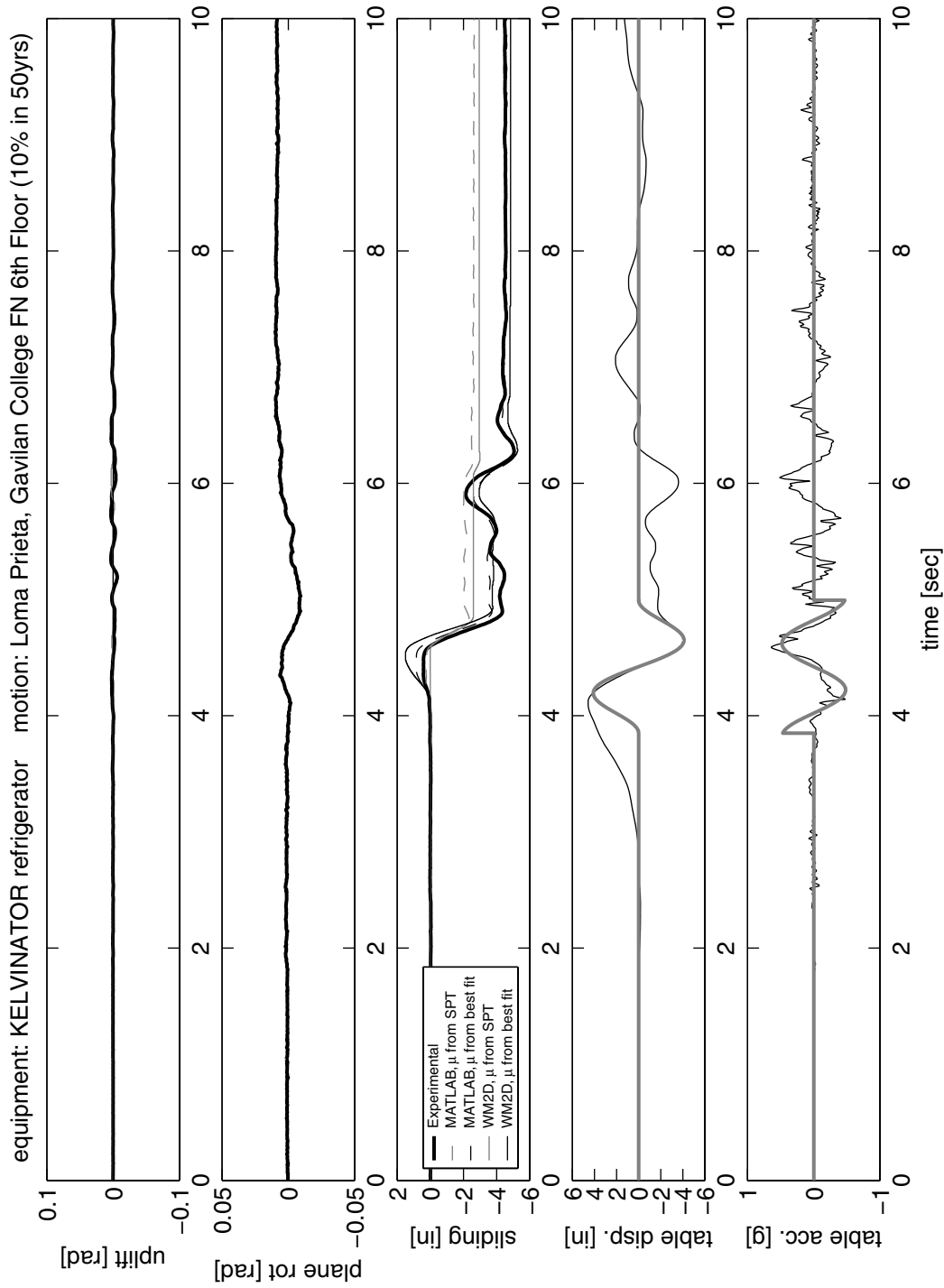


Figure 4.12 Response of the Kelvinator refrigerator subjected to the UC Science Building 6th floor motion of the Gavilan College (10% in 50 years) record of the 1989 Loma Prieta, California, earthquake. The heavy grey lines on the bottom two graphs plot a Type-C₁ trigonometric pulse that approximates the main pulse of the motion record.

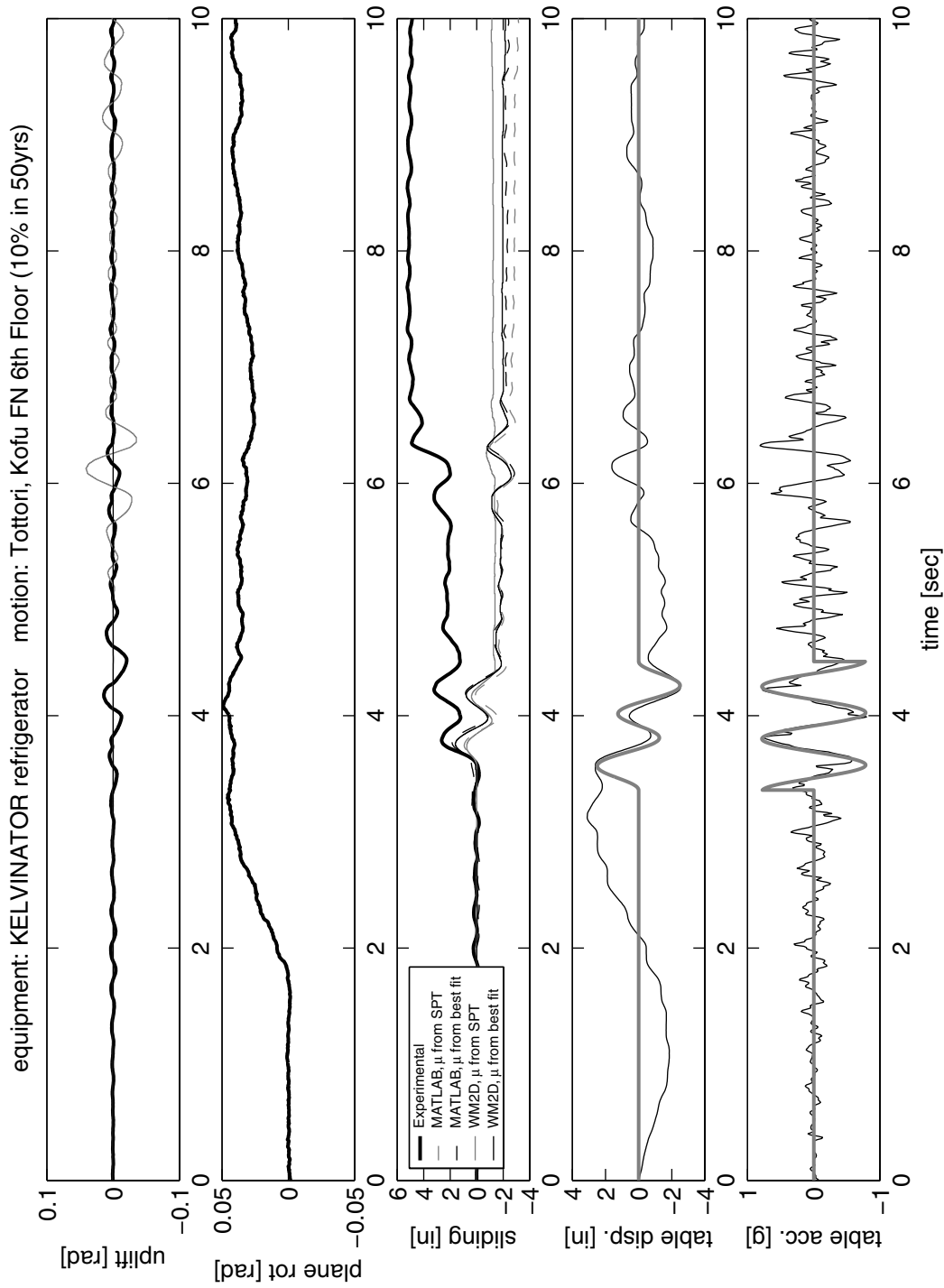


Figure 4.13 Response of the Kelvinator refrigerator subjected to the UC Science Building 6th floor motion of the Kofu FN (10% in 50 years) record of the 2000 Tottori, Japan, earthquake. The heavy grey lines on the bottom two graphs plot a Type-C₂ trigonometric pulse that approximates the main pulse of the motion record.

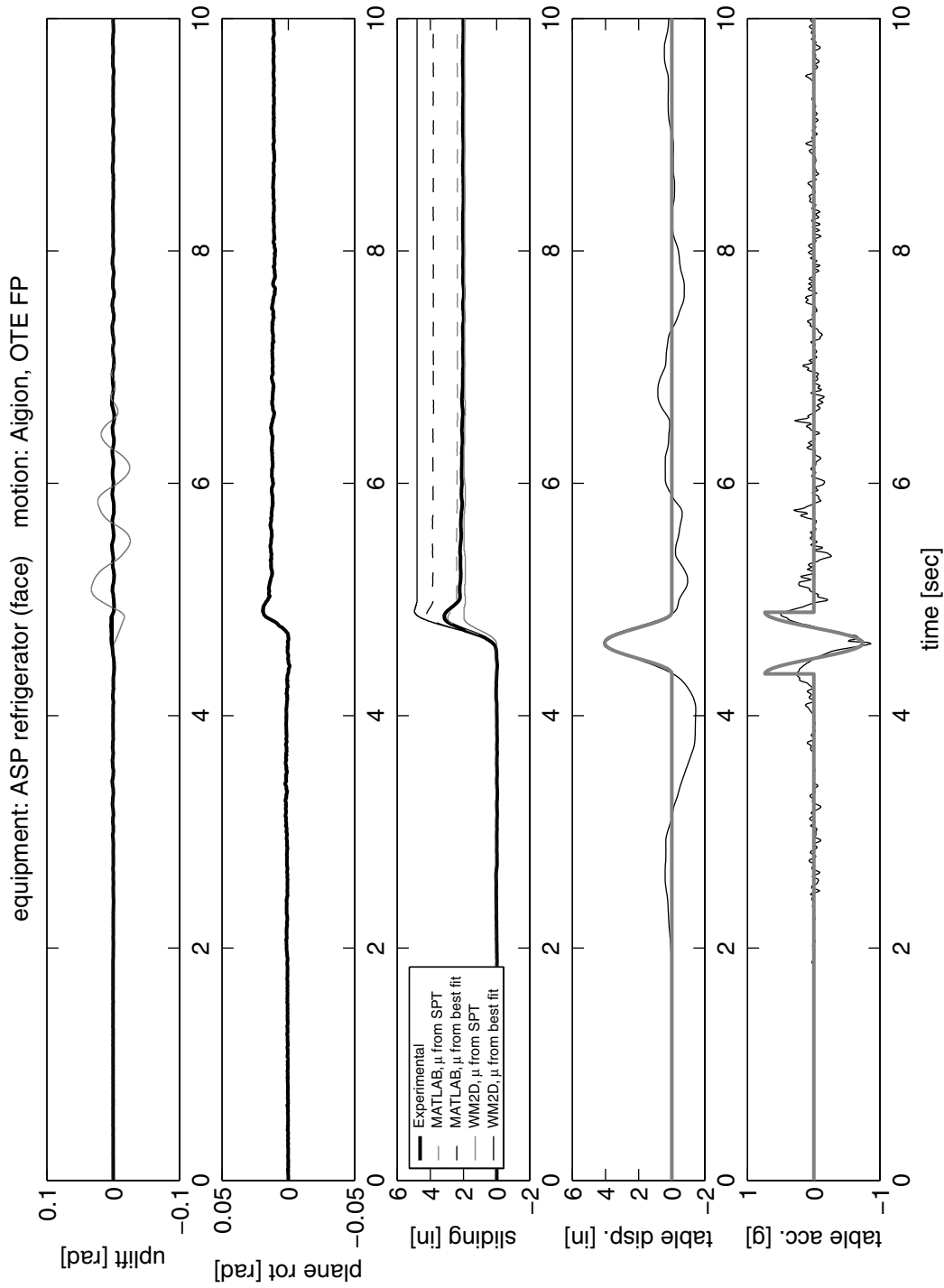


Figure 4.14 Response of the ASP refrigerator (*face* configuration) subjected to the OTE FP motion recorded during the 1995 Aigion, Greece, earthquake. The heavy grey lines on the bottom two graphs plot a Type-B trigonometric pulse that approximates the main pulse of the motion record.

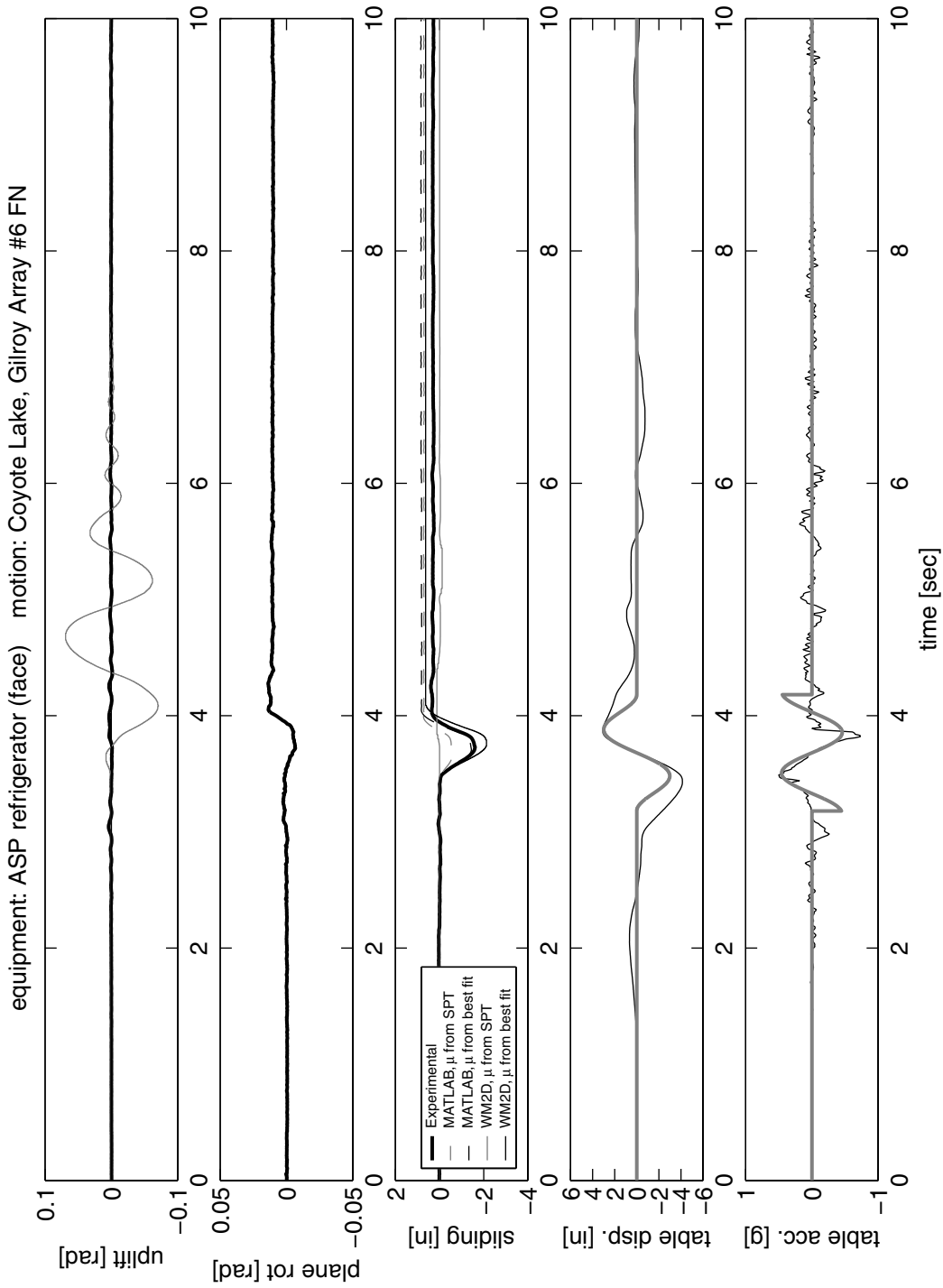


Figure 4.15 Response of the ASP refrigerator (*face* configuration) subjected to the Gilroy Array #6 motion recorded during the 1979 Coyote Lake, California, earthquake. The heavy grey lines on the bottom two graphs plot a Type-C₁ trigonometric pulse that approximates the main pulse of the motion record.

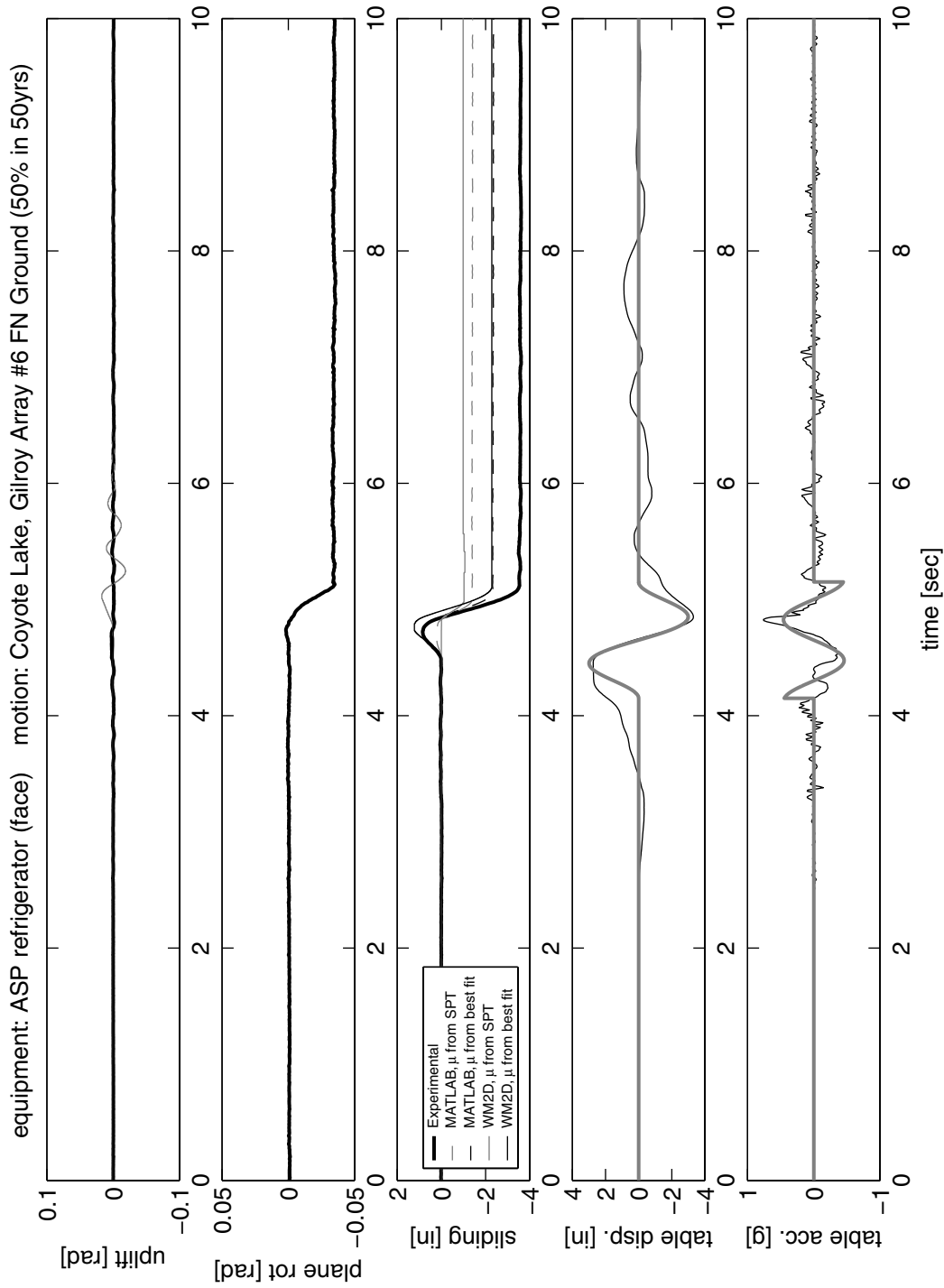


Figure 4.16 Response of the ASP refrigerator (*face* configuration) subjected to the Gilroy Array #6 ground motion (50% in 50 years) recorded during the 1979 Coyote Lake, California, earthquake. The heavy grey lines on the bottom two graphs plot a Type-C₁ trigonometric pulse that approximates the main pulse of the motion record.

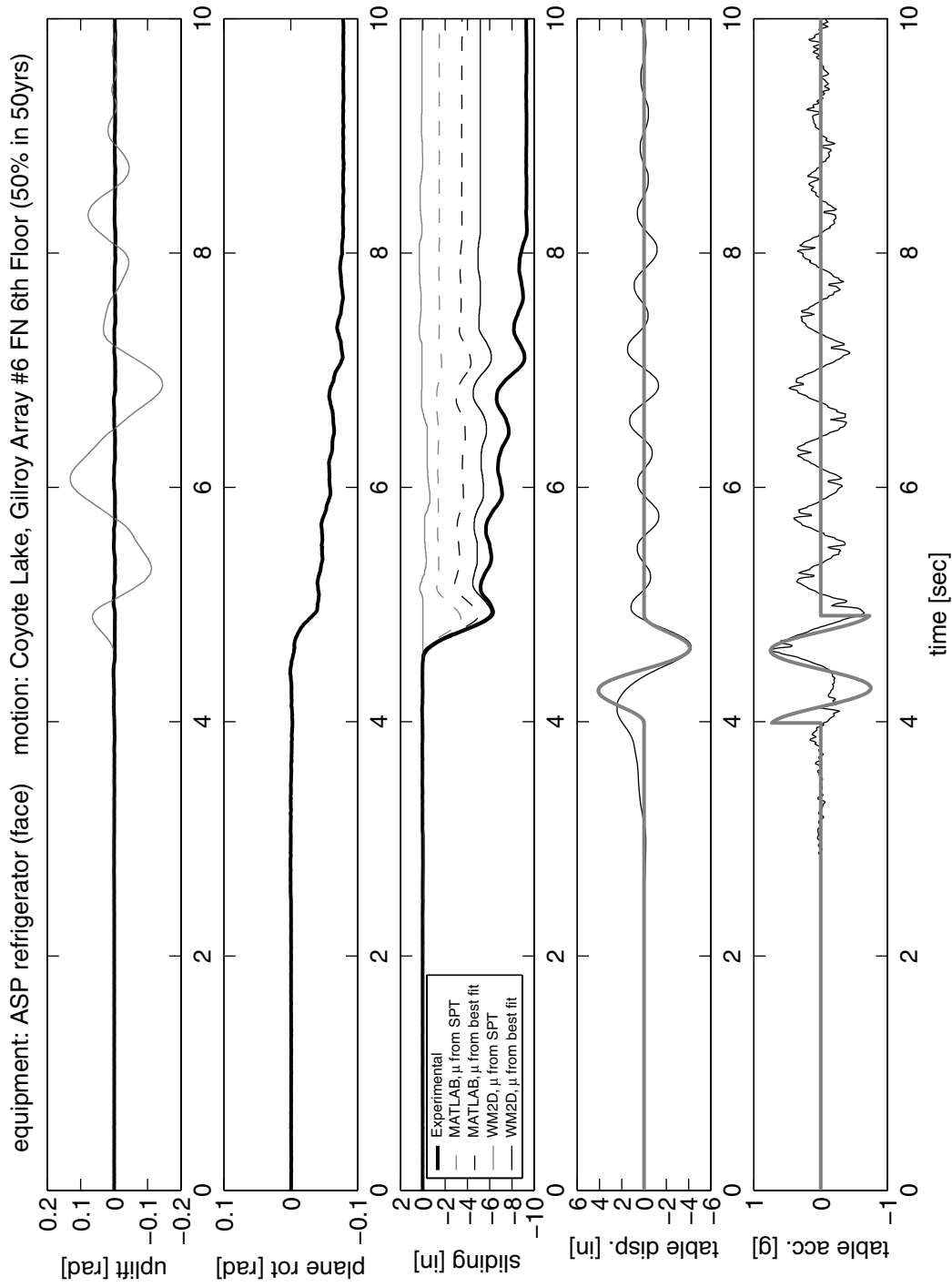


Figure 4.17 Response of the ASP refrigerator (*face* configuration) subjected to the UC Science Building 6th floor motion of the Gilroy Array #6 (50% in 50 years) record of the 1979 Coyote Lake, California, earthquake. The heavy grey lines on the bottom two graphs plot a Type-C₁ trigonometric pulse that approximates the main pulse of the motion record.

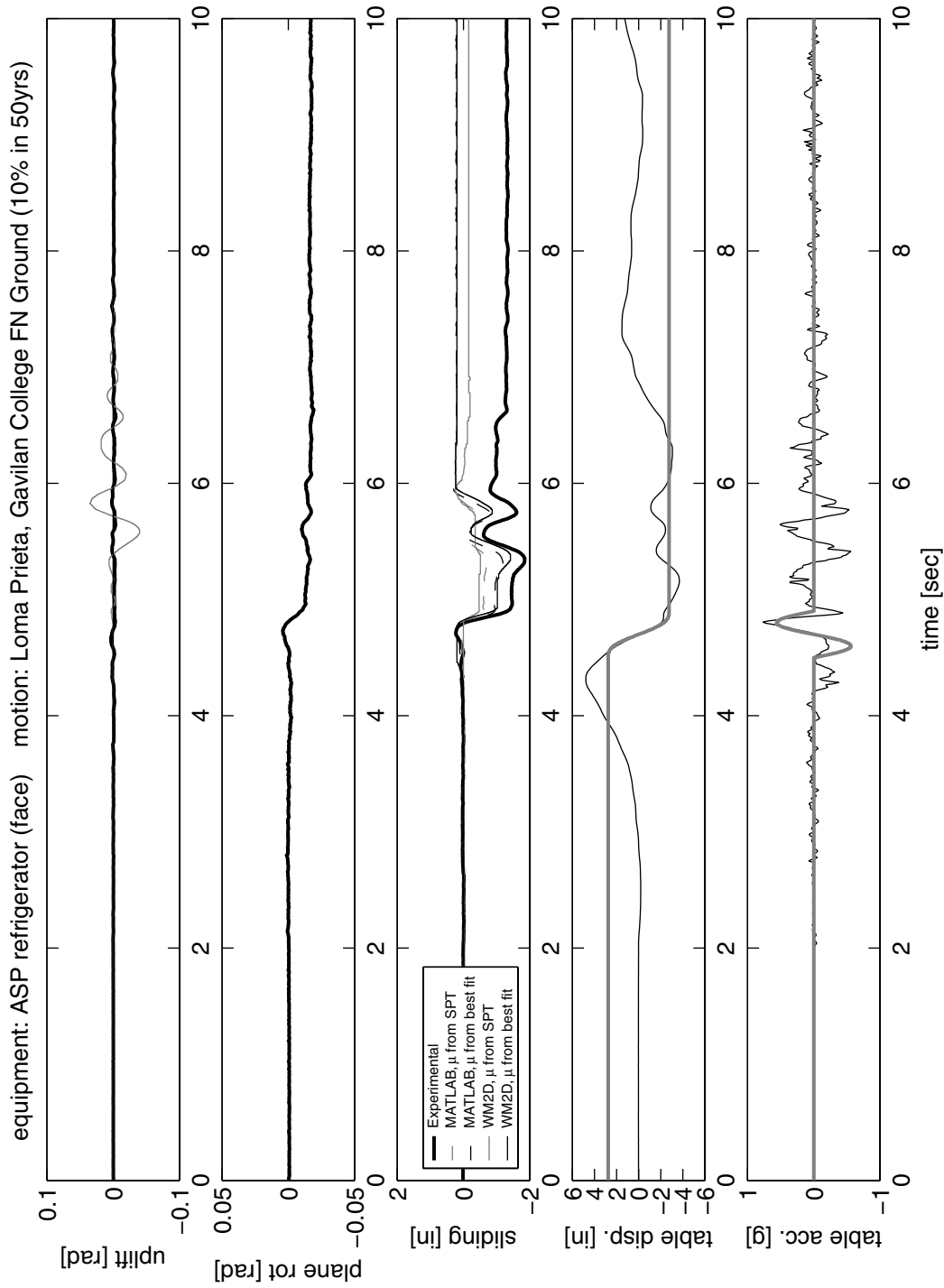


Figure 4.18 Response of the ASP refrigerator (*face* configuration) subjected to the Gavilan College ground motion (10% in 50 years) recorded during the 1989 Loma Prieta, California, earthquake. The heavy grey lines on the bottom two graphs plot a Type-A trigonometric pulse that approximates the main pulse of the motion record.

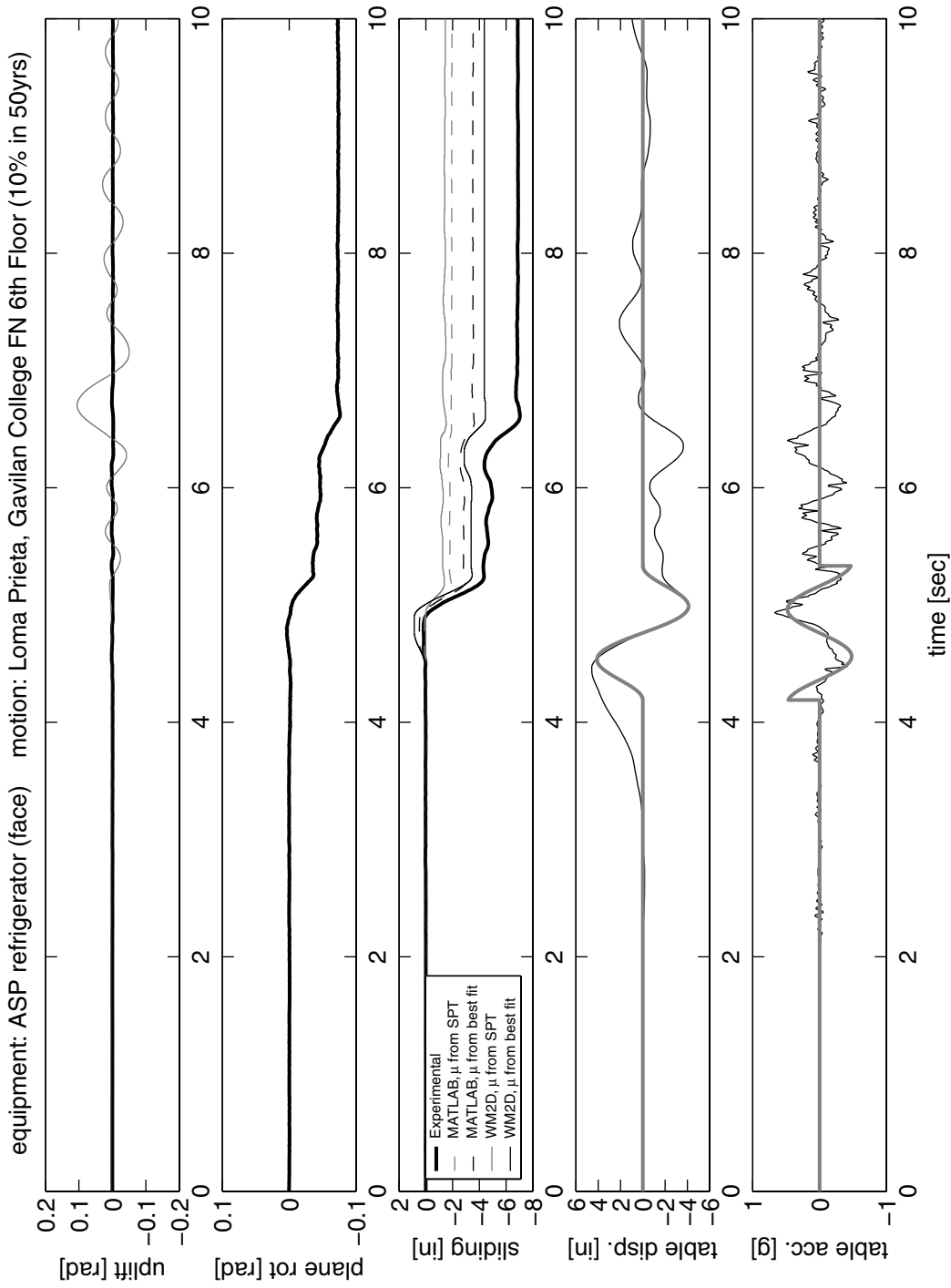


Figure 4.19 Response of the ASP refrigerator (*face* configuration) subjected to the UC Science Building 6th floor motion of the Gavilan College (10% in 50 years) record of the 1989 Loma Prieta, California, earthquake. The heavy grey lines on the bottom two graphs plot a Type-C₁ trigonometric pulse that approximates the main pulse of the motion record.

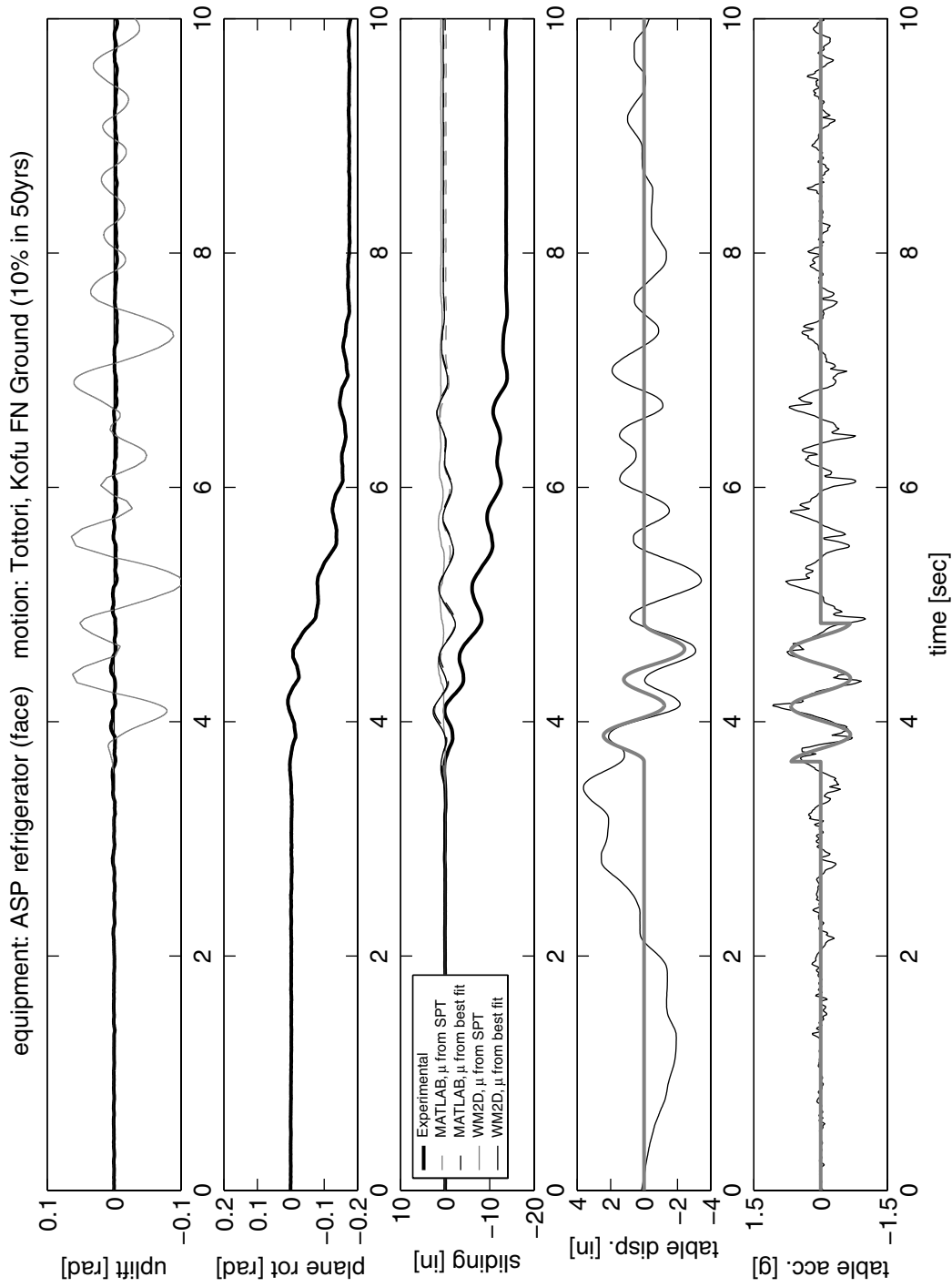


Figure 4.20 Response of the ASP refrigerator (*face* configuration) subjected to the Kofu FN motion (10% in 50 years) recorded during the 2000 Tottori, Japan, earthquake. The heavy grey lines on the bottom two graphs plot a Type-C₂ trigonometric pulse that approximates the main pulse of the motion record.

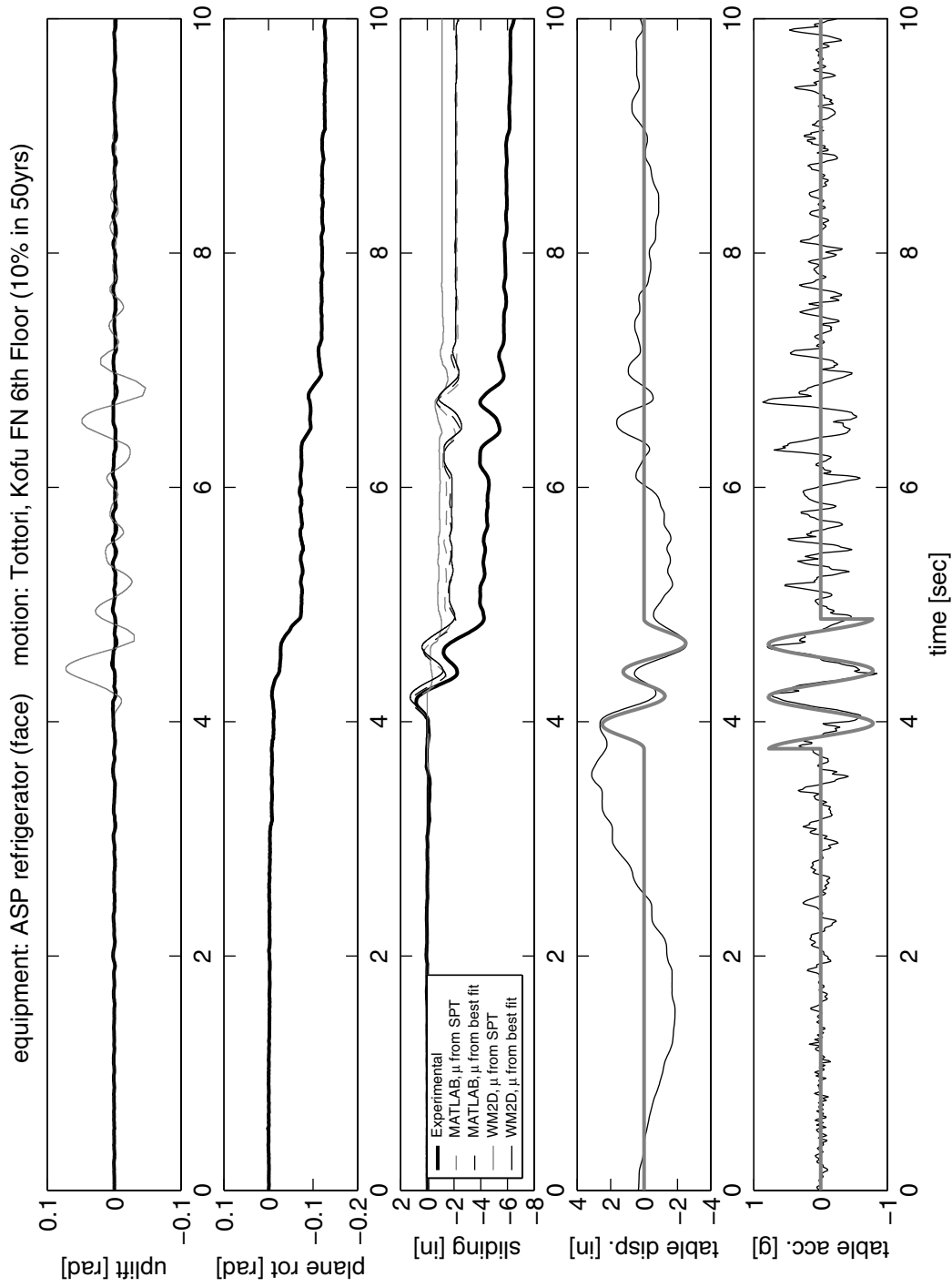


Figure 4.21 Response of the ASP refrigerator (*face* configuration) subjected to the UC Science Building 6th floor motion of the Kofu FN (10% in 50 years) record of the 2000 Tottori, Japan, earthquake. The heavy grey lines on the bottom two graphs plot a Type-C₂ trigonometric pulse that approximates the main pulse of the motion record.

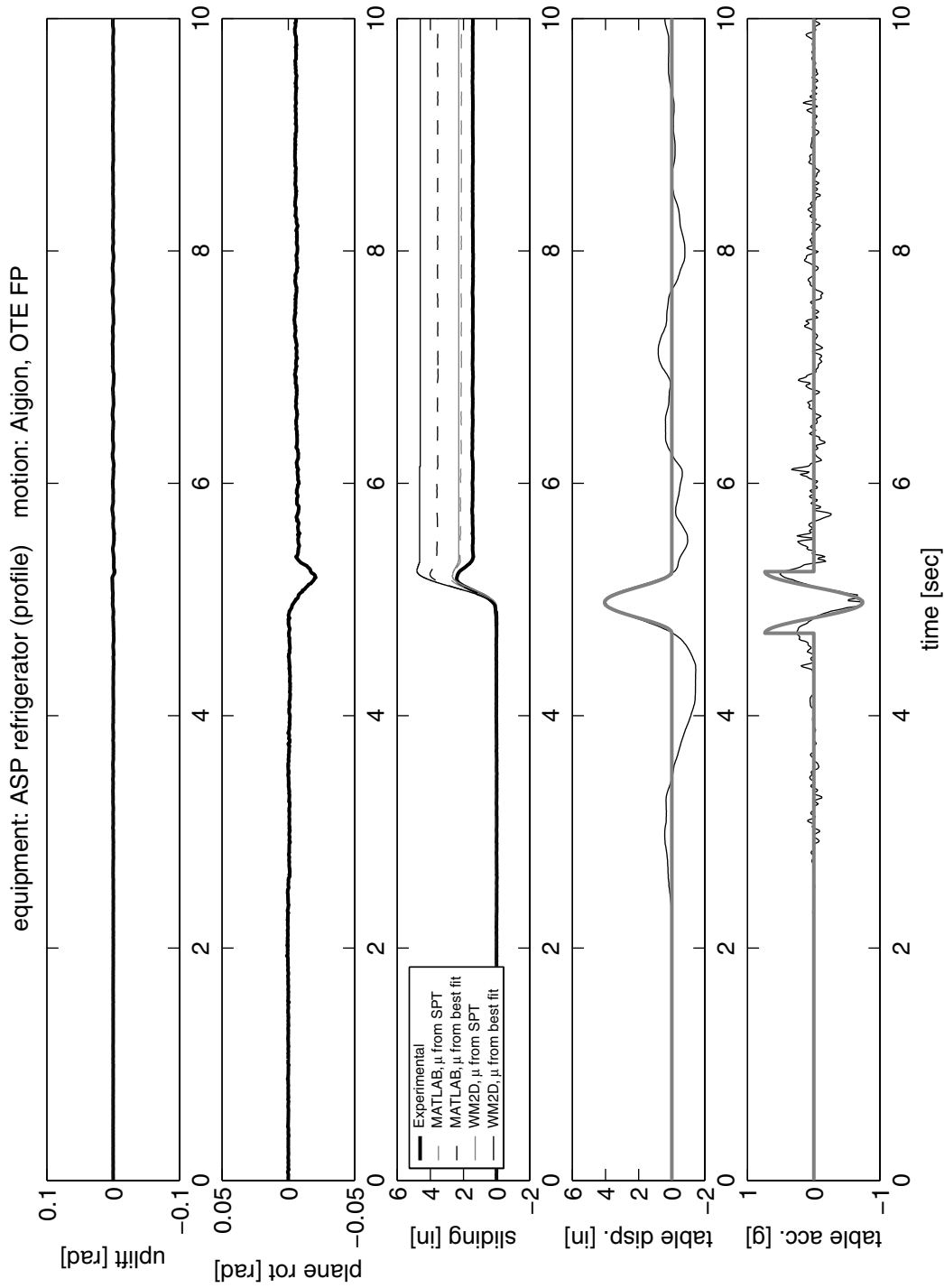


Figure 4.22 Response of the ASP refrigerator (*profile* configuration) subjected to the OTE FP motion recorded during the 1995 Aigion, Greece, earthquake. The heavy grey lines on the bottom two graphs plot a Type-B trigonometric pulse that approximates the main pulse of the motion record.

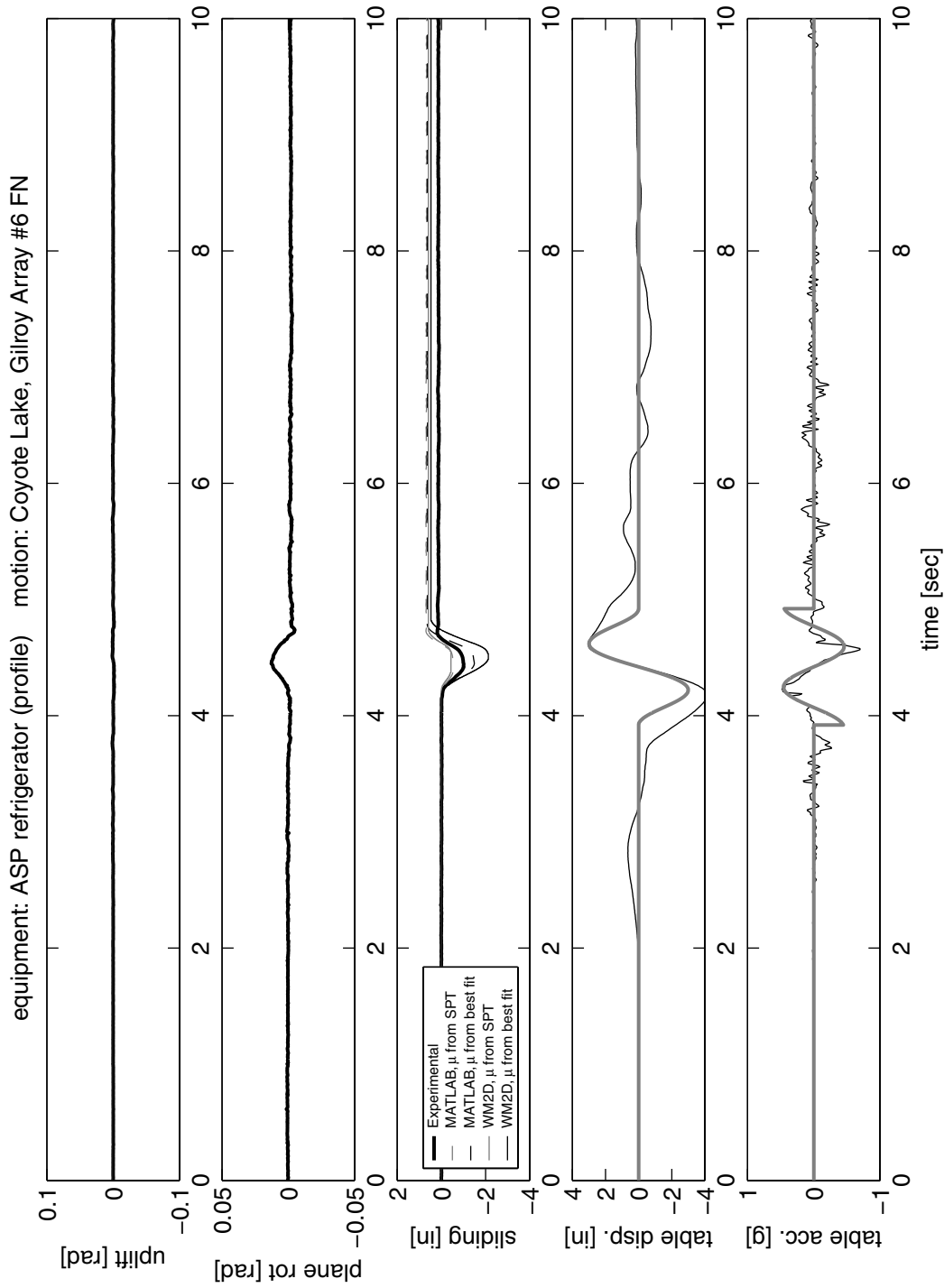


Figure 4.23 Response of the ASP refrigerator (*profile* configuration) subjected to the Gilroy Array #6 motion recorded during the 1979 Coyote Lake, California, earthquake. The heavy grey lines on the bottom two graphs plot a Type-C₁ trigonometric pulse that approximates the main pulse of the motion record.

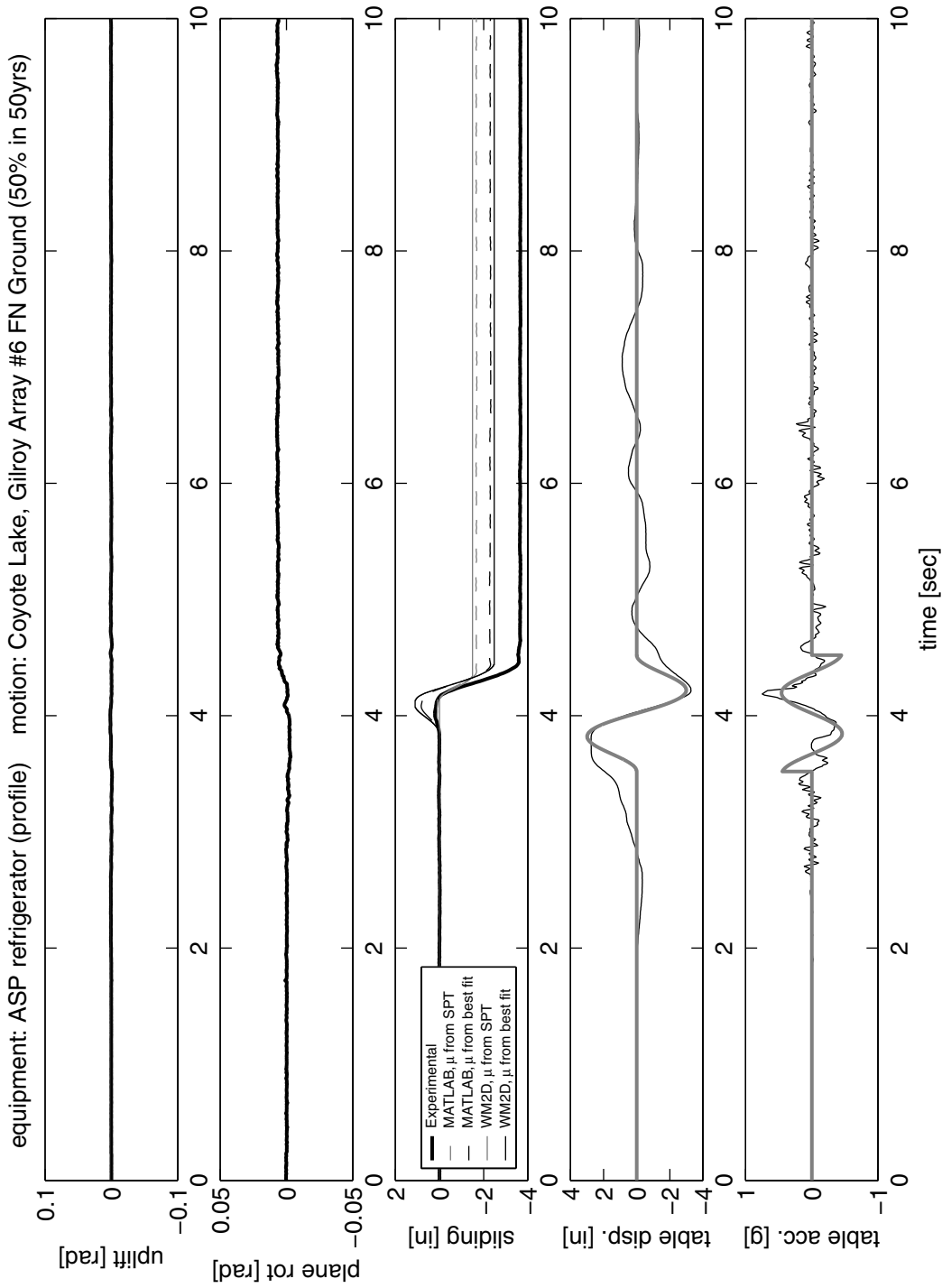


Figure 4.24 Response of the ASP refrigerator (*profile* configuration) subjected to the Gilroy Array #6 ground motion (50% in 50 years) recorded during the 1979 Coyote Lake, California, earthquake. The heavy grey lines on the bottom two graphs plot a Type-C₁ trigonometric pulse that approximates the main pulse of the motion record.

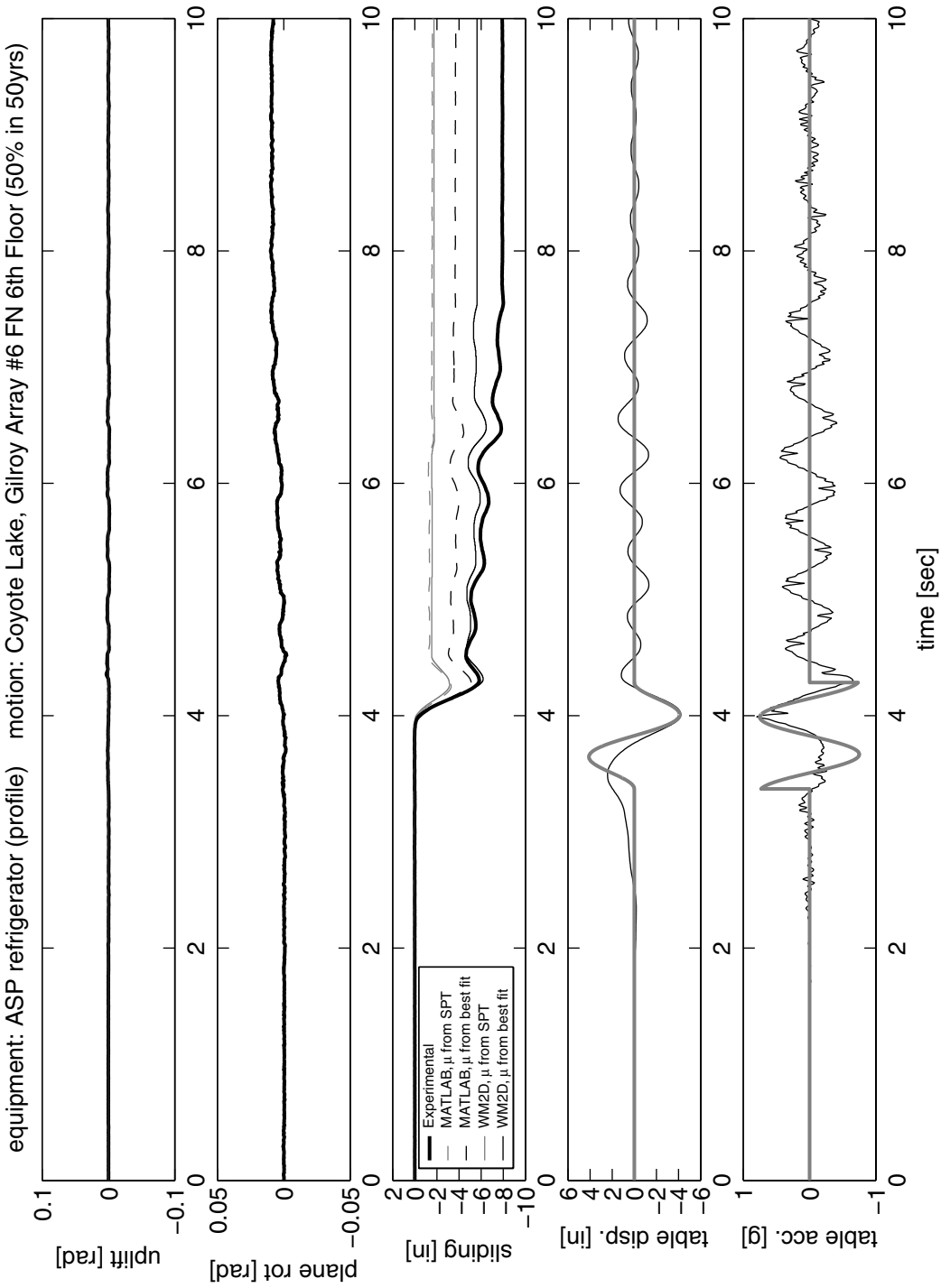


Figure 4.25 Response of the ASP refrigerator (*profile* configuration) subjected to the UC Science Building 6th floor motion of the Gilroy Array #6 (50% in 50 years) record of the 1979 Coyote Lake, California, earthquake. The heavy grey lines on the bottom two graphs plot a Type-C₁ trigonometric pulse that approximates the main pulse of the motion record.

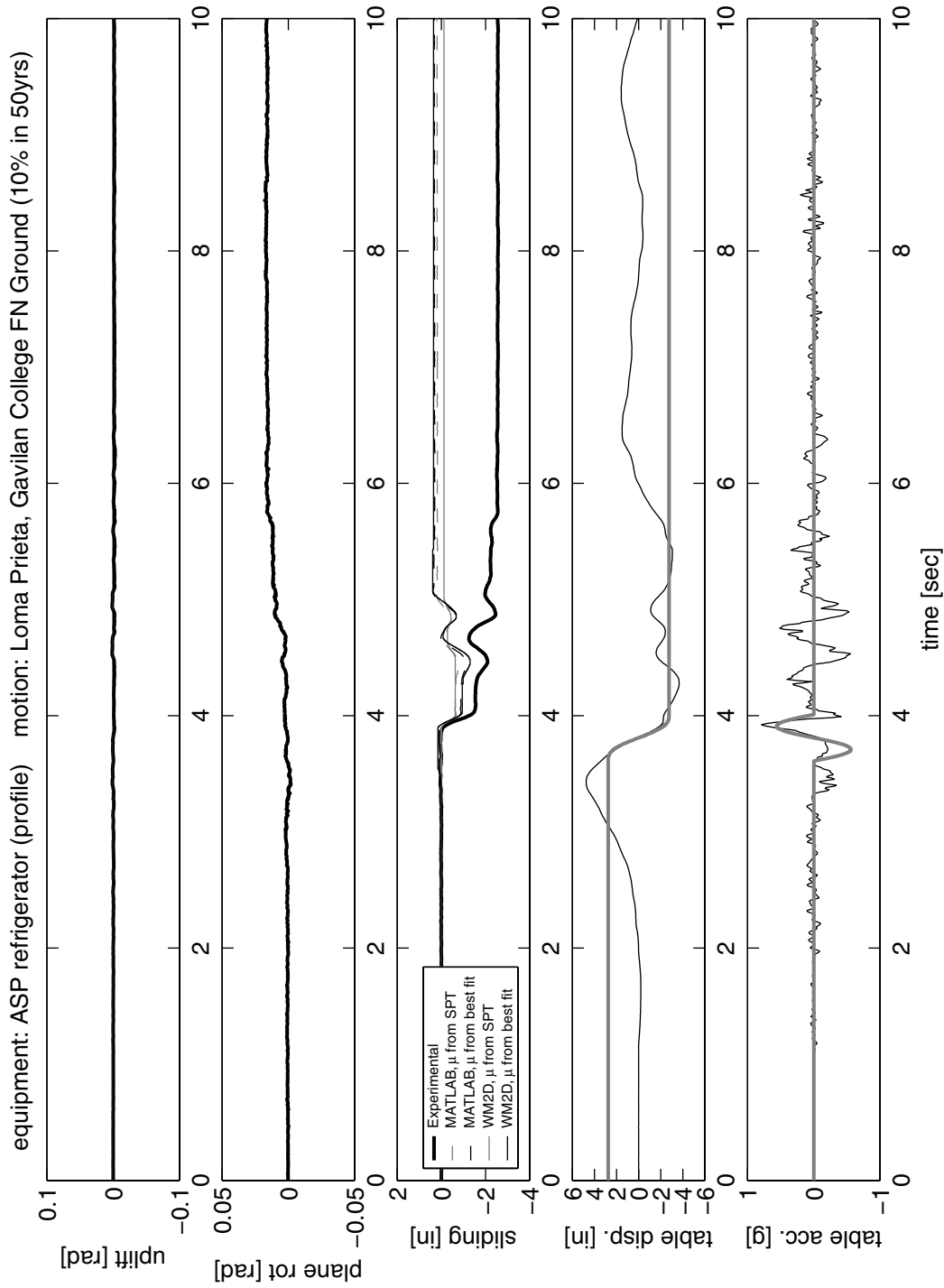


Figure 4.26 Response of the ASP refrigerator (*profile* configuration) subjected to the Gavilan College ground motion (10% in 50 years) recorded during the 1989 Loma Prieta, California, earthquake. The heavy grey lines on the bottom two graphs plot a Type-A trigonometric pulse that approximates the main pulse of the motion record.

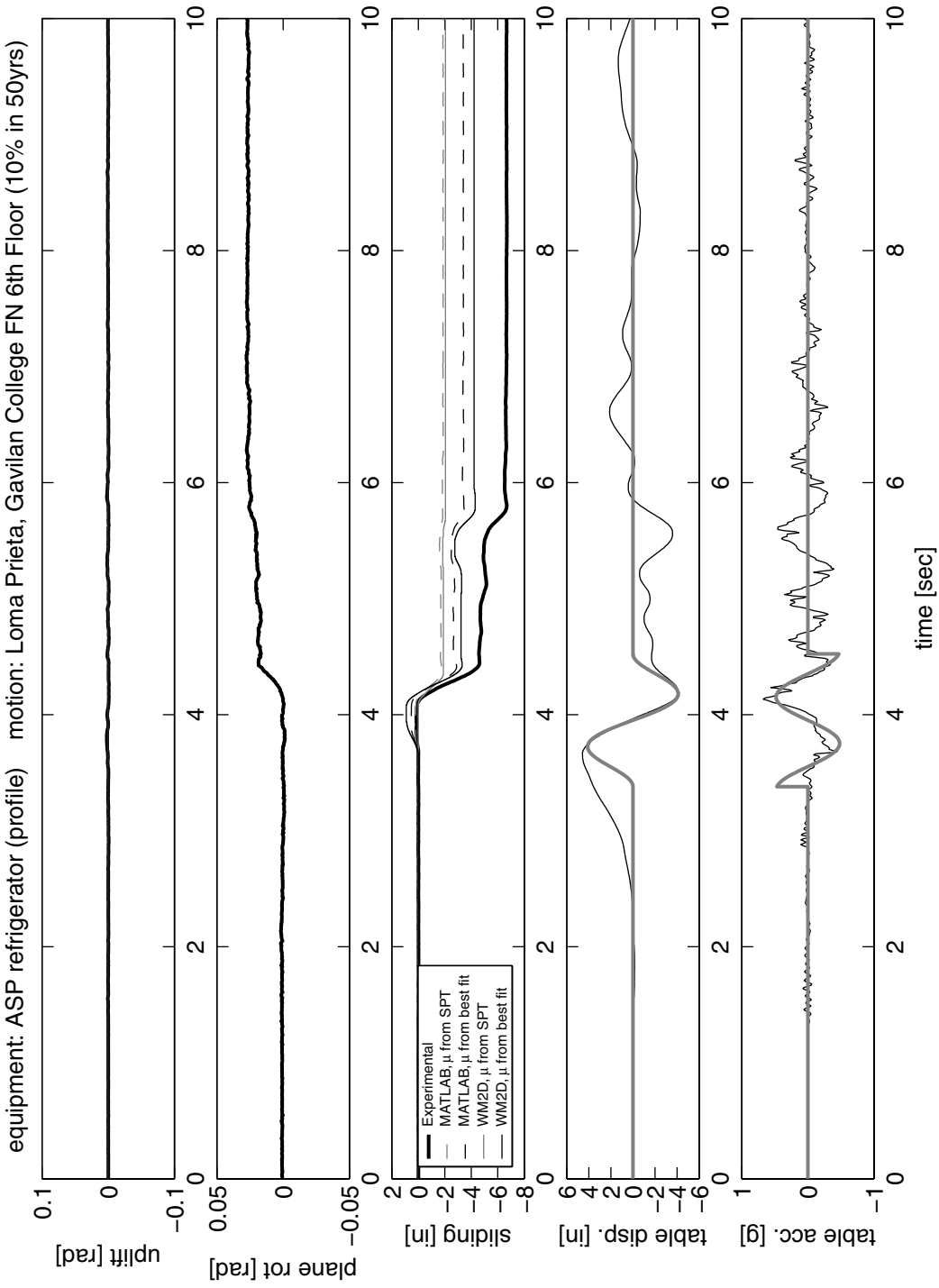


Figure 4.27 Response of the ASP refrigerator (*profile configuration*) subjected to the UC Science Building 6th floor motion of the Gavilan College (10% in 50 years) record of the 1989 Loma Prieta, California, earthquake. The heavy grey lines on the bottom two graphs plot a Type-C₁ trigonometric pulse that approximates the main pulse of the motion record.

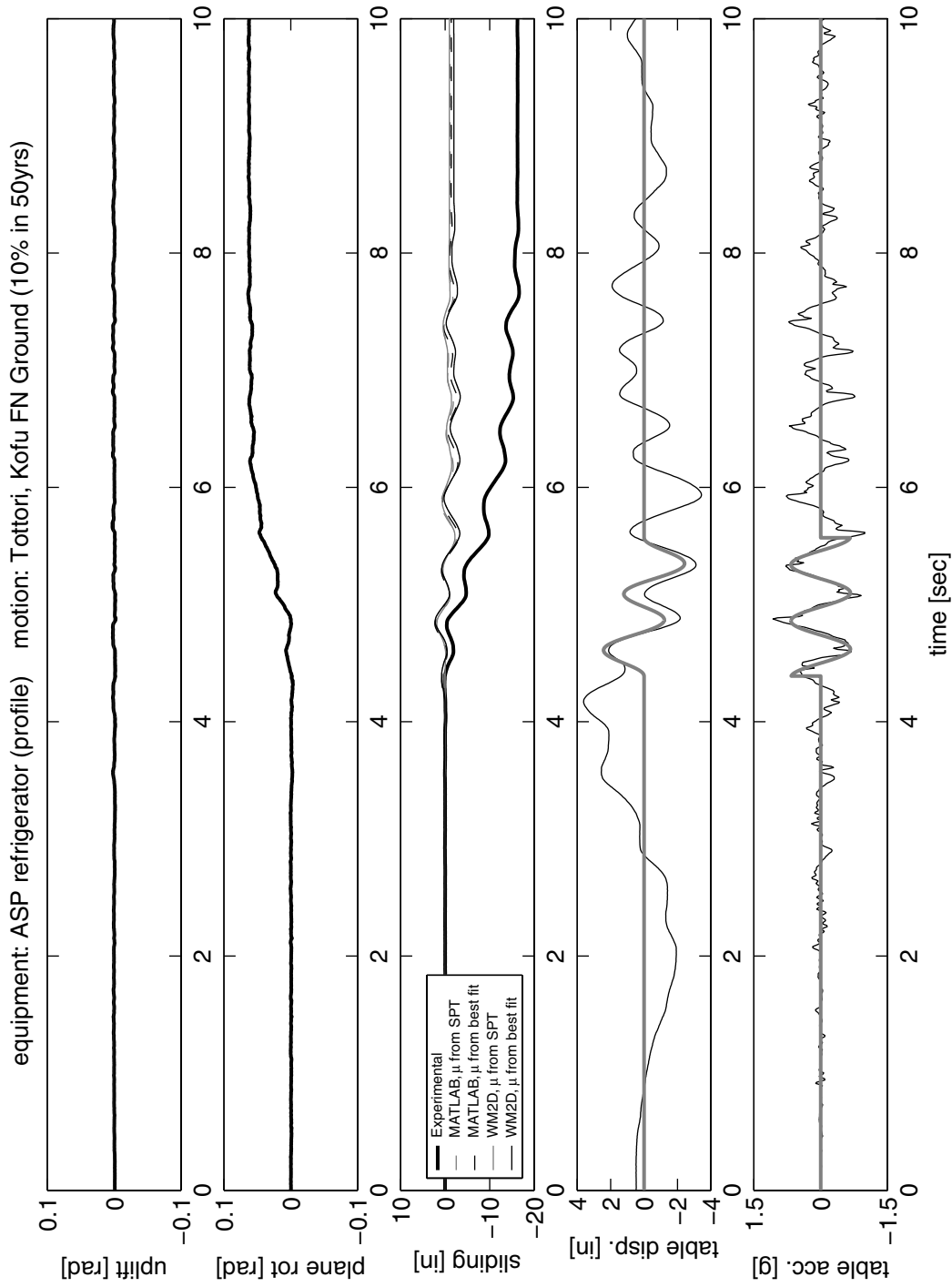


Figure 4.28 Response of the ASP refrigerator (*profile* configuration) subjected to the Kofu FN motion (10% in 50 years) recorded during the 2000 Tottori, Japan, earthquake. The heavy grey lines on the bottom two graphs plot a Type- C_2 trigonometric pulse that approximates the main pulse of the motion record.

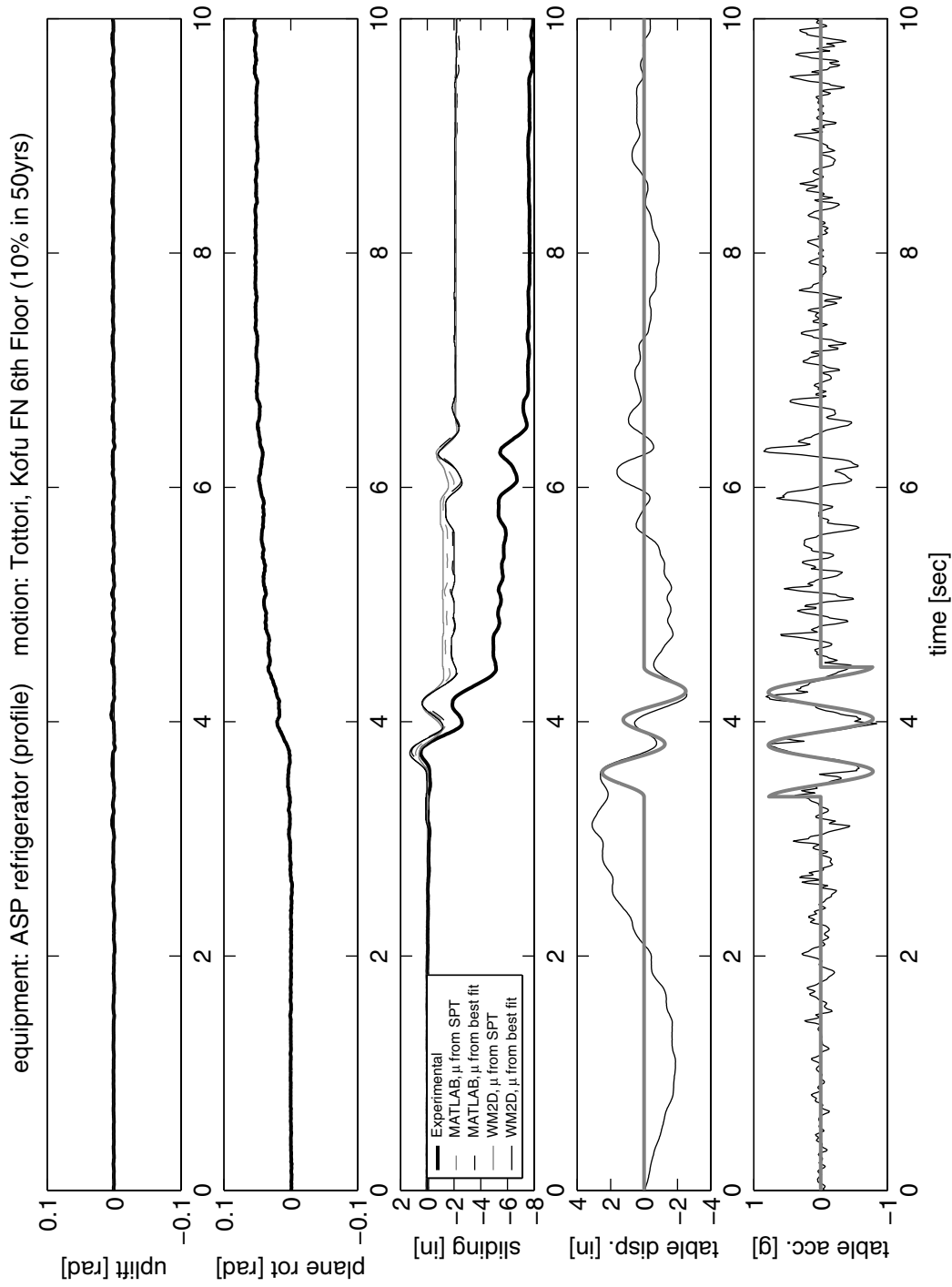


Figure 4.29 Response of the ASP refrigerator (*profile* configuration) subjected to the UC Science Building 6th floor motion of the Kofu FN (10% in 50 years) record of the 2000 Tottori, Japan, earthquake. The heavy grey lines on the bottom two graphs plot a Type-C₂ trigonometric pulse that approximates the main pulse of the motion record.

5 Regression Analysis and Fragility Curves for 50% in 50 Years and 10% in 50 Years Hazard Motions

5.1 SLIDING AND GOVERNING PARAMETERS

The shake table experiments on freestanding equipment presented in Chapter 4 indicated that although rocking was realizable, overturning did not occur (except for the one case when the FORMA incubator toppled due to a low-cycle fatigue failure of one of its leg supports). For the practical purposes of this study, therefore, the major concern is the sliding displacement that a piece of equipment will exhibit during earthquake shaking.

Many parameters influence the full behavior of a piece of equipment subjected to seismic motion. However, since we are primarily concerned with sliding, the governing parameters become those that describe (a) the mechanical characteristics of the equipment-floor interface and (b) the kinematic characteristics of the base motion. From the slow pull tests performed on the equipment (see Chapter 3), the load-displacement curves show that there is a pre-yielding elasticity due to the flexibility of the legs. A peak value of force is reached (associated with the static coefficient of friction μ_s) after which the equipment starts sliding with a relatively constant force (associated with the kinetic coefficient of friction μ_k). Three parameters would therefore be necessary to describe this model. Since the goal of this study is to develop a *practical* methodology for estimating the sliding displacements and the probability that this will not exceed a certain capacity limit, a *limited* number of parameters had to be selected. The one parameter that best describes the sliding resistance of the interface is the kinetic coefficient of friction μ_k , designated hereafter simply as μ .

Figures 4.2 to 4.29 that plot the results of the shake table tests on the freestanding equipment also plot the results obtained by numerical simulations for two different models of the slid-

ing interface: an elastoplastic model (*MATLAB*) and a Coulomb friction model (*WM2D*). It was noted that when the values μ obtained from the slow pull tests (see Figs. 3.4 to 3.6 and Table 3.2) were used, the numerical predictions of the elastoplastic model (plotted with dashed grey lines in Figs. 4.2 to 4.29) are, in general, somewhat closer to the experimental results (heavy black lines) than the numerical prediction offered by the Coulomb friction model (solid grey lines). Nevertheless, even the elastoplastic model predictions are only in fair agreement with the experimental results. A considerably improved agreement between experimental and numerical results from either model is observed when the numerical value of μ is reduced in the numerical simulations. Interestingly, reducing μ in the Coulomb friction model (solid black lines) yields results that are generally just as close to the experimental results as the elastoplastic model predictions (dashed black lines).

The characterization of the base earthquake motions is more complicated. The most widely used parameter to indicate the strength of the motion is the Peak Ground Acceleration, *PGA*. Since this study also deals with floor motions, the peak value of the motion is generically designated Peak Table Acceleration, *PTA*. However, this one value is not sufficient to characterize the catastrophic potential of earthquake shaking. Past studies have demonstrated that strong near-fault motions contain a predominant pulse that can be used to model some of the most prevalent kinematic characteristics of the motion (Makris and Roussos 2000; Makris and Chang 2000; and references reported therein). Besides the *PTA*, this study also uses the predominant trigonometric pulse's circular frequency, ω_p . Note that PTA / ω_p^2 is a characteristic length scale of the excitation that serves as a measure of its intensity (Makris and Black 2003). The following section is a discussion on trigonometric pulses that can be used to approximate the predominant pulse of an earthquake motion.

5.2 CLOSED-FORM DETERMINISTIC APPROXIMATION OF PULSE-TYPE AND NEAR-SOURCE EARTHQUAKE MOTIONS

The bottom window of Figure 4.6 plots the fault-normal component of the ground acceleration recorded at the Gavilan College station during the 1989 Loma Prieta, California, earthquake, together with a one-sine acceleration pulse (heavy grey line) that approximates the main pulse of the ground motion. The window above plots the resulting ground displacements of the recorded motion and the trigonometric pulse that approximates it. The ground moves forward, and it recov-

ers only partially after the equipment stops sliding. Note that the main pulse of the record coincides with the initiation of sliding around $t = 4.2$ sec. A forward-displacement such as this can be approximated by a Type-A pulse given by (Jacobsen and Ayre 1958; Veletsos et al. 1965; Makris 1997)

$$\begin{aligned}\ddot{u}_g^A(t) &= \frac{1}{2}\omega_p v_p \sin(\omega_p t), & 0 \leq t \leq T_p \\ \dot{u}_g^A(t) &= \frac{1}{2}v_p [1 - \cos(\omega_p t)], & 0 \leq t \leq T_p \\ u_g^A(t) &= \frac{1}{2}v_p \left[t - \frac{1}{\omega_p} \sin(\omega_p t) \right], & 0 \leq t \leq T_p\end{aligned}\quad (5.1)$$

where v_p is the amplitude of the velocity pulse and $\omega_p = 2\pi / T_p$ is the circular frequency of the pulse, which are selected judiciously to approximate the main displacement and velocity pulse. In constructing Figure 4.6, the values of pulse duration $T_p = 0.4$ sec and pulse velocity $v_p = -28$ in./sec were used.

Figure 4.2 (bottom) plots the fault-parallel acceleration history recorded at the OTE station during the 1995 Aigion, Greece, earthquake, and a one-cosine acceleration pulse that approximates it. The window above plots the displacement of the ground obtained by twice-integrating the recorded ground acceleration. It can be seen that in this case the ground moves in one direction, then reverses, fully recovering. This forward-and-back pulse can be approximated by a Type-B pulse (Makris 1997)

$$\begin{aligned}\ddot{u}_g^B(t) &= \omega_p v_p \cos(\omega_p t), & 0 \leq t \leq T_p \\ \dot{u}_g^B(t) &= v_p \sin(\omega_p t), & 0 \leq t \leq T_p \\ u_g^B(t) &= \frac{v_p}{\omega_p} [1 - \cos(\omega_p t)], & 0 \leq t \leq T_p\end{aligned}\quad (5.2)$$

In constructing Figure 4.2, a pulse duration $T_p = 0.53$ sec and a velocity amplitude of $v_p = 24$ in./sec were used.

Not all near-source motions are forward or forward-and-back pulses. Figure 4.3 plots the fault-normal component of the Gilroy Array #6 motion recorded during the 1979 Coyote Lake, California, earthquake together with a Type-C₁ trigonometric pulse that approximates it. Figure 4.13 plots the 6th floor motion resulting from the nonlinear dynamic analysis of the UC Science

Building subjected to the fault-normal component of the Kofu motion recorded during the 2000 Tottori, Japan, earthquake, together with a Type-C₂ pulse that approximates the two-cycle predominant pulse of the floor motion. Near-fault ground motions where the displacement history exhibits one or more long duration cycles are approximated by Type-C pulses. An n-cycle ground displacement is approximated by a Type-C_n pulse, which is defined by (Makris and Chang 2000; Makris and Roussos 2000)

$$\begin{aligned}
\ddot{u}_g^{C_n}(t) &= \omega_p v_p \cos(\omega_p t + \varphi), & 0 \leq t \leq \left(n + \frac{1}{2} - \frac{\varphi}{\pi}\right) T_p \\
\dot{u}_g^{C_n}(t) &= v_p [\sin(\omega_p t + \varphi) - \sin \varphi], & 0 \leq t \leq \left(n + \frac{1}{2} - \frac{\varphi}{\pi}\right) T_p \\
u_g^{C_n}(t) &= \frac{v_p}{\omega_p} [-\cos(\omega_p t + \varphi) - \omega_p t \sin \varphi + \cos \varphi], & 0 \leq t \leq \left(n + \frac{1}{2} - \frac{\varphi}{\pi}\right) T_p
\end{aligned} \tag{5.3}$$

In deriving Equation (5.3), it is required that the resulting displacement and velocity be differentiable signals. The value of the phase angle, φ , is determined by requiring that the ground displacement at the end of the pulse be zero.

$$\int_0^{\left(n + 1/2 - \varphi/\pi\right)T_p} \dot{u}_g^{C_n}(t) dt = 0 \tag{5.4}$$

Evaluating this integral gives

$$\cos[(2n + 1)\pi - \varphi] + [(2n + 1)\pi - 2\varphi] \sin \varphi - \cos \varphi = 0 \tag{5.5}$$

The solution of the transcendental equation given by (5.5) gives the value of the phase angle φ . For example, for a Type-C₁ pulse ($n = 1$), φ is equal to 0.0697π ; whereas for a for a Type-C₂ pulse ($n = 2$), φ is equal to 0.0410π .

Table 5.1 lists the input motions used for this shake table test study. The third column of Table 5.1 also lists the type and defining parameters (T_p and v_p) of the trigonometric pulse that approximates the predominant pulse of each of the earthquake input motions. The acceleration and displacement time histories of these trigonometric pulses are plotted on the bottom two windows of Figures 4.2 to 4.29 (heavy grey lines) together with their corresponding earthquake records (black lines).

Table 5.1 Kinematic characteristic of the 50% and 10% in 50 years hazard level earthquake motions used in this study. The motion PTA and pulse $\omega_p=2\pi/T_p$ together with the maximum recorded equipment sliding displacement U_{max} and interface friction coefficient μ produce the intensity measure IM and engineering demand parameter EDP .

Equipment	Earthquake Motion (Probability of Exceedence in 50 years)	Pulse, T_p [sec], v_p [in/sec]	PTA [g]	U_{max} [in]	μ (slow pull)	μ (best fit)	IM $PTA / \mu g - 1$	EDP $U_{max} \omega_p^2 / PTA$
FORMA	Aigion, OTE	B, 0.53, 24	0.75	6.87	0.23	0.13	2.26	3.34
	Coyote Lake, Gilroy #6	C1, 0.70, -20	0.68	2.57	0.23	0.13	1.96	0.79
	Coyote Lake, Gilroy #6 ground (50%)	C1, 0.70, 20	0.75	3.07	0.23	0.13	2.26	0.85
	Coyote Lake, Gilroy #6 6th floor (50%)	C1, 0.64, 30	0.75	5.80	0.23	0.13	2.26	1.93
	Loma Prieta, Gavilan College ground (10%)	A, 0.40, -28	0.73	3.79	0.23	0.13	2.17	3.32
Kelvinator	Aigion OTE	B, 0.53, 24	0.76	6.00	0.28	0.17	1.71	2.87
	Coyote Lake, Gilroy #6	C1, 0.70, -20	0.69	2.13	0.28	0.17	1.46	0.64
	Coyote Lake, Gilroy #6 ground (50%)	C1, 0.70, 20	0.74	3.26	0.28	0.17	1.64	0.92
	Coyote Lake, Gilroy #6 6th floor (50%)	C1, 0.64, 30	0.76	7.37	0.28	0.17	1.71	2.42
	Loma Prieta, Gavilan College ground (10%)	A, 0.40, -28	0.76	2.26	0.28	0.17	1.71	1.90
ASP (Face)	Loma Prieta, Gavilan College 6th floor (10%)	C1, 0.80, 24	0.64	5.06	0.28	0.17	1.29	1.26
	Tottori, Kofu 6th floor (10%)	C2, 0.45, 22	0.81	5.24	0.28	0.17	1.89	3.27
	Aigion OTE	B, 0.53, 24	0.86	3.16	0.31	0.20	1.77	1.34
	Coyote Lake, Gilroy #6	C1, 0.70, -20	0.73	1.61	0.31	0.20	1.35	0.46
	Coyote Lake, Gilroy #6 ground (50%)	C1, 0.70, 20	0.76	3.61	0.31	0.20	1.45	0.99
ASP (Profile)	Coyote Lake, Gilroy #6 6th floor (50%)	C1, 0.64, 30	0.77	9.35	0.31	0.20	1.48	3.03
	Loma Prieta, Gavilan College ground (10%)	A, 0.40, -28	0.77	1.85	0.31	0.20	1.48	1.54
	Loma Prieta, Gavilan College 6th floor (10%)	C1, 0.80, 24	0.67	7.03	0.31	0.20	1.16	1.68
	Tottori, Kofu ground (10%)	C2, 0.48, 20	1.07	13.89	0.31	0.20	2.45	5.76
	Tottori, Kofu 6th floor (10%)	C2, 0.45, 22	0.87	6.63	0.31	0.20	1.80	3.86
ASP (Profile)	Aigion, OTE	B, 0.53, 24	0.73	2.41	0.31	0.20	1.35	1.20
	Coyote Lake, Gilroy #6	C1, 0.70, -20	0.70	1.02	0.31	0.20	1.26	0.30
	Coyote Lake, Gilroy #6 ground (50)	C1, 0.70, 20	0.75	3.68	0.31	0.20	1.42	1.02
	Coyote Lake, Gilroy #6 6th floor (50)	C1, 0.64, 30	0.80	8.01	0.31	0.20	1.58	2.50
	Loma Prieta, Gavilan College ground (10)	A, 0.40, -28	0.79	2.59	0.31	0.20	1.55	2.10
Tottori, Kofu ground (10%)	Gavilan College 6th floor	C1, 0.80, 24	0.67	6.70	0.31	0.20	1.16	1.60
	Tottori, Kofu ground (10%)	C2, 0.48, 20	1.07	16.62	0.31	0.20	2.45	6.90
	Tottori, Kofu 6th floor (10%)	C2, 0.45, 22	0.85	7.96	0.31	0.20	1.74	4.73

5.3 INTENSITY MEASURE AND ENGINEERING DEMAND PARAMETER

5.3.1 Intensity Measure, IM

As mentioned earlier, the attempt to estimate the sliding response of the heavy laboratory equipment that is the focus of this study is cast in a probabilistic framework. The PEER performance-based earthquake engineering (PBEE) methodology suggests the identification of an intensity measure, IM . After several considerations, a meaningful and, at the same time, simple, dimensionless IM is

$$IM = \frac{PTA}{\mu g} - 1 \quad (5.6)$$

where PTA is the peak table acceleration, μ is the interface kinetic friction coefficient, and g is the acceleration of gravity. Recall that the condition for sliding to occur is $PTA / \mu_s g > 1$, and since generally $\mu_s > \mu$, it is possible for sliding to occur even for negative values of the chosen IM . However, the amount of sliding that corresponds to such small IM values is extremely unlikely to exceed preset sliding capacity limits, and is therefore of little importance for practical engineering purposes. Moreover, the numerical simulation studies that were done in parallel with the experimental studies showed that the coefficient of static friction μ_s had little influence on the maximum sliding displacement that the equipment exhibited. On the other hand, this maximum sliding displacement was considerably more sensitive to the *kinetic* coefficient of friction μ . For this reason, the expression for IM given by (5.6) features μ and not μ_s .

Typically the IM is a characteristic of the ground motion irrespective of the characteristics of the structural components themselves—which are denoted by D . In this case, it was found necessary to incorporate the coefficient of friction μ (which would otherwise be classified as a design parameter, D) in the IM in order to be able to present an Engineering Demand Parameter, EDP , as a simple function of one IM .

5.3.2 Engineering Demand Parameter, EDP

The chosen Engineering Demand Parameter, EDP , will be henceforth designated as Δ . It is given by

$$\Delta = \frac{U_{max} \omega_p^2}{PTA} \quad (5.7)$$

where U_{max} is the maximum sliding displacement recorded, ω_p is the circular frequency of the pulse that approximates the predominant pulse of the earthquake excitation, and PTA is the Peak Table Acceleration of the earthquake excitation.

The choice for the *EDP* emerges from *dimensional analysis* in conjunction with previously published results on the response of a sliding block. Within the context of earthquake engineering, an early solution to the response of a rigid-plastic system like that shown on the bottom of Figure 6.1 (a rigid mass sliding on a moving base with interface coefficient of friction $\mu = \mu_s = \mu_k$) subjected to a rectangular acceleration pulse was presented by Newmark (1965). Under a rectangular acceleration pulse with amplitude $a_p > \mu g$ and duration T_p , the acceleration, velocity, and displacement of the base are respectively

$$\begin{aligned} \ddot{u}_g(t) &= a_p, & 0 \leq t \leq T_p \\ \dot{u}_g(t) &= a_p t, & 0 \leq t \leq T_p \\ u_g(t) &= \frac{1}{2} a_p t^2, & 0 \leq t \leq T_p \end{aligned} \quad (5.8)$$

and the maximum relative-to-the-base displacement of the mass is (Newmark 1965)

$$U_{max} = 2\pi^2 \frac{a_p}{\omega_p^2} \left(\frac{a_p}{\mu g} - 1 \right) \quad (5.9)$$

which can be rewritten as

$$\frac{U_{max} \omega_p^2}{a_p} = 2\pi^2 \left(\frac{a_p}{\mu g} - 1 \right) \quad (5.10)$$

Equation (5.10) states that the graph of $U_{max} \omega_p^2 / a_p$ as a function of $a_p / \mu g - 1$ is one master line with slope $2\pi^2$, regardless of what a_p , ω_p , and μ are. The maximum sliding displacement U_{max} can be extracted from this master line. This physical quality that different graphs can be morphed into one master graph by appropriate scaling of their axes is called *similarity*—an invariance with respect to changes in scale—which is a decisive symmetry that shapes nonlinear behavior.

Our quantity of interest U_{max} can be expressed as a function of independent variables a_p , ω_p , and μg

$$U_{max} = f(a_p, \omega_p, \mu g) \quad (5.11)$$

the dependent variable U_{max} and independent variables a_p , ω_p , and μg , have reference dimensions

$$[U_{max}] = L, \quad [a_p] = LT^{-2}, \quad [\omega_p] = T^{-1}, \quad [\mu g] = LT^{-2} \quad (5.12)$$

Therefore, there are altogether 4 variables and 2 independent dimensions, L and T . Buckingham's *Pi Theorem*, the central theorem of Dimensional Analysis, states that a dimensionally homogeneous equation with a total of k variables and r reference dimensions, can be reduced to a relationship among $k - r$ independent *dimensionless* Π -products (Barenblatt 1996). Two obvious choices for Π -products for the present problem are

$$\Pi_1 = \frac{U_{max}\omega_p^2}{a_p} \quad \text{and} \quad \Pi_2 = \frac{\mu g}{a_p} \quad (5.13)$$

and the two are related by a function

$$\Pi_1 = \phi(\Pi_2) \quad (5.14)$$

or

$$\frac{U_{max}\omega_p^2}{a_p} = \phi\left(\frac{\mu g}{a_p}\right) \quad (5.15)$$

Referring to Equation (5.10), we see that, for the rectangular acceleration pulse, this function is in fact

$$\Pi_1 = 2\pi^2\left(\frac{1}{\Pi_2} - 1\right) \quad (5.16)$$

Note from Equations (5.6) and (5.16) that the *IM* chosen is exactly the quantity in parenthesis in (5.16) except that the *IM* uses for simplicity *PTA* instead of a_p . The two values are expected to be close. For the case of trigonometric pulses such as Type-A, Type-B, and Type-C_n, the response of the rigid-plastic system is again described by Equation (5.15) (Makris and Black 2003; Konstantinidis and Makris 2005), and the form of the function ϕ is obtained numerically. Figure 5.1 plots with solid lines the response of the rigid-plastic system when subjected to a rectangular pulse and to a one-sine (i.e., Type-A) trigonometric pulse. The dimensionless displacement $\Pi_1 = U_{max}\omega_p^2 / a_p$ is plotted on a logarithmic scale in order to illustrate the relative strengths of the two types of pulses. The closed-form solution due to the rectangular pulse is given by Equ-

Peak Displacement of a Sliding Block Subjected to Square and Type-A Pulse Excitations

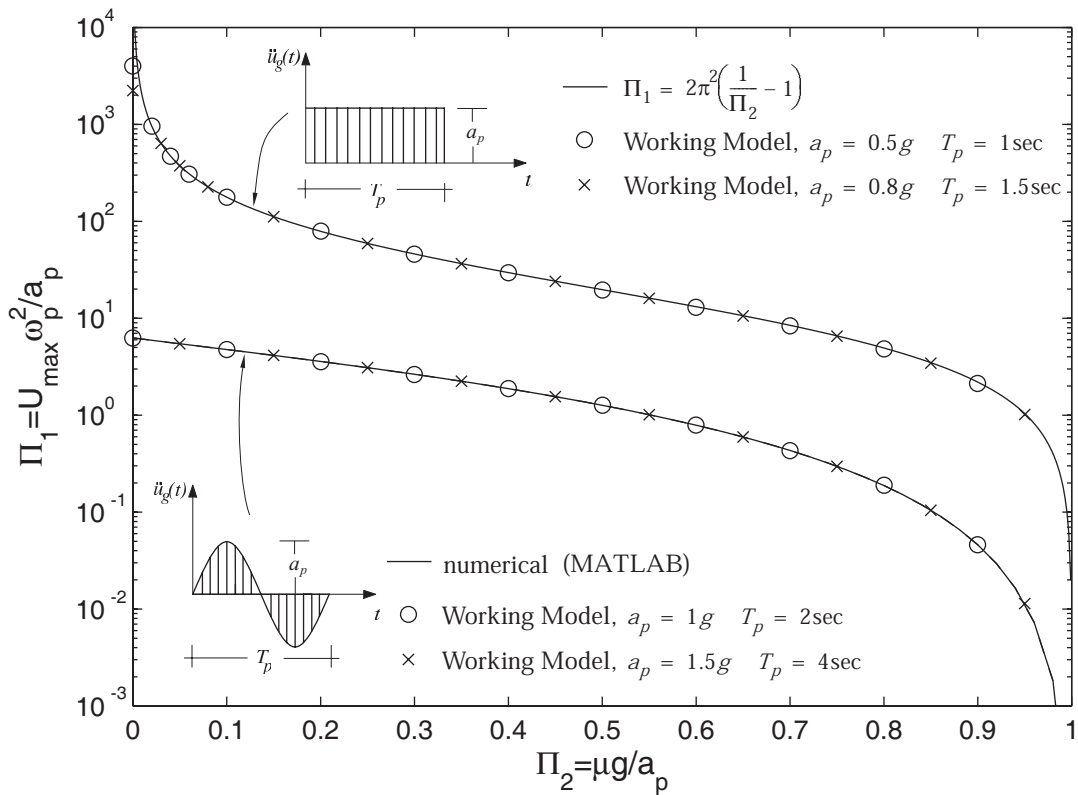


Figure 5.1 Dimensionless displacement Π_1 as a function of the dimensionless strength Π_2 for rigid-plastic system subjected to rectangular and Type-A acceleration pulses with amplitude a_p and duration $T_p=2\pi/\omega_p$. The response saturates into a single master curve for each pulse, indicating the physical similarity.

tion (5.10), while the solution due to the one-sine pulse is obtained numerically using standard ODE solvers available in *MATLAB* (2002).

5.4 FRAGILITY ANALYSIS FOR 50% AND 10% IN 50 YEARS HAZARD LEVEL MOTIONS

5.4.1 Regression of the Experimental Data

Figure 5.2 (top) plots the Engineering Demand Parameter $\Delta = U_{max}\omega_p^2 / PTA$ as a function of the Intensity Measure $PTA / \mu g - 1$ for the shake table tests performed on the three pieces of equipment. The value of the coefficient of friction, μ , is that obtained by the slow pull tests (see Chapter 3). It is obvious that the data exhibits considerable scattering, which suggests that Δ has to be treated as a random variable. A least-squares linear regression of the data is plotted with a solid line, and it provides the mean value $\bar{\Delta}$ of the random variable Δ as a function of the intensity measure

$$\bar{\Delta}\left(\frac{PTA}{\mu g}\right) = 1.31\left(\frac{PTA}{\mu g} - 1\right) \quad (5.17)$$

The *coefficient of determination*, r^2 , for this regression is equal to 0.25 (Scheaffer and McClave 1995). This value is a quantitative confirmation for the necessity to consider Δ as a random variable. The shaded bars on the top graph of Figure 5.2 are statistical bins that are used to create a graph of the standard deviation to the mean as a function of the Intensity Measure. This standard deviation, $\sigma_{\Delta}(PTA / \mu g)$, is plotted on the bottom graph of Figure 5.2 together with a linear regression given by

$$\sigma_{\Delta}\left(\frac{PTA}{\mu g}\right) = 0.76\left(\frac{PTA}{\mu g} - 1\right) \quad (5.18)$$

with $r^2 = 0.80$.

Figure 5.3 (top) also plots $\Delta = U_{max}\omega_p^2 / PTA$ as a function of the Intensity Measure $PTA / \mu g - 1$ for the shake table tests performed on the three pieces of equipment; however, the value of the coefficient of friction, μ , is not that obtained by the slow pull tests but rather that obtained by best-fitting numerical simulation time history results to results recorded during the shake table experiments. The middle window of Figures 4.2 to 4.29 plots sliding displacement time histories obtained for two numerical simulation models where the coefficient of friction μ is

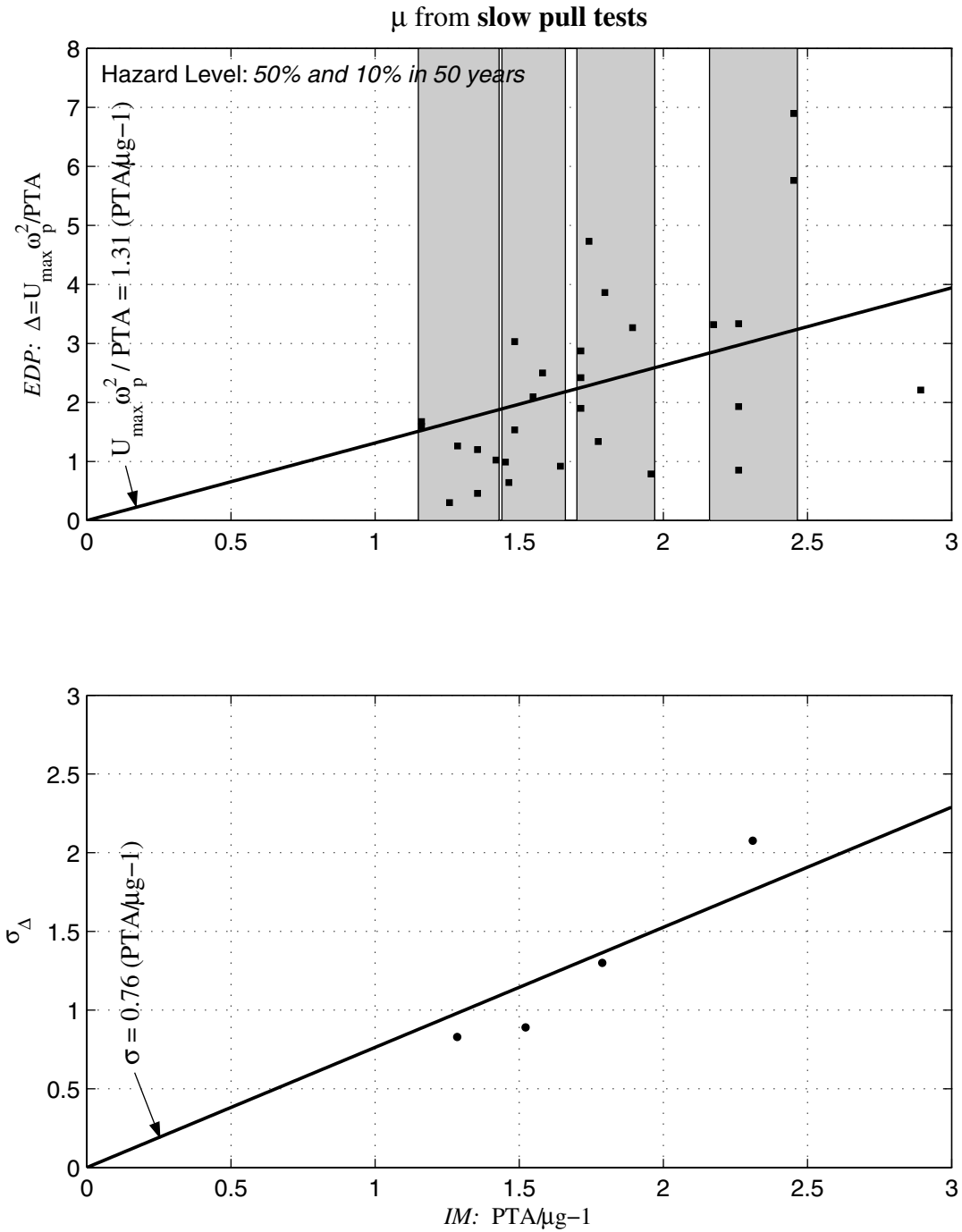


Figure 5.2 *Top:* The Engineering Demand Parameter $\Delta = U_{max} \omega_p^2 / PTA$ as a function of the Intensity Measure $PTA / \mu g^{-1}$ for the shake table tests performed on the three pieces of equipment. The value of μ is that obtained by the *slow pull tests*. *Bottom:* Standard deviation to the mean as a function of the Intensity Measure $PTA / \mu g^{-1}$.

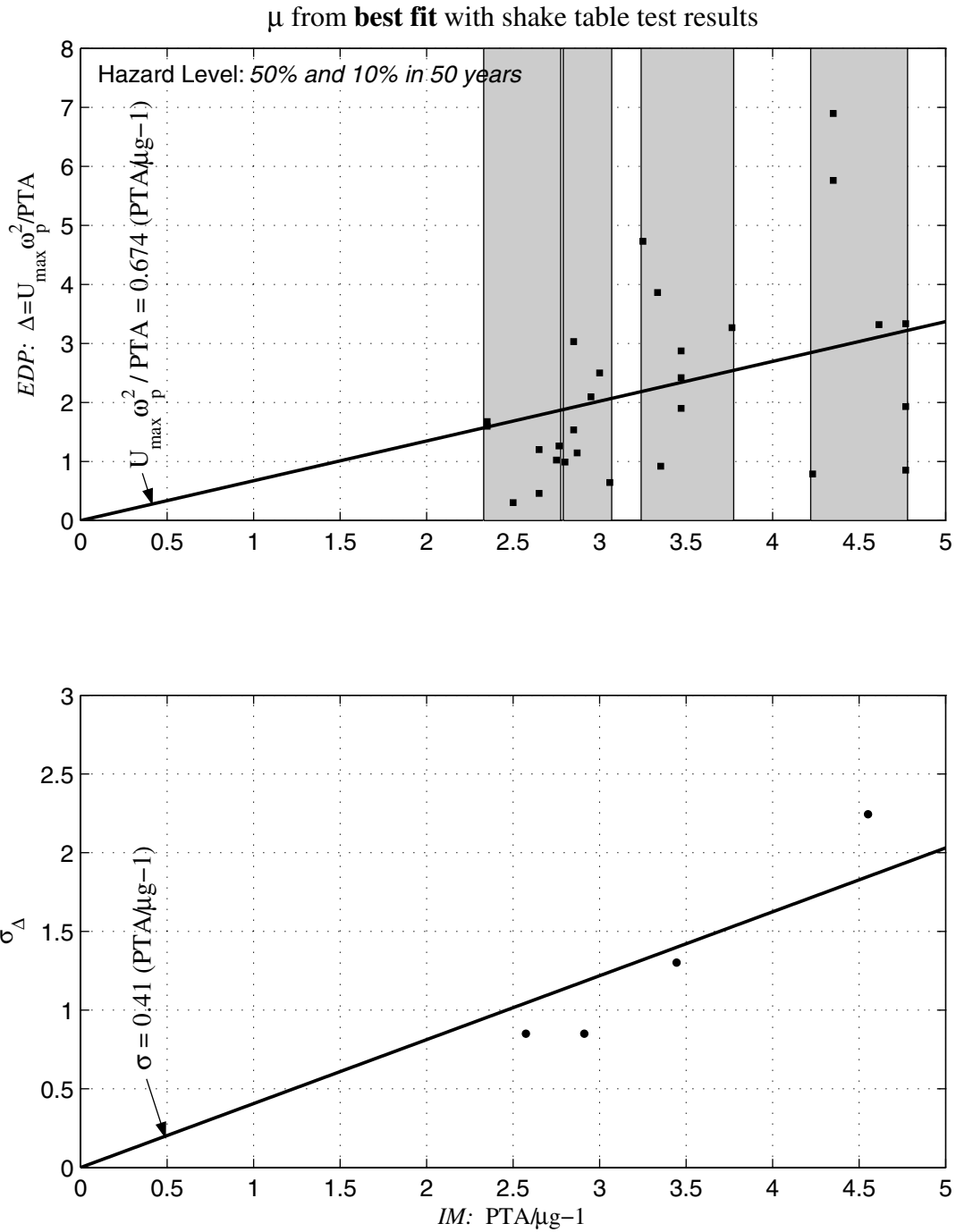


Figure 5.3 *Top:* The Engineering Demand Parameter $\Delta = U_{\max} \omega_p^2 / PTA$ as a function of the Intensity Measure $PTA / \mu g^{-1}$ for the shake table tests performed on the three pieces of equipment. The value of μ is obtained by *best-fit* of numerical simulation results to shake table test results. *Bottom:* Standard deviation to the mean as a function of the Intensity Measure $PTA / \mu g^{-1}$.

chosen so that the response approximates with better accuracy the experimental results (see Figs. 3.4 to 3.6 and Table 3.2). The displacement history plotted with a dashed black line is the response of an elastoplastic model obtained by *MATLAB*, while the displacement history plotted with a solid black line is the response of a Coulomb friction model obtained by *Working Model*. Note that the *Working Model* analysis also permits rocking to occur. The uplift history obtained by this model is plotted on the top window of Figures 4.2 to 4.29 together with the experimental results. The linear regression of the data plotted with a solid line in Figure 5.3 (top) is

$$\bar{\Delta}\left(\frac{PTA}{\mu g}\right) = 0.67\left(\frac{PTA}{\mu g} - 1\right) \quad (5.19)$$

with $r^2 = 0.19$. This standard deviation, σ , is plotted on the bottom graph of Figure 5.2 together with a linear regression given by

$$\sigma_{\Delta}\left(\frac{PTA}{\mu g}\right) = 0.41\left(\frac{PTA}{\mu g} - 1\right) \quad (5.20)$$

with $r^2 = 0.76$.

5.4.2 The *EDP* as a Lognormally Distributed Random Variable

When a random variable expresses a mechanical system's response that is necessarily positive ($\Delta > 0$), it is common to assume that the variable is lognormally distributed. In this study we hypothesize that the *EDP*, Δ , is lognormally distributed, and we test this hypothesis with the experimental results. The reason behind the name *lognormal* is that the lognormally distributed variable Δ is related to a normally distributed variable X by $X = \ln \Delta$. Note that Δ attains only positive values, $\delta > 0$, while the corresponding X variable is unrestricted, $-\infty < x < \infty$. The two-parameter lognormally distributed variable Δ has the probability density function

$$f_{\Delta}(\delta) = \frac{1}{\sqrt{2\pi\omega\delta}} \exp\left[-\frac{1}{2}\left(\frac{\ln\delta - \lambda}{\omega}\right)^2\right], \quad \delta > 0 \quad (5.21)$$

where the two defining parameters λ and ω of the distribution are in fact the mean and standard deviation of the corresponding normally distributed variable X (Crow and Shimizu 1988). The cumulative distribution function of Δ is given by

$$F_{\Delta}(\delta) = \int_0^{\delta} \frac{1}{\sqrt{2\pi\omega\delta'}} \exp\left[-\frac{1}{2}\left(\frac{\ln\delta' - \lambda}{\omega}\right)^2\right] d\delta' \quad (5.22)$$

Using the substitution $u = (\ln\delta' - \lambda) / \omega$, we obtain

$$\begin{aligned} F_{\Delta}(\delta) &= \int_{-\infty}^{\frac{\ln\delta - \lambda}{\omega}} \frac{1}{\sqrt{2\pi}} \exp\left(-\frac{u^2}{2}\right) du \\ &= \Phi\left(\frac{\ln\delta - \lambda}{\omega}\right) \end{aligned} \quad (5.23)$$

where Φ is the cumulative distribution function of a *standard* normal distribution (i.e., $\lambda = 0$ and $\omega = 1$). The mean, $\bar{\Delta}$ and standard deviation σ_{Δ} , of the lognormal variable Δ are related to the mean, λ , and standard deviation, ω , of the normal variable X by

$$\bar{\Delta} = \exp\left(\lambda + \frac{\omega^2}{2}\right) \quad \text{and} \quad \sigma_{\Delta} = \exp\left(\lambda + \frac{\omega^2}{2}\right) \sqrt{\exp(\omega^2) - 1} \quad (5.24)$$

or

$$\lambda = \ln\bar{\Delta} - \frac{1}{2} \ln\left[1 + \left(\frac{\sigma_{\Delta}}{\bar{\Delta}}\right)^2\right] \quad \text{and} \quad \omega = \sqrt{\ln\left[1 + \left(\frac{\sigma_{\Delta}}{\bar{\Delta}}\right)^2\right]} \quad (5.25)$$

Note that for the problem at hand, the statistical estimation of $\bar{\Delta} = \bar{\Delta}(PTA / \mu g)$ is given by Equation (5.17) or by Equation (5.19), and that of $\sigma_{\Delta} = \sigma_{\Delta}(PTA / \mu g)$ is given by Equation (5.18) or by Equation (5.20), depending on the choice for μ (either obtained by the slow pull tests or by the best-fit of numerical simulation results to the shake table test results). Correspondingly, the mean and standard deviation of the normally distributed variable X are themselves functions of the intensity measure—that is $\lambda = \lambda(PTA / \mu g)$ and $\omega = \omega(PTA / \mu g)$.

In order to not reject the hypothesis that Δ has a lognormal distribution, a goodness-of-fit test is to be performed. The Kolmogorov-Smirnov is such a statistical test; it compares the empirical distribution function of a random sample with a hypothesized theoretical distribution function (Scheaffer and McClave 1995). First we define the empirical cumulative distribution function $F_{\Delta}^*(\delta)$. The shake table experiments provided a random sample of n realizations of Δ . It is convenient to order these δ_i 's so that $\delta_1 \leq \delta_2 \leq \dots \leq \delta_n$. The empirical cumulative distribution function is given by

$$F_{\Delta}^*(\delta) = \begin{cases} \frac{i-1}{n} & \text{if } \delta_{i-1} \leq \delta < \delta_i \\ 1 & \text{if } \delta \geq \delta_n \end{cases} \quad (5.26)$$

where $i = 1, \dots, n$ and $\delta_0 = 0^+$. If the hypothesized distribution given by (5.22) or (5.23) is the true distribution, then $F_{\Delta}^*(\delta)$ and $F_{\Delta}(\delta)$ should be close. The Kolmogorov-Smirnov test uses this closeness as the metric by which the hypothesized distribution is evaluated. If the test fails, the hypothesized distribution must be rejected. Figure 5.4 plots the empirical cumulative distribution function. Together is plotted the cumulative distribution function of the hypothesized lognormally distributed random variable Δ , where the coefficient of friction μ is that obtained by the slow pull tests. The Kolmogorov-Smirnov test is based on the *maximum* distance between $F_{\Delta}(\delta)$ and $F_{\Delta}^*(\delta)$. That is

$$S = \max_{\delta} |F_{\Delta}(\delta) - F_{\Delta}^*(\delta)| \quad (5.27)$$

Now, since $F_{\Delta}^*(\delta)$ and $F_{\Delta}(\delta)$ are nondecreasing and $F_{\Delta}^*(\delta)$ is constant between sample observations, the maximum distance between $F_{\Delta}^*(\delta)$ and $F_{\Delta}(\delta)$ will occur either at one of the observation points or immediately to the left of one of these points. So

$$S = \max(S^+, S^-) \quad (5.28)$$

where

$$S^+ = \max_{1 \leq i \leq n} \left[\frac{i}{n} - F_{\Delta}(\delta_i) \right] \quad (5.29)$$

and

$$S^- = \max_{1 \leq i \leq n} \left[F_{\Delta}(\delta_i) - \frac{i-1}{n} \right] \quad (5.30)$$

For a certain level of significance α , the hypothesis is rejected if S exceeds a critical value of S_{cr} . The value of S_{cr} depends on α and the size of the sample, n . The shake table test sample size of this study is $n = 28$. For the distribution functions presented in Figure 5.4 (μ from slow pull tests), $S = 0.133$. Tables for the Kolmogorov-Smirnov test provide (Daniel 1990)

$$S_{cr}(\alpha, n=28) = \begin{cases} 0.197, & \alpha=0.80 \\ 0.225, & \alpha=0.90 \\ 0.250, & \alpha=0.95 \\ 0.279, & \alpha=0.98 \\ 0.300, & \alpha=0.99 \end{cases} \quad (5.31)$$

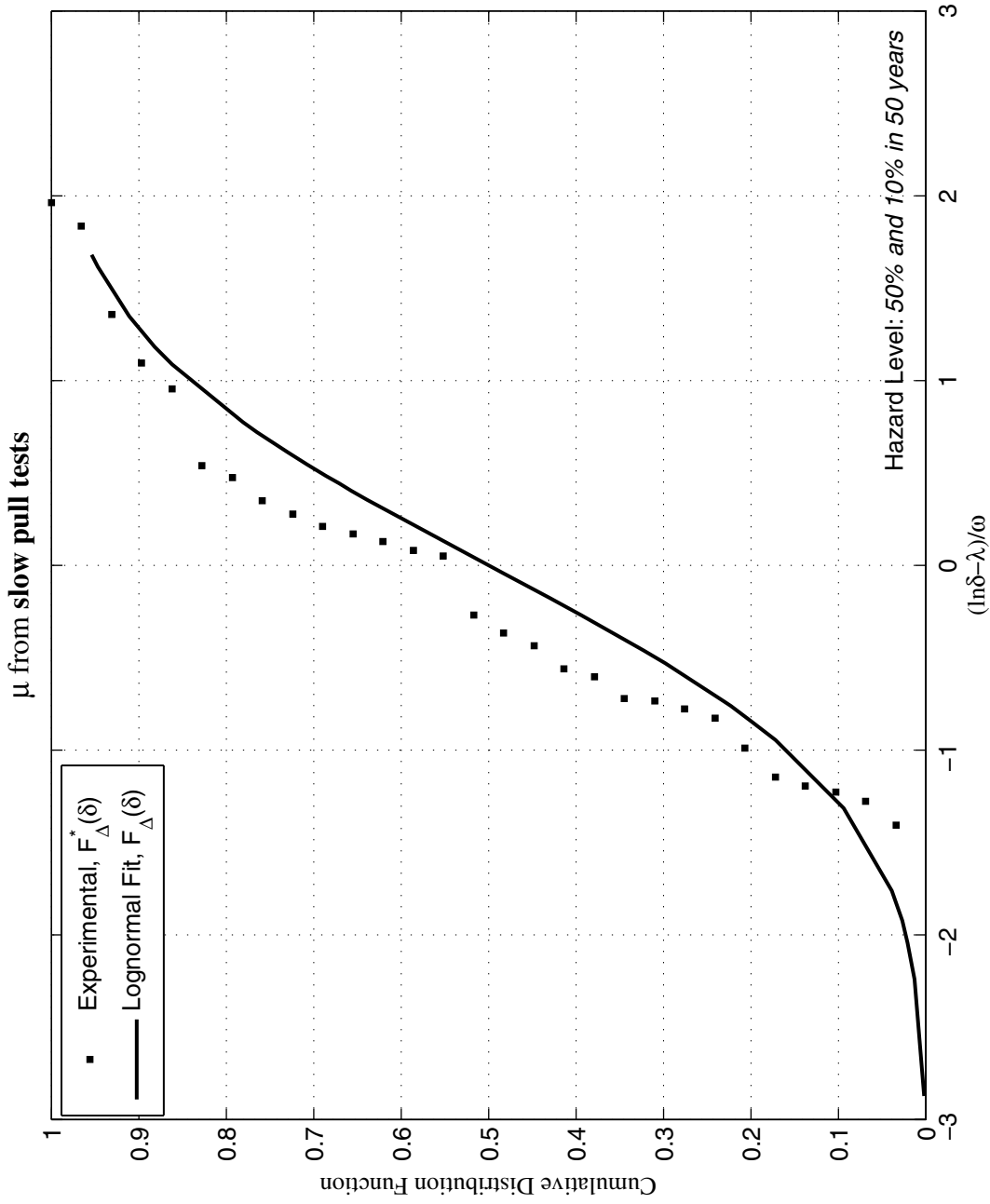


Figure 5.4 The empirical cumulative distribution function of the EDP Δ (50% and 10% hazard level motions) and the theoretical cumulative distribution function of its hypothesized lognormal distribution. The value of the friction coefficient μ that the random variable Δ depends on is that obtained from the slow pull tests.

Figure 5.5 plots the empirical and hypothesized theoretical cumulative distribution functions of the *EDP* Δ (μ from slow pull tests) where the values of the friction coefficient μ for the equipment are not those obtained from the slow pull tests but rather those whereby μ has been reduced in order to obtain numerical simulation results that are close to the experimentally observed response (last column of Table 3.2). For these $F_{\Delta}^*(\delta)$ and $F_{\Delta}(\delta)$, $S = 0.144$. Since $S < S_{cr}$ for both Figure 5.4 and 5.5, the hypothesis that Δ is lognormally distributed is *not* rejected.

5.4.3 Fragility Curves

Fragility is broadly defined as a conditional probability of failure. For the problem at hand, where we want to characterize the seismic response of heavy laboratory equipment in a probabilistic framework, we define fragility as the probability P_f that the Engineering Demand Parameter $\Delta = U_{max}\omega_p^2 / PTA$ for a piece of equipment will exceed a certain threshold (capacity) C , given the intensity measure, $IM = PTA / \mu g - 1$. For the lognormally distributed random variable Δ ,

$$P_f \equiv P(\Delta > C | IM) = 1 - P(\Delta < C | IM) = 1 - F_{\Delta}(\delta=C) = 1 - \Phi\left(\frac{\ln C - \lambda}{\omega}\right) \quad (5.32)$$

where Φ is the standard normal cumulative distribution function. Substituting (5.25) into (5.32) and rearranging, gives the fragility function

$$P_f = 1 - \Phi\left(\frac{\ln\left[\frac{C}{\bar{\Delta}(IM)}\sqrt{1 + \left(\frac{\sigma_{\Delta}(IM)}{\bar{\Delta}(IM)}\right)^2}\right]}{\sqrt{\ln\left[1 + \left(\frac{\sigma_{\Delta}(IM)}{\bar{\Delta}(IM)}\right)^2\right]}}\right) \quad (5.33)$$

Regression Equations (5.17) and (5.18), or (5.19) and (5.20), provide the functional dependence of $\bar{\Delta}$ and σ_{Δ} on the intensity measure, $IM = PTA / \mu g - 1$.

Figures 5.6 and 5.7 plot fragility curves for four values of capacity C . Note that each graph includes two curves; one is the fragility curve that corresponds to values of μ obtained from the slow pull tests, while the other corresponds to values of μ obtained by tailoring numerical simulations to approximate shake table experiment results. The shaded area between the two curves provides an envelope for the fragility. Typically fragility curves are plotted against the *EDP*. In this study, however, they are plotted against the *IM*, as this makes their use more direct.

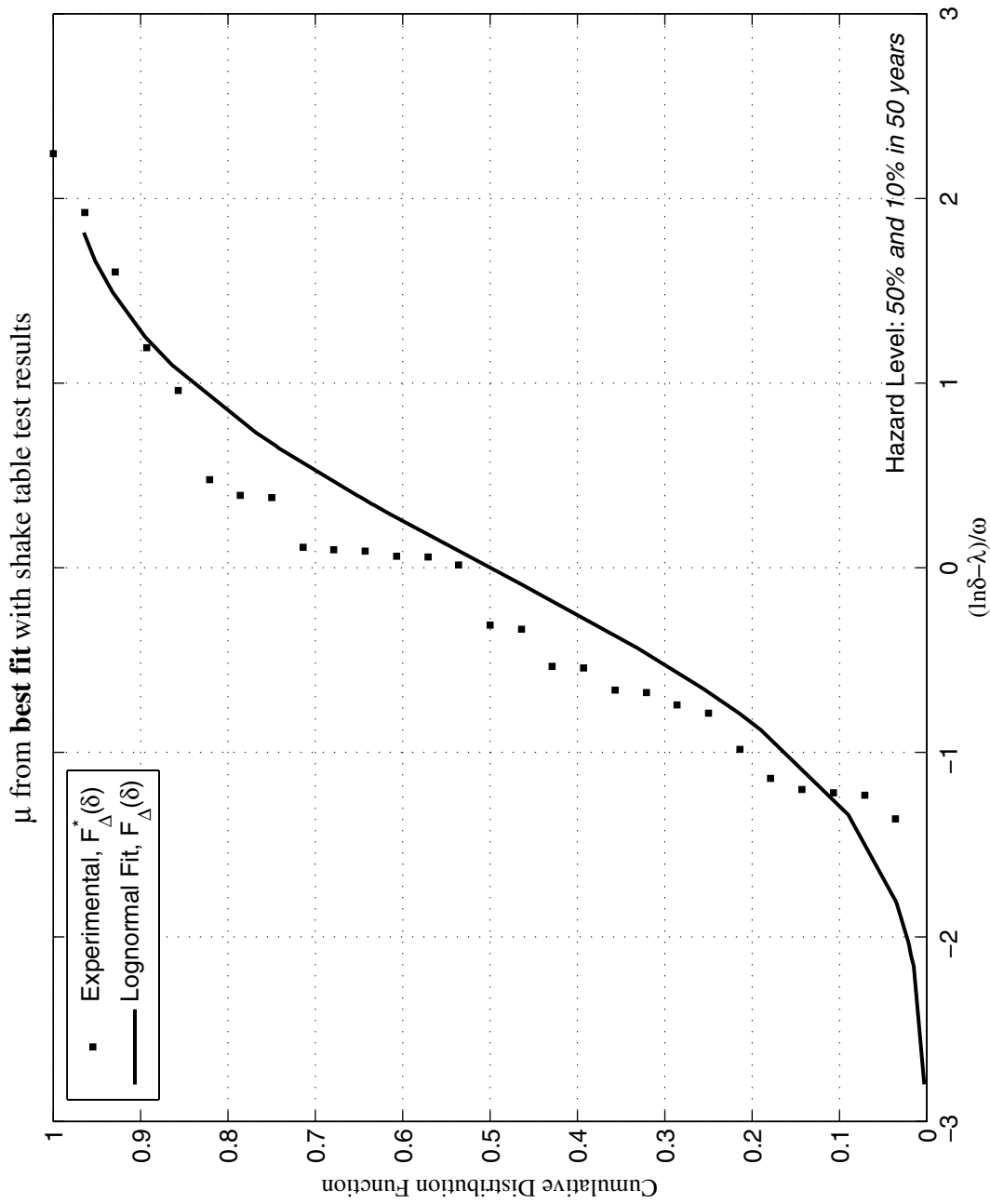


Figure 5.5 The empirical cumulative distribution function of the $EDP \Delta$ (50% and 10% hazard level motions) and the theoretical cumulative distribution function of its hypothesized lognormal distribution. The value of the friction coefficient μ that the random variable Δ depends on is that obtained from best-fitting numerical simulation results to the results obtained from the shake table tests.

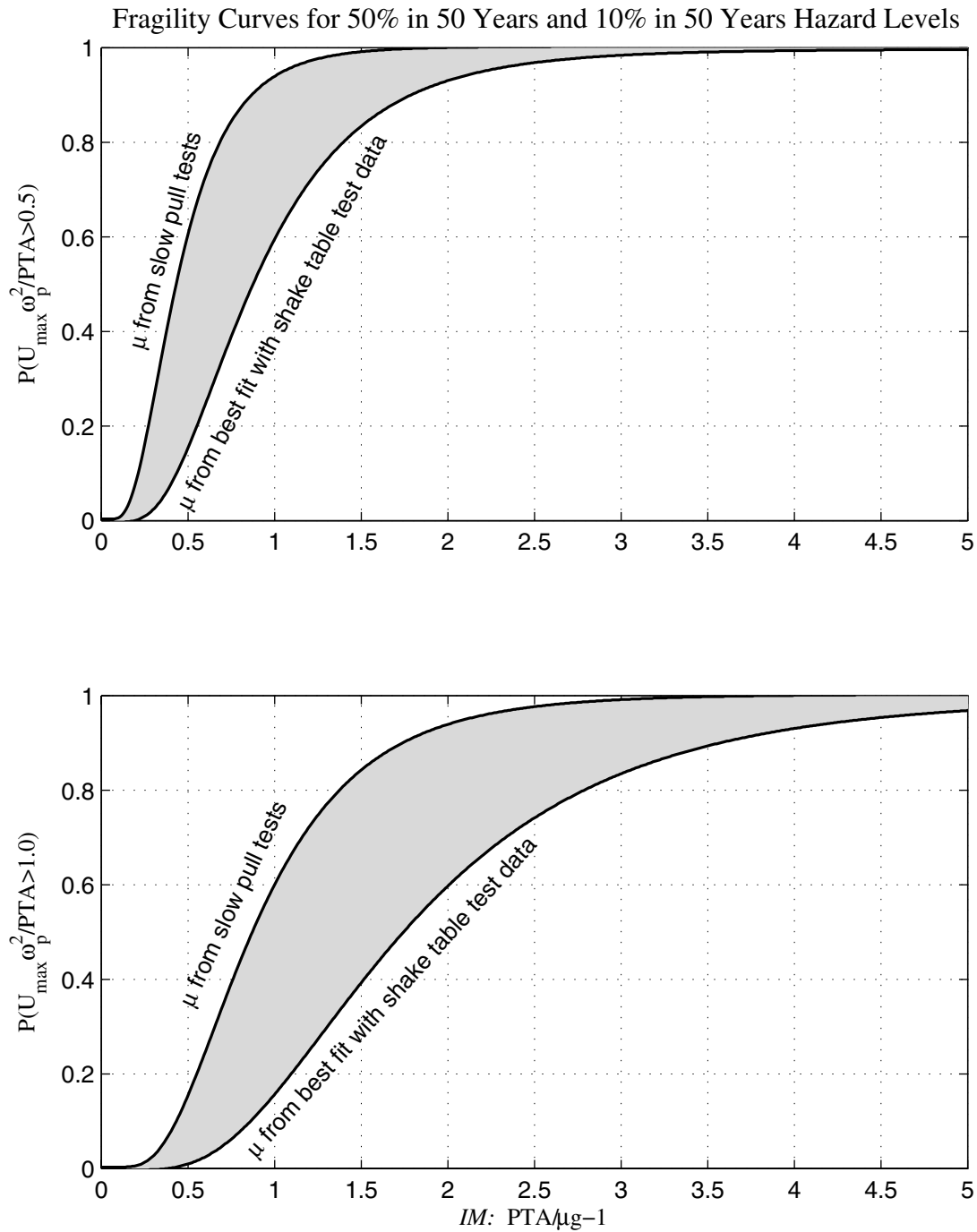


Figure 5.6 Fragility curves for $C=0.5$ (top) and $C=1.0$ (bottom). Two curves are plotted in each graph. The top curve corresponds to values of μ obtained by slow pull tests, while the bottom curve corresponds to values of μ obtained by best-fitting numerical simulation results to shake table experiment results.

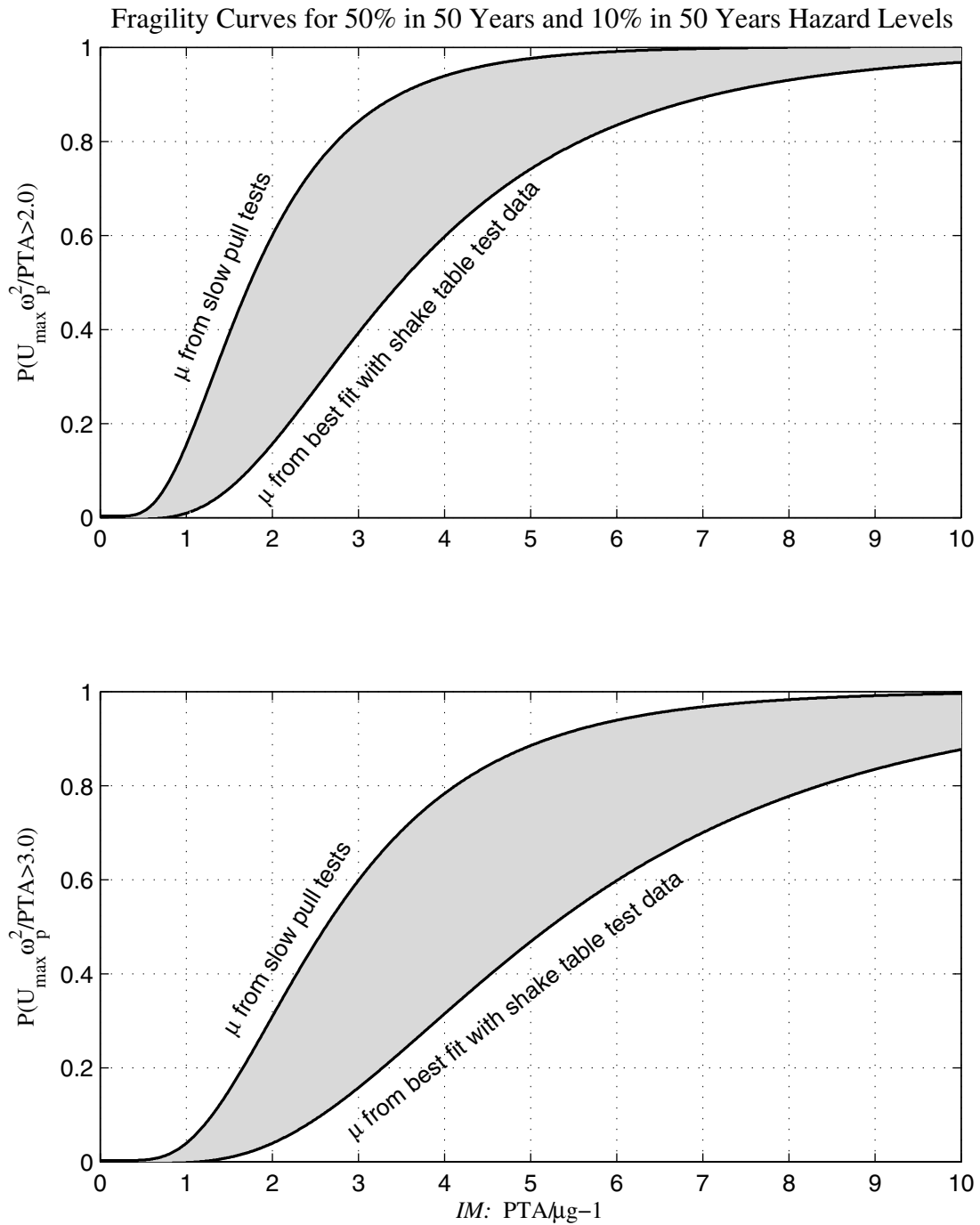


Figure 5.7 Fragility curves for $C=2.0$ (top) and $C=3.0$ (bottom). Two curves are plotted in each graph. The top curve corresponds to values of μ obtained by slow pull tests, while the bottom curve corresponds to values of μ obtained by best-fitting numerical simulation results to shake table experiment results.

Once relationships between the mean of the *EDP* and the *IM* (such as Equations (5.17) and (5.19)) and between the standard deviation to the mean of the *EDP* and the *IM* (such as Equations (5.18) and (5.20)), fragility curves such as those presented in Figures 5.6 and 5.7 can be generated by use of expression (5.33) for desired values of the threshold *C*. Given (or generating) a family of such fragility curves, a practicing engineer who wants to evaluate the probability that a piece of equipment will not exceed a threshold displacement could proceed as follows.

Example: How to Use a Fragility Curve

Suppose that an engineer is concerned with a piece of laboratory equipment that is located on the 6th floor of a hospital near an emergency exit. The design floor spectral acceleration is $S_a = 1.4g$ and the expected period of vibration is about $T_p = 0.8$ sec (say, the first modal period of the building). The engineer wants to estimate the probability that the piece of equipment with $\mu = 0.5$ will exceed a displacement of 18 in., which will result in blocking an emergency exit. The engineer would compute the intensity measure by Equation (5.6), obtaining

$$IM = PTA / \mu g - 1 = 1.4g / 0.5g - 1 = 1.8$$

The capacity value *C* that corresponds to the above design parameters is

$$C = U_{max} \omega_p^2 / PTA = 18 \text{ in.} (2\pi / 0.8 \text{ sec})^2 / (1.4 \cdot 386 \text{ in./sec}^2) \approx 2$$

The engineer would then refer to a fragility curve generated for $C = 2$ and read off the value of P_f . Figure 5.8 plots the generated fragility curve that corresponds to $C = 2$ (same as the top graph of Fig. 5.7). With the computed Intensity Measure of $IM = 1.8$, a conservative-average value of

$$P(U_{max} \omega_p^2 / PTA > 2) = P(U_{max} > 18 \text{ in.}) \approx 0.4$$

is read.

If the value of *C* that the engineer computes falls between already-available fragility curves—and the engineer does not want to generate a suitable fragility curve for the *C* in question—interpolation between the curves could be used.

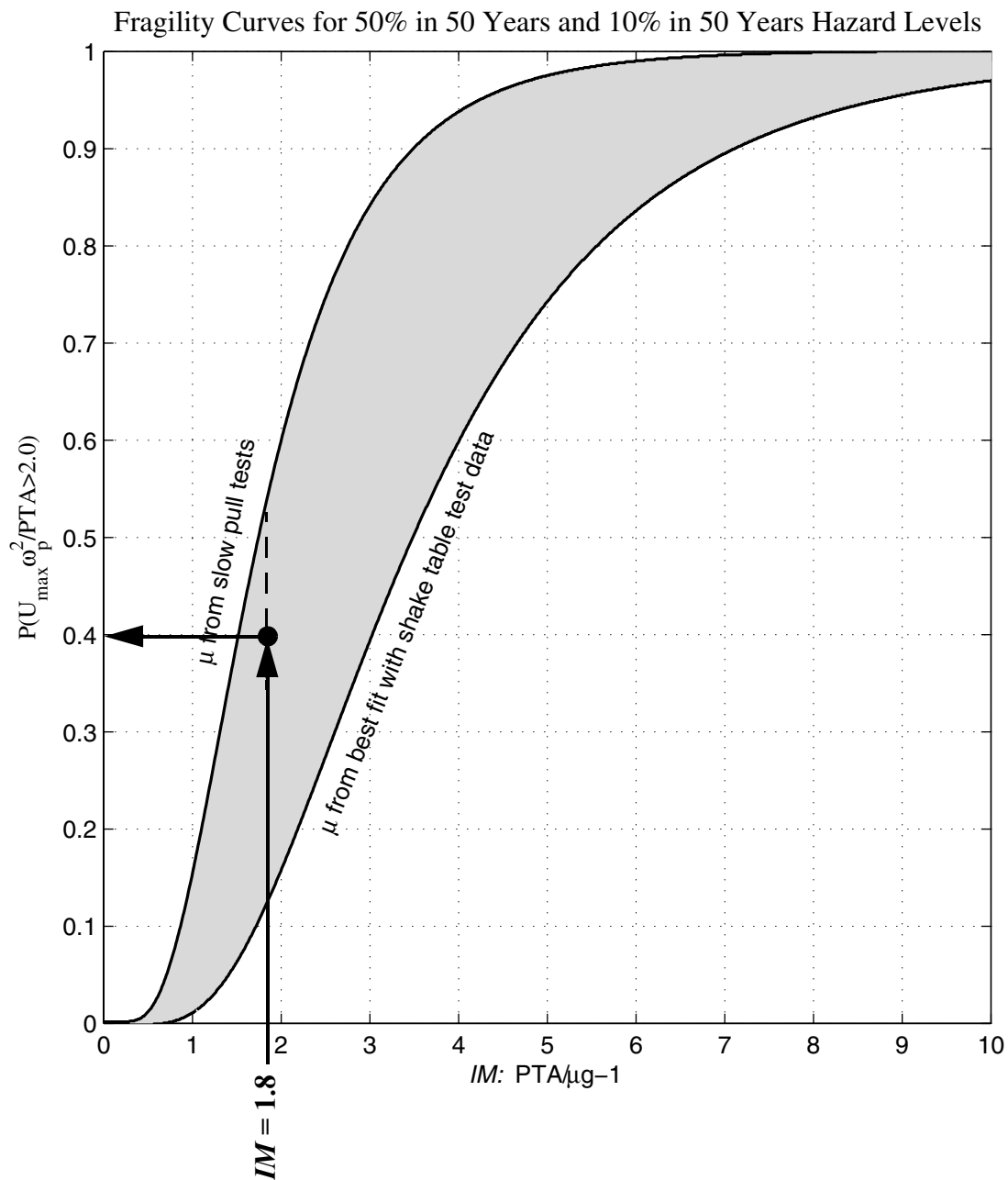


Figure 5.8 Fragility curve for $C=2.0$. With $PTA=1.4g$ and $\mu=0.5$, the Intensity Measure is $IM=PTA/\mu g-1=1.8$ and the probability that $U_{\max}>18$ in. for $\omega_p=2\pi/0.8$ rad/sec is roughly $P(U_{\max}\omega_p^2/PTA>2)=P(U_{\max}>18 \text{ in.})\sim 0.4$.

6 Response Analysis of Freestanding Equipment and Validation of Existing Software

For input motions resulting from seismic events with probability of exceedence of 50% and 10% in 50 years, the shake table experiments presented in Chapter 4 of this report indicated that there was no incidence of overturning due to excessive uplift (there was only one incidence of overturning, but it was due to failure of one of the equipment leg supports). Uplift rotations ranged from very low (for the Kelvinator and ASP refrigerators), to moderate (for the FORMA incubator), but never exceeding 50% of the equipment's stockiness α . For motions in that hazard level, the primary concern for the equipment tested was excessive sliding displacement, which reached up to 2 ft. The collected experimental data were used to construct sliding fragility curves that were presented in Chapter 5.

The horizontal displacement capacity of the shaking table at the Richmond Field Station Earthquake Simulation Laboratory, UC Berkeley, is ± 6 in. Due to this constraint, it was not possible to run tests with table displacements equal to the large ground and floor displacements of earthquakes that correspond to the 2% in 50 years hazard level. The predicted response of equipment subjected to 2% in 50 years motions was done with the use of numerical tools. In this chapter, we first review the dynamics of a piece of equipment resting on an accelerated base and then present a validation of numerical tools that can be used to estimate the response.

6.1 DYNAMIC RESPONSE OF A PIECE OF EQUIPMENT

A piece of equipment resting on a horizontally accelerated base can slide, rock, or slide-rock. Rocking, even if it does not result in overturning, is an undesirable mode of seismic response for the laboratory equipment, since it can result in serious damage to sensitive contents or to the equipment itself. In the following sections we review the possible modes of response for the

equipment. We present the pure rocking response and the pure sliding response of a rigid block, and we demonstrate the ability of the commercially available software *Working Model* (2000) to capture with high fidelity those two modes of response by testing it against in-house numerical codes (in *MATLAB*) that the authors and former advisees of the second author have developed in the past. Moreover, the response obtained by *Working Model* dynamic simulations is compared to experimental observations from the shake table tests. The good predictions offered by *Working Model* provide us with confidence in its ability to be used for analyzing the seismic response of heavy laboratory equipment.

6.1.1 Pure, Planar Rocking Motion of a Rigid Block

First we review the pure, planar rocking response of a rigid block subjected to a base acceleration. The assumption that the equipment can be modelled as rigid was confirmed during the shake table experiments by attaching sensitive DCDT displacement transducers across the faces of the equipment. The recorded displacements were indeed very small (the maximum recorded strain did not exceed 0.0001).

A schematic diagram of the rocking block of interest is shown in Figure 6.1 (top). The block has width W and height H . Under pure rocking, it is assumed that the frictional resistance of the interface is large enough to prevent sliding. The block can pivot about the centers of rotation O and O' when it is set to rocking. Depending on the level and form of the ground excitation, the block may translate with the ground, slide, rock, or slide-rock. Before 1996, the mode of rigid body motion that prevailed was determined by comparing the available static friction to the width-to-height ratio of the block, irrespective of the magnitude of the horizontal ground acceleration. At about the same time, Scalia and Sumbatyan (1996) and, independently, Shenton (1996) indicated that, in addition to pure sliding and pure rocking, there is a slide-rocking mode, and its manifestation depends not only on the width-to-height ratio and the static friction coefficient but also on the magnitude of the ground acceleration.

With no sliding occurring, under a positive horizontal acceleration that is sufficiently large, a rigid block will initially rotate with a negative rotation, $\theta < 0$, and, if it does not overturn, it will eventually assume a positive rotation; and so on. The equations of motion are obtained following a Lagrangian approach. We utilize a right corotational basis $\{\mathbf{e}_1, \mathbf{e}_2, \mathbf{e}_3\}$ as shown in Figure 6.1.

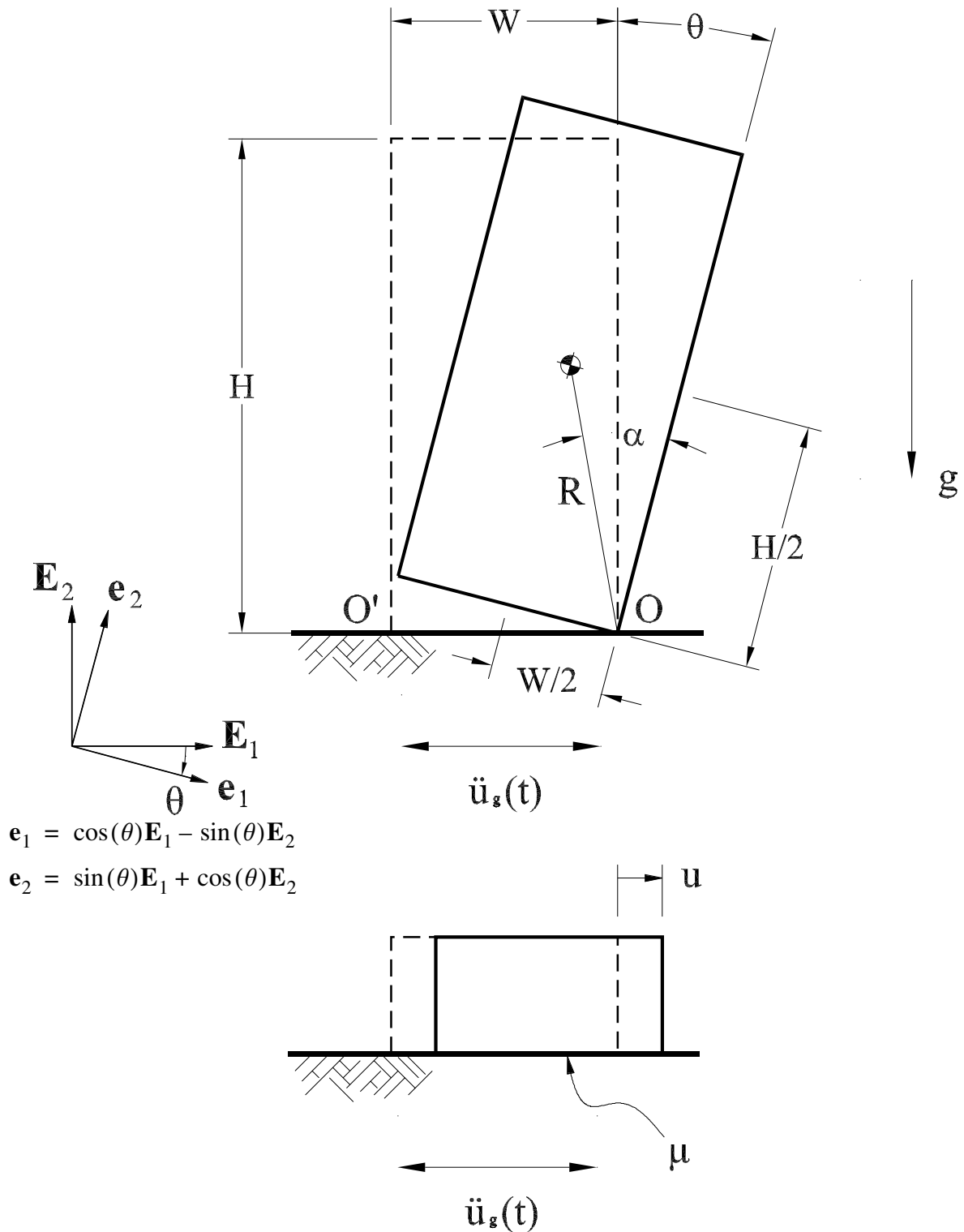


Figure 6.1 *Top:* Schematic of a rigid block in pure, planar rocking motion induced by base acceleration \ddot{u}_g . *Bottom:* Schematic of a rigid block in pure sliding motion induced by base acceleration \ddot{u}_g .

When $\theta > 0$ (i.e., the block pivoting about O), the position of the center of mass of the block is given by $\bar{\mathbf{r}} = \mathbf{r}_O + (-W\mathbf{e}_1 + H\mathbf{e}_2) / 2$, while when $\theta < 0$ (i.e., the block pivots about O'), the position of the center of mass of the block is given by $\bar{\mathbf{r}} = \mathbf{r}_{O'} + (W\mathbf{e}_1 + H\mathbf{e}_2) / 2$. The position of the center of mass of the block can be written more compactly as

$$\bar{\mathbf{r}} = \mathbf{r}_p + \frac{1}{2}[-\text{sgn}(\theta)W\mathbf{e}_1 + H\mathbf{e}_2] \quad (6.1)$$

where \mathbf{r}_p is the position of the pivot, and sgn is the signum function

$$\text{sgn}(\theta) = \begin{cases} +1, & \text{if } \theta > 0 \\ -1, & \text{if } \theta < 0 \end{cases} \quad (6.2)$$

With the angular velocity of the block given by $\boldsymbol{\omega} = -\dot{\theta}\mathbf{E}_3 = -\dot{\theta}\mathbf{e}_3$, the velocity of the center of mass of the block is given by

$$\bar{\mathbf{v}} = \boldsymbol{\omega} \times \frac{1}{2}[-\text{sgn}(\theta)W\mathbf{e}_1 + H\mathbf{e}_2] = \frac{\dot{\theta}}{2}[H\mathbf{e}_1 + \text{sgn}(\theta)W\mathbf{e}_2] \quad (6.3)$$

By König's decomposition theorem (Greenwood 1977), the kinetic energy can be expressed as the sum of the translational kinetic energy and the rotational kinetic energy $T = \bar{T} + T^\circ$,

$$T = \frac{1}{2}m\bar{\mathbf{v}} \cdot \bar{\mathbf{v}} + \frac{1}{2}\boldsymbol{\omega} \cdot \mathbf{J}\boldsymbol{\omega} \quad (6.4)$$

where m is the mass of the block, and \mathbf{J} is the inertia tensor about its center of mass. For the rectangular block in question, $\mathbf{J}\mathbf{e}_3 = m(W^2 + H^2)\mathbf{e}_3 / 12$, and using $R^2 = (W^2 + H^2) / 4$, the total kinetic energy is

$$T = \frac{2}{3}mR^2\dot{\theta}^2 \quad (6.5)$$

The force on the system is given by

$$\mathbf{F} = (f_x - m\ddot{u}_g)\mathbf{E}_1 + (f_y - mg)\mathbf{E}_2 \quad (6.6)$$

where f_x and f_y are, respectively, the horizontal and vertical components of the reaction force at the pivot point. The moment about the center of mass of the block is

$$\bar{\mathbf{M}} = -\frac{1}{2}[-\text{sgn}(\theta)W\mathbf{e}_1 + H\mathbf{e}_2] \times (f_x\mathbf{E}_1 + f_y\mathbf{E}_2) \quad (6.7)$$

Based on the geometric viewpoint of Lagrangian dynamics, every motion of a rigid body in two dimensions not subjected to any holonomic constraints can be represented by a particle moving on a three-dimensional *configuration manifold*. If the rigid body is subject to holonomic con-

straints, then each holonomic constraint defines a hypersurface of dimension two in the three-dimensional manifold. If the system is subject to $k < 3$ holonomic constraints, then the intersection of the k hypersurfaces is a manifold of dimension $n = 3 - k$. This is the configuration manifold of the body whose motion is constrained (Casey 1995; O'Reilly 2003). For the problem at hand, since the pivoting corner of the block stays on the ground (i.e., $\mathbf{r}_p \cdot \mathbf{E}_2$ is constant), and the block does not slip (i.e., $\mathbf{r}_p \cdot \mathbf{E}_1$ is constant), the configuration manifold is of dimension $n = 3 - 2 = 1$. Therefore the coordinate θ fully describes the position of the body. Lagrange's equation can be expressed as

$$\frac{d}{dt} \left(\frac{\partial T}{\partial \dot{\theta}} \right) - \frac{\partial T}{\partial \theta} = Q_\theta \quad (6.8)$$

where Q_θ is the generalized force along coordinate θ given by

$$\begin{aligned} Q_\theta &= \mathbf{F} \cdot \frac{\partial \bar{\mathbf{r}}}{\partial \theta} + \bar{\mathbf{M}} \cdot \frac{\partial \omega}{\partial \dot{\theta}} \\ &= [(f_x - m\ddot{u}_g)\mathbf{E}_1 + (f_y - mg)\mathbf{E}_2] \cdot \frac{1}{2} [H\mathbf{e}_1 + \text{sgn}(\theta)W\mathbf{e}_2] \\ &\quad + \left\{ -\frac{1}{2} [-\text{sgn}(\theta)W\mathbf{e}_1 + H\mathbf{e}_2] \times (f_x\mathbf{E}_1 + f_y\mathbf{E}_2) \right\} \cdot (-\mathbf{e}_3) \\ &= -m\ddot{u}_g R \cos(\alpha - |\theta|) - \text{sgn}(\theta) mg R \sin(\alpha - |\theta|) \end{aligned} \quad (6.9)$$

where $\alpha = \tan^{-1}(W/H)$. Note that although the force due to gravity is a conservative force and could therefore be expressed as a potential energy in Lagrange's equation, we chose to subsume it in \mathbf{F} along with the remaining non-conservative forces. Furthermore, note that the horizontal, f_x , and vertical, f_y , components of the reaction force at the stationary pivot point do not do any work and therefore should not appear in the equation of motion. Substitution of Equations (6.5) and (6.9) into (6.8) gives the equation of motion

$$\ddot{\theta} = -p^2 \left[\text{sgn}(\theta) \sin(\alpha - |\theta|) + \frac{\ddot{u}_g}{g} \cos(\alpha - |\theta|) \right] \quad (6.10)$$

where $p = \sqrt{3g/4R}$ is the *frequency parameter* of the block. The larger the block (larger R), the smaller p . In his seminal work, Housner (1963) showed that the vibration frequency of a rigid block under free vibration is *not* constant, since it depends on the vibration amplitude. Nevertheless, when two geometrically similar blocks (same α) of different size (different p) experience free vibrations with the same initial conditions, $\theta(0) = \theta_0$ and $\dot{\theta}(0) = 0$, each response-cycle of

the larger block (smaller p) is longer than the corresponding response-cycle of the smaller block (larger p). Accordingly, the quantity p is a measure of the dynamic characteristics of the block. It depends on the size of the block, R , and the intensity of the gravitational field, g . Equation (6.10) is well known in the literature (Yim et al. 1980; Hogan 1989; Shenton 1996; Makris and Roussos 2000; among others) and is valid for arbitrary values of the stockiness angle α . The solution of Equation (6.10) is obtained numerically via a state-space formulation where the state vector \mathbf{x} of the system is

$$\mathbf{x} = \begin{Bmatrix} \theta \\ \dot{\theta} \end{Bmatrix} \quad (6.11)$$

and the time-derivative vector $\mathbf{f}(\mathbf{x}, t)$ is

$$\dot{\mathbf{x}} = \mathbf{f}(\mathbf{x}, t) = \begin{Bmatrix} \dot{\theta} \\ -p^2 \left[\text{sgn}[\theta] \sin(\alpha - |\theta|) + \frac{\ddot{u}_g(t)}{g} \cos(\alpha - |\theta|) \right] \end{Bmatrix} \quad (6.12)$$

Energy Lost during Impact

The numerical integration of (6.12) is performed with standard ODE solvers available in *MATLAB* (2002). The solution of (6.10) is constructed by accounting for the energy lost at every impact. Using the classical idea of a coefficient of restitution, e , the ratio of the angular speed of the block immediately after impact to the angular speed immediately before impact is

$$e = \frac{\dot{\theta}_+}{\dot{\theta}_-} \quad (6.13)$$

where the + and - subscripts respectively denote “after impact” and “before impact.” Note that the ratio of the kinetic energies immediately before and after impact is $\dot{\theta}_+^2 / \dot{\theta}_-^2 = e^2$, so that the energy lost during an impact is $2(1 - e^2)mR^2\dot{\theta}_-^2 / 3$.

Now as an impact occurs, if the impact is such that there is no bouncing, the block *smoothly* switches pivot points (say from O to O'), and angular momentum is conserved. Figure 6.2 shows a schematic of the uniform-density, ρ , rigid block that pivots about point O and is about to impact (i.e., switch pivots) at point O' . We first consider the angular momentum of the block about point O' *before* impact. An infinitesimal mass element dm located at a distance r from point O has

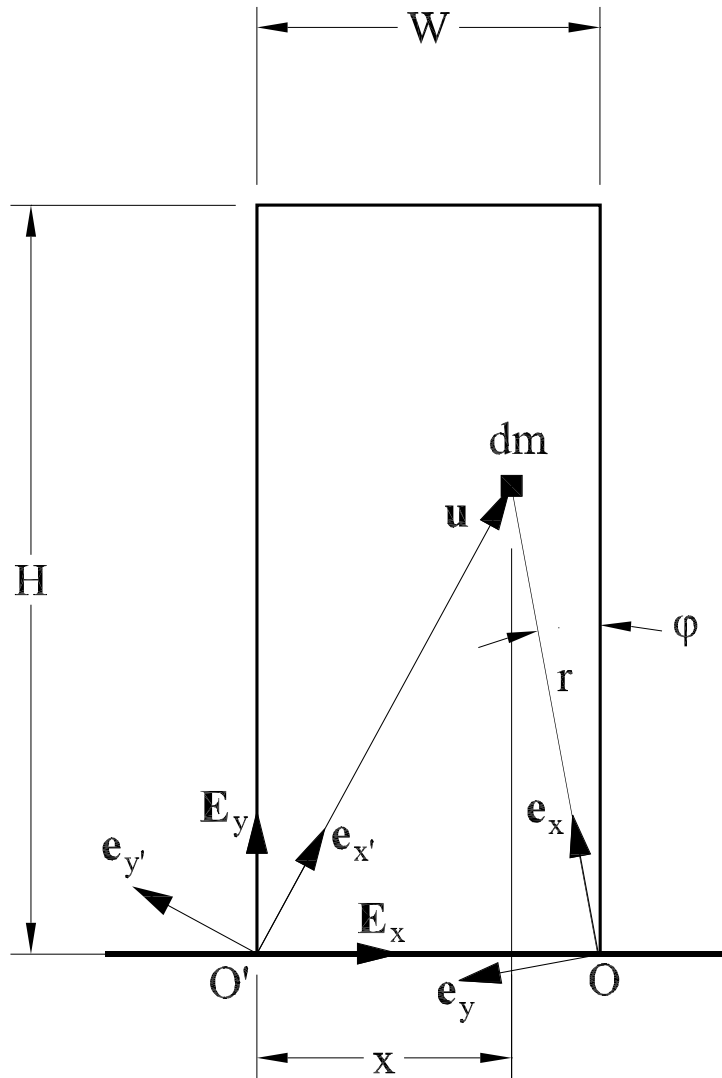


Figure 6.2 Schematic diagram of a rocking block just before it impacts point O' .

velocity $\mathbf{v}_- = r\dot{\theta}_-\mathbf{e}_y$. The position of the mass element is $\mathbf{u} = W\mathbf{E}_x + r\mathbf{e}_x$, and therefore the angular momentum of the block \mathbf{B} about O' before the impact is

$$\begin{aligned}
\mathbf{H}_-^{O'} &= \int_{\mathbf{B}} \mathbf{u} \times \mathbf{v}_- dm \\
&= \left(\int_{\mathbf{B}} (r^2 - Wr \sin \varphi) dm \right) \dot{\theta}_- \mathbf{e}_z \\
&= \left(\rho \int_0^H \int_0^W [r^2 - W(W-x)] dx dy \right) \dot{\theta}_- \mathbf{e}_z \\
&= \left(\frac{4}{3}mR^2 - 2mR^2 \sin^2 \alpha \right) \dot{\theta}_- \mathbf{e}_z
\end{aligned} \tag{6.14}$$

The position of the infinitesimal mass element dm immediately *after* impact is $\mathbf{u} = r\mathbf{e}_x$ and the velocity is $\mathbf{v}_+ = r\dot{\theta}_+\mathbf{e}_y$. Therefore, the angular momentum of the block \mathbf{B} about O' after the impact is

$$\begin{aligned}
\mathbf{H}_+^{O'} &= \int_{\mathbf{B}} \mathbf{u} \times \mathbf{v}_+ dm \\
&= \left(\int_{\mathbf{B}} r^2 dm \right) \dot{\theta}_+ \mathbf{e}_z \\
&= \frac{4}{3}mR^2 \dot{\theta}_+ \mathbf{e}_z
\end{aligned} \tag{6.15}$$

By conservation of angular momentum, $\mathbf{H}_-^{O'} = \mathbf{H}_+^{O'}$. Equating expressions (6.14) and (6.15) gives (Housner 1963)

$$\left(\frac{4}{3}mR^2 - 2mR^2 \sin^2 \alpha \right) \dot{\theta}_- = \frac{4}{3}mR^2 \dot{\theta}_+ \tag{6.16}$$

and using (6.13), we obtain

$$e_{max} = 1 - \frac{3}{2} \sin^2 \alpha \tag{6.17}$$

The value of e given by (6.17) depends only on the geometry of the block, and it is the maximum value of the coefficient of restitution for which a block of stockiness α will undergo rocking motion. Since $e_{max} < 1$, we see that the impacts have to be inelastic. In fact, the stockier a block, the more energy has to be lost during impact in order to observe rocking motion. The stockiness of a rocking block is therefore a measure of the minimum damping of the system. If additional

energy is lost because of dissipation mechanisms, the value of the true coefficient of restitution will be less than the value computed by (6.17) (Zhang and Makris 2001). An impact is perfectly plastic when the coefficient of restitution is zero. Equation (6.17) provides the lower bound $W/H = \sqrt{2}$ that corresponds to $e_{max} = 0$; for a stockier block, e_{max} is negative, which would imply that upon impact the block will not uplift and the rocking motion will end (in reality, upon impact the stocky block may slide for a short distance before its motion comes to a stop).

Condition for Sustaining Rocking Motion

Shenton (1996) and subsequently Pompei et al. (1998) demonstrated that the condition for a block to enter rocking motion without slipping depends on the value of the acceleration amplitude \ddot{u}_g at the instant when rocking initiates. The minimum static coefficient of friction, μ_s , of the interface necessary to avoid slipping is

$$\mu_s \geq \left| \frac{\frac{|\ddot{u}_g|}{g} - \frac{3}{4} \cos \alpha \sin \alpha \left(\frac{|\ddot{u}_g|}{g \tan \alpha} - 1 \right)}{1 + \frac{3}{4} \sin^2 \alpha \left(\frac{|\ddot{u}_g|}{g \tan \alpha} - 1 \right)} \right| \quad (6.18)$$

Equation (6.18) is valid for a finite ground acceleration that at the instant of impending uplift may be equal or may exceed the minimum ground acceleration necessary to induce uplift (e.g., a constant acceleration pulse of positive amplitude $\ddot{u}_g = a_p > g \tan \alpha$). Note that in the case of a ground acceleration that builds up gradually, rocking will initiate when $|\ddot{u}_g|$ is exactly $g \tan \alpha$, and Equation (6.18) reduces to the well-known expression derived from statics

$$\mu_s \geq \tan \alpha = \frac{W}{H} \quad (6.19)$$

Equations (6.18) and (6.19) provide conditions for which slipping will not occur at the instant when rocking initiates. Now we present a condition necessary for sliding not to occur during the *entire* rocking motion of the block. This condition was first presented by Zhang and Makris (2001). When a block is rocking, the horizontal, f_x , and vertical, f_y , components of the reaction force at the pivot points O (for when $\theta > 0$) and O' (for when $\theta < 0$) vary with time. Dynamic equilibrium in their respective directions gives expressions for these forces

$$f_x = m(\ddot{x} + \ddot{u}_g) \quad (6.20)$$

$$f_y = m(\ddot{y} + g) \quad (6.21)$$

where \ddot{x} and \ddot{y} are the horizontal and vertical components of the acceleration of the center of mass of the block. Expressions for these can be obtained by twice-differentiating the components of the displacement of the center of mass, $\bar{x} = \text{sgn}(\theta)[W/2 - R\sin(\alpha - |\theta|)]$ and $\bar{y} = R\cos(\alpha - |\theta|)$, to obtain

$$\ddot{x} = R\ddot{\theta}\cos(\alpha - |\theta|) + \text{sgn}(\theta)R\dot{\theta}^2\sin(\alpha - |\theta|) \quad (6.22)$$

$$\ddot{y} = \text{sgn}(\theta)R\ddot{\theta}\sin(\alpha - |\theta|) - R\dot{\theta}^2\cos(\alpha - |\theta|) \quad (6.23)$$

Substituting Equation (6.10) for $\ddot{\theta}$ into (6.22) and (6.23), and those in turn into (6.20) and (6.21), gives expression for the horizontal and vertical components of the reaction force at the pivot. Sliding is prevented during the entire rocking motion if $|f_x/f_y| < \mu_s$ for all time. Substituting the expressions derived for f_x and f_y into this inequality gives the minimum coefficient of friction required to sustain pure rocking motion (Zhang and Makris 2001)

$$\mu_s \geq \left| \frac{\frac{\ddot{u}_g}{g}[5 - 3\cos 2(\alpha - |\theta|)] - 3\text{sgn}(\theta)\sin 2(\alpha - |\theta|) + \frac{6\dot{\theta}^2}{p^2}\text{sgn}(\theta)\sin(\alpha - |\theta|)}{5 + 3\cos 2(\alpha - |\theta|) - \frac{3\ddot{u}_g}{g}\text{sgn}(\theta)\sin 2(\alpha - |\theta|) - \frac{6\dot{\theta}^2}{p^2}\cos(\alpha - |\theta|)} \right| \quad (6.24)$$

It can be verified that at the instant when rocking initiates due to a positive ground acceleration $\ddot{u}_g > g \tan \alpha$ (which implies $\theta = 0^-$ and $\dot{\theta} = 0$), Equation (6.24) reduces to (6.18). If the ground acceleration is $\ddot{u}_g = g \tan \alpha$, then (6.24) reduces to (6.19).

6.1.2 Pure Sliding Motion of a Rigid Block

We consider a rigid block of mass m resting on a horizontal plane which is subjected to a horizontal base excitation $\ddot{u}_g(t)$ as it shown in Figure 6.1 (bottom). The interface has coefficient of static friction μ_s and kinetic friction μ . Provided that the block does not uplift, the block will start sliding once the force due the ground excitation overcomes the frictional resistance of the interface. This is prescribed by the condition

$$|\ddot{u}_g| > \mu_s g \quad (6.25)$$

While the block slides, the equation of motion is

$$\ddot{u} + \mu g \text{sgn}[\dot{u}] = -\ddot{u}_g \quad (6.26)$$

where u is the displacement of the mass relative to the ground. If \dot{u} becomes zero and the condition prescribed by Equation (6.25) is not satisfied, then the block sticks.

To solve Equation (6.26) numerically, the singularity is smoothed. This is achieved by instead solving

$$\ddot{u} + \mu g z = -\ddot{u}_g \quad (6.27)$$

where $z(t)$ is a hysteretic dimensionless quantity with $|z(t)| \leq 1$ given by

$$u_y \dot{z} + \gamma |\dot{u}| z |z|^{n-1} + \beta \dot{u} |z|^n - \dot{u} = 0 \quad (6.28)$$

The model given by Equations (6.27) and (6.28) is a special case of the Bouc-Wen model (1975; 1976) suitable for elastoplastic behavior. The parameters β and γ are dimensionless quantities that control the shape of the hysteretic loop, while the parameter n controls the smoothness of the transition from the elastic to the plastic region. To model the sharp corner of the rigid-plastic behavior, n must be set to a high value (e.g., $n > 20$). In Equation (6.28), u_y is a yield displacement that for the case of rigid-plastic behavior is set very small (e.g., $u_y = 10^{-5}$ in.). However, the great benefit of the Bouc-Wen formulation for modelling laboratory equipment is in fact that it allows for the elasticity of the equipment leg supports. The value of u_y can be set to the yield values of the equipment supports obtained from the slow-pull friction tests (see Figs. 3.4 to 3.6 and Table 3.2). The disadvantage of the Bouc-Wen formulation is that it does not consider that the initiation of motion actually occurs when the forcing term $\ddot{u}_g(t)$ overcomes the resistance provided by of the *static* coefficient of friction μ_s . In effect, for the Bouc-Wen model, $\mu_s = \mu$.

The problem is cast in state-space with the state vector

$$\mathbf{x} = \begin{Bmatrix} u \\ \dot{u} \\ z \end{Bmatrix} \quad (6.29)$$

and its time-derivative vector $\mathbf{f}(t)$

$$\dot{\mathbf{x}} = \mathbf{f}(\mathbf{x}, t) = \begin{Bmatrix} \dot{u} \\ -\ddot{u}_g - \mu g z \\ \frac{1}{u_y} [-\gamma |\dot{u}| z |z|^{n-1} - \beta \dot{u} |z|^n + \dot{u}] \end{Bmatrix} \quad (6.30)$$

The solution is obtained with standard ODE solvers available in *MATLAB* (2002).

6.1.3 Planar Slide-Rocking Motion of a Rigid Block

We observed from the experimental results presented in Chapter 4 that the rocking and sliding modes are commonly coupled. We now relax the constraint that the rocking block of Figure 6.1 (top) is not allowed to slide. The slide-rocking problem is considerably more complex, and, besides the work of Taniguchi (2002), it has not enjoyed the treatment that researchers have given to the pure rocking problem. In this section we present a Lagrangian approach to formulating the equations of motion.

The position of the center of mass of the block can be written more compactly as

$$\bar{\mathbf{r}} = x\mathbf{E}_1 + \frac{1}{2}[-\text{sgn}(\theta)W\mathbf{e}_1 + H\mathbf{e}_2] \quad (6.31)$$

where x is the position of the pivot point O or O' . In the numerical solution, once impact occurs (and the pivot point switches), x is modified by

$$x_+ = x_- + \text{sgn}[\dot{\theta}(t^*)]W \quad (6.32)$$

where the + and - subscripts respectively indicate “after impact” and “before impact,” and t^* indicates the time when the impact occurs. With $\boldsymbol{\omega} = -\dot{\theta}\mathbf{E}_3 = -\dot{\theta}\mathbf{e}_3$, the velocity of the center of mass of the block is given by

$$\bar{\mathbf{v}} = \dot{x}\mathbf{E}_1 + \boldsymbol{\omega} \times \frac{1}{2}[-\text{sgn}(\theta)W\mathbf{e}_1 + H\mathbf{e}_2] = \dot{x}\mathbf{E}_1 - \frac{\dot{\theta}}{2}[H\mathbf{e}_1 - \text{sgn}(\theta)W\mathbf{e}_2] \quad (6.33)$$

The total kinetic energy $T = \bar{T} + T^\circ = (m\bar{\mathbf{v}} \cdot \bar{\mathbf{v}} + \boldsymbol{\omega} \cdot \mathbf{J}\boldsymbol{\omega}) / 2$, where $\mathbf{J}\boldsymbol{\omega} = -mR^2\dot{\theta}\mathbf{e}_3 / 3$, is given by

$$\begin{aligned} T &= \left\{ \frac{1}{2}m\dot{x}^2 + \frac{1}{2}mR^2\dot{\theta}^2 + \frac{1}{2}m\dot{x}\dot{\theta}[H\cos\theta + \text{sgn}(\theta)W\sin\theta] \right\} + \frac{1}{6}mR^2\dot{\theta}^2 \\ &= \frac{1}{2}m\dot{x}^2 + \frac{2}{3}mR^2\dot{\theta}^2 + m\dot{x}\dot{\theta}R\cos(\alpha - |\theta|) \end{aligned} \quad (6.34)$$

Note that there is one constraint on the system: the pivoting corner of the block stays on the ground (i.e., $\mathbf{r}_p \cdot \mathbf{E}_2$ is constant), and therefore, the configuration manifold is of dimension $n = 3 - 1 = 2$. The generalized coordinates x and θ describe the position of the block. Lagrange's equations are

$$\frac{d}{dt}\left(\frac{\partial T}{\partial \dot{x}}\right) - \frac{\partial T}{\partial x} = Q_x \quad (6.35)$$

and

$$\frac{d}{dt}\left(\frac{\partial T}{\partial \dot{\theta}}\right) - \frac{\partial T}{\partial \theta} = Q_\theta \quad (6.36)$$

The force on the system is $\mathbf{F} = (f_x - m\ddot{u}_g)\mathbf{E}_1 + (f_y - mg)\mathbf{E}_2$, and the moment about the center of mass of the block is $\bar{\mathbf{M}} = -[-\text{sgn}(\theta)W/2\mathbf{e}_1 + H/2\mathbf{e}_2] \times (f_x\mathbf{E}_1 + f_y\mathbf{E}_2)$. Therefore the generalized force along coordinate x is

$$Q_x = \mathbf{F} \cdot \frac{\partial \bar{\mathbf{r}}}{\partial x} + \bar{\mathbf{M}} \cdot \frac{\partial \boldsymbol{\omega}}{\partial \dot{x}} = f_x - m\ddot{u}_g \quad (6.37)$$

Note here that the horizontal component of the reaction force at the pivot, f_x , appears in Equation (6.37), since it does work when the block slides. The generalized force along coordinate θ is the same as for the pure-rocking case

$$Q_\theta = \mathbf{F} \cdot \frac{\partial \bar{\mathbf{r}}}{\partial \theta} + \bar{\mathbf{M}} \cdot \frac{\partial \boldsymbol{\omega}}{\partial \dot{\theta}} = -m\ddot{u}_g R \cos(\alpha - |\theta|) - \text{sgn}(\theta)mgR \sin(\alpha - |\theta|) \quad (6.38)$$

Substitution of Equations (6.34) and (6.37) into Equation (6.35) gives the first equation of motion

$$\ddot{x} + \frac{3g}{4p^2}\ddot{\theta} \cos(\alpha - |\theta|) = -\text{sgn}(\theta)\frac{3g}{4p^2}\dot{\theta}^2 \sin(\alpha - |\theta|) + \frac{f_x}{m} - \ddot{u}_g \quad (6.39)$$

and substitution of Equations (6.34) and (6.38) into Equation (6.36) gives the second equation of motion

$$\frac{p^2}{g}\ddot{x} \cos(\alpha - |\theta|) + \ddot{\theta} = -p^2 \left[\text{sgn}(\theta) \sin(\alpha - |\theta|) + \frac{\ddot{u}_g}{g} \cos(\alpha - |\theta|) \right] \quad (6.40)$$

While no slipping occurs, Equations (6.39) and (6.40) reduce to Equation (6.10) that describes pure rocking. The integration of (6.12) in association with the constraint described by Equation (6.13) provide a solution. The block will start to slide if the condition expressed by (6.24) is violated. While the block is sliding, the friction force that appears in Equation (6.39) is given by

$$f_x = -\text{sgn}(\dot{x})\mu f_y \quad (6.41)$$

where μ is the coefficient of kinetic friction. The normal force, f_y , is expected to be non-negative (Pompei et al. 1998). Substituting Equation (6.23) into (6.21), and that in turn into (6.41) gives

$$f_x = -\text{sgn}(\dot{x})\mu mg \left\{ 1 + \frac{3}{4p^2} [\text{sgn}(\theta)\ddot{\theta} \sin(\alpha - |\theta|) - \dot{\theta}^2 \cos(\alpha - |\theta|)] \right\} \quad (6.42)$$

where we have used $R = 3g / 4p^2$. The solution to the equations of slide-rocking motion expressed by (6.39) and (6.40) is obtained numerically via a state-space formulation where the state vector of the system \mathbf{x} is

$$\mathbf{x} = \begin{Bmatrix} x \\ \dot{x} \\ \theta \\ \dot{\theta} \end{Bmatrix} \quad (6.43)$$

and the ODE system is of the form that involves a “mass matrix” \mathbf{M}

$$\mathbf{M}(\mathbf{x}, t)\dot{\mathbf{x}} = \mathbf{f}(\mathbf{x}, t) \quad (6.44)$$

In detail,

$$\mathbf{M}(\mathbf{x}, t) = \begin{bmatrix} 1 & 0 & 0 & 0 \\ 0 & 1 & 0 & \frac{3g}{4p^2}\cos(\alpha - |\theta|) \\ 0 & 0 & 1 & 0 \\ 0 & \frac{p^2}{g}\cos(\alpha - |\theta|) & 0 & 1 \end{bmatrix} \quad (6.45)$$

and

$$\mathbf{f}(\mathbf{x}, t) = \begin{Bmatrix} \dot{x} \\ -\operatorname{sgn}(\theta)\frac{3g}{4p^2}\dot{\theta}^2\sin(\alpha - |\theta|) + \frac{f_x}{m} - \ddot{u}_g \\ \dot{\theta} \\ -p^2\left[\operatorname{sgn}(\theta)\sin(\alpha - |\theta|) + \frac{\ddot{u}_g(t)}{g}\cos(\alpha - |\theta|)\right] \end{Bmatrix} \quad (6.46)$$

where f_x is given by Equation (6.42). Note that the mass matrix \mathbf{M} is never singular.

Energy Lost during Impact

The numerical integration of (6.46) can be performed with standard ODE solvers available in *MATLAB* (2002). In the construction of the solution, the energy lost during impact has to some-

how be accounted for. When dealing with pure-rocking motion, the friction of the interface is assumed to not have an effect on the impact, since the velocities of the material points on the edge of the block that impacts with the ground are orthogonal to the ground surface. In the case of slide-rocking, however, the mechanics of the impact are considerably more complex. Since the velocities of the material points that come in contact with the ground are not orthogonal to the surface, the impact is not “frictionless.” If we assume that the impact occurs instantaneously and that consequently, there is no energy lost due to the friction, we can employ the previous idea of simply reducing the angular velocity of the block immediately after the impact by using $\dot{\theta}_+ = e\dot{\theta}_-$.

6.2 VALIDATION OF *WORKING MODEL* SOFTWARE

As this study is part of a comprehensive study that employs the PEER Center’s performance-based earthquake engineering practical methodology, it was decided to utilize for the analysis a commercial software; one that the practicing engineer could easily use to predict the response of heavy laboratory equipment and other building contents alike. The shake table experiments presented in Chapter 4 indicated that the primary mode of response is sliding. However, this is not grounds to exclude the possibility of rocking and possible overturning for interfaces with larger coefficients of friction μ and for equipment with more slender configurations (smaller α). The software of choice had to therefore be able to capture both sliding and rocking response. *Working Model 2D* is a software that combines robust numerical techniques with sophisticated editing capabilities. Its main attraction is its capability to compute the motion of mechanically interacting rigid bodies under a variety of constraints and the action of time-varying forces. Sensitive displacement transducers attached across the faces of the equipment during the shake table experiments recorded extremely small displacements, which justifies the assumption that the equipment can be modeled as rigid in *Working Model*. Figure 6.3 shows the working environment of the software.

One of the most challenging tasks in the dynamic simulation of rigid bodies is the treatment of the contact interfaces. In *Working Model*, the satisfaction of all imposed constraints at the contact interfaces is enforced simultaneously during the numerical integration. In the tangential direction, the contact interface of adjacent bodies is modeled by static and kinetic Coulomb friction (Working Model 2000). Regardless of whether there is sliding or not, the rigid body that models

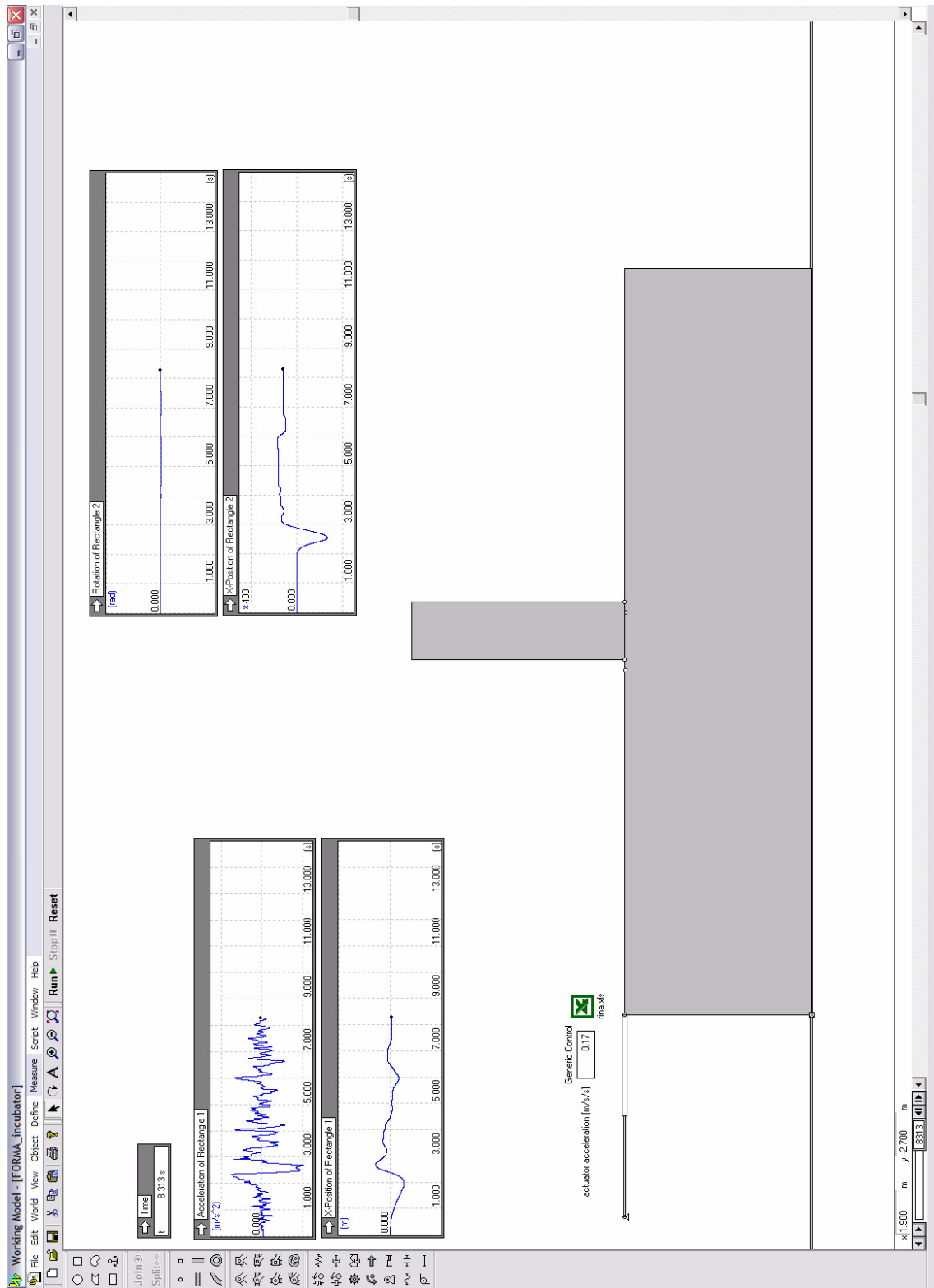


Figure 6.3 The Working Model 2D software environment.

the equipment while engaging in rocking motion can impact the rigid body that models the ground. During an integration step, two colliding bodies may overlap by a small amount. In *Working Model*, collisions are detected by finding intersections between the geometries of bodies. Since the bodies are assumed rigid, for any two points of body \mathbf{B} , $\|\mathbf{x}_1 - \mathbf{x}_2\| = \|\mathbf{X}_1 - \mathbf{X}_2\|$, for all time, where \mathbf{x} is the one-to-one mapping $\mathbf{x} = \chi(\mathbf{X}, t)$, and \mathbf{X} is the position in some reference configuration. This implies that the position and orientation of the edges of a rigid body are known for any time by tracking a *master* node. When intersection between edges is detected, *Working Model* computes forces sufficient to “repel” the bodies. *Working Model* employs an impulse-based collision model in which the coefficient of restitution is used (Working Model 2000).

The numerical integration of the equations of motion in conjunction with the satisfaction of the constraint conditions (friction and restitution), is done using a robust Kutta-Merson method (5th order Runge-Kutta). Integration error as well as model assembly and collision overlap tolerances can be set to achieve the desired precision. With the available variable timestep Kutta-Merson scheme, near collision, the timestep is reduced appropriately to restrict the overlap between bodies from exceeding the specified overlap tolerance. For all the simulations presented in this report, the overlap error tolerance was set to 10^{-6} in.

6.2.1 Pure-Rocking Response Analysis

In this section, we present a comparison of results obtained with *Working Model* to results obtained by numerically solving the pure-rocking equation of motion (6.10). The integration of (6.12) in association with the constraint expressed by (6.13) yields time histories of the rotation and angular velocity of a rocking block. Standard ODE solvers available in *MATLAB* (2002) and a custom routine that detects impacts and imposes the reduction in angular velocity are used. Figure 6.4 plots the rotation and angular velocity histories of a rigid block with frequency parameter $p = 1.25$ rad/sec and stockiness $\alpha = 0.16$ rad when subjected to two strong ground motions. The solid line is the numerical solution of Equation (6.12) using *MATLAB* (pure-rocking). The block survives the Rinaldi 228 motion (left) recorded during the 1994 Northridge, California, earthquake yet topples when subjected to the TCU052NS motion (right) recorded during the 1999 Chi-Chi, Taiwan, earthquake. The dashed line is the prediction of the software *Working Model*

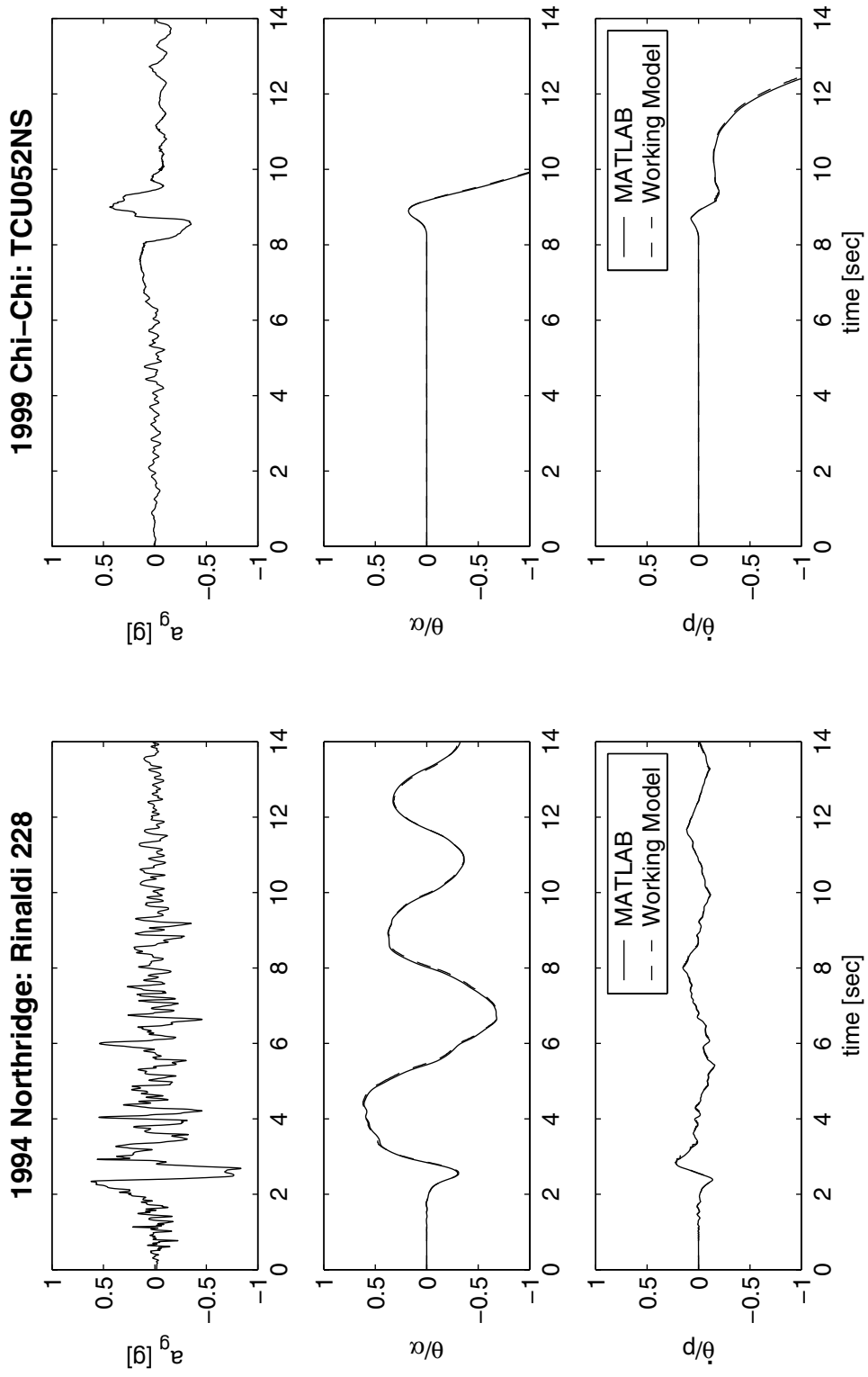


Figure 6.4 Rotation and angular velocity of a rigid block with frequency parameter $p=1.25$ rad/sec and stockiness $\alpha=0.16$ rad subjected to two strong ground motions.

where the coefficient of friction has been set to a high value in order to avoid slipping. The solutions obtained with the two numerical codes are in excellent agreement.

Figure 6.5 plots the minimum overturning acceleration spectrum of the same block when subjected to a one-sine acceleration pulse (Type-A pulse) with acceleration amplitude a_p and duration $T_p = 2\pi / \omega_p$. Notice the multivaluedness of $a_p / \alpha g$ that implies that a block can survive a pulse with acceleration amplitude larger than the minimum acceleration pulse necessary to overturn it. This interesting fact was first exposed by Zhang and Makris (2001). The shaded area in Figure 6.5 is the unsafe region (i.e., where overturning occurs), while the blank area is the safe region (i.e., where overturning does not occur). Note that the software *Working Model* successfully predicts this multivaluedness of the response where a safe cape appears above the minimum overturning acceleration line. The overall performance of *Working Model* is very good, with only minor degradation for shorter-period pulses ($\omega_p / p > 10$, or $T_p < 0.5$ sec) with large acceleration amplitudes ($a_p / \alpha g > 15$, or $a_p > 2.4g$).

6.2.2 Pure-Sliding Response Analysis

We consider again the sliding block of Figure 6.1 (bottom) subjected to a base excitation \ddot{u}_g . The interface coefficient of friction is μ . An in-depth study of the response of a sliding mass on a moving base has been presented by Younis and Tadjbakhsh (1884). As discussed in Chapter 5, the solution to a constant acceleration pulse with amplitude a_p and duration $T_p = 2\pi / \omega_p$ presented by Newmark (1965) is

$$\frac{U_{max}\omega_p^2}{a_p} = 2\pi^2\left(\frac{a_p}{\mu g} - 1\right) \quad (6.47)$$

Figure 5.1 plots with a solid line this dimensionless maximum relative displacement as a function of the dimensionless strength $\mu g / a_p$. The \circ and \times points shown in Figure 5.1 plot the results obtained with the software *Working Model* where various combinations of the values of a_p , T_p , and μ have been used. It is shown that *Working Model* captures with high fidelity the closed-form solution given by Equation (6.47), which is plotted with a solid line.

Figure 5.1 also plots with a solid line the solution $U_{max}\omega_p^2 / a_p$ due to a Type-A (forward-displacement) pulse with acceleration amplitude a_p and duration $T_p = 2\pi / \omega_p$ as a function of $\mu g / a_p$. The solution is obtained by integrating numerically (in *MATLAB*) the system of first-

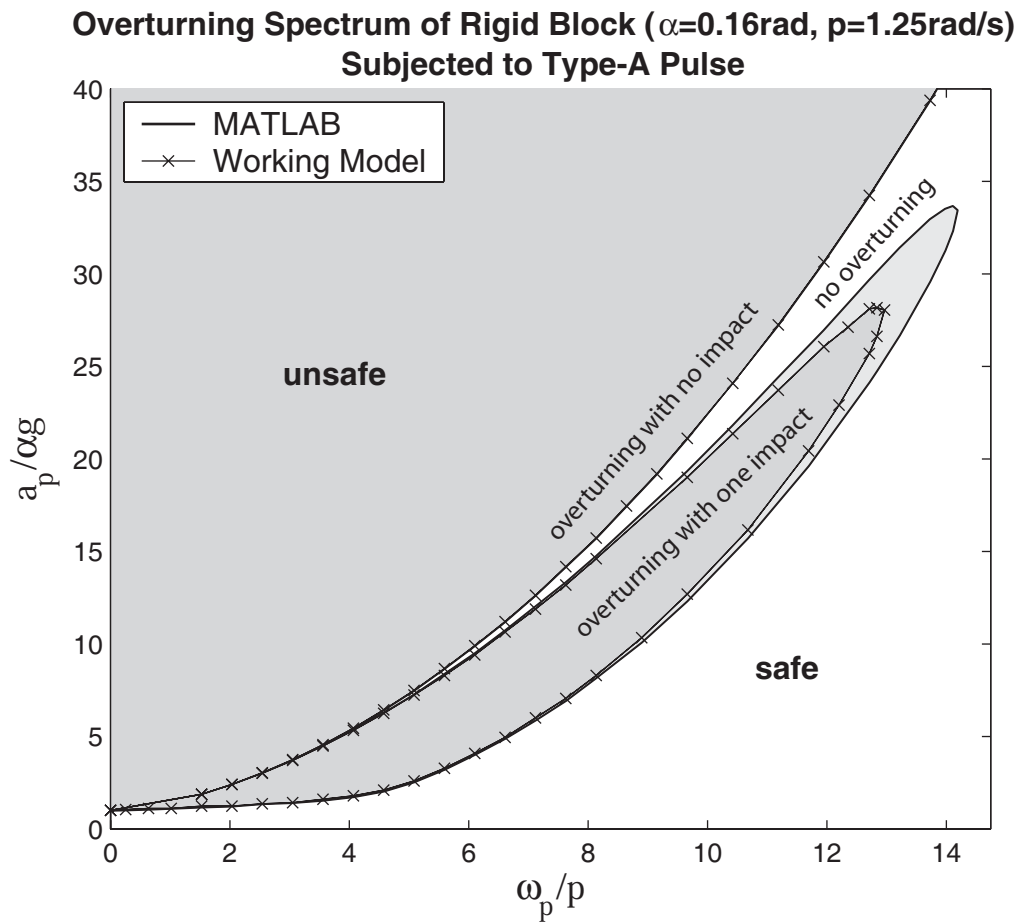


Figure 6.5 Overturning acceleration spectrum of a rigid block with frequency parameter $p=1.25$ rad/sec and stockiness $\alpha=0.16$ rad subjected to a one-sine (Type-A) pulse.

order nonlinear ODE's given by Equation (6.30) derived for the Bouc-Wen model. The values of $\beta = \gamma = 0.5$, $n = 20$, and $u_y = 10^{-5}$ in. were used to model the rigid-plastic behavior. The \circ and \times points are the solutions obtained using *Working Model* for different combinations of a_p , T_p , and μ . It is shown that the *Working Model* solution is in excellent agreement with the solution obtained by numerical integration of (6.30) in *MATLAB*.

More evidence of the accuracy of the solutions obtained with *Working Model* is offered in Figure 6.6 which plots the sliding response of a rigid mass subjected to three strong earthquakes. Note that despite the large variability in the peak values of the sliding displacements, the solutions obtained with *Working Model* are in excellent agreement with the *MATLAB* numerical solution.

6.2.3 Slide-Rocking Response Analysis

Testing the ability of *Working Model* to capture with accuracy the slide-rocking response of a freestanding block requires the development of a numerical code that solves Equations (6.44)-(6.46) in association with a constraint that imposes the energy lost during impact. The development of such a code, and particularly the algorithm that tracks the impact, sticking, and slipping of the block, is of considerable effort. It was therefore decided to limit the validation of *Working Model* to pure-rocking and pure-sliding.

The ability of *Working Model* to predict the pure-rocking and pure-sliding response of the mechanical systems shown in Figure 6.1 with high fidelity in association with its ability to provide numerical simulation results that are in fairly good agreement with experimental results obtained from the shake table experiments (presented in Chapter 4; see Figs. 4.2 to 4.29) of this study gives us confidence of its ability to analyze the response of laboratory equipment for motions of various hazard levels.

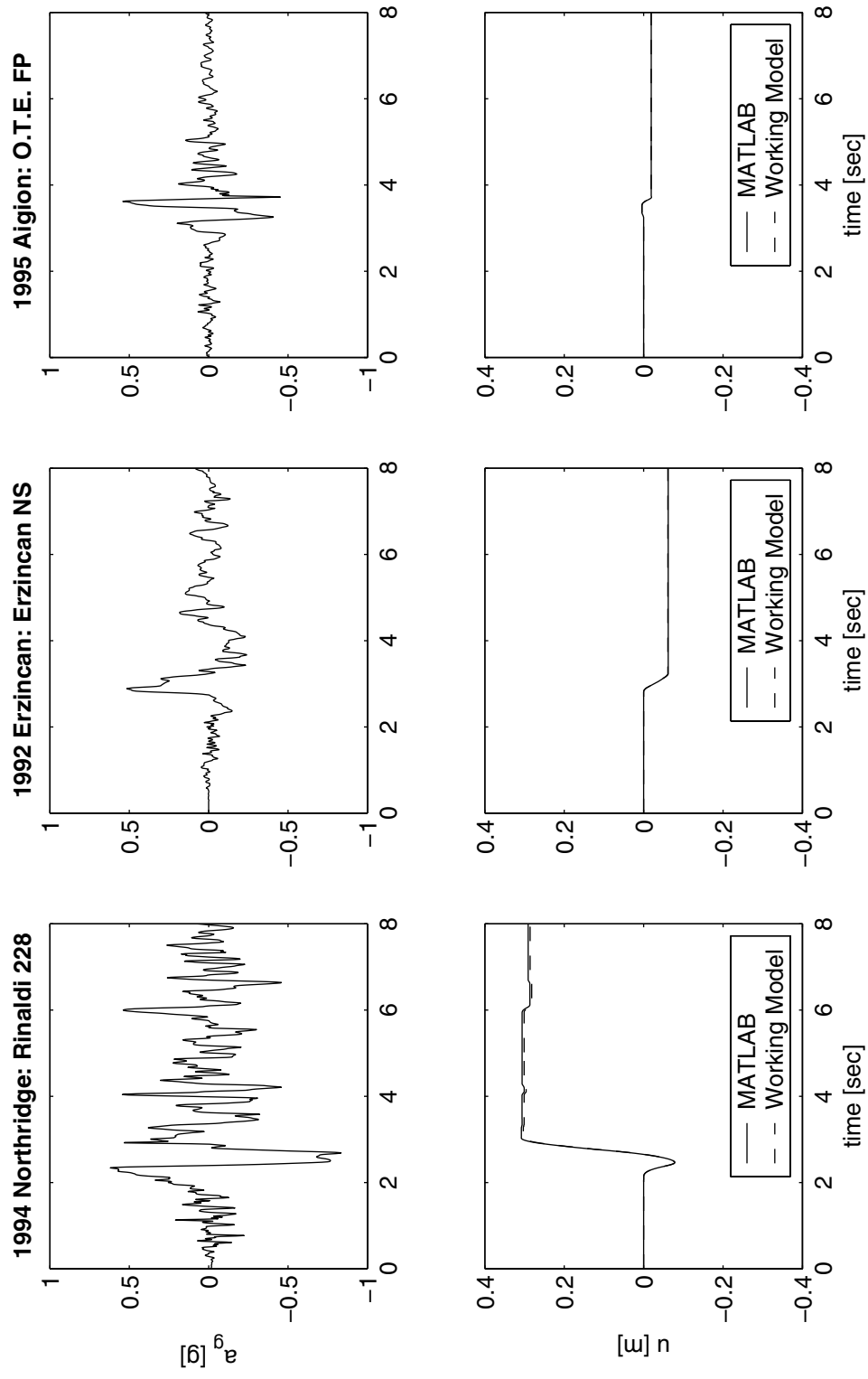


Figure 6.6 Sliding displacement of a freestanding rigid mass ($\mu=0.3$) subjected to three strong earthquakes. The response obtained with the software *Working Model* is in excellent agreement with the numerical solution obtained with *MATLAB*.

7 Shake Table Tests of Wooden Blocks

7.1 WOODEN BLOCK MODELS

Given the ± 6 in limitation in the horizontal displacement of the shaking table, it was not possible to run tests with table displacements equal to the ground and floor displacements of earthquakes that correspond to the 2% in 50 years hazard level. To address this challenge, we conducted shake table tests on quarter-scale wooden block models of the full-scale equipment prototypes. A reduction in length by a factor of 4 corresponds to a reduction in time by a factor of $\sqrt{4} = 2$. This can be shown by dimensional analysis for both sliding (Makris and Black 2003) and rocking motions (Makris and Konstantinidis 2003b). The sizes of the prototype equipment are given in Table 3.1. Figure 7.1 is a photograph of the three wooden block models resting on the shaking table.

7.2 EVALUATION OF THE FRICTION COEFFICIENT OF THE WOODEN BLOCKS

Figure 7.2 shows results obtained from quasi-static pull tests on the wooden blocks which approximate 1/4-scale models of the prototype equipment. The behavior of the contact interface between the wooden blocks and the concrete surface of the shaking table atop which the blocks rested is nearly rigid-plastic without exhibiting any difference between the static and kinetic values of the frictional coefficient. The average value of the coefficient of friction from the quasi-static pull tests on the three wooden blocks is about $\mu_s = \mu_k = 0.68$, and this value is used in the analyses that follow.

7.3 SHAKE TABLE EXPERIMENTS ON WOODEN BLOCK MODELS

The compressed records that were used as input motions for the shake table tests of wooden blocks are listed in Table 7.1. Since in most cases the wooden blocks overturned, it was decided not to instrument the blocks but only to record whether the block survived the motion or over-



Figure 7.1 Quarter-scale wooden block models of the full-scale prototype equipment (pictured in Fig. 3.1) resting on the shaking table at the Richmond Field Station Earthquake Simulation Laboratory, UC Berkeley. The excitation of the table is parallel to the more slender face of the models (labelled “SMALL α ”).

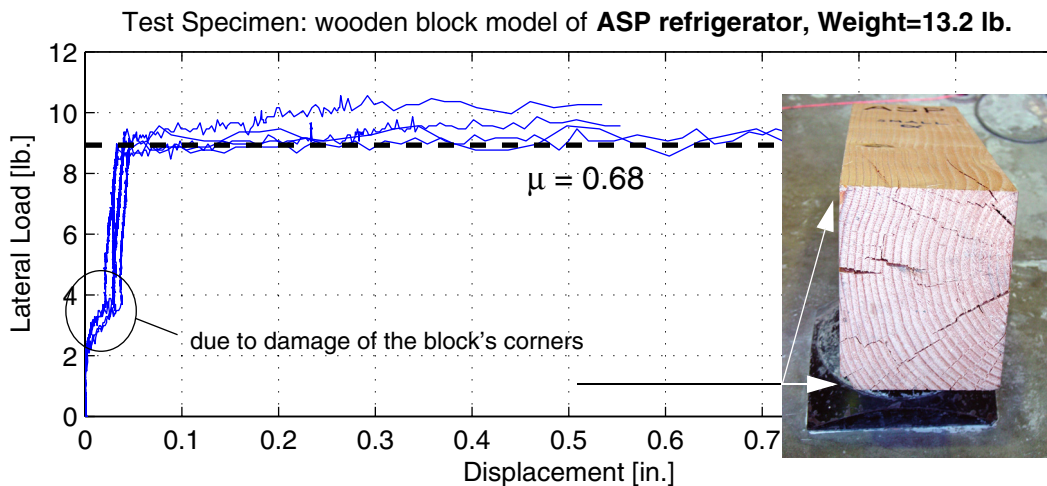
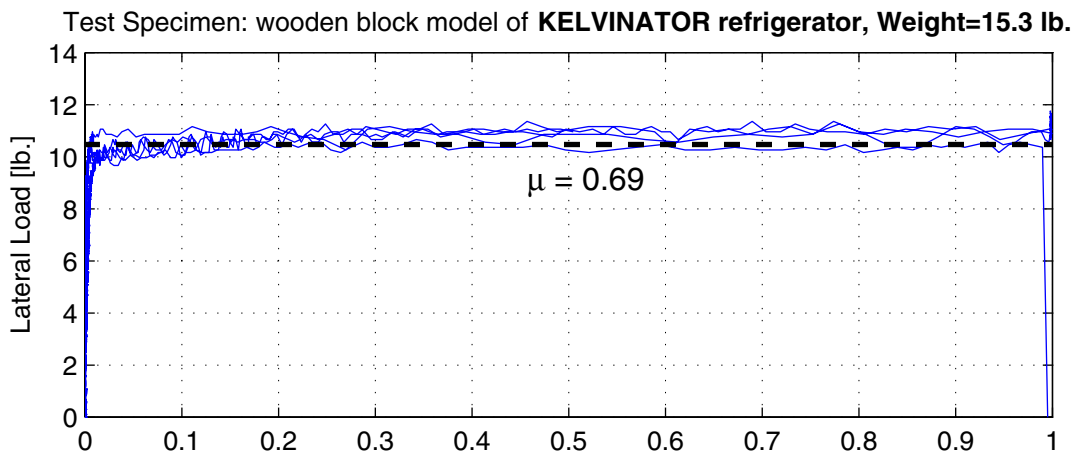
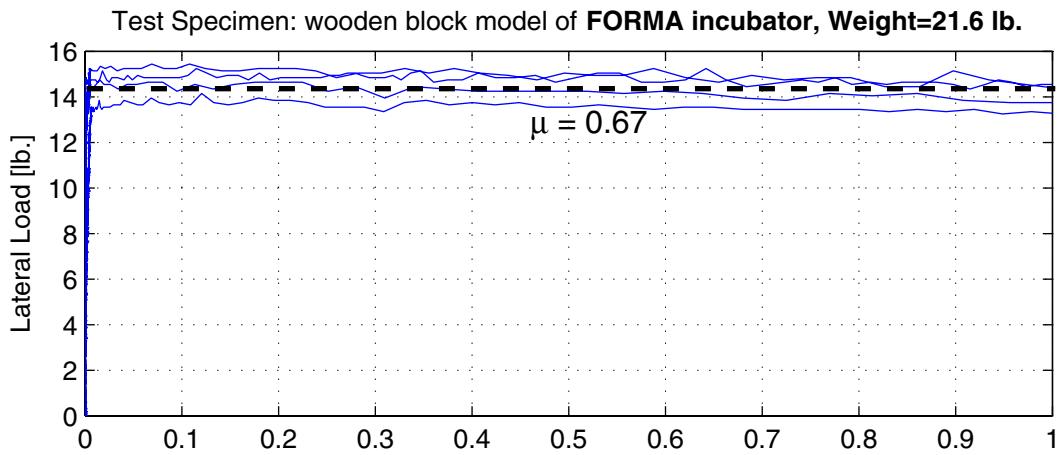


Figure 7.2 Recorded load-displacement plots for the wooden block models obtained from quasi-static pull tests. The wood-concrete interface exhibits a nearly perfect rigid-plastic behavior.

Table 7.1 Results of shake table tests on the wooden block models subjected to compressed 2% in 50 years earthquake motions. Listed are also the outcomes predicted by *Working Model* simulations on full-scale prototypes subjected to the corresponding uncompressed motions.

Equipment Prototype	Compressed Earthquake Motion	<i>PTA</i> [g]	Wooden Block Model μ (slow pull)	Shake Table Experimental Outcome	<i>Working Model</i> Simulation Outcome
FORMA	Loma Prieta, Los Gatos PC, ground	0.54	0.68	overturn	no overturn**
	Loma Prieta, Los Gatos PC, ground	0.60	0.68	overturn	overturn
	Loma Prieta, Los Gatos PC FP, ground	0.57	0.68	overturn	overturn
	Loma Prieta, Corralitos, ground	0.84	0.68	overturn	no overturn**
	Loma Prieta, Corralitos, ground	0.83	0.68	overturn	overturn
	Loma Prieta, Gilroy Hist. Bldg., ground	0.59	0.68	overturn	overturn
	Loma Prieta, Gilroy Hist. Bldg., ground	0.58	0.68	overturn	no overturn*
	Loma Prieta, Gilroy Hist. Bldg., ground	0.59	0.68	overturn	no overturn**
	Loma Prieta, Gilroy Hist. Bldg., 6th floor	0.96	0.68	overturn	overturn
Kelvinator	Loma Prieta, Los Gatos PC, ground	0.54	0.68	overturn	overturn
	Loma Prieta, Los Gatos PC, ground	0.60	0.68	overturn	overturn
	Loma Prieta, Los Gatos PC FP, ground	0.57	0.68	overturn	overturn
	Loma Prieta, Corralitos, ground	0.84	0.68	no overturn	no overturn
	Loma Prieta, Corralitos, ground	0.83	0.68	no overturn	no overturn
	Loma Prieta, Gilroy Hist. Bldg., ground	0.59	0.68	overturn	overturn
	Loma Prieta, Gilroy Hist. Bldg., ground	0.58	0.68	overturn	overturn
	Loma Prieta, Gilroy Hist. Bldg., ground	0.59	0.68	overturn	overturn
	Loma Prieta, Gilroy Hist. Bldg., 6th floor	0.96	0.68	overturn	overturn
ASP	Loma Prieta, Los Gatos PC, ground	0.54	0.68	overturn	no overturn
	Loma Prieta, Los Gatos PC, ground	0.60	0.68	overturn	overturn
	Loma Prieta, Los Gatos PC FP, ground	0.57	0.68	overturn	no overturn
	Loma Prieta, Corralitos, ground	0.84	0.68	overturn	no overturn
	Loma Prieta, Corralitos, ground	0.83	0.68	overturn	no overturn
	Loma Prieta, Gilroy Hist. Bldg., ground	0.59	0.68	overturn	overturn
	Loma Prieta, Gilroy Hist. Bldg., ground	0.58	0.68	overturn	overturn
	Loma Prieta, Gilroy Hist. Bldg., ground	0.59	0.68	overturn	overturn
	Loma Prieta, Gilroy Hist. Bldg., 6th floor	0.96	0.68	overturn	overturn

* although the block does not overturn, θ_{max} nearly reaches α .

** although the block does not overturn, θ_{max} exceeds α .

turned. The outcome of each experiment is also listed in Table 7.1. More than one experiment were conducted for each 2% in 50 years hazard-level motion in an effort to examine the repeatability of the outcome.

7.4 SIMULATION STUDIES ON EQUIPMENT PROTOTYPES

The results of the shake table experiments that were carried on the quarter-scale wooden block models are of great value because they can validate the fidelity of results of numerical simulation studies conducted on the full-scale prototype equipment. Since the friction coefficients of the model-base interfaces were different from the friction coefficients of the prototype-base interfaces, two sets of simulation studies were conducted. First, the responses of the full-scale prototype equipment were computed with *Working Model* by using a coefficient of friction at the sliding interface equal to $\mu_s = \mu_k = 0.68$, the value obtained from the slow pull tests on the wooden blocks. The results of this analysis demonstrated that the simulation program can capture well the experimentally observed behavior. Then, once the fidelity of *Working Model* had been validated, the response of the full-scale prototype equipment was computed with the actual friction coefficients of the sliding interface, as shown in Table 3.2.

The bottom plot on the left column of Figure 7.3 shows the time-compressed (by a factor of 2) acceleration history of the motion recorded at the Los Gatos Presentation Center during the 1989 Loma Prieta, California, earthquake. The plot above the acceleration history plots the resulting displacement history. This time-compressed motion was used as shake table input to test the quarter-scale wooden block model of the FORMA incubator. The final outcome of the experiment was that the wooden model overturned. The right-column plots of Figure 7.3 show the simulated response computed with *Working Model* for the full-scale FORMA incubator prototype subjected to the uncompressed motion. Note that the base displacement history of the uncompressed motion is $2^2 = 4$ times larger in amplitude than the table displacement history of the compressed motion. The heavy solid lines of the top two windows on the right column of Figure 7.3 plot the simulated sliding and uplift responses of the full-scale equipment with a coefficient of friction $\mu = 0.68$, as obtained from the quasi-static pull tests on the wooden blocks. While the simulated response predicts that the incubator does not overturn (as the experiment on the scaled model showed), the negative rotation θ of the equipment is so large that it in fact exceeds the stockiness value α at around $t = 7.5$ sec. Luckily, at the same time, the negative table acceleration which

opposes the overturning of the equipment (see Fig. 6.1 for the definition of positive/negative θ) marginally saves it from catastrophe.

This behavior whereby the equipment prototype marginally survives, while its corresponding wooden model overturns, is observed for a few of the motions. As shown in Table 7.1, when subjected to the Corralitos motion recorded during the 1989 Loma Prieta, California, earthquake, the wooden block overturns. The full-scale FORMA incubator, on the other hand, survives the motion. Figure 7.6 (right) which plots the response computed with *Working Model*, shows that around $t = 5.5$ sec the rotation θ exceeds α , and the equipment hangs on the verge of overturning; yet the restoring base acceleration spares the equipment. When the experiment was repeated on the shake table with the same motion but a slightly different Peak Ground Acceleration ($0.83g$ instead of $0.84g$, due to imprecision of the shake table actuators), the wooden model again overturned. Interestingly, the *Working Model* simulation with this slightly different base motion did result in overturning.

Figures 7.9 and 7.10, which plot the response due to the Gilroy Historic Building motion recorded during and 1989 Loma Prieta, California, earthquake (2 tests), show that the wooden model overturns, while the equipment prototype survives despite the fact that in one case the computed rotation θ nearly reaches α , and in the other it exceeds it. Except for these marginal cases, *Working Model* manages to capture very well the overturning of the wooden models. It also predicts correctly the two cases when the wooden model of the Kelvinator incubator does not overturn (Figs. 7.15 and 7.16) for the Corralitos motion.

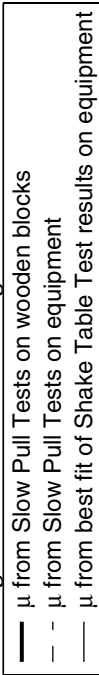
Although they are presented here for completeness, the *Working Model* simulations for the ASP refrigerator (Table 7.1 and Figs. 7.21 to 7.29) cannot be compared to the shake table experimental outcomes of the wooden model because the wooden model of the ASP refrigerator suffered damage that reduced its seismic stability. Figure 7.2 (bottom) shows a photograph of the damage on the corners of the wooden model and how this damage is also evident in the load-displacement curve. The reduced base (and therefore stability) due to the damage of the block's corners explains why, despite the large stockiness of the ASP refrigerator, the wooden model toppled in all cases, while the *Working Model* simulation predicted that the prototype topples in only 5 out of the 9 cases.

The above comparisons between experimental and computed results demonstrate *Working Model's* ability to capture the experimentally observed behavior. This provides us with confidence

that the program can compute the seismic response of laboratory equipment for a wider range of friction coefficients and hazard-level base motions.

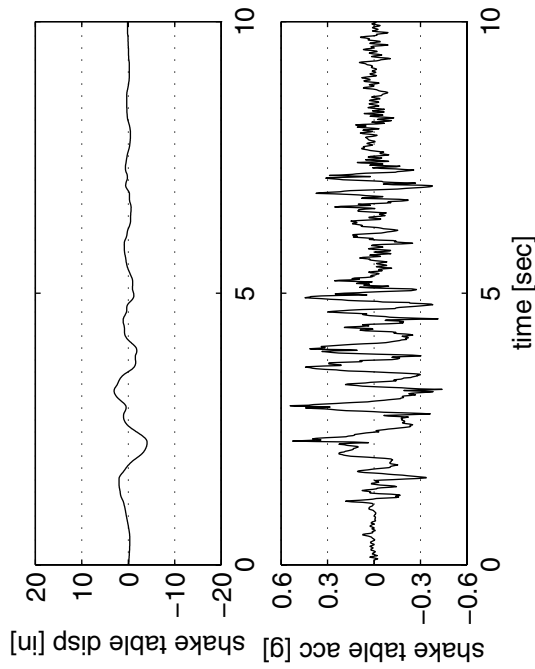
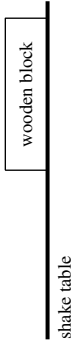
equipment: *FORMA incubator*
 motion: *Loma Prieta, Los Gatos PC, FP GROUND (2% in 50 years)*

Working Model 2D simulation legend:



Quarter-Scale Wooden Block (Model)

overturning



Full-Scale Equipment (Prototype)

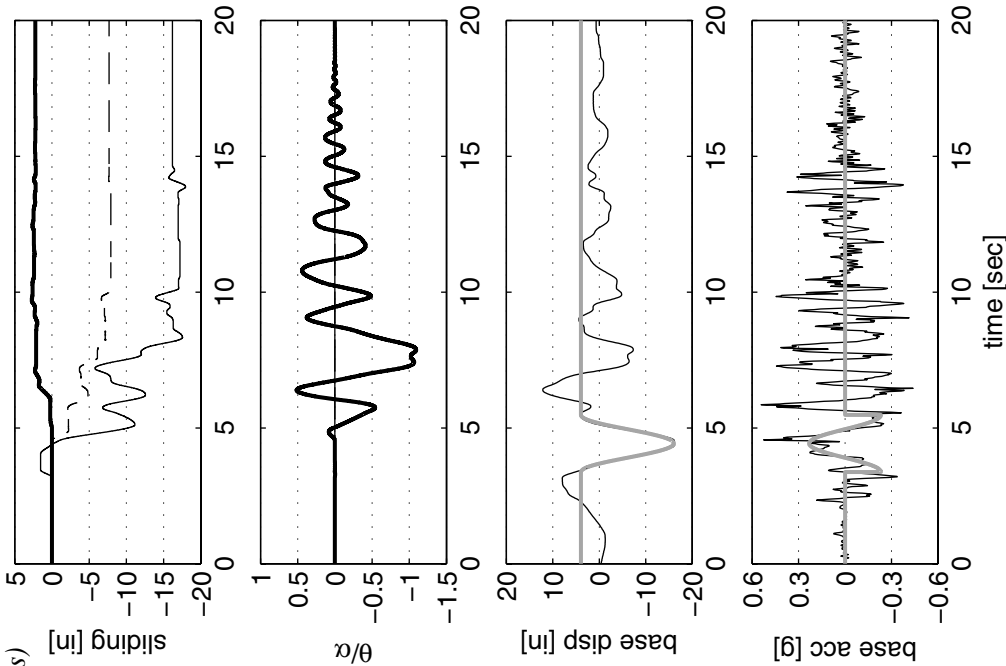
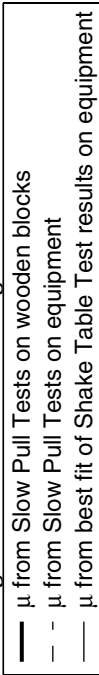


Figure 7.3 *Left:* Outcome of the shake table experiment on the quarter-scale wooden block model together with the table acceleration and displacement of the compressed (by a factor of 2) motion to which the block was subjected. *Right:* Computed response by *Working Model* simulations on the full-scale equipment prototype subjected to the uncompressed motion. The simulations were done for three values of the friction coefficient μ .

equipment: *FORMA incubator*
 motion: *Loma Prieta, Los Gatos PC, FP GROUND (2% in 50 years)*

Working Model 2D simulation legend:



Quarter-Scale Wooden Block (Model)

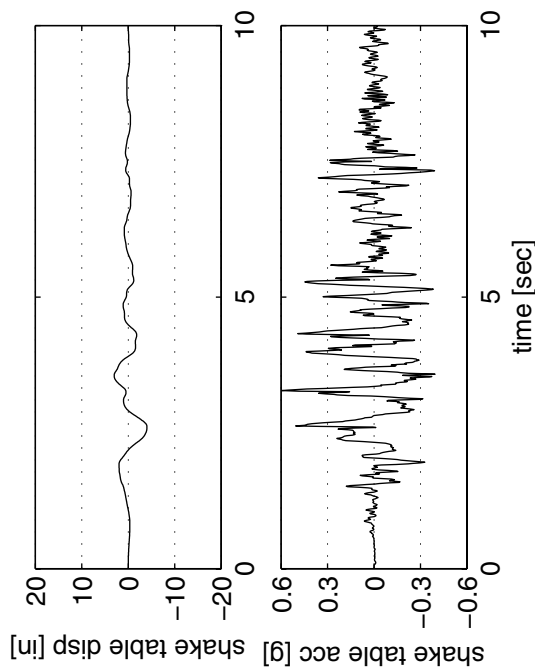
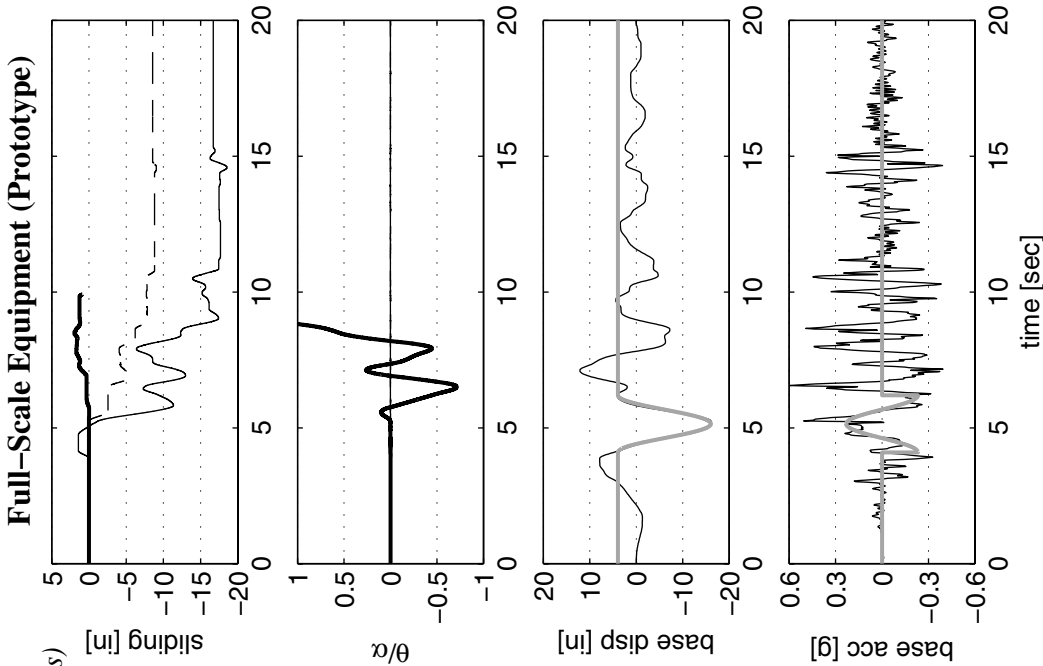
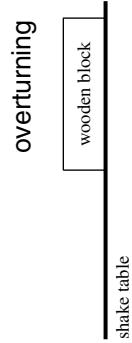
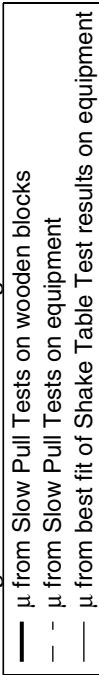


Figure 7.4 *Left: Outcome of the shake table experiment on the quarter-scale wooden block model together with the table acceleration and displacement of the compressed (by a factor of 2) motion to which the block was subjected. Right: Computed response by Working Model simulations on the full-scale equipment prototype subjected to the uncompressed motion. The simulations were done for three values of the friction coefficient μ .*

equipment: *FORMA incubator*
 motion: *Loma Prieta, Los Gatos PC, FP GROUND (2% in 50 years)*

Working Model 2D simulation legend:



Quarter-Scale Wooden Block (Model)

overturning

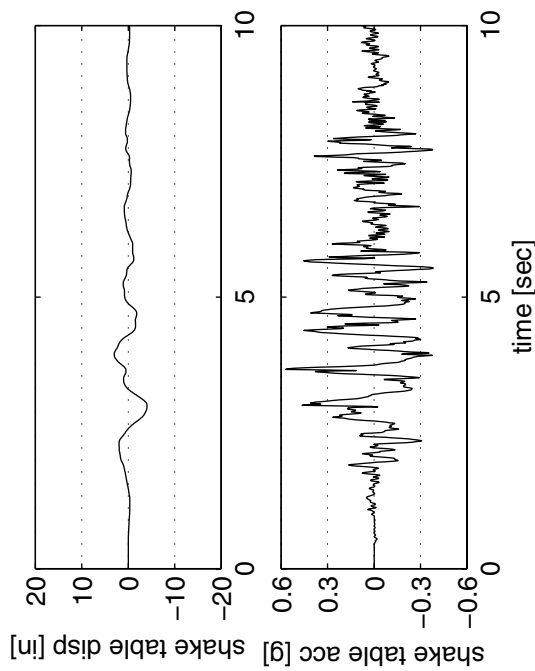
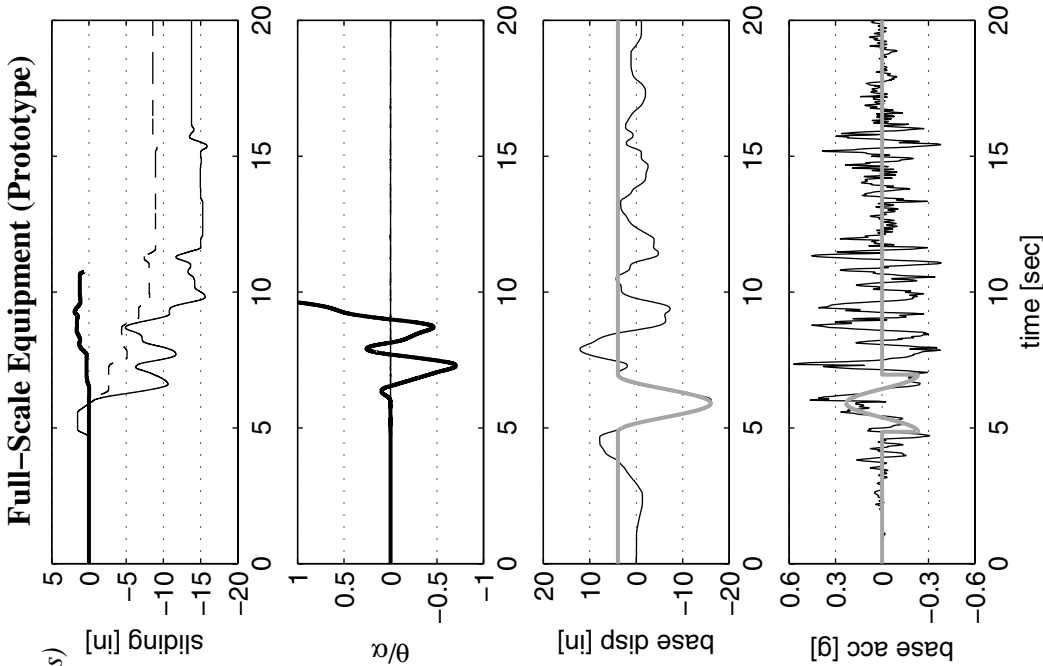
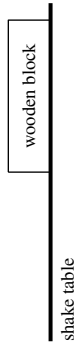
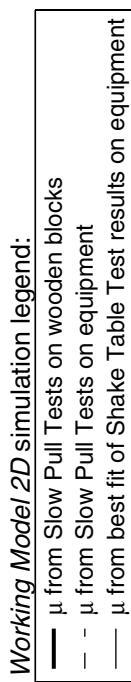


Figure 7.5 *Left: Outcome of the shake table experiment on the quarter-scale wooden block model together with the table acceleration and displacement of the compressed (by a factor of 2) motion to which the block was subjected. Right: Computed response by Working Model simulations on the full-scale equipment prototype subjected to the uncompressed motion. The simulations were done for three values of the friction coefficient μ .*

equipment: *FORMA incubator*
 motion: *Loma Prieta, Corralitos, FP GROUND (2% in 50 years)*



Quarter-Scale Wooden Block (Model)

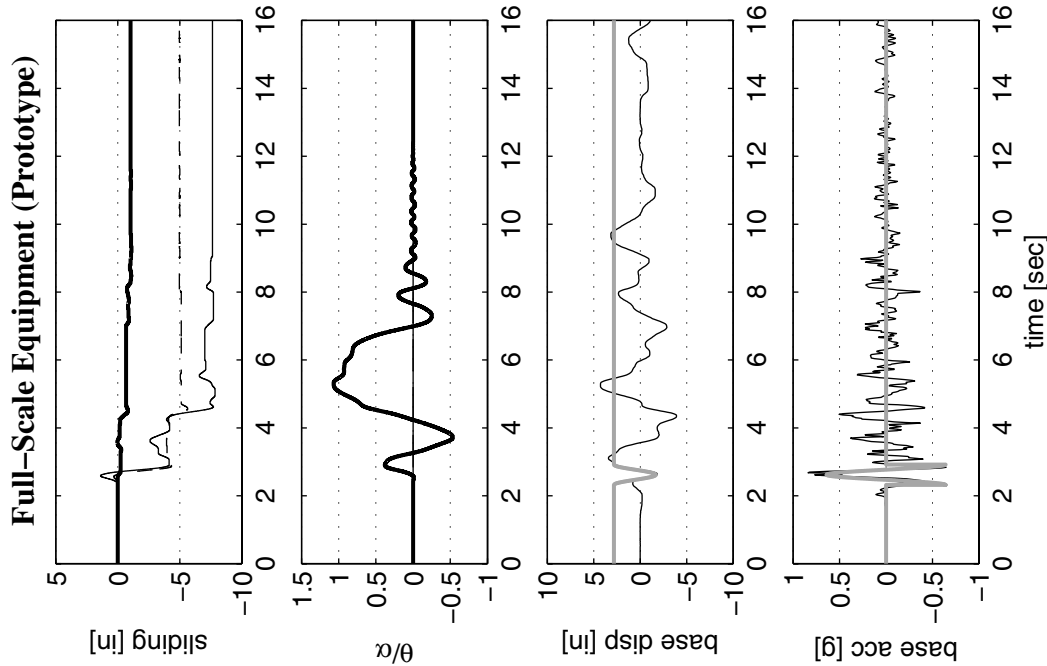
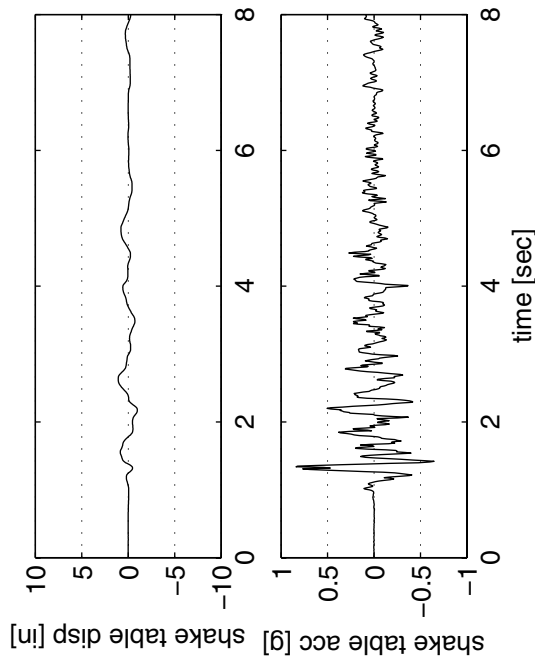
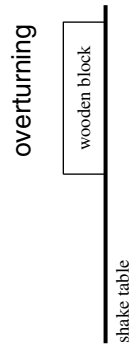
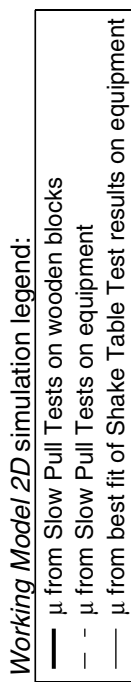


Figure 7.6 **Left:** Outcome of the shake table experiment on the quarter-scale wooden block model together with the table acceleration and displacement of the compressed (by a factor of 2) motion to which the block was subjected. **Right:** Computed response by *Working Model* simulations on the full-scale equipment prototype subjected to the uncompressed motion. The simulations were done for three values of the friction coefficient μ .

equipment: *FORMA incubator*
 motion: *Loma Prieta, Corralitos, FP GROUND (2% in 50 years)*



Quarter-Scale Wooden Block (Model)

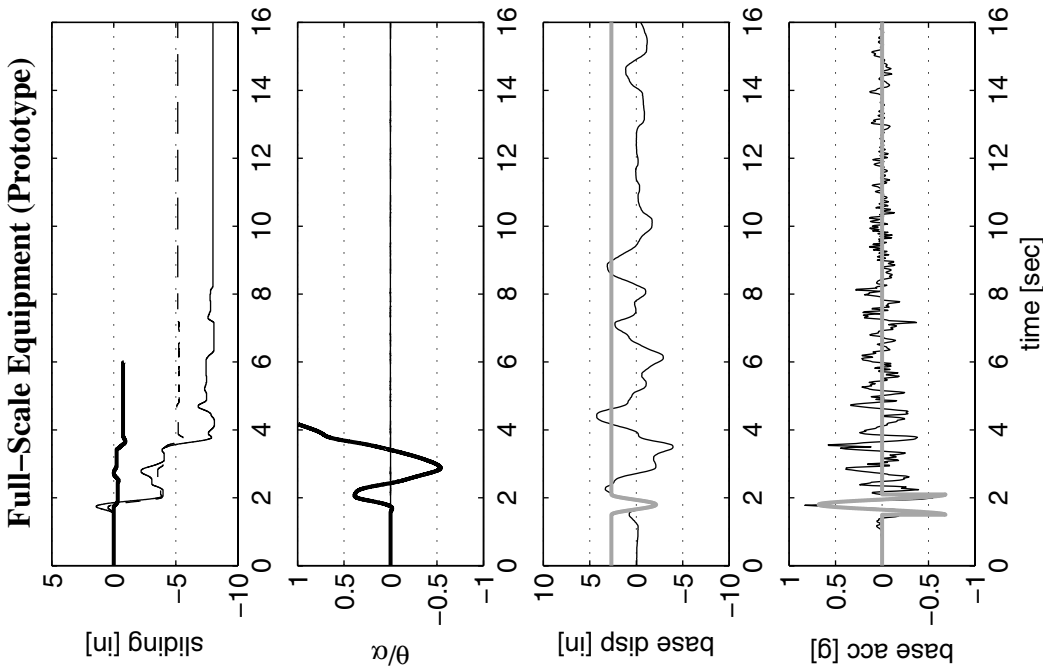
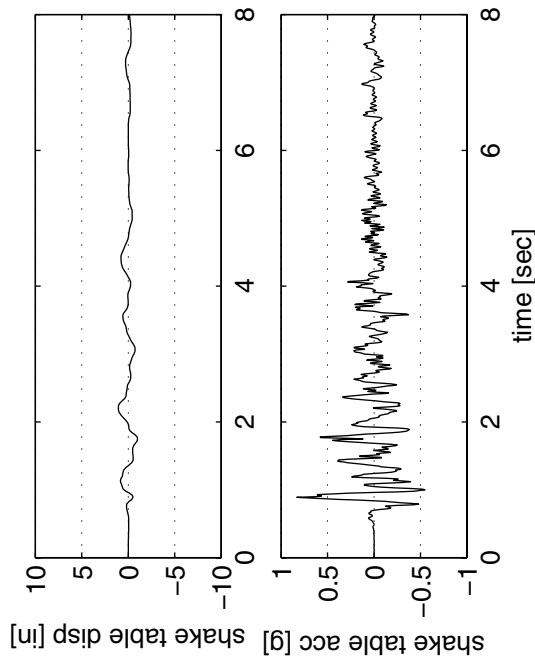
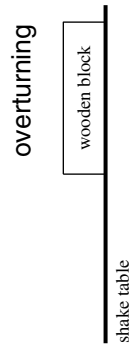
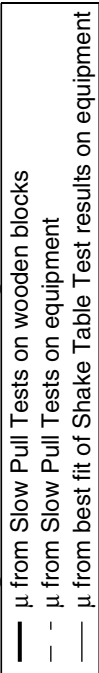


Figure 7.7 *Left: Outcome of the shake table experiment on the quarter-scale wooden block model together with the table acceleration and displacement of the compressed (by a factor of 2) motion to which the block was subjected. Right: Computed response by Working Model simulations on the full-scale equipment prototype subjected to the uncompressed motion. The simulations were done for three values of the friction coefficient μ .*

equipment: *FORMA incubator*
 motion: *Loma Prieta, Gilroy Hist. Bldg FN GROUND (2% in 50 years)*

Working Model 2D simulation legend:



Quarter-Scale Wooden Block (Model)

overturning

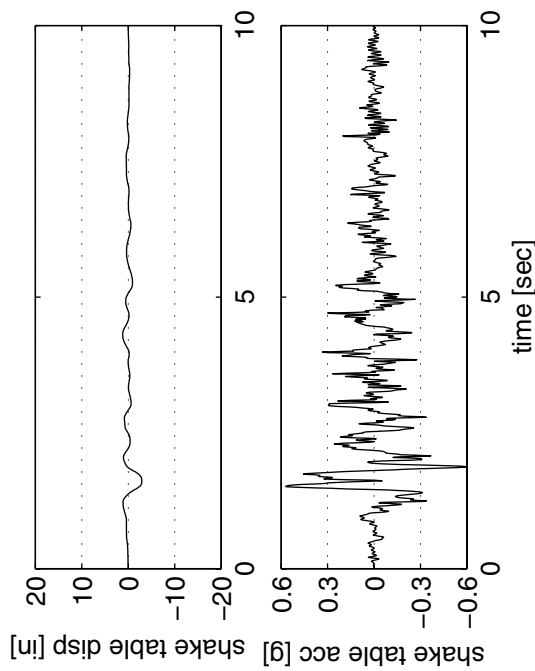
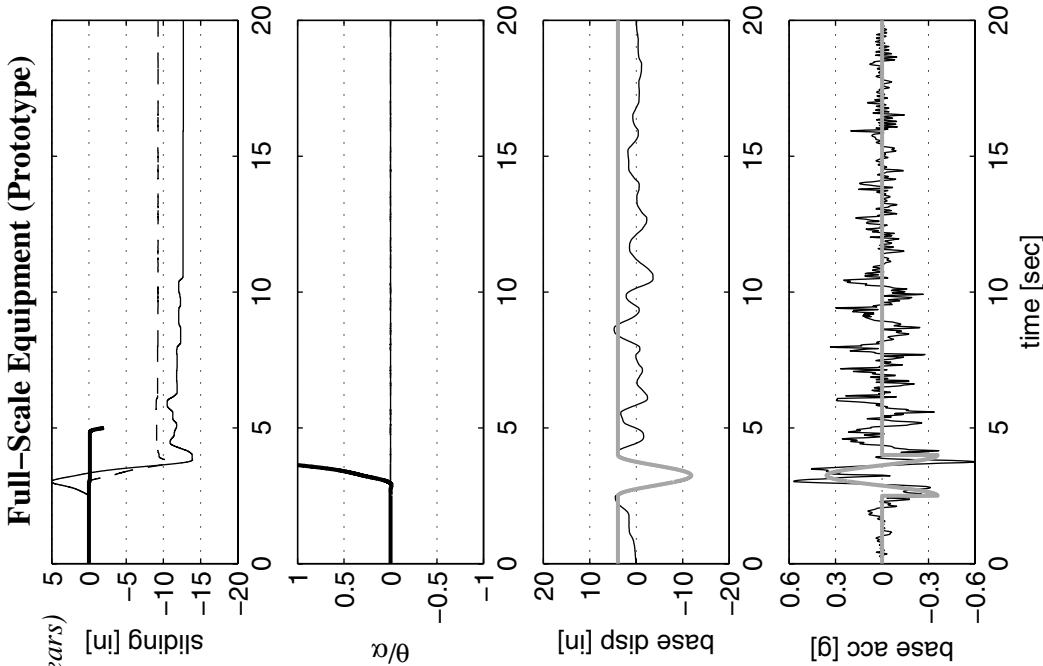
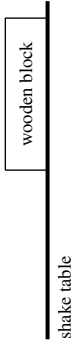
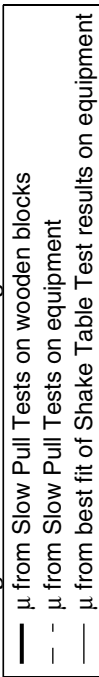


Figure 7.8 *Left:* Outcome of the shake table experiment on the quarter-scale wooden block model together with the table acceleration and displacement of the compressed (by a factor of 2) motion to which the block was subjected. *Right:* Computed response by *Working Model* simulations on the full-scale equipment prototype subjected to the uncompressed motion. The simulations were done for three values of the friction coefficient μ .

equipment: *FORMA incubator*
 motion: *Loma Prieta, Gilroy Hist. Bldg FN GROUND (2% in 50 years)*

Working Model 2D simulation legend:



Quarter-Scale Wooden Block (Model)

overturning

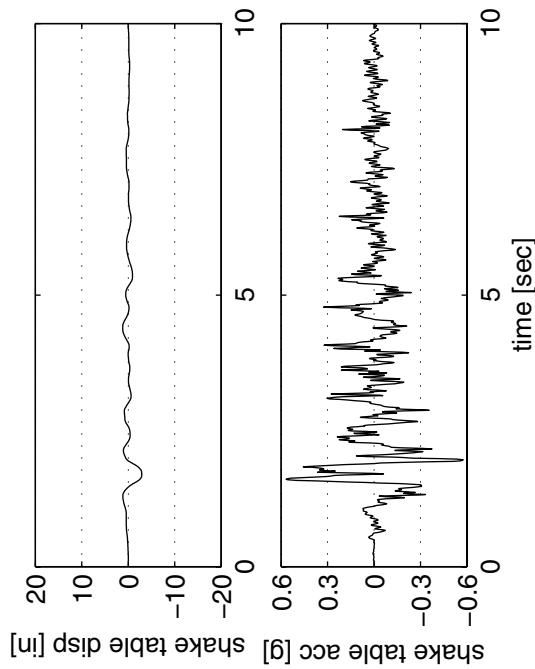
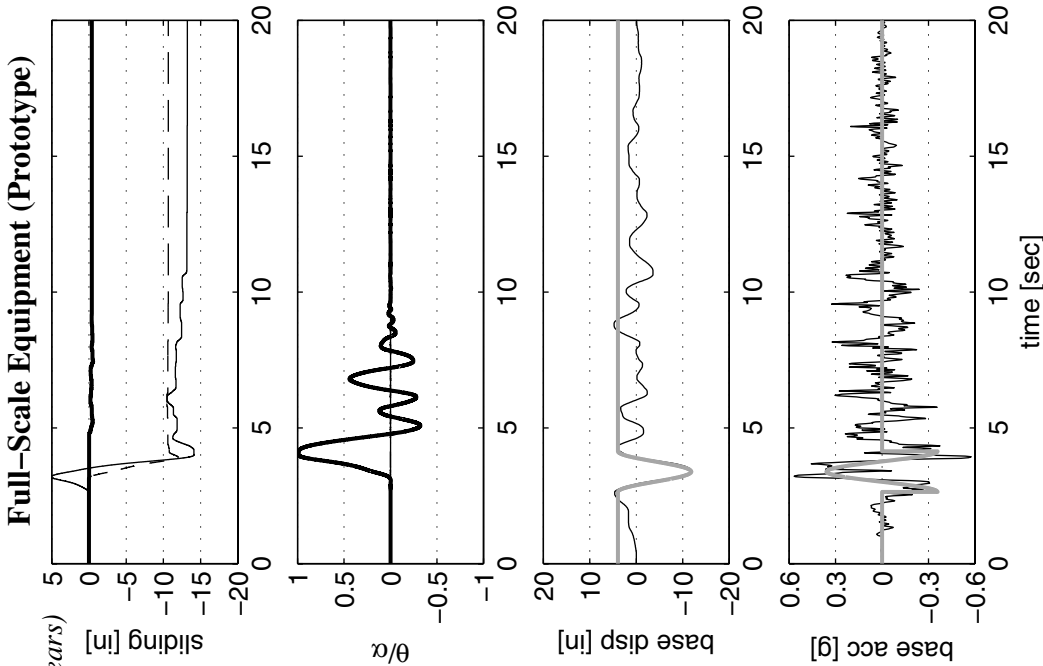
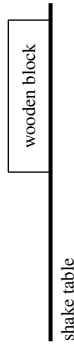
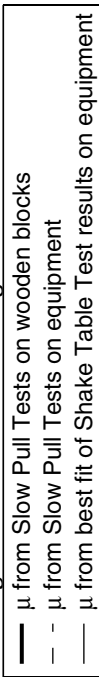


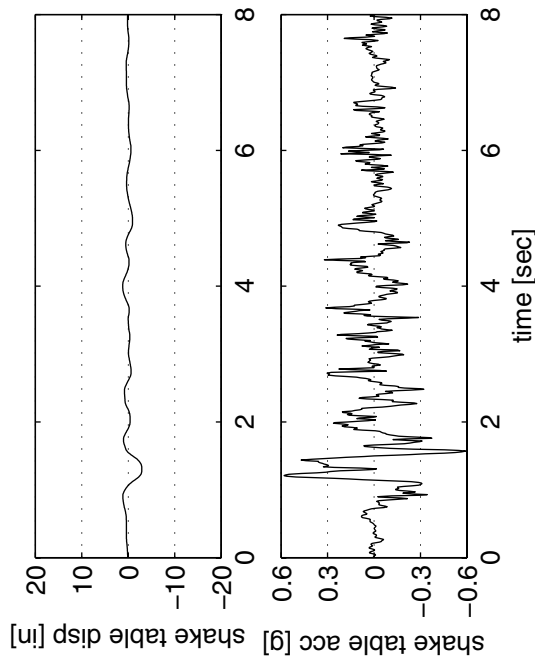
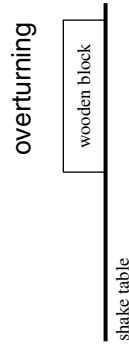
Figure 7.9 *Left:* Outcome of the shake table experiment on the quarter-scale wooden block model together with the table acceleration and displacement of the compressed (by a factor of 2) motion to which the block was subjected. *Right:* Computed response by *Working Model* simulations on the full-scale equipment prototype subjected to the uncompressed motion. The simulations were done for three values of the friction coefficient μ .

equipment: *FORMA incubator*
 motion: *Loma Prieta, Gilroy Hist. Bldg FN GROUND (2% in 50 years)*

Working Model 2D simulation legend:



Quarter-Scale Wooden Block (Model)



Full-Scale Equipment (Prototype)

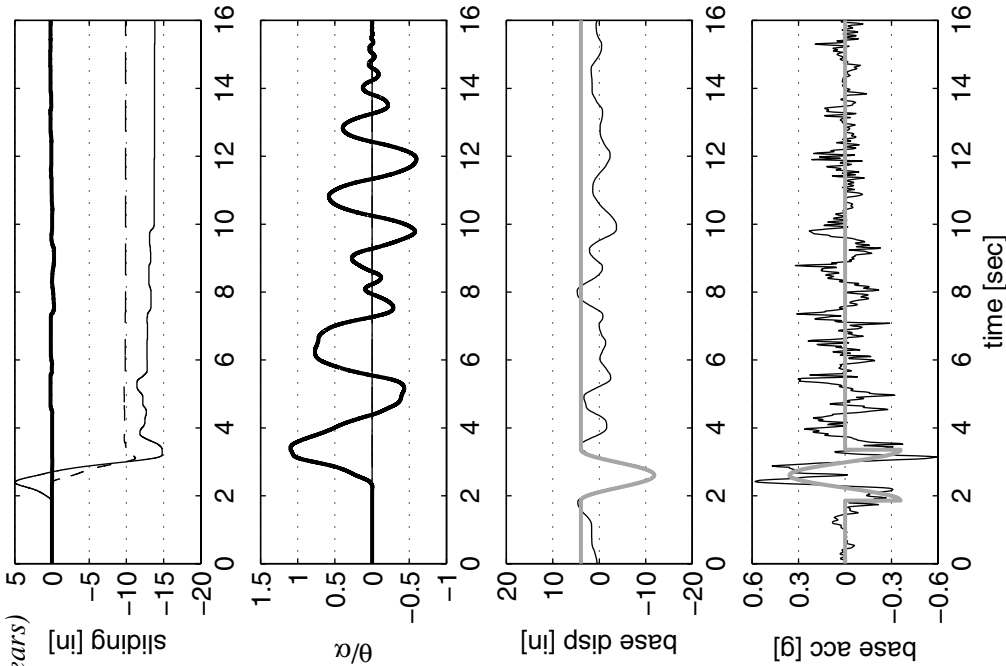
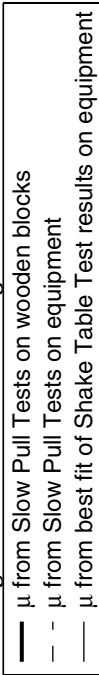


Figure 7.10 *Left:* Outcome of the shake table experiment on the quarter-scale wooden block model together with the table acceleration and displacement of the compressed (by a factor of 2) motion to which the block was subjected. *Right:* Computed response by *Working Model* simulations on the full-scale equipment prototype subjected to the uncompressed motion. The simulations were done for three values of the friction coefficient μ .

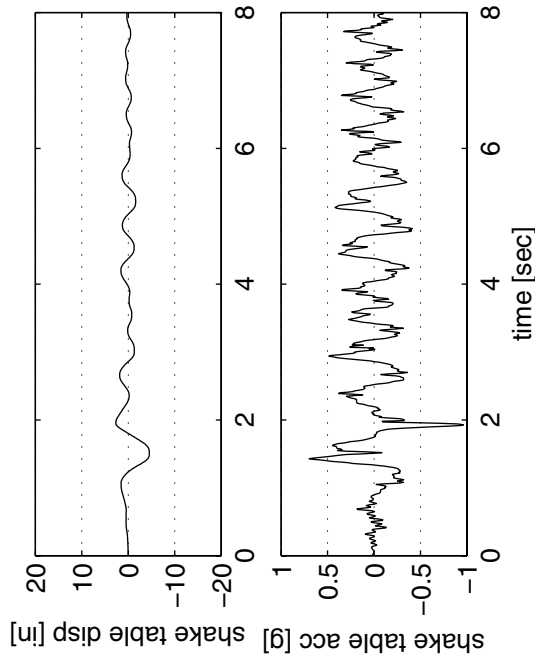
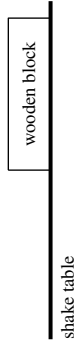
equipment: *FORMA incubator*
 motion: *Loma Prieta, Gilroy Hist. Bldg FN 6th (2% in 50 years)*

Working Model 2D simulation legend:



Quarter-Scale Wooden Block (Model)

overturning



Full-Scale Equipment (Prototype)

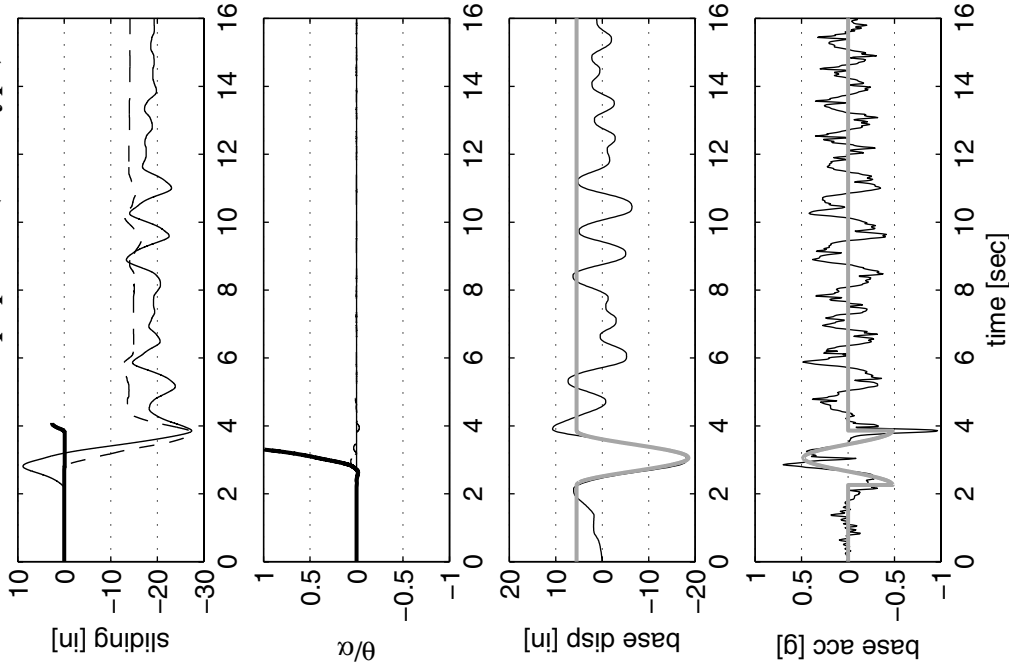
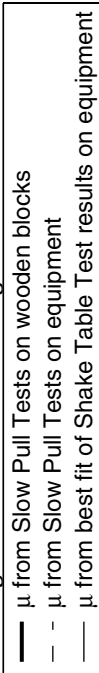


Figure 7.11 *Left:* Outcome of the shake table experiment on the quarter-scale wooden block model together with the table acceleration and displacement of the compressed (by a factor of 2) motion to which the block was subjected. *Right:* Computed response by *Working Model* simulations on the full-scale equipment prototype subjected to the uncompressed motion. The simulations were done for three values of the friction coefficient μ .

equipment: *Kelvinator refrigerator*
 motion: *Loma Prieta, Los Gatos PC, FP GROUND (2% in 50 years)*

Working Model 2D simulation legend:



Quarter-Scale Wooden Block (Model)

overturning

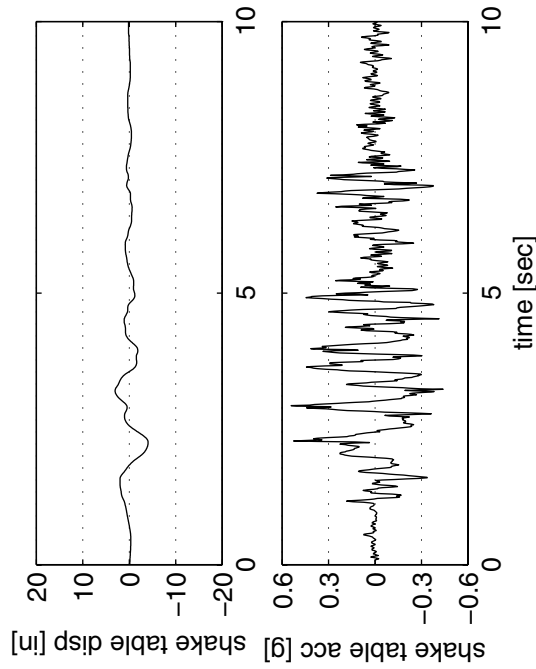
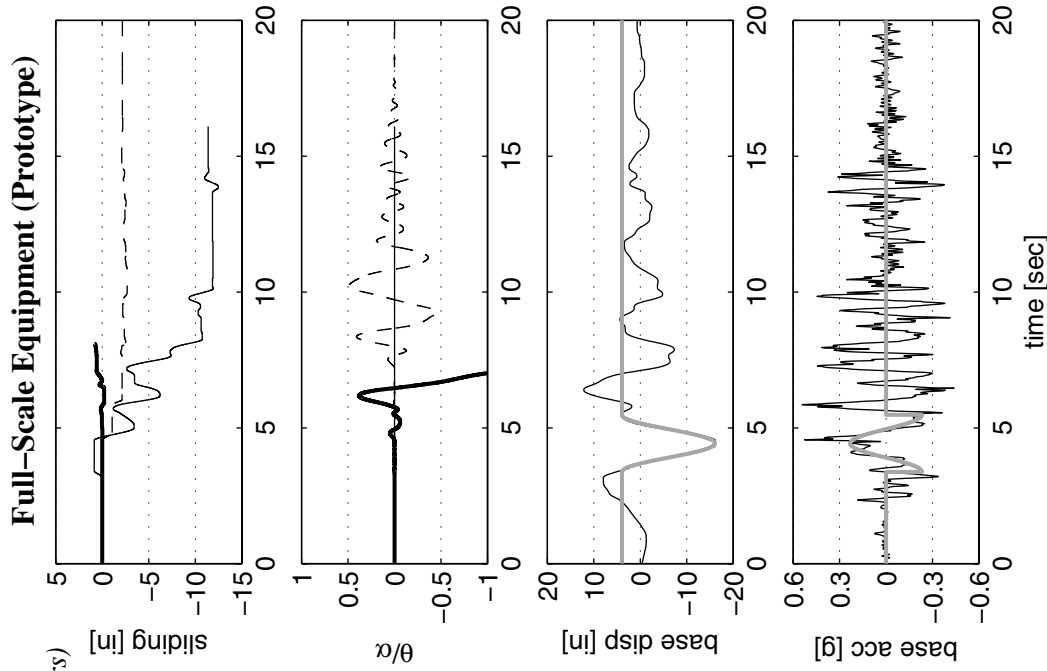
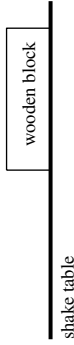


Figure 7.12 *Left:* Outcome of the shake table experiment on the quarter-scale wooden block model together with the table acceleration and displacement of the compressed (by a factor of 2) motion to which the block was subjected. *Right:* Computed response by *Working Model* simulations on the full-scale equipment prototype subjected to the uncompressed motion. The simulations were done for three values of the friction coefficient μ .

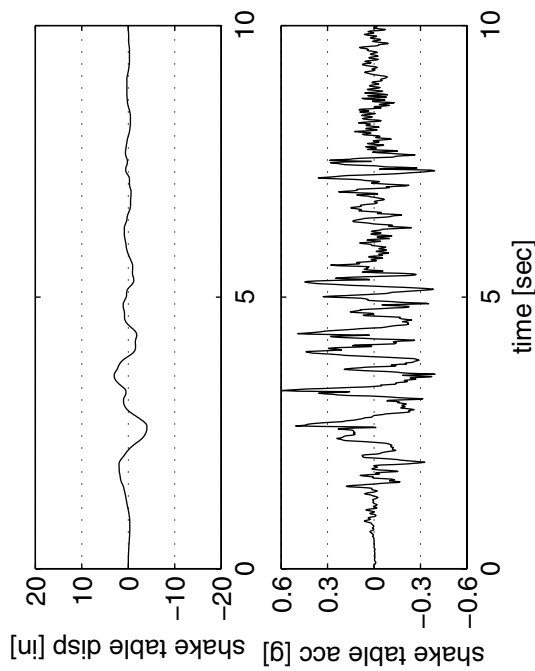
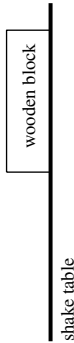
equipment: *Kelvinator refrigerator*
 motion: *Loma Prieta, Los Gatos PC, FP GROUND (2% in 50 years)*

Working Model 2D simulation legend:

- μ from Slow Pull Tests on wooden blocks
- - μ from Slow Pull Tests on equipment
- μ from best fit of Shake Table Test results on equipment

Quarter-Scale Wooden Block (Model)

overturning



Full-Scale Equipment (Prototype)

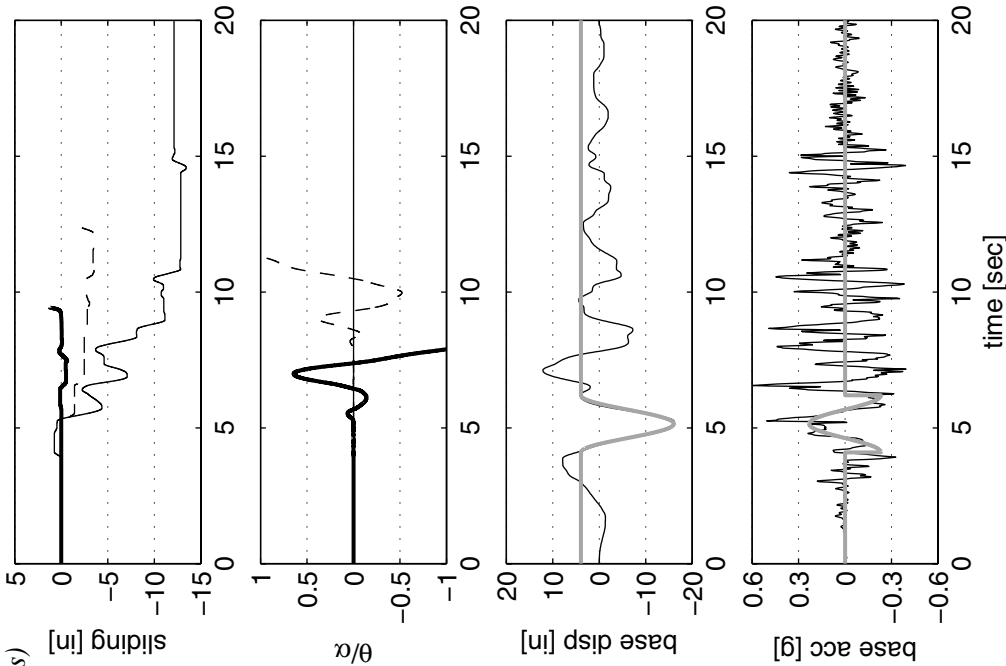


Figure 7.13 *Left:* Outcome of the shake table experiment on the quarter-scale wooden block model together with the table acceleration and displacement of the compressed (by a factor of 2) motion to which the block was subjected. *Right:* Computed response by *Working Model* simulations on the full-scale equipment prototype subjected to the uncompressed motion. The simulations were done for three values of the friction coefficient μ .

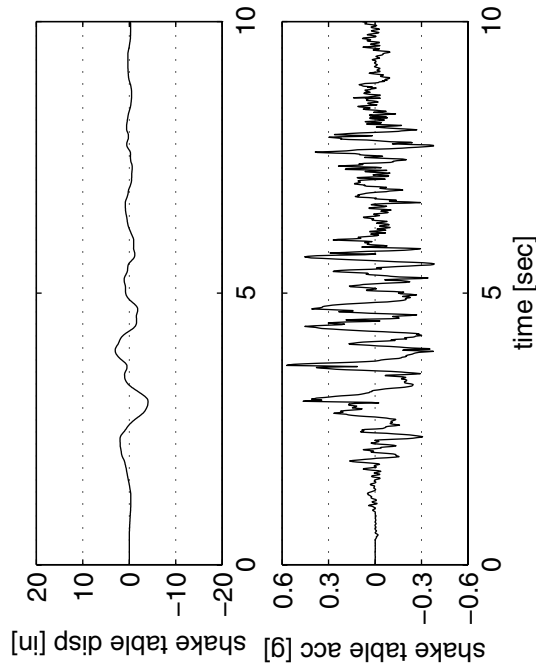
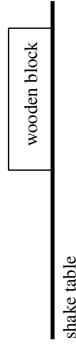
equipment: *Kelvinator refrigerator*
 motion: *Loma Prieta, Los Gatos PC, FP GROUND (2% in 50 years)*

Working Model 2D simulation legend:

- μ from Slow Pull Tests on wooden blocks
- - μ from Slow Pull Tests on equipment
- μ from best fit of Shake Table Test results on equipment

Quarter-Scale Wooden Block (Model)

overturning



Full-Scale Equipment (Prototype)

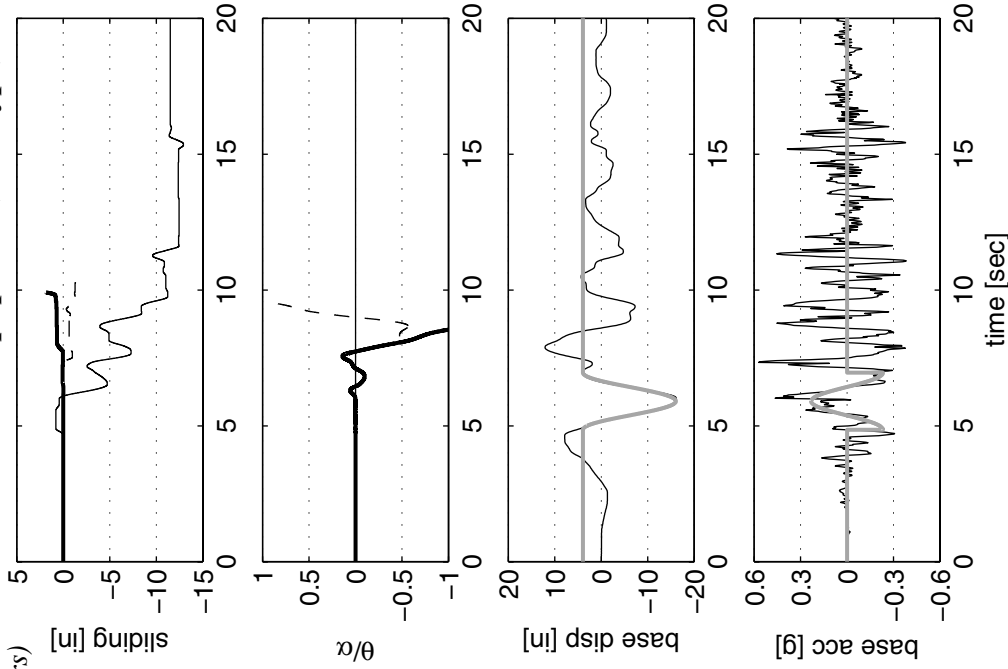
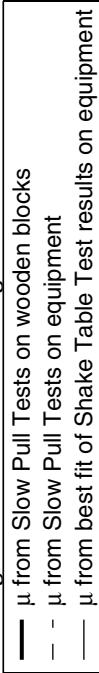


Figure 7.14 *Left:* Outcome of the shake table experiment on the quarter-scale wooden block model together with the table acceleration and displacement of the compressed (by a factor of 2) motion to which the block was subjected. *Right:* Computed response by *Working Model* simulations on the full-scale equipment prototype subjected to the uncompressed motion. The simulations were done for three values of the friction coefficient μ .

equipment: *Kelvinator refrigerator*
 motion: *Loma Prieta, Corralitos, FP GROUND (2% in 50 years)*

Working Model 2D simulation legend:



Quarter-Scale Wooden Block (Model)

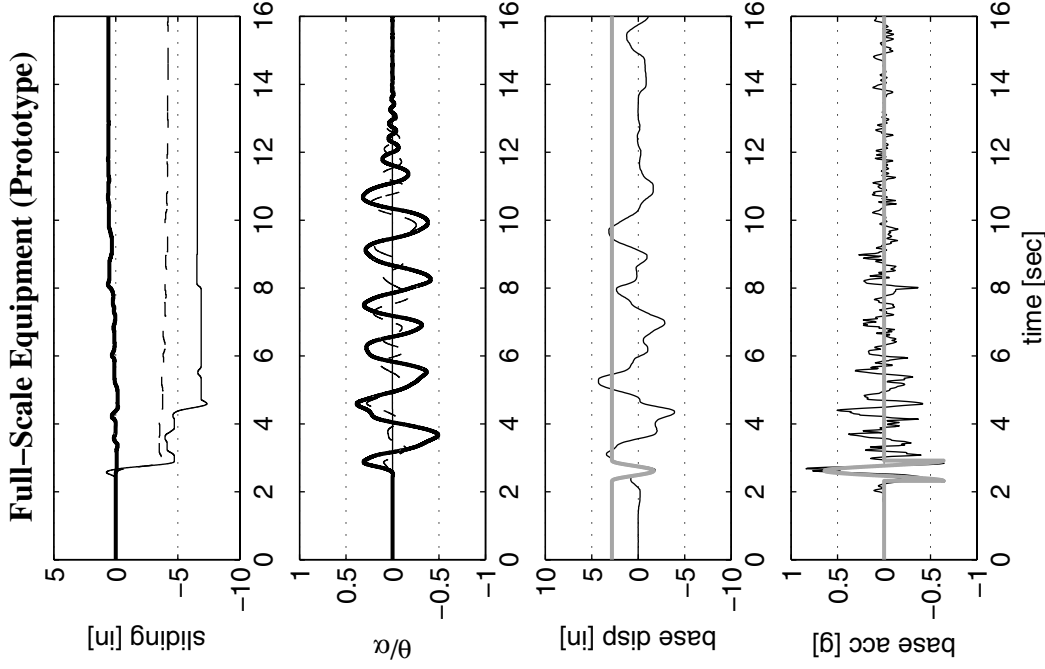
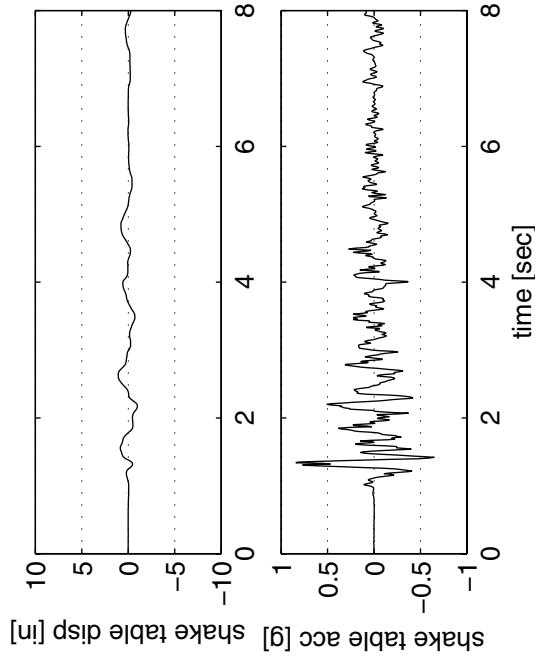
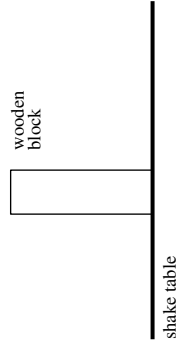
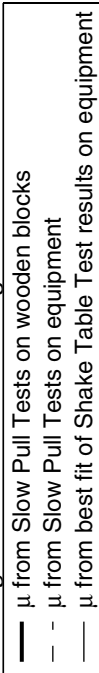


Figure 7.15 *Left: Outcome of the shake table experiment on the quarter-scale wooden block model together with the table acceleration and displacement of the compressed (by a factor of 2) motion to which the block was subjected. Right: Computed response by Working Model simulations on the full-scale equipment prototype subjected to the uncompressed motion. The simulations were done for three values of the friction coefficient μ .*

equipment: *Kelvinator refrigerator*
 motion: *Loma Prieta, Corralitos, FP GROUND (2% in 50 years)*

Working Model 2D simulation legend:



Quarter-Scale Wooden Block (Model)

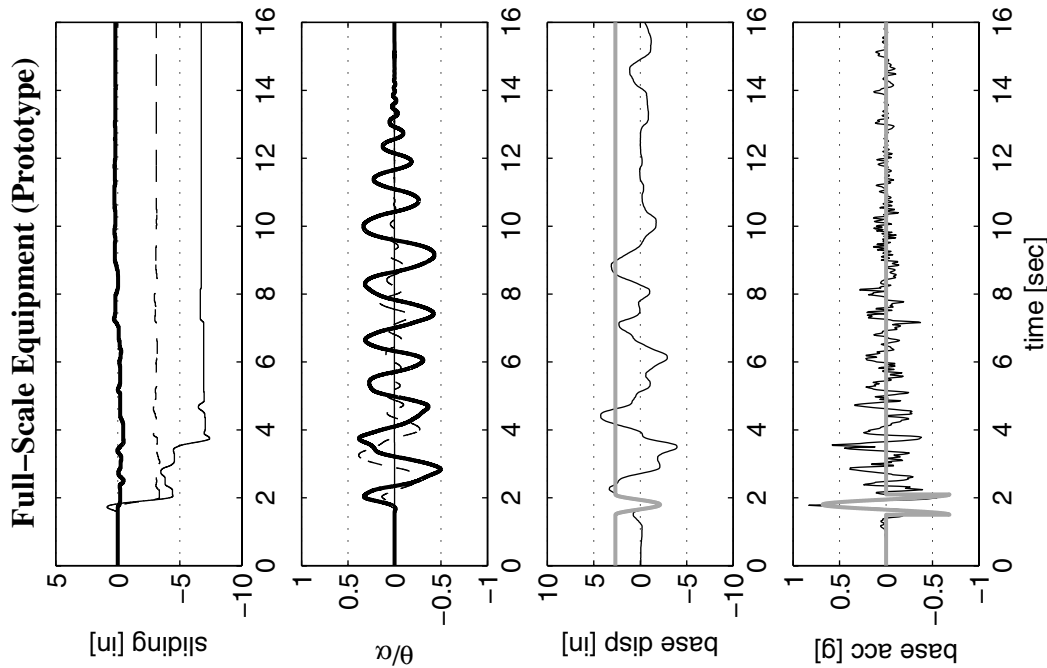
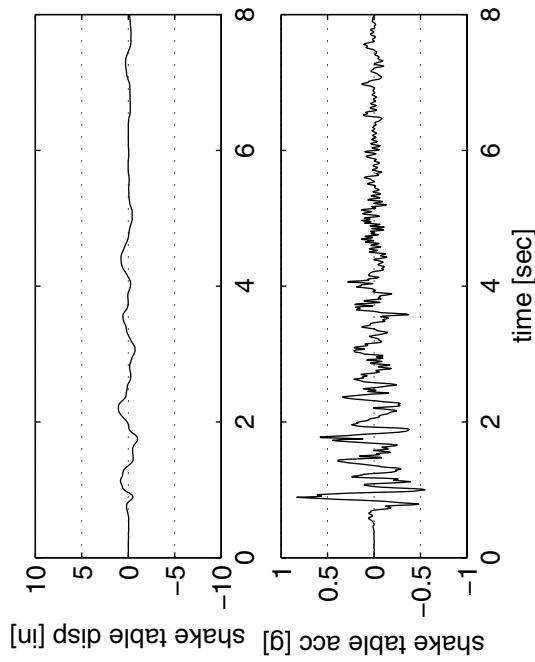
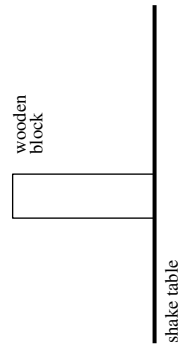
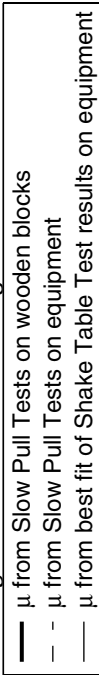


Figure 7.16 *Left: Outcome of the shake table experiment on the quarter-scale wooden block model together with the table acceleration and displacement of the compressed (by a factor of 2) motion to which the block was subjected. Right: Computed response by Working Model simulations on the full-scale equipment prototype subjected to the uncompressed motion. The simulations were done for three values of the friction coefficient μ .*

equipment: *Kelvinator refrigerator*

motion: *Loma Prieta, Gilroy Hist. Bldg FN GROUND (2% in 50 years)*

Working Model 2D simulation legend:



Quarter-Scale Wooden Block (Model)

overturning

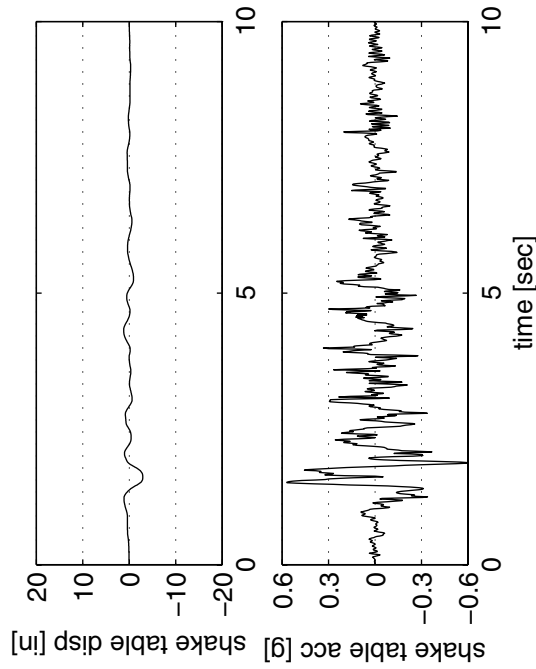
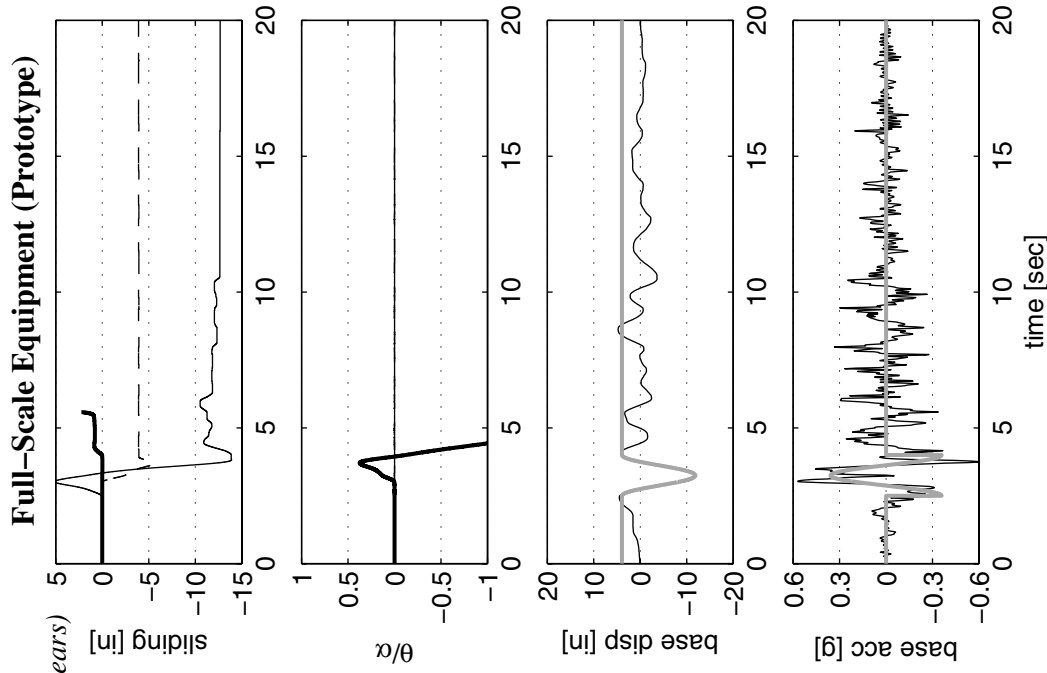
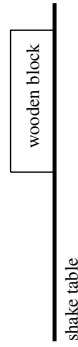
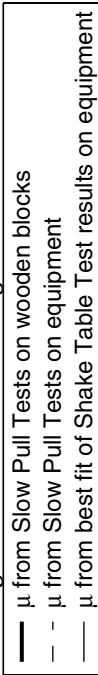


Figure 7.17 *Left:* Outcome of the shake table experiment on the quarter-scale wooden block model together with the table acceleration and displacement of the compressed (by a factor of 2) motion to which the block was subjected. *Right:* Computed response by *Working Model* simulations on the full-scale equipment prototype subjected to the uncompressed motion. The simulations were done for three values of the friction coefficient μ .

equipment: *Kelvinator refrigerator*

motion: *Loma Prieta, Gilroy Hist. Bldg FN GROUND (2% in 50 years)*

Working Model 2D simulation legend:



Quarter-Scale Wooden Block (Model)

overturning

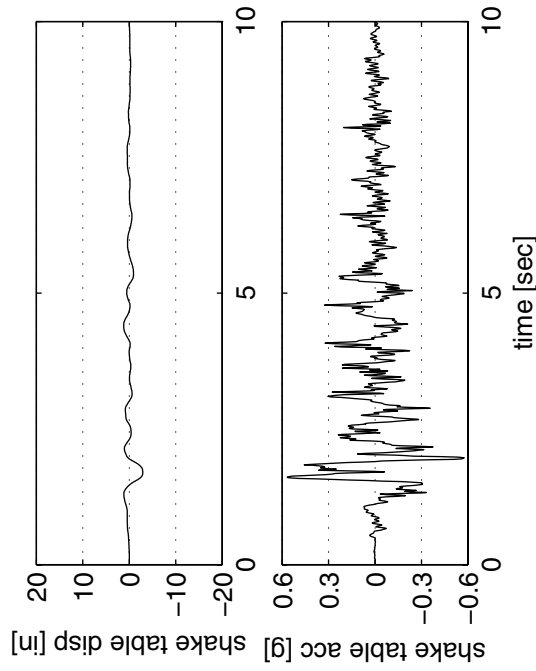
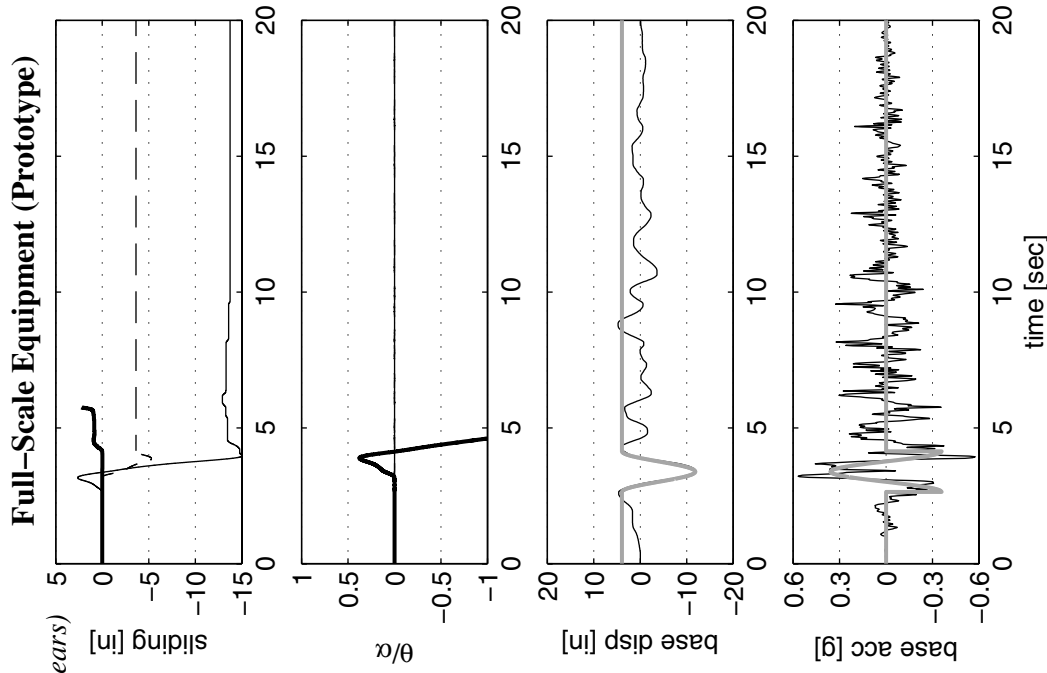
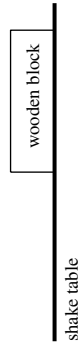


Figure 7.18 *Left:* Outcome of the shake table experiment on the quarter-scale wooden block model together with the table acceleration and displacement of the compressed (by a factor of 2) motion to which the block was subjected. *Right:* Computed response by *Working Model* simulations on the full-scale equipment prototype subjected to the uncompressed motion. The simulations were done for three values of the friction coefficient μ .

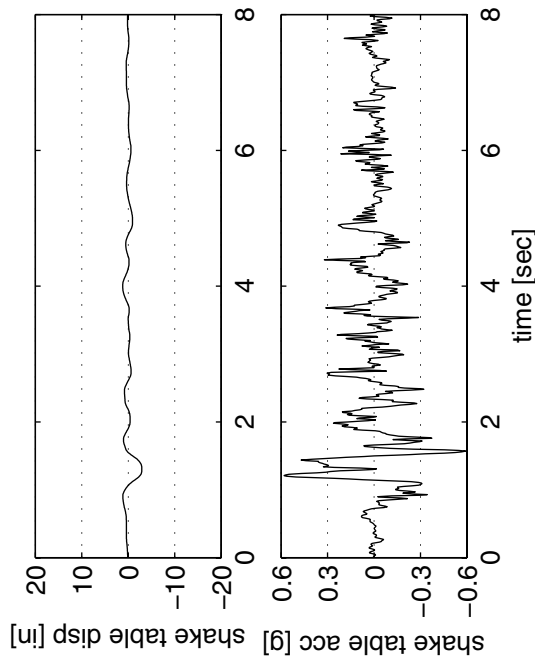
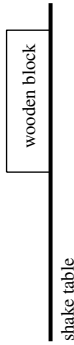
equipment: *Kelvinator refrigerator*
 motion: *Loma Prieta, Gilroy Hist. Bldg FN GROUND (2% in 50 years)*

Working Model 2D simulation legend:

- μ from Slow Pull Tests on wooden blocks
- - μ from Slow Pull Tests on equipment
- μ from best fit of Shake Table Test results on equipment

Quarter-Scale Wooden Block (Model)

overturning



Full-Scale Equipment (Prototype)

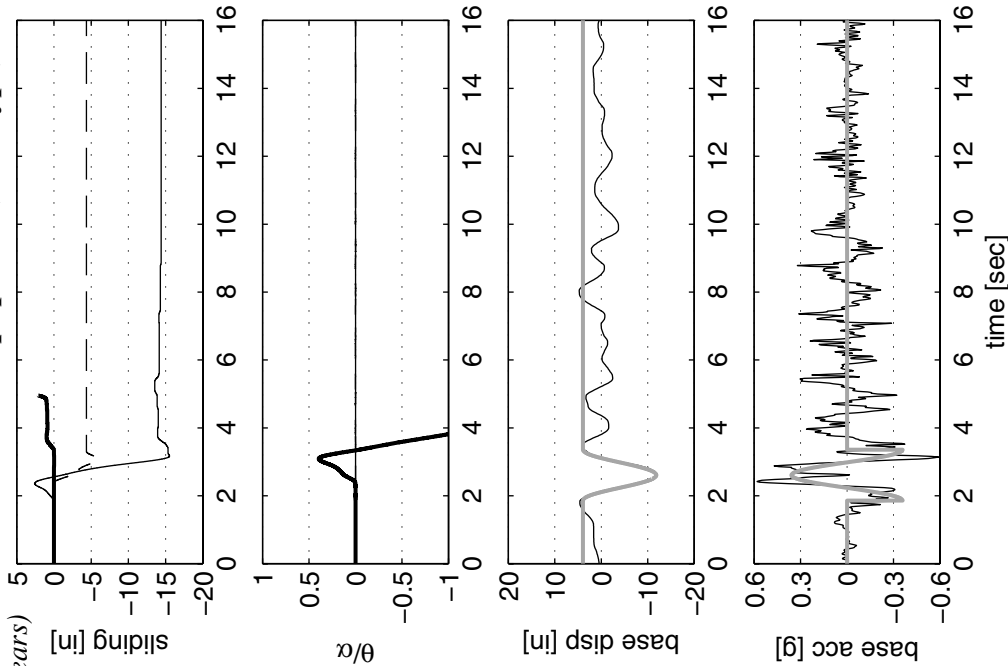
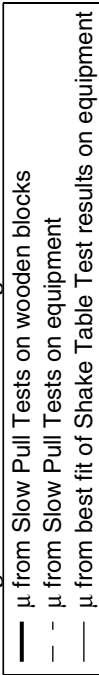


Figure 7.19 *Left:* Outcome of the shake table experiment on the quarter-scale wooden block model together with the table acceleration and displacement of the compressed (by a factor of 2) motion to which the block was subjected. *Right:* Computed response by *Working Model* simulations on the full-scale equipment prototype subjected to the uncompressed motion. The simulations were done for three values of the friction coefficient μ .

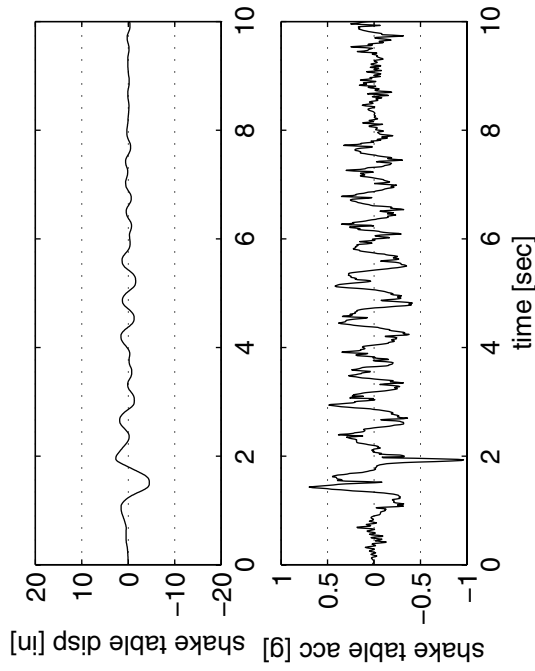
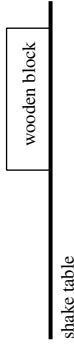
equipment: *Kelvinator refrigerator*
 motion: *Loma Prieta, Gilroy Hist. Bldg FN 6th (2% in 50 years)*

Working Model 2D simulation legend:



Quarter-Scale Wooden Block (Model)

overturning



Full-Scale Equipment (Prototype)

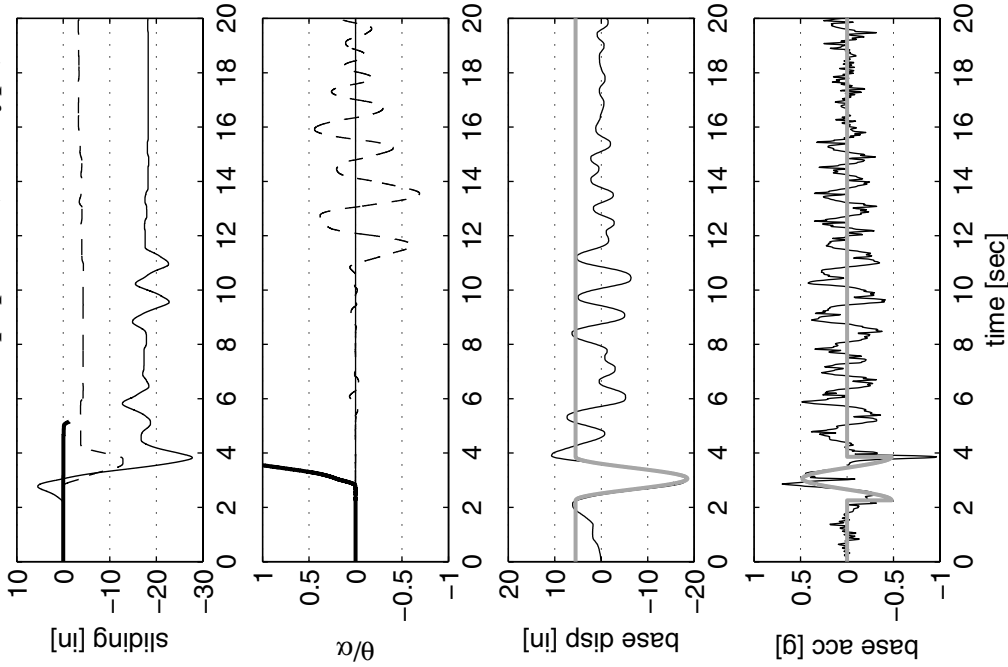


Figure 7.20 *Left:* Outcome of the shake table experiment on the quarter-scale wooden block model together with the table acceleration and displacement of the compressed (by a factor of 2) motion to which the block was subjected. *Right:* Computed response by *Working Model* simulations on the full-scale equipment prototype subjected to the uncompressed motion. The simulations were done for three values of the friction coefficient μ .

equipment: ASP refrigerator

motion: Loma Prieta, Los Gatos PC, FP GROUND (2% in 50 years)

Working Model 2D simulation legend:

- μ from Slow Pull Tests on wooden blocks
- - μ from Slow Pull Tests on equipment
- μ from best fit of Shake Table Test results on equipment

Quarter-Scale Wooden Block (Model)

overturning

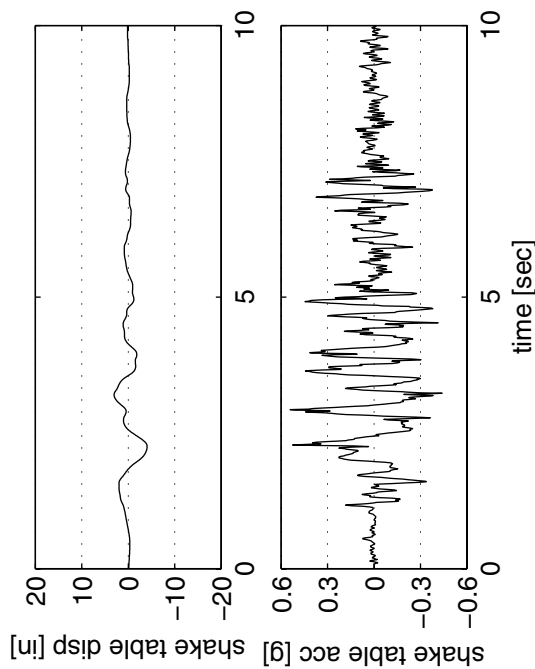
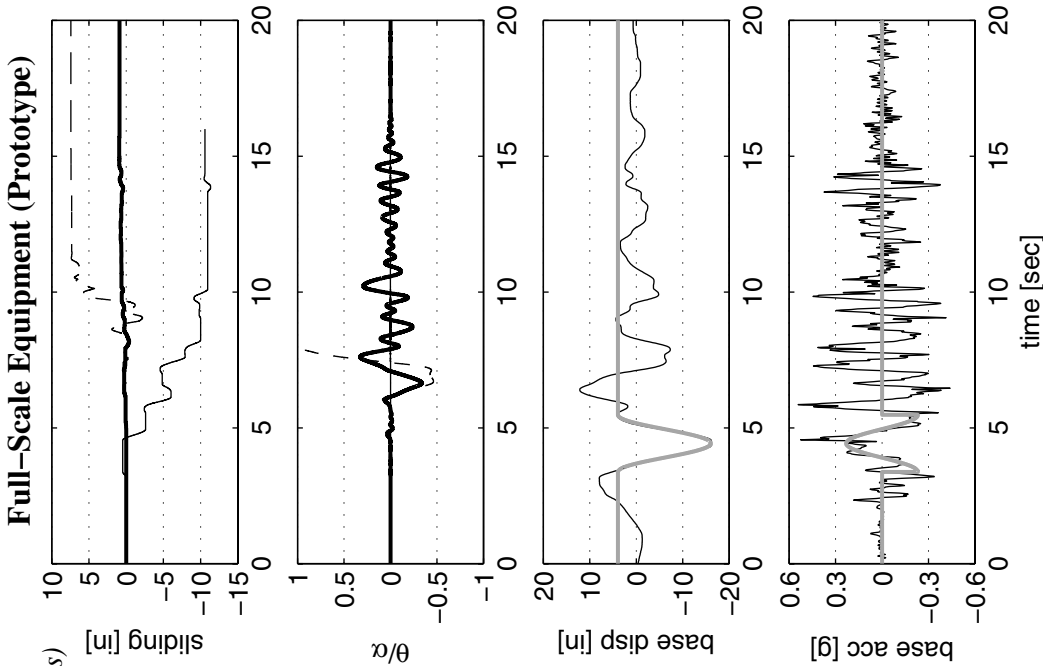
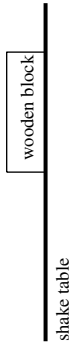


Figure 7.21 *Left:* Outcome of the shake table experiment on the quarter-scale wooden block model together with the table acceleration and displacement of the compressed (by a factor of 2) motion to which the block was subjected. *Right:* Computed response by *Working Model* simulations on the full-scale equipment prototype subjected to the uncompressed motion. The simulations were done for three values of the friction coefficient μ .

equipment: ASP refrigerator
 motion: Loma Prieta, Los Gatos PC, FP GROUND (2% in 50 years)

Working Model 2D simulation legend:

- μ from Slow Pull Tests on wooden blocks
- - μ from Slow Pull Tests on equipment
- μ from best fit of Shake Table Test results on equipment

Quarter-Scale Wooden Block (Model)

overturning

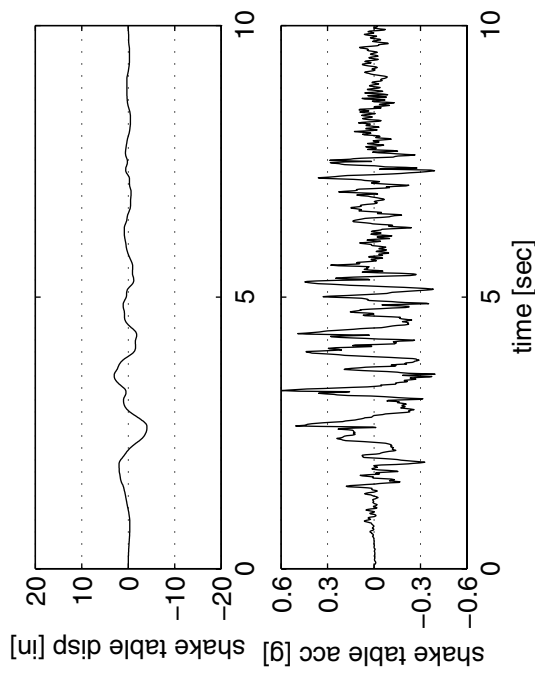
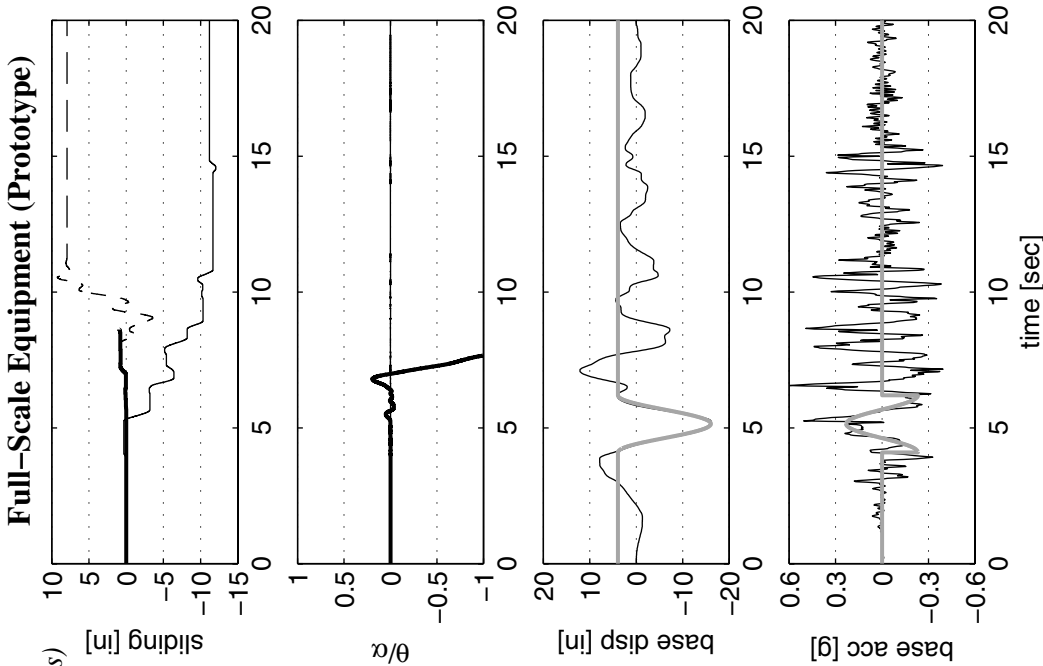
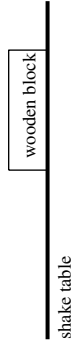


Figure 7.22 *Left:* Outcome of the shake table experiment on the quarter-scale wooden block model together with the table acceleration and displacement of the compressed (by a factor of 2) motion to which the block was subjected. *Right:* Computed response by *Working Model* simulations on the full-scale equipment prototype subjected to the uncompressed motion. The simulations were done for three values of the friction coefficient μ .

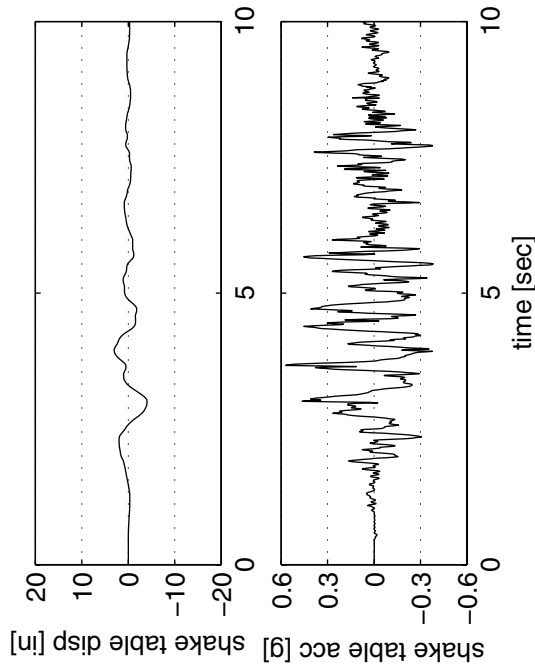
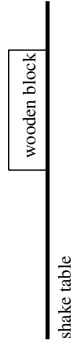
equipment: ASP refrigerator
 motion: Loma Prieta, Los Gatos PC, FP GROUND (2% in 50 years)

Working Model 2D simulation legend:

- μ from Slow Pull Tests on wooden blocks
- - μ from Slow Pull Tests on equipment
- μ from best fit of Shake Table Test results on equipment

Quarter-Scale Wooden Block (Model)

overturning



Full-Scale Equipment (Prototype)

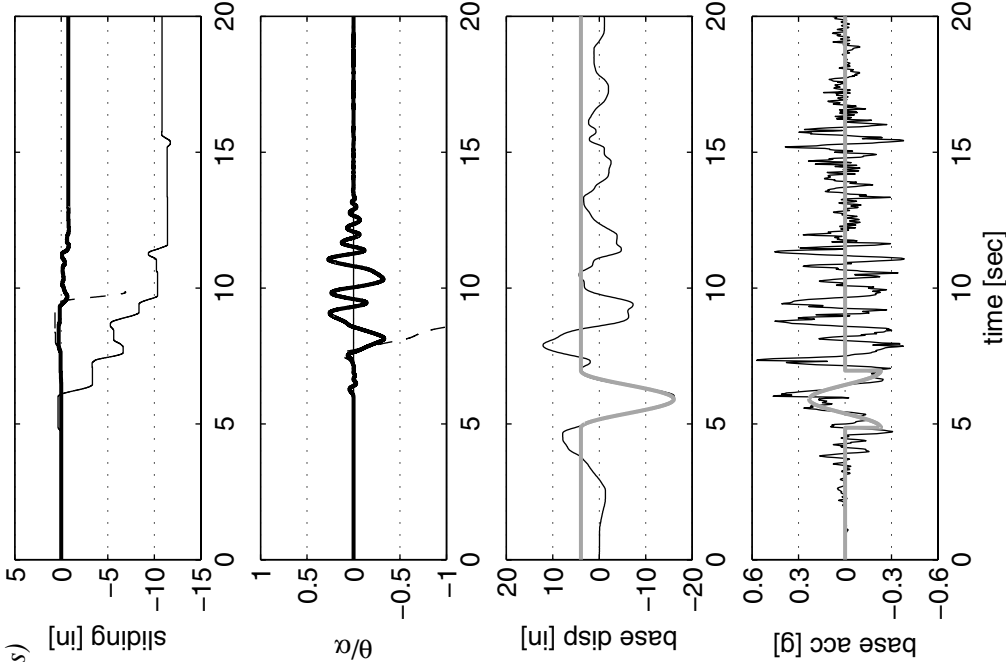
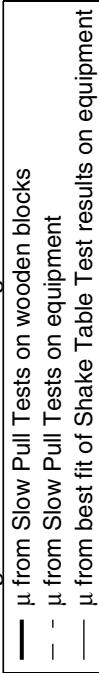


Figure 7.23 *Left:* Outcome of the shake table experiment on the quarter-scale wooden block model together with the table acceleration and displacement of the compressed (by a factor of 2) motion to which the block was subjected. *Right:* Computed response by *Working Model* simulations on the full-scale equipment prototype subjected to the uncompressed motion. The simulations were done for three values of the friction coefficient μ .

equipment: ASP refrigerator
 motion: Loma Prieta, Corralitos, FP GROUND (2% in 50 years)

Working Model 2D simulation legend:



Quarter-Scale Wooden Block (Model)

overturning

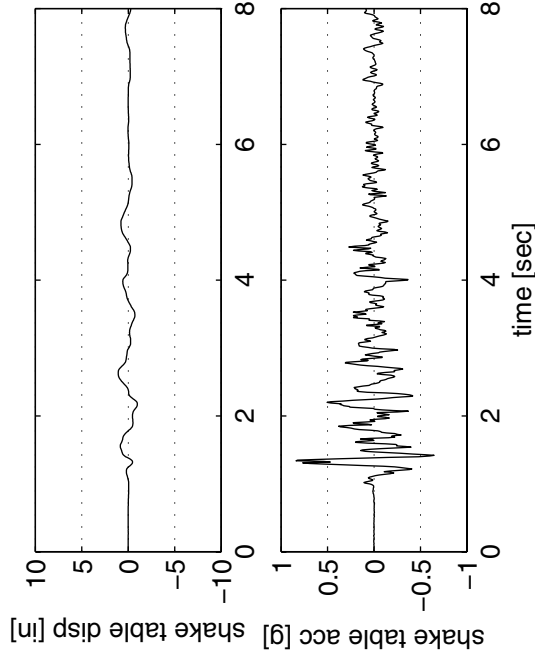
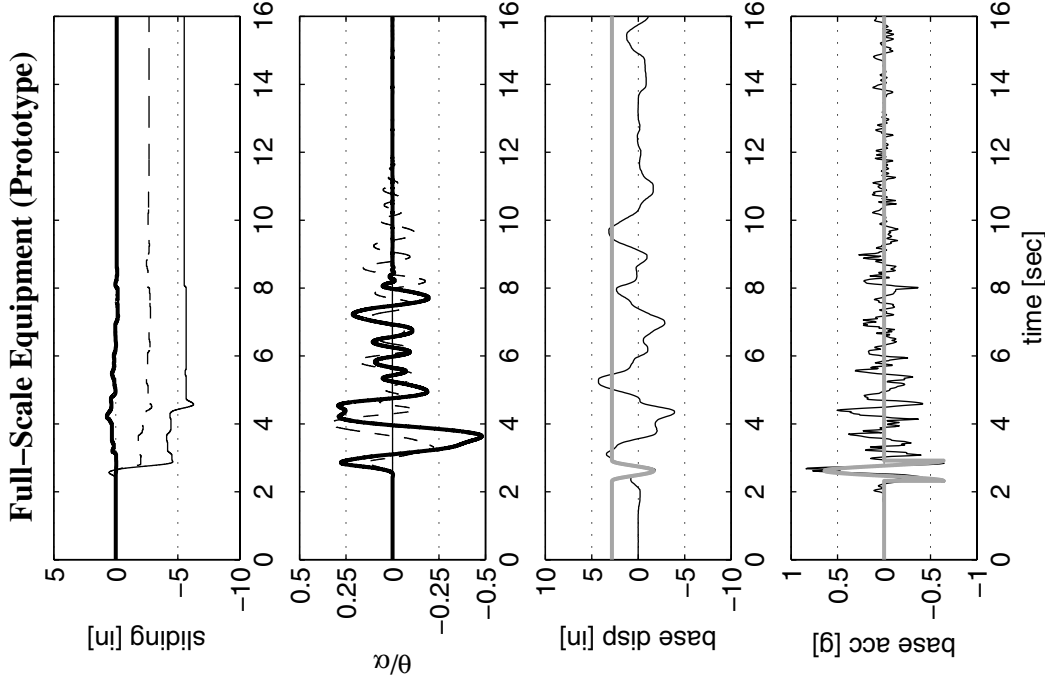
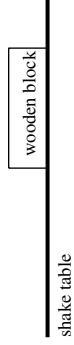
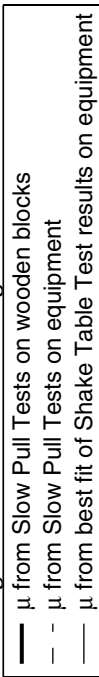


Figure 7.24 *Left*: Outcome of the shake table experiment on the quarter-scale wooden block model together with the table acceleration and displacement of the compressed (by a factor of 2) motion to which the block was subjected. *Right*: Computed response by *Working Model* simulations on the full-scale equipment prototype subjected to the uncompressed motion. The simulations were done for three values of the friction coefficient μ .

equipment: ASP refrigerator
 motion: Loma Prieta, Corralitos, FP GROUND (2% in 50 years)

Working Model 2D simulation legend:



Quarter-Scale Wooden Block (Model)

overturning

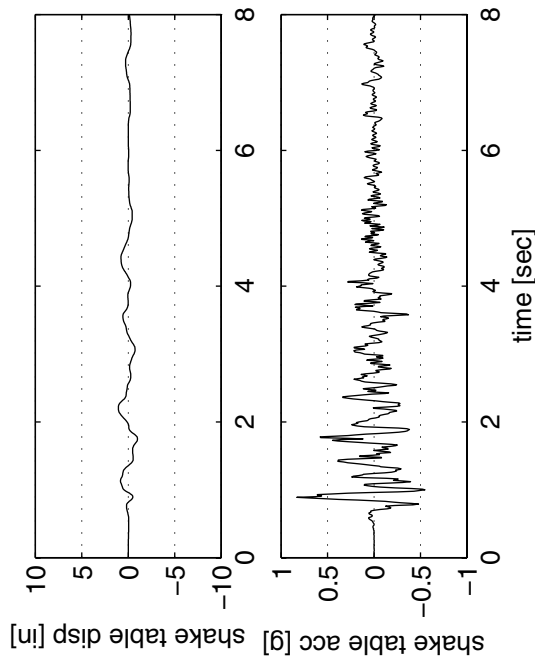
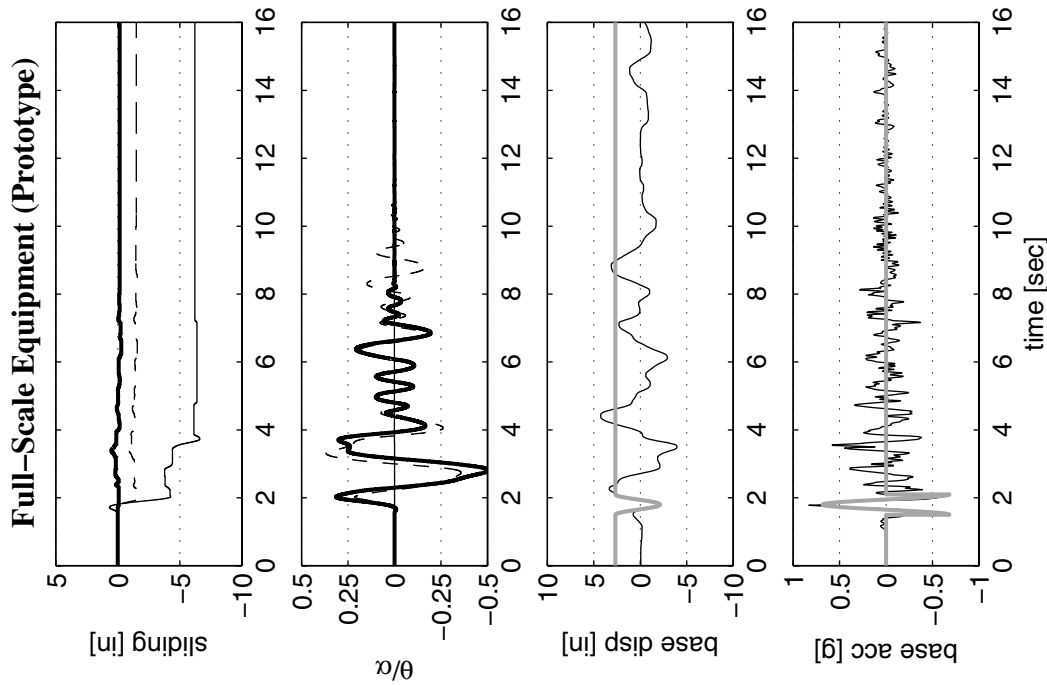
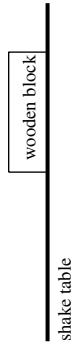


Figure 7.25 *Left*: Outcome of the shake table experiment on the quarter-scale wooden block model together with the table acceleration and displacement of the compressed (by a factor of 2) motion to which the block was subjected. *Right*: Computed response by *Working Model* simulations on the full-scale equipment prototype subjected to the uncompressed motion. The simulations were done for three values of the friction coefficient μ .

equipment: ASP refrigerator

motion: Loma Prieta, Gilroy Hist. Bldg FN GROUND (2% in 50 years)

Working Model 2D simulation legend:

- μ from Slow Pull Tests on wooden blocks
- - μ from Slow Pull Tests on equipment
- μ from best fit of Shake Table Test results on equipment

Quarter-Scale Wooden Block (Model)

overturning

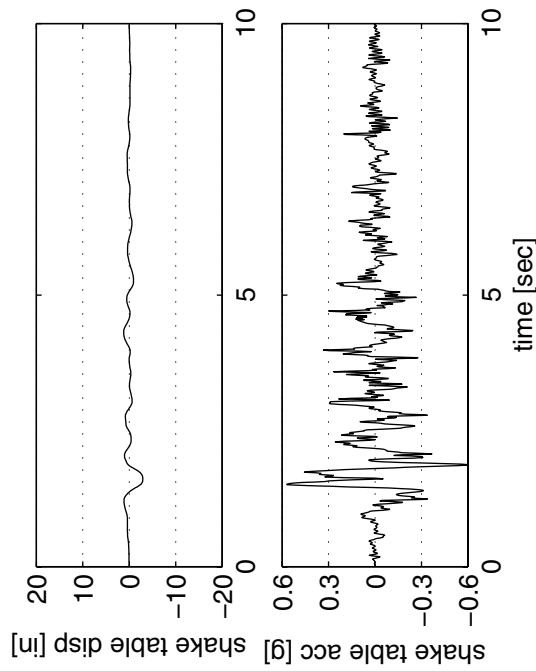
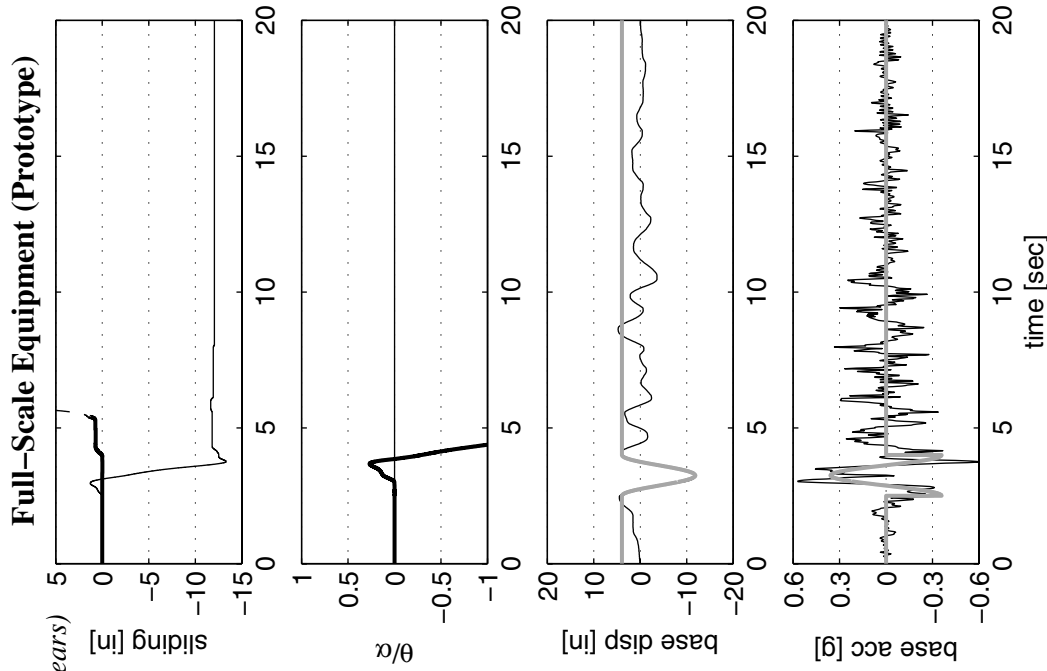
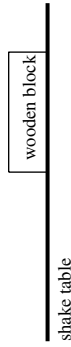


Figure 7.26 *Left:* Outcome of the shake table experiment on the quarter-scale wooden block model together with the table acceleration and displacement of the compressed (by a factor of 2) motion to which the block was subjected. *Right:* Computed response by *Working Model* simulations on the full-scale equipment prototype subjected to the uncompressed motion. The simulations were done for three values of the friction coefficient μ .

equipment: ASP refrigerator

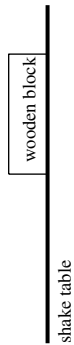
motion: Loma Prieta, Gilroy Hist. Bldg FN GROUND (2% in 50 years)

Working Model 2D simulation legend:

- μ from Slow Pull Tests on wooden blocks
- - μ from Slow Pull Tests on equipment
- μ from best fit of Shake Table Test results on equipment

Quarter-Scale Wooden Block (Model)

overturning



Full-Scale Equipment (Prototype)

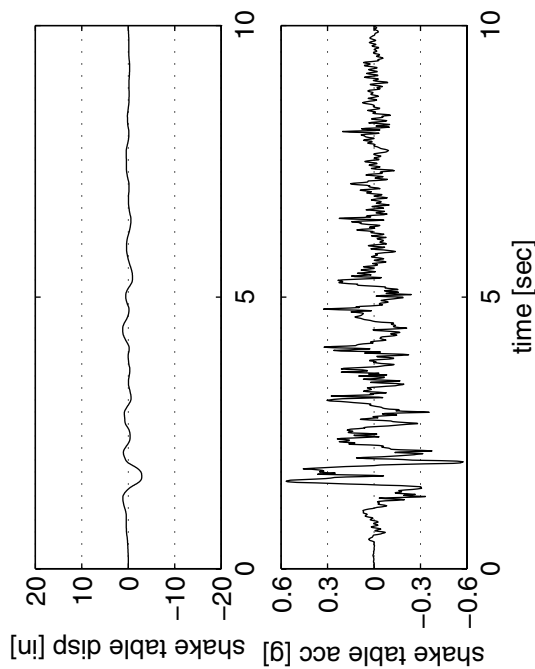
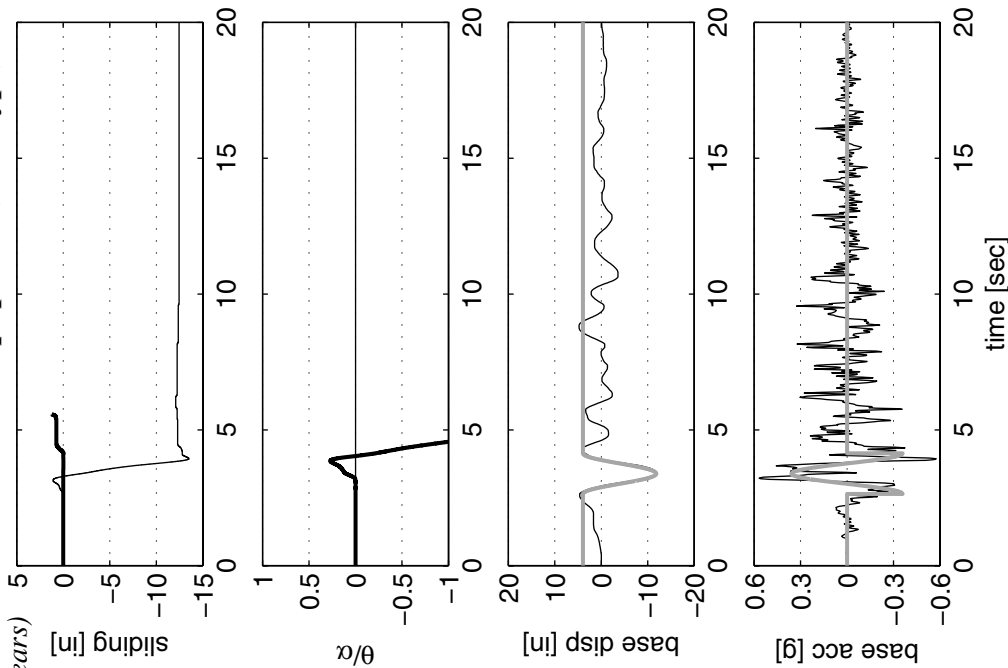


Figure 7.27 *Left:* Outcome of the shake table experiment on the quarter-scale wooden block model together with the table acceleration and displacement of the compressed (by a factor of 2) motion to which the block was subjected. *Right:* Computed response by *Working Model* simulations on the full-scale equipment prototype subjected to the uncompressed motion. The simulations were done for three values of the friction coefficient μ .

equipment: ASP refrigerator

motion: Loma Prieta, Gilroy Hist. Bldg FN GROUND (2% in 50 years)

Working Model 2D simulation legend:

- μ from Slow Pull Tests on wooden blocks
- - μ from Slow Pull Tests on equipment
- μ from best fit of Shake Table Test results on equipment

Quarter-Scale Wooden Block (Model)

overturning

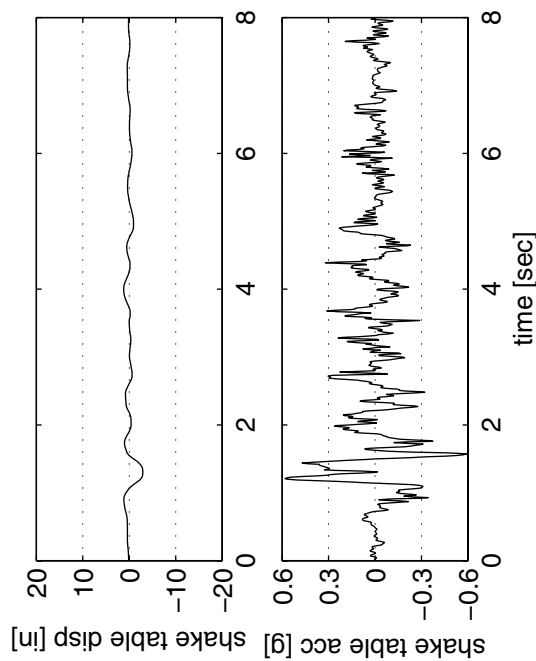
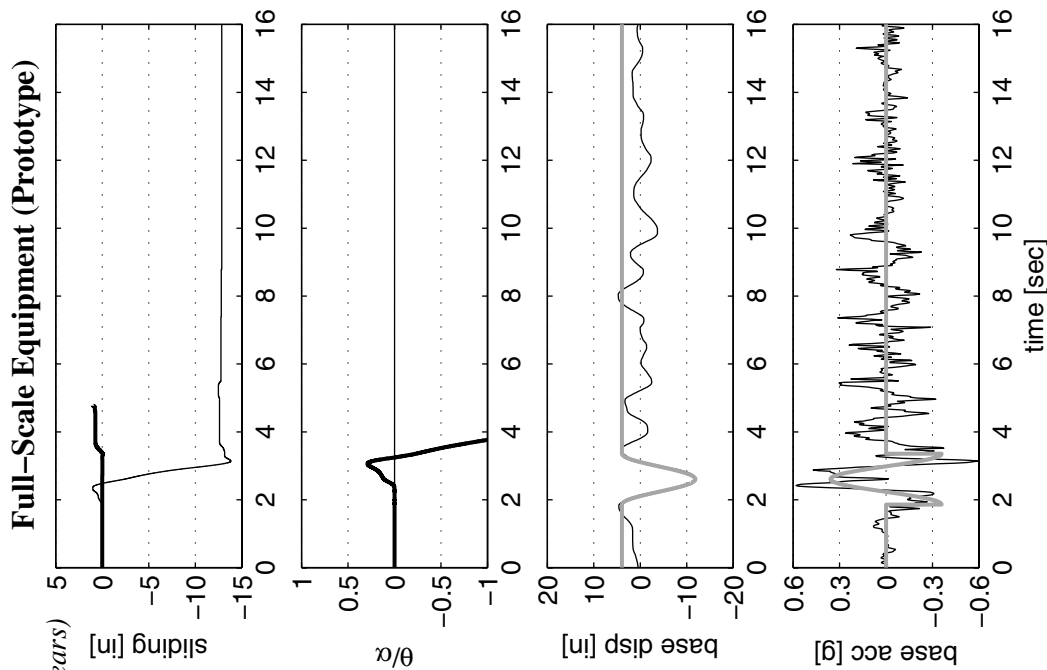
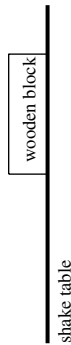


Figure 7.28 *Left:* Outcome of the shake table experiment on the quarter-scale wooden block model together with the table acceleration and displacement of the compressed (by a factor of 2) motion to which the block was subjected. *Right:* Computed response by *Working Model* simulations on the full-scale equipment prototype subjected to the uncompressed motion. The simulations were done for three values of the friction coefficient μ .

equipment: ASP refrigerator
 motion: Loma Prieta, Gilroy Hist. Bldg FN 6th (2% in 50 years)

Working Model 2D simulation legend:

- μ from Slow Pull Tests on wooden blocks
- - μ from Slow Pull Tests on equipment
- μ from best fit of Shake Table Test results on equipment

Quarter-Scale Wooden Block (Model)

overturning

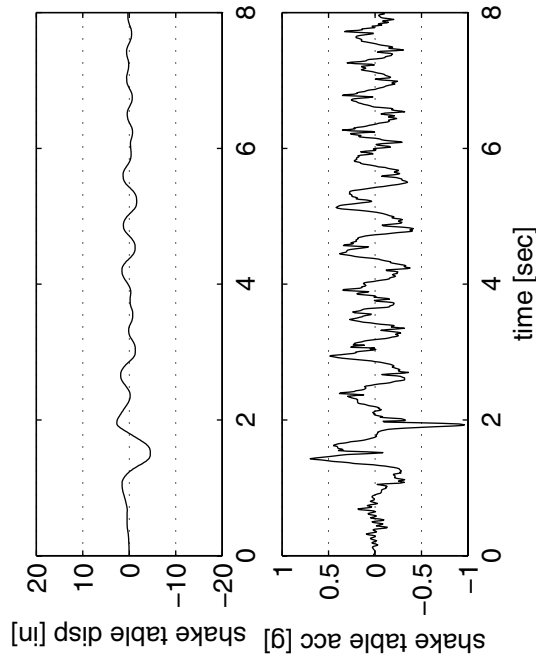
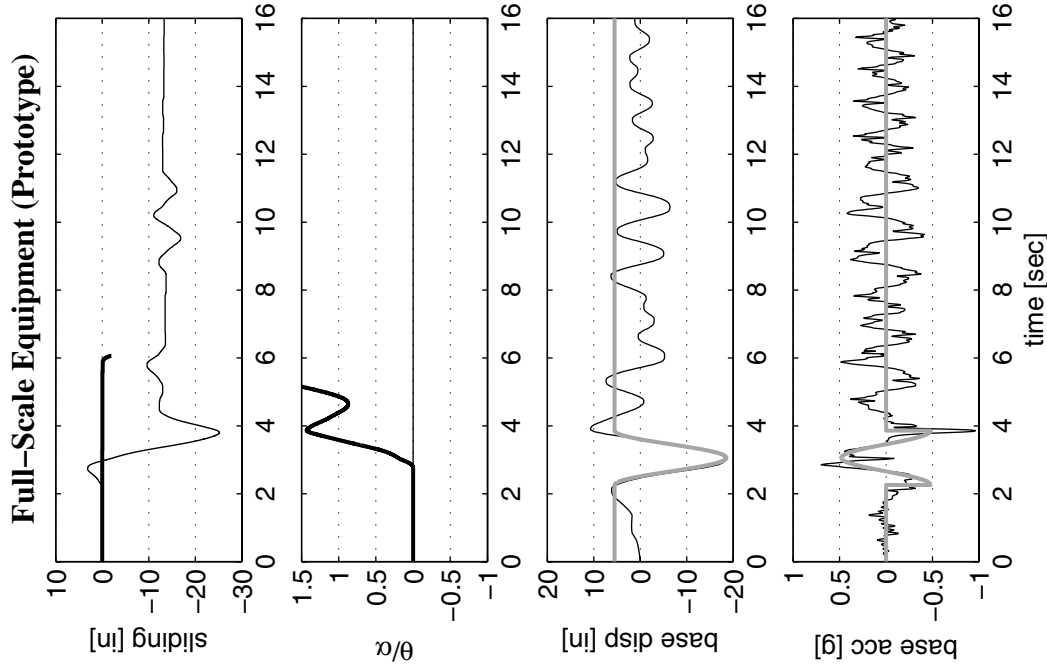
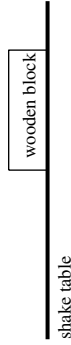


Figure 7.29 *Left:* Outcome of the shake table experiment on the quarter-scale wooden block model together with the table acceleration and displacement of the compressed (by a factor of 2) motion to which the block was subjected. *Right:* Computed response by *Working Model* simulations on the full-scale equipment prototype subjected to the uncompressed motion. The simulations were done for three values of the friction coefficient μ .

8 Regression Analysis and Fragility Curves for 2% in 50 Years Hazard Motions

8.1 SLIDING RESPONSE DUE TO 2% IN 50 YEARS HAZARD MOTIONS

The top two windows of the right columns in Figures 7.3 to 7.29 plot the computed (with *Working Model*) response of the full-scale freestanding equipment subjected to the earthquake motions with probability of exceedence 2% in 50 years used in this study. The solid lines plot the computed response where the coefficient of friction used is that obtained from best-fitting the numerical results of *Working Model* simulations to the experimental results obtained from the shake table tests for the 50% and 10% in 50 years hazard level motions (Figs. 3.4 to 3.6 and Table 3.2). The dashed lines plot the computed response where the coefficient of friction used is that obtained from the quasi-static pull tests described in Chapter 3. Note that the computed sliding and rocking time histories plotted with dashed lines show a response that is contrary to the primarily *sliding* response that was experimentally observed for the 10% and 50% in 50 years motions (presented in Chapter 4). In particular, Figures 7.12 to 7.29 show that the Kelvinator and ASP refrigerators experience large rotations—and even overturning in a few occasions. In light of the earlier observations where the Kelvinator and ASP refrigerators in fact experienced very small rotations, it was concluded that the friction coefficients from the slow pull test are too large, and consequently they cause the equipment to engage in rocking during the numerical simulations. *Working Model* simulations with the best-fitted friction coefficient values result in the predominant sliding response that is anticipated (plotted with solid black lines in Figs. 7.3 to 7.29). For this reason, the analysis presented in this chapter uses the reduced, best-fitted friction coefficients listed in Table 3.2.

Table 8.1 lists the 2% in 50 years input motions used with the *Working Model* simulations and the computed peak sliding displacement, U_{max} , of the laboratory equipment. The third col-

Table 8.1 Kinematic characteristic of the 2% in 50 years hazard level earthquake motions used in this study. Together with the maximum computed equipment sliding displacement U_{max} and interface friction coefficient μ , the motion PTA and pulse $\omega_p = 2\pi/T_p$ produce the intensity measure IM and engineering demand parameter EDP .

Equipment	Earthquake Motion (Probability of Exceedence in 50 years)	Pulse, T_p [sec], v_p [in/sec]	PTA [g]	U_{max} [in]	μ (slow pull)	μ (best fit)	IM $PTA / \mu g - 1$	EDP $U_{max} \omega_p^2 / PTA$	
FORMA	Loma Prieta, Los Gatos PC ground (2%)	B, 2.10, -30	0.54	17.95	0.23	0.13	3.17	0.77	
	Loma Prieta, Los Gatos PC ground (2%)	B, 2.10, -30	0.60	18.54	0.23	0.13	3.58	0.72	
	Loma Prieta, Los Gatos PC, FP ground (2%)	B, 2.10, -30	0.57	15.87	0.23	0.13	3.39	0.64	
	Loma Prieta, Corralitos, ground (2%)	B, 0.60, -24	0.84	7.83	0.23	0.13	5.45	2.65	
	Loma Prieta, Corralitos, ground (2%)	B, 0.60, -24	0.83	8.11	0.23	0.13	5.38	2.78	
	Loma Prieta, Gilroy Hist. Bldg. ground (2%)	B, 1.50, -33	0.59	13.90	0.23	0.13	3.57	1.06	
	Loma Prieta, Gilroy Hist. Bldg. ground (2%)	B, 1.50, -33	0.58	14.13	0.23	0.13	3.43	1.12	
	Loma Prieta, Gilroy Hist. Bldg. ground (2%)	B, 1.50, -33	0.59	14.80	0.23	0.13	3.55	1.14	
	Loma Prieta, Gilroy Hist. Bldg. 6th floor (2%)	B, 1.60, -47	0.96	27.40	0.23	0.13	6.40	1.14	
	Kelvinator	Loma Prieta, Los Gatos PC ground (2%)	B, 2.10, -30	0.54	12.48	0.28	0.17	2.19	0.53
		Loma Prieta, Los Gatos PC ground (2%)	B, 2.10, -30	0.60	13.43	0.28	0.17	2.50	0.52
		Loma Prieta, Los Gatos PC, FP ground (2%)	B, 2.10, -30	0.57	12.91	0.28	0.17	2.36	0.52
Loma Prieta, Corralitos, ground (2%)		B, 0.60, -24	0.84	7.36	0.28	0.17	3.94	2.49	
Loma Prieta, Corralitos, ground (2%)		B, 0.60, -24	0.83	7.40	0.28	0.17	3.88	2.53	
Loma Prieta, Gilroy Hist. Bldg. ground (2%)		B, 1.50, -33	0.59	13.90	0.28	0.17	2.50	1.06	
Loma Prieta, Gilroy Hist. Bldg. ground (2%)		B, 1.50, -33	0.58	15.04	0.28	0.17	2.39	1.19	
Loma Prieta, Gilroy Hist. Bldg. ground (2%)		B, 1.50, -33	0.59	15.51	0.28	0.17	2.48	1.19	
Loma Prieta, Gilroy Hist. Bldg. 6th floor (2%)		B, 1.60, -47	0.96	27.76	0.28	0.17	4.66	1.15	
ASP		Loma Prieta, Los Gatos PC ground (2%)	B, 2.10, -30	0.54	11.34	0.31	0.20	1.71	0.49
		Loma Prieta, Los Gatos PC ground (2%)	B, 2.10, -30	0.60	12.05	0.31	0.20	1.98	0.47
		Loma Prieta, Los Gatos PC, FP ground (2%)	B, 2.10, -30	0.57	11.73	0.31	0.20	1.86	0.48
	Loma Prieta, Corralitos, ground (2%)	B, 0.60, -24	0.84	6.26	0.31	0.20	3.20	2.12	
	Loma Prieta, Corralitos, ground (2%)	B, 0.60, -24	0.83	6.61	0.31	0.20	3.15	2.26	
	Loma Prieta, Gilroy Hist. Bldg. ground (2%)	B, 1.50, -33	0.59	13.31	0.31	0.20	1.97	1.02	
	Loma Prieta, Gilroy Hist. Bldg. ground (2%)	B, 1.50, -33	0.58	13.50	0.31	0.20	1.88	1.07	
	Loma Prieta, Gilroy Hist. Bldg. ground (2%)	B, 1.50, -33	0.59	13.82	0.31	0.20	1.96	1.06	
	Loma Prieta, Gilroy Hist. Bldg. 6th floor (2%)	B, 1.60, -47	0.96	25.20	0.31	0.20	3.81	1.05	

umn of Table 8.1 lists the defining parameters (pulse type, pulse duration T_p , and velocity amplitude v_p) of the trigonometric pulses that approximate the predominant distinguishable pulse of the excitation motion. The acceleration and displacement histories of these pulses are plotted with heavy grey lines on the bottom two windows of Figures 7.3 to 7.29 (right) together with their corresponding earthquake records (black lines). The last two columns plot the Intensity Measure $PTA / \mu g - 1$ and Engineering Demand Parameter $\Delta = U_{max}\omega_p^2 / PTA$.

8.2 FRAGILITY ANALYSIS FOR 2% IN 50 YEARS HAZARD LEVEL MOTIONS

8.2.1 Regression of the Experimental Data

Figure 8.1 (top) plots the Engineering Demand Parameter $\Delta = U_{max}\omega_p^2 / PTA$ as a function of the Intensity Measure $PTA / \mu g - 1$ obtained from the *Working Model* simulations on the three pieces of equipment. The value of the coefficient of friction, μ , is that obtained by best fit (see Chapter 3). A least-squares linear regression of the data, plotted with a solid line, provides the mean value $\bar{\Delta}$ of the random variable Δ as a function of the intensity measure

$$\bar{\Delta}\left(\frac{PTA}{\mu g}\right) = 0.38\left(\frac{PTA}{\mu g} - 1\right) \quad (8.1)$$

The *coefficient of determination*, r^2 , for this regression is equal to 0.32. The shaded bars on the top graph of Figure 8.1 are statistical bins that are used to create a graph of the standard deviation to the mean as a function of the Intensity Measure. This standard deviation, $\sigma_{\Delta}(PTA / \mu g)$, is plotted on the bottom graph of Figure 8.1 together with a linear regression given by

$$\sigma_{\Delta}\left(\frac{PTA}{\mu g}\right) = 0.17\left(\frac{PTA}{\mu g} - 1\right) \quad (8.2)$$

with $r^2 = 0.93$.

8.2.1 The *EDP* as a Lognormally Distributed Random Variable

As discussed in Chapter 5, the random variable Δ is assumed to be lognormally distributed with probability density function

$$f_{\Delta}(\delta) = \frac{1}{\sqrt{2\pi}\omega\delta} \exp\left[-\frac{1}{2}\left(\frac{\ln\delta - \lambda}{\omega}\right)^2\right], \quad \delta > 0 \quad (8.3)$$

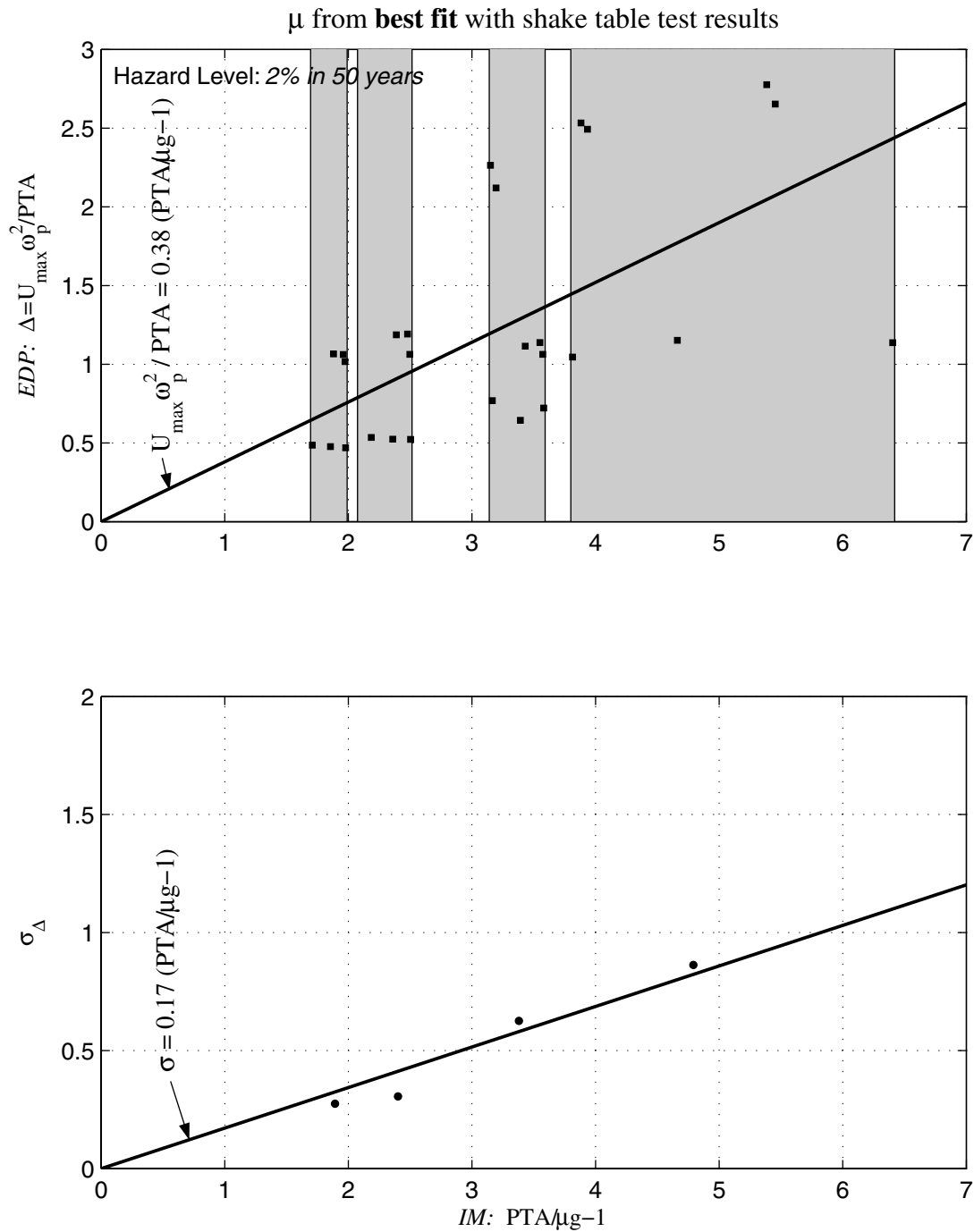


Figure 8.1 *Top:* The Engineering Demand Parameter $\Delta = U_{\max} \omega_p^2 / PTA$ as a function of the Intensity Measure $PTA/\mu g^{-1}$ for the *Working Model* simulations on the three pieces of equipment. The value of μ is obtained by *best-fit* of numerical simulation results to shake table test results. *Bottom:* Standard deviation to the mean as a function of the Intensity Measure $PTA/\mu g^{-1}$.

where the two defining parameters θ and ω of the distribution are in fact the mean and standard deviation of the corresponding normally distributed variable X (Crow and Shimizu 1988). The cumulative distribution function of Δ is given by

$$F_{\Delta}(\delta) = \int_0^{\delta} \frac{1}{\sqrt{2\pi}\omega\delta'} \exp\left[-\frac{1}{2}\left(\frac{\ln\delta' - \lambda}{\omega}\right)^2\right] d\delta' = \Phi\left(\frac{\ln\delta - \lambda}{\omega}\right) \quad (8.4)$$

where Φ is the cumulative distribution function of a *standard* normal distribution (i.e., $\lambda = 0$ and $\omega = 1$). Presented in Chapter 5 and repeated here for convenience, the mean, $\bar{\Delta}$, and standard deviation, σ_{Δ} , of the lognormal variable Δ are related to the mean, λ , and standard deviation, ω , of the normal variable X by

$$\bar{\Delta} = \exp\left(\lambda + \frac{\omega^2}{2}\right) \quad \text{and} \quad \sigma_{\Delta} = \exp\left(\lambda + \frac{\omega^2}{2}\right) \sqrt{\exp(\omega^2) - 1} \quad (8.5)$$

or

$$\lambda = \ln\bar{\Delta} - \frac{1}{2} \ln\left[1 + \left(\frac{\sigma_{\Delta}}{\bar{\Delta}}\right)^2\right] \quad \text{and} \quad \omega = \sqrt{\ln\left[1 + \left(\frac{\sigma_{\Delta}}{\bar{\Delta}}\right)^2\right]} \quad (8.6)$$

The statistical estimation of $\bar{\Delta} = \bar{\Delta}(PTA / \mu g)$ is given by Equation (8.1), and that of $\sigma_{\Delta} = \sigma_{\Delta}(PTA / \mu g)$ is given by Equation (8.2). The mean and standard deviation of the normally distributed variable X are themselves functions of the intensity measure—that is, $\lambda = \lambda(PTA / \mu g)$ and $\omega = \omega(PTA / \mu g)$.

In order to not reject the hypothesis that Δ has a lognormal distribution, the Kolmogorov-Smirnov goodness-of-fit test is used as in Chapter 5. Figure 8.2 plots the empirical cumulative distribution function, $F_{\Delta}^*(\delta)$, for the 2% in 50 years motions. Together is plotted the cumulative distribution function of the hypothesized lognormally distributed random variable Δ , $F_{\Delta}(\delta)$. The maximum distance between the distribution functions presented in Figure 8.2 is

$$S = \max_{\delta} |F_{\Delta}(\delta) - F_{\Delta}^*(\delta)| = \max(S^+, S^-) = 0.185 \quad (8.7)$$

where S^+ and S^- are given by Equations (5.29) and (5.30).

For a certain level of significance α , the hypothesis is rejected if S exceeds a critical value of S_{cr} . The value of S_{cr} depends on α and the size of the sample, n . The sample size of this study for the 2% in 50 years motions is $n = 27$. Tables for the Kolmogorov-Smirnov test provide (Daniel 1990)

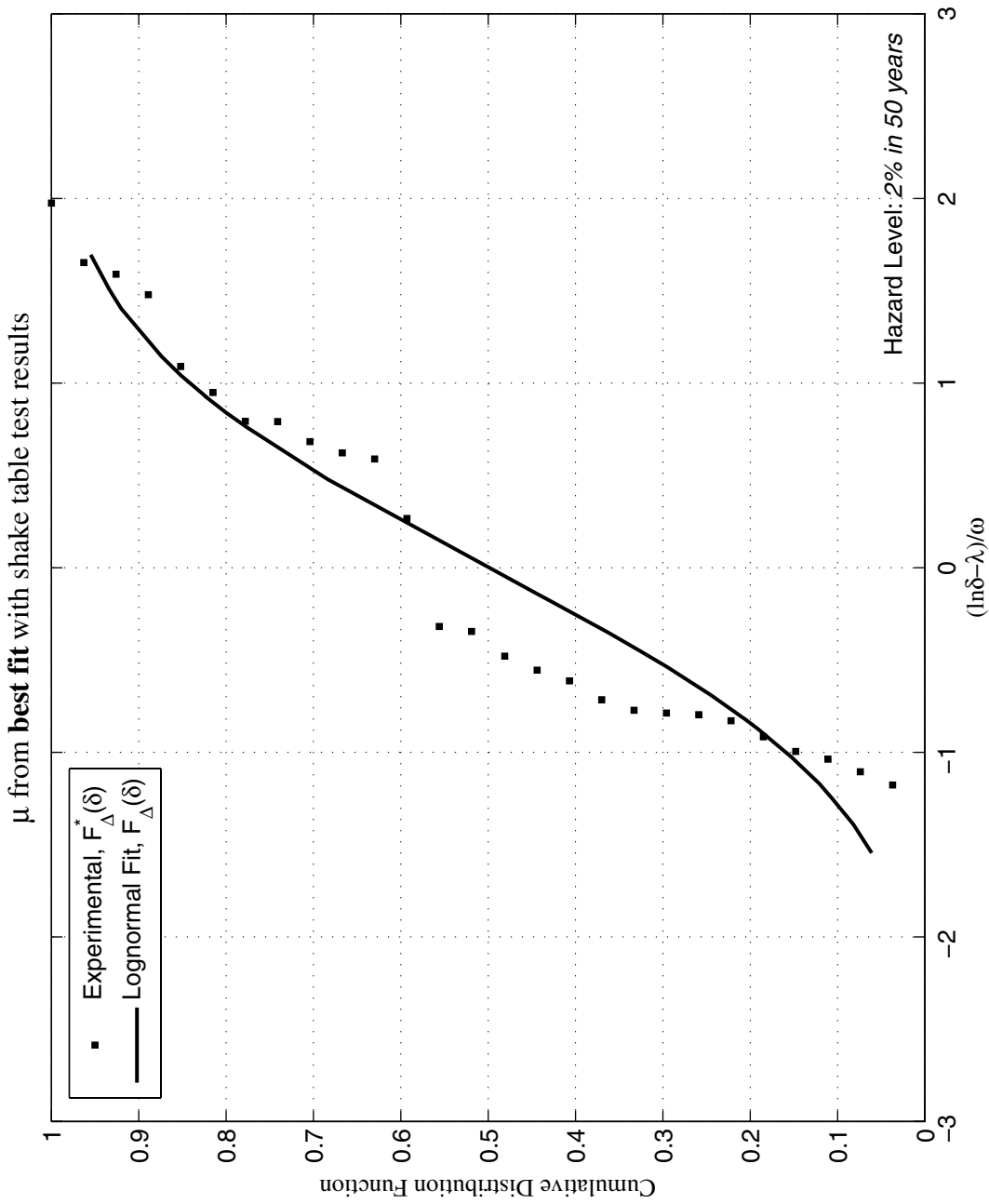


Figure 8.2 The empirical cumulative distribution function of the EDP Δ (50% and 10% hazard level motions) and the theoretical cumulative distribution function of its hypothesized lognormal distribution. The value of the friction coefficient μ that the random variable Δ depends on is that obtained from the slow pull tests.

$$S_{cr}(\alpha, n=27) = \begin{cases} 0.200, & \alpha=0.80 \\ 0.229, & \alpha=0.90 \\ 0.254, & \alpha=0.95 \\ 0.284, & \alpha=0.98 \\ 0.305, & \alpha=0.99 \end{cases} \quad (8.8)$$

Since $S < S_{cr}$, the hypothesis that Δ is lognormally distributed is *not* rejected.

8.2.2 Fragility Curves

Recall from Chapter 5 that fragility was defined as the probability P_f that the Engineering Demand Parameter $\Delta = U_{max}\omega_p^2 / PTA$ for a piece of equipment will exceed a certain threshold (capacity) C , given the intensity measure, $IM = PTA / \mu g - 1$. For the lognormally distributed random variable Δ ,

$$P_f = 1 - \Phi \left(\frac{\ln \left[\frac{C}{\bar{\Delta}(IM)} \sqrt{1 + \left(\frac{\sigma_{\Delta}(IM)}{\bar{\Delta}(IM)} \right)^2} \right]}{\sqrt{\ln \left[1 + \left(\frac{\sigma_{\Delta}(IM)}{\bar{\Delta}(IM)} \right)^2 \right]}} \right) \quad (8.9)$$

Regression Equations (8.1) and (8.2) provide the functional dependence of $\bar{\Delta}$ and σ_{Δ} on the intensity measure, $IM = PTA / \mu g - 1$. Figure 8.3 plots fragility curves that have been generated by use of expression (8.9) for four values of capacity C .

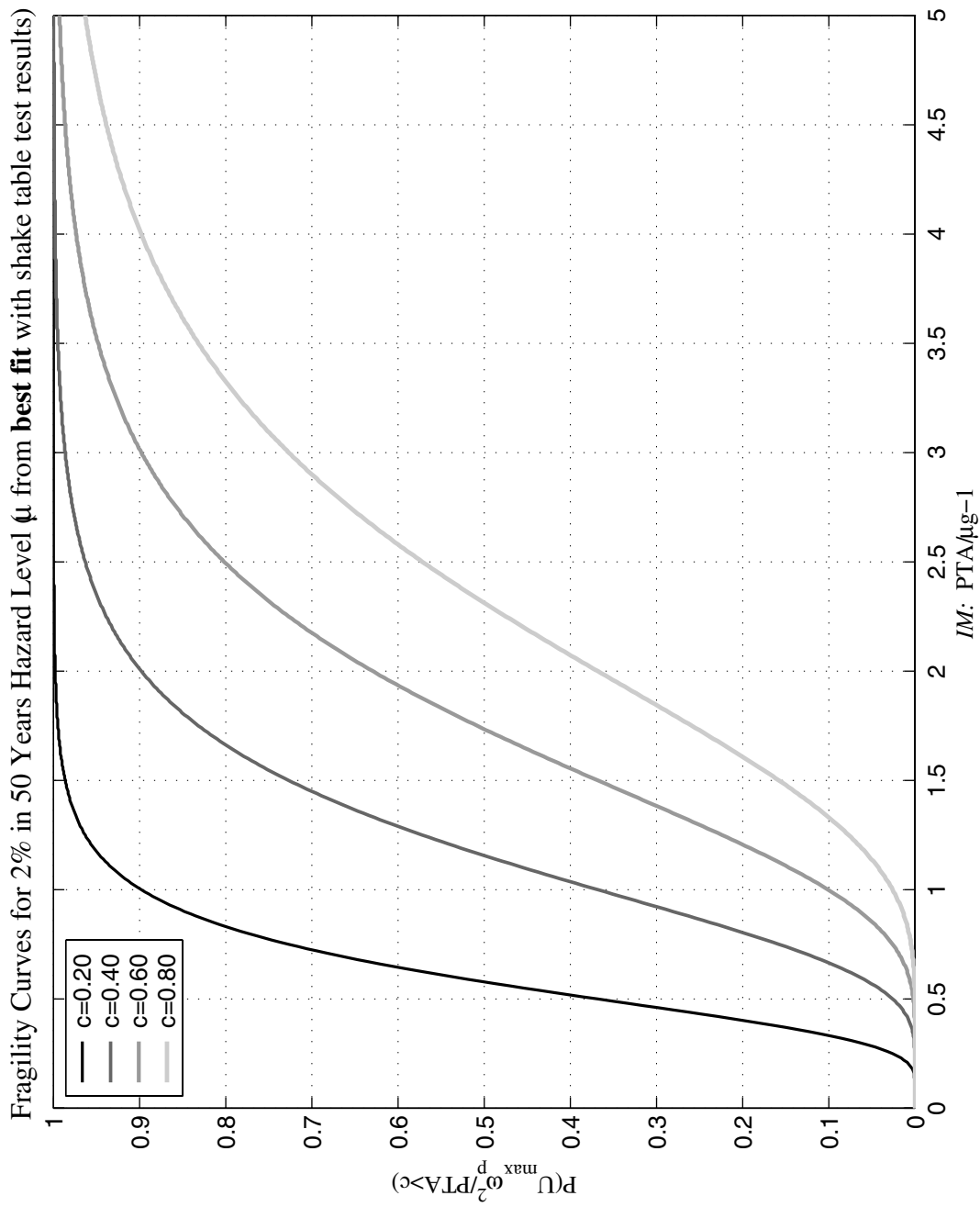


Figure 8.3 Fragility curves for various threshold limits, C . The curves are constructed based on the results obtained by *Working Model* simulations on the three pieces of equipment subjected to 2% in 50 years hazard level motions.

9 Shake Table Tests of Anchored Laboratory Equipment

9.1 ANCHORING OF LABORATORY EQUIPMENT

In order to simulate the conditions present in the UC Sciences laboratories a mock 12-ft-tall non-structural wall was built (Figs. 4.1 and 9.1) onto which the equipment was anchored with chains. The wall was built with light (20-gauge) steel studs and 5/8"-thick sheetrock. Figure 9.1 is a photograph of the ASP refrigerator anchored to the wall at a typical clearance distance of 8-10 in. The chains which are attached to the top of the equipment are intended to restrain the equipment from exhibiting excessive displacements or possible overturning during a seismic event. The top photograph of Figure 9.2 shows the detail of the connection to the wall. The chains are connected on one end to a light-gauge metal plate that is glued to the equipment surface with a urethane adhesive. On the other end, the chains are connected to a metal anchor that is screwed into the light steel framing of the wall. The chains are either cross-tied as shown in Figure 9.2 (top) or they go from the equipment straight to the nearest wall anchor. Both anchoring configurations were tested during the shake table tests.

No failure of the connection was observed in any of the shake table tests. Even after repeated tests, the connection appeared in good condition. Only minor local damage was observed in the relatively soft sheetrock. The bottom photograph of Figure 9.2 shows the condition of the connection after the cross-chained ASP refrigerator was subjected to the very violent shaking induced by the UC Science Building 6th Floor Motion for the Cholome Array #8 record of the 1966 Parkfield, California, earthquake. The slight depression which is evident in the sheetrock on one side of the connection was caused by the eccentricity of the load in the cross-tied chains. The connection held well for the remaining tests.

After completion of the shake table tests, static pull-out tests were performed in order to



Figure 9.1 The ASP refrigerator anchored to the mock non-structural wall that is nearly identical to those present at the UC Science laboratories.



Figure 9.2 The top photograph shows how the equipment is typically cross-chained to anchors that are screwed into the light steel framing of the wall. The bottom photograph shows the minor damage of the connection even under the very violent shaking induced by the UC Science Building 6th Floor Motion for the Cholome Array #8 record of the 1966 Parkfield, California, earthquake.

Table 9.1 Results of the static pull-out tests performed in order to determine the strength of the connection. Tabulated is the force on the chain required to fail the connection when the chain is (a) at a 15°-angle from the wall (*cross-chained*) and (b) perpendicular to the wall (*straight-chained*).

Test Number	<i>Cross-Chained</i>		<i>Straight-Chained</i>	
	Strength [lb.]		Strength [lb.]	
1	680		565	
2	720		585	
3	690		695	
4	750		625	
5	715		595	
6	680		620	
Average	705		615	
Std. Dev.	30		45	

determine the strength of the connection. Table 9.1 lists the results of the tests which were performed for the two configurations shown in the schematic diagrams.

9.2 SHAKE TABLE TESTS OF ANCHORED EQUIPMENT

The input motions used to test the freestanding equipment were also used to test the anchored equipment. The FORMA incubator was not tested anchored due to the damage it sustained in the earlier series of experiments. The Kelvinator refrigerator was tested with the chains cross-tied and straight-tied to the wall, while the ASP refrigerator was tested only cross-tied. The motion of the table was in the direction perpendicular to the wall.

The results of the shake table tests are presented in Table 9.2 which lists the recorded Peak Equipment Accelerations (*PEA*, i.e., the peak value of the vectorial sum of horizontal and vertical equipment acceleration histories) of the freestanding equipment from the tests presented in Chapter 4 together with the corresponding values of the anchored equipment. These results are also presented in Figure 9.3. The top bar plot of Figure 9.3 compares the recorded *PEA* of the Kelvinator refrigerator tested in the freestanding, cross-chained, and straight-chained configurations, while the bottom bar plot compares the recorded *PEA* of the ASP refrigerator tested in the free-

Table 9.2 Recorded Peak Equipment Acceleration (PEA) for the freestanding and anchored shake table tests on the Kelvinator and ASP refrigerators.

Earthquake	Record	Hazard Level	Equipment						
			KELVINATOR			ASP			
			PTA [g]	Free-standing PEA [g]	Cross-Chained PEA [g]	Straight-Chained PEA [g]	PTA [g]	Free-standing PEA [g]	Cross-Chained PEA [g]
Aigion, Greece 6/15/1995	OTE FP		0.76	0.47	1.57	1.76	0.86	0.54	0.61
Coyote Lake, California 8/6/1979	Gilroy Array #6 FN		0.69	0.43	3.22	3.25	0.73	0.52	0.49
Parkfield, California 6/27/1966	Cholome Array #8 FN GROUND	(50% in 50 yrs)	0.75	0.94	1.40	1.29	0.77	0.63	1.45
Parkfield, California 6/27/1966	Cholome Array #8 FN 6TH LEVEL	(50% in 50 yrs)	1.66	1.09	4.80	4.61	1.70	0.92	6.51
Coyote Lake, California 6/8/1979	Gilroy Array #6 FN GROUND	(50% in 50 yrs)	0.74	0.73	0.90	1.95	0.76	0.45	2.18
Coyote Lake, California 6/8/1979	Gilroy Array #6 FN 6TH LEVEL	(50% in 50 yrs)	0.76	0.59	3.28	3.47	0.77	0.55	3.41
Loma Prieta, California 10/17/1989	Gavilan College FN GROUND	(10% in 50 yrs)	0.76	0.63	1.99	1.50	0.77	0.61	3.28
Loma Prieta, California 10/17/1989	Gavilan College FN 6TH LEVEL	(10% in 50 yrs)	0.64	0.63	2.49	2.15	0.67	0.43	3.44
Tottori, Japan 10/6/2000	Kofu FN GROUND	(10% in 50 yrs)	1.09	2.85	3.50	2.87	1.08	0.69	4.96
Tottori, Japan 10/6/2000	Kofu FN 6TH LEVEL	(10% in 50 yrs)	0.81	1.68	2.64	2.07	0.87	0.83	3.77

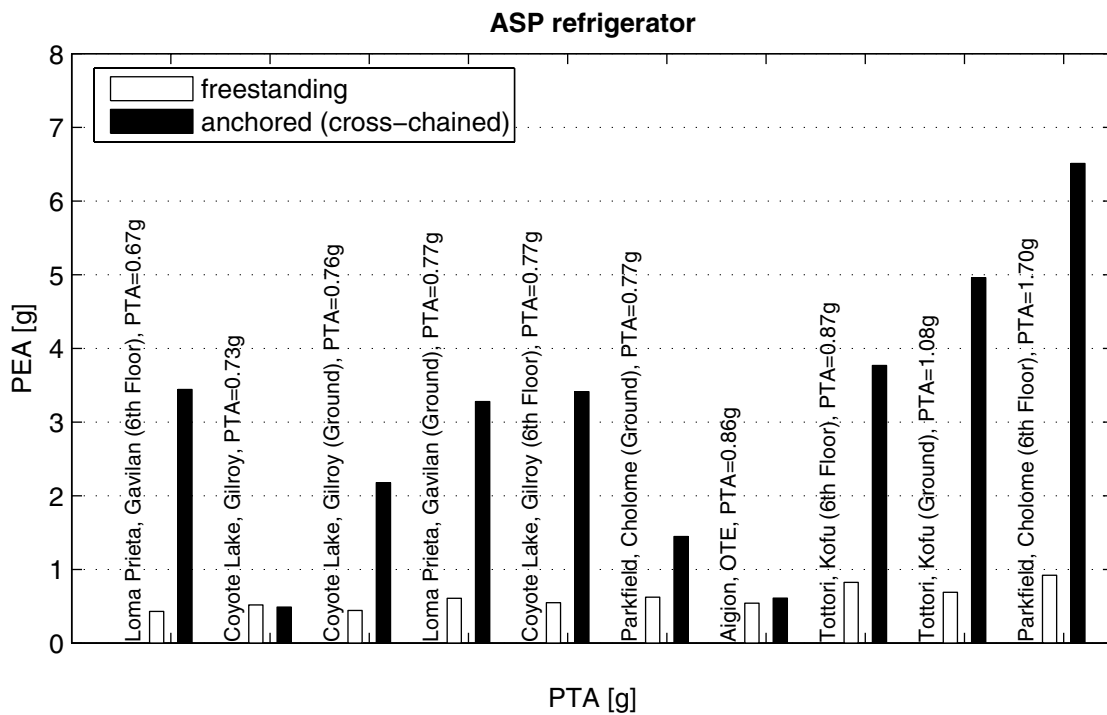
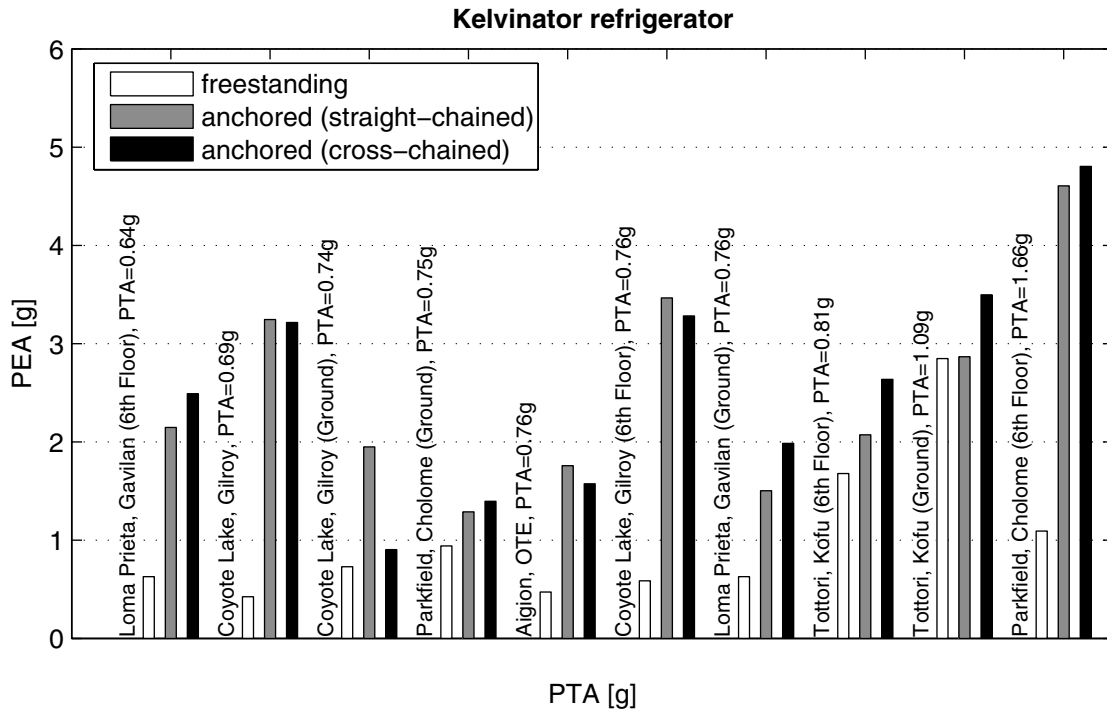
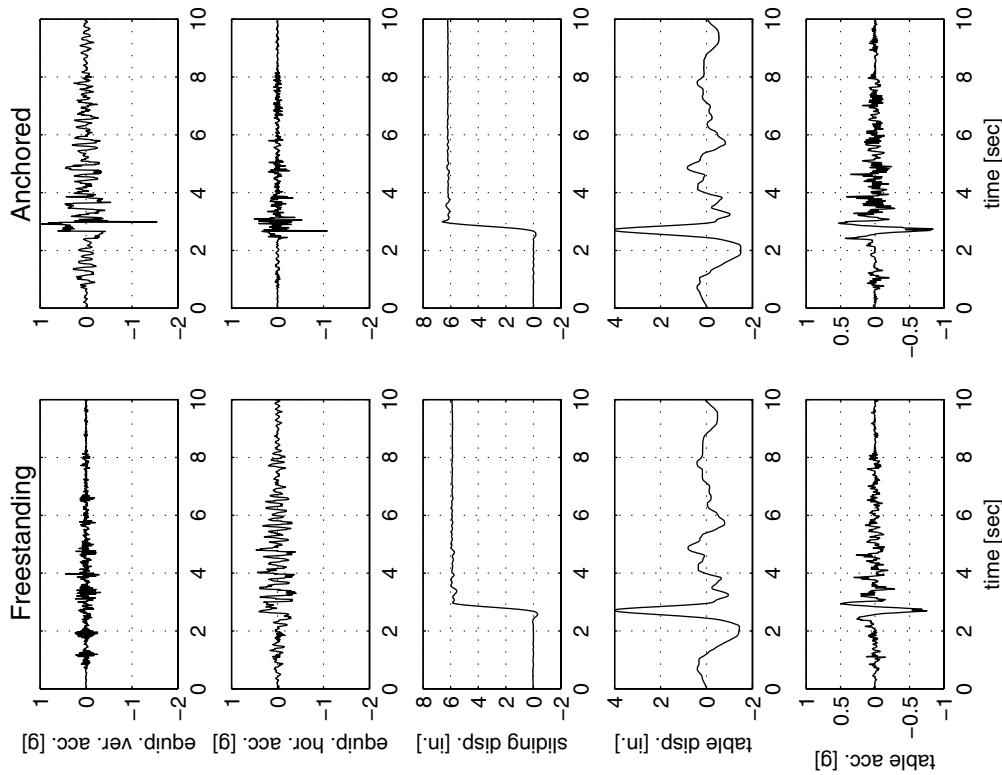


Figure 9.3 Comparison between recorded Peak Equipment Acceleration (PEA) for the Kelvinator and ASP refrigerator in freestanding and anchored configurations.

standing and cross-chained configurations. The recorded values of *PEA* for the anchored equipment were considerably higher in all instances but one. In fact, in several instances the *PEA* of the restrained equipment exceeded 700% that of the freestanding equipment.

The left side of Figure 9.4 plots the horizontal and vertical acceleration histories of the freestanding and anchored (cross-chained) Kelvinator refrigerator subjected to the OTE FP motion recorded during the 1995 Aigion, Greece, earthquake. The *PEA* is more than three times larger when the refrigerator is restrained (1.57g) than when it is freestanding (0.47g). The right side of Figure 9.4, which plots the acceleration histories of the freestanding and anchored Kelvinator refrigerator subjected to the to the Gilroy Array #6 FN motion of the 1979 Coyote Lake, California, earthquake, shows that the *PEA* of the anchored refrigerator is 3.22g, or 7.5 times larger than the *PEA* of the freestanding equipment (0.43g). The time histories of the equipment horizontal and vertical accelerations show the large acceleration spikes that develop when the chains become taut. As aforementioned, these large accelerations may be very damaging to the sensitive contents of the equipment. Figures 9.5 to 9.18 which plot side-by-side the response of the freestanding and anchored equipment for the remaining motions used in this study demonstrate the significant increase in equipment accelerations that results from restraining the equipment.

equipment: Kelvinator refrigerator (cross-chained)
 motion: Aigion, OTE FP



equipment: Kelvinator refrigerator (cross-chained)
 motion: Coyote Lake, Gilroy Array #6 FN

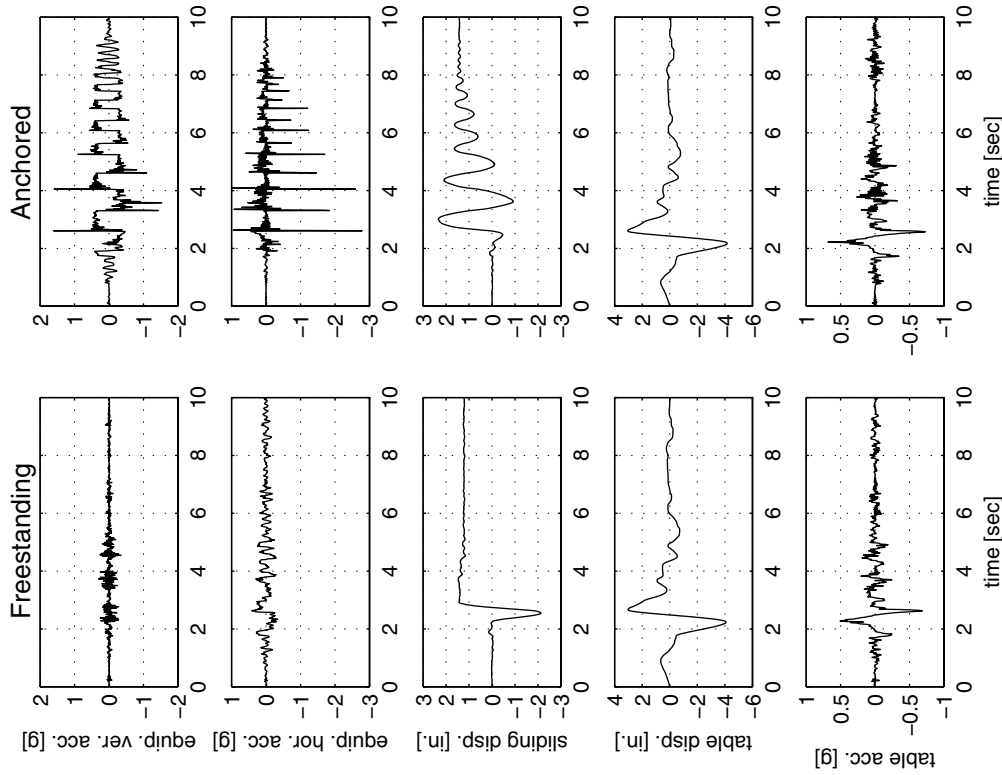
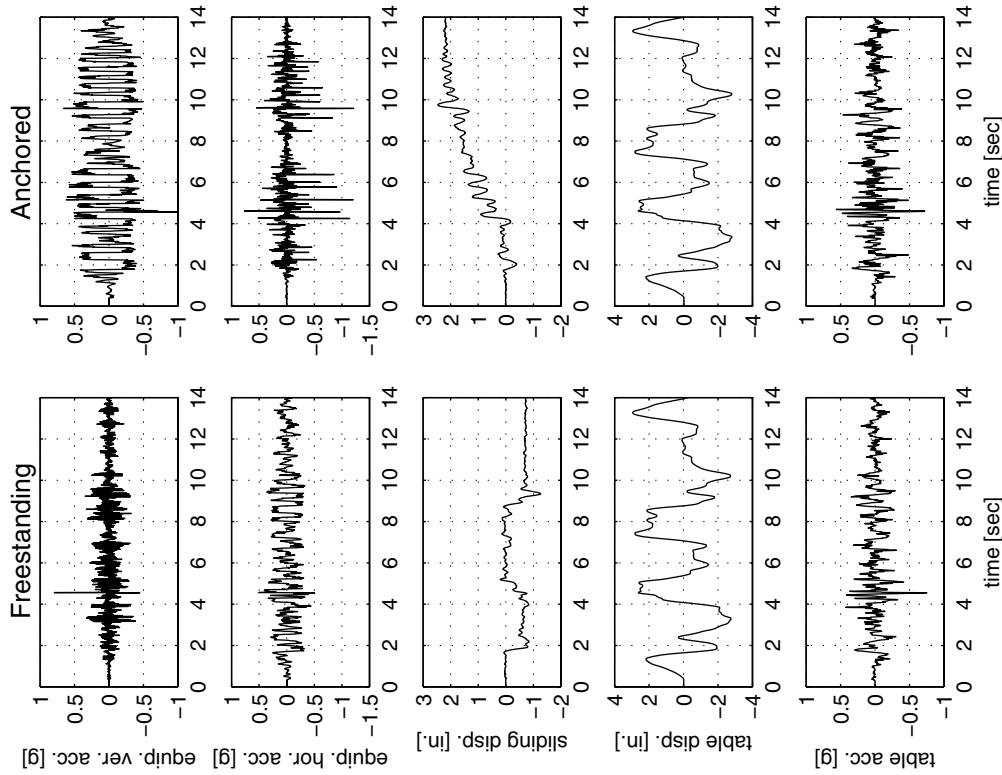


Figure 9.4 Shake table test results of the freestanding and anchored (cross-chained) Kelvinator refrigerator subjected to the OTE FP motion recorded during the 1995 Aigion, Greece, earthquake (left) and to the Gilroy Array #6 FN motion recorded during the 1979 Coyote Lake, California, earthquake (right).

equipment: Kelvinator refrigerator (cross-chained)
 motion: Parkfield, Cholome Array #8 FN Ground (50% in 50 yrs)



equipment: Kelvinator refrigerator (cross-chained)
 motion: Parkfield, Cholome Array #8 FN 6th Floor (50% in 50 yrs)

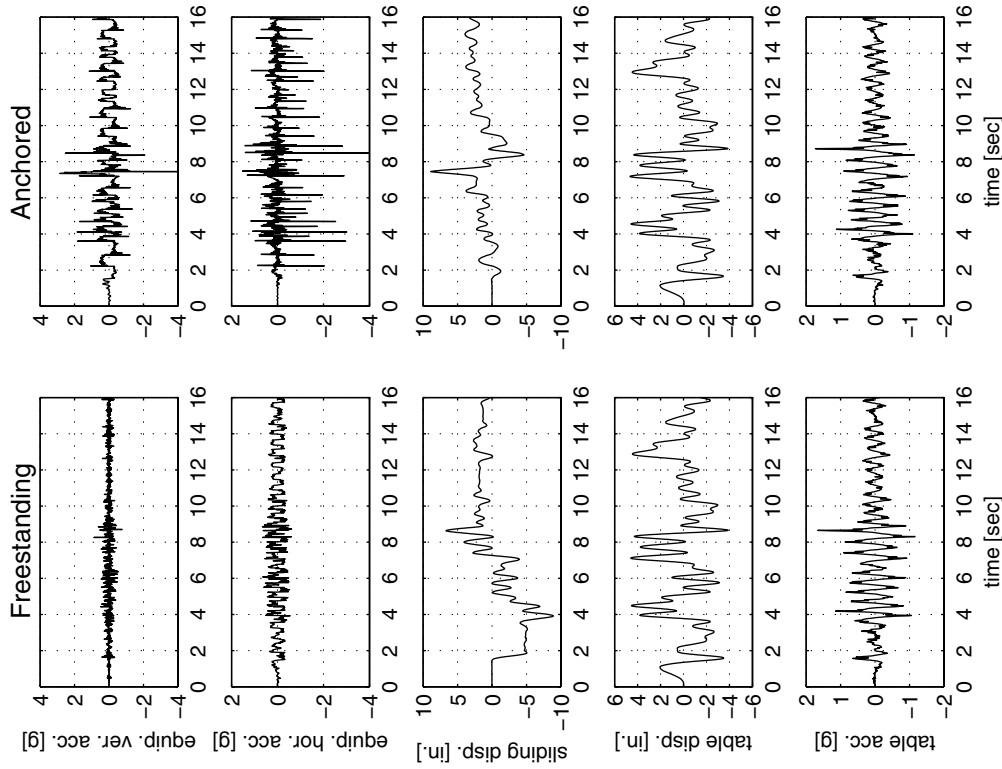
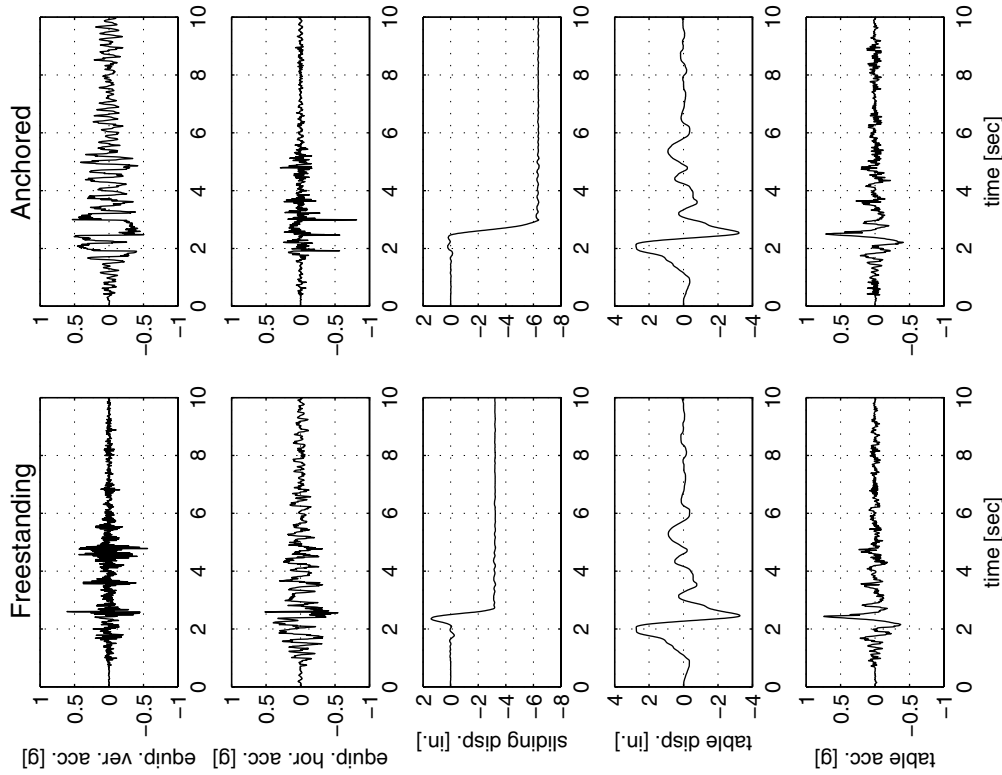


Figure 9.5 Shake table test results of the freestanding and anchored (cross-chained) Kelvinator refrigerator subjected to the Cholome Array #8 FN (50% in 50 years) ground motion recorded during the 1966 Parkfield, California, earthquake (left) and to its corresponding UC Science Building 6th floor motion (right).

equipment: Kelvinator refrigerator (cross-chained)
 motion: Coyote Lake, Gilroy Array #6 FN Ground (50% in 50 yrs)



equipment: Kelvinator refrigerator (cross-chained)
 motion: Coyote Lake, Gilroy Array #6 FN 6th Floor (50% in 50 yrs)

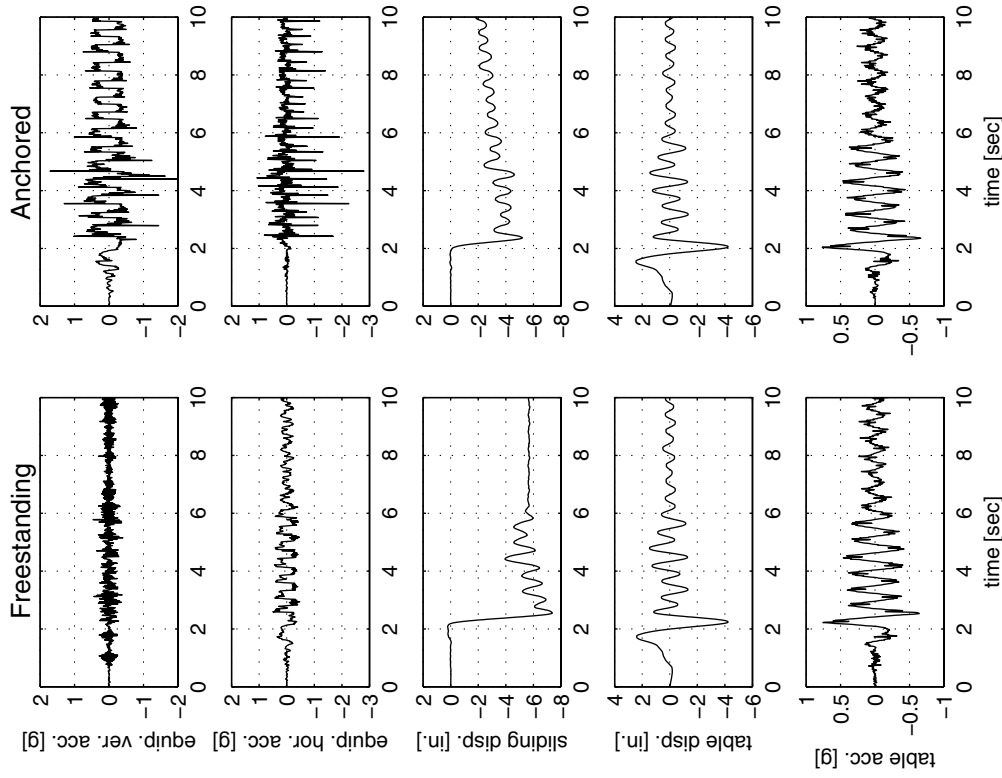
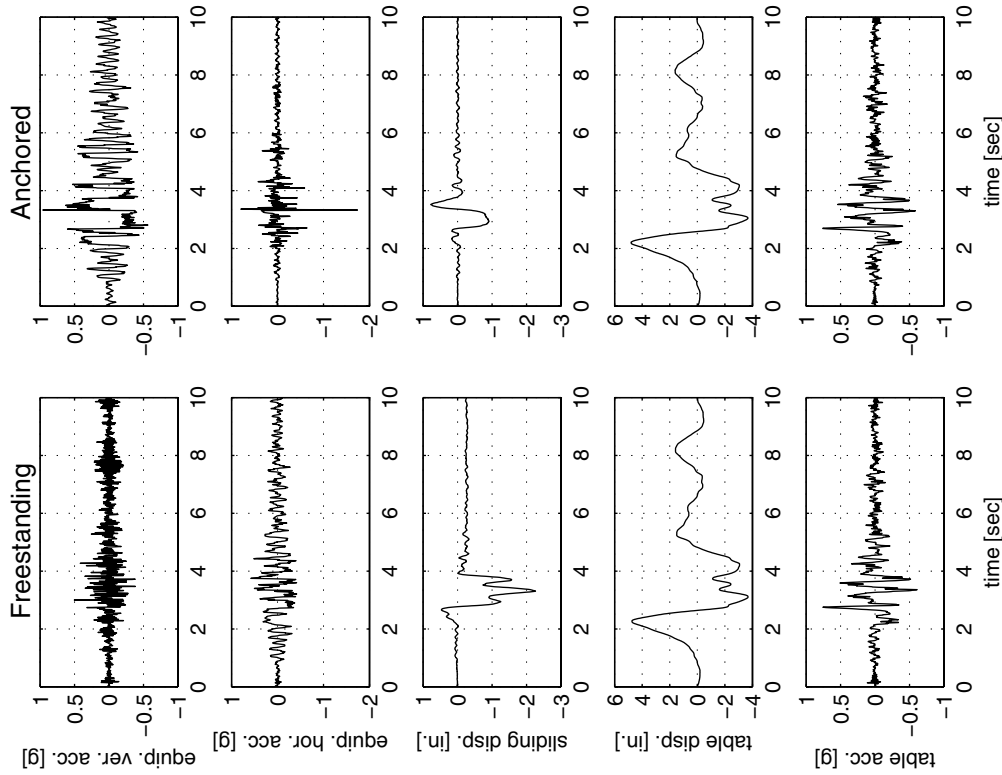


Figure 9.6 Shake table test results of the freestanding and anchored (cross-chained) Kelvinator refrigerator subjected to the Gilroy Array #6 FN (50% in 50 years) ground motion recorded during the 1979 Coyote Lake, California, earthquake (left) and to its corresponding UC Science Building 6th floor motion (right).

equipment: Kelvinator refrigerator (cross-chained)
 motion: Loma Prieta, Gavilan College FN Ground (10% in 50 yrs)



equipment: Kelvinator refrigerator (cross-chained)
 motion: Loma Prieta, Gavilan College FN 6th Floor (10% in 50 yrs)

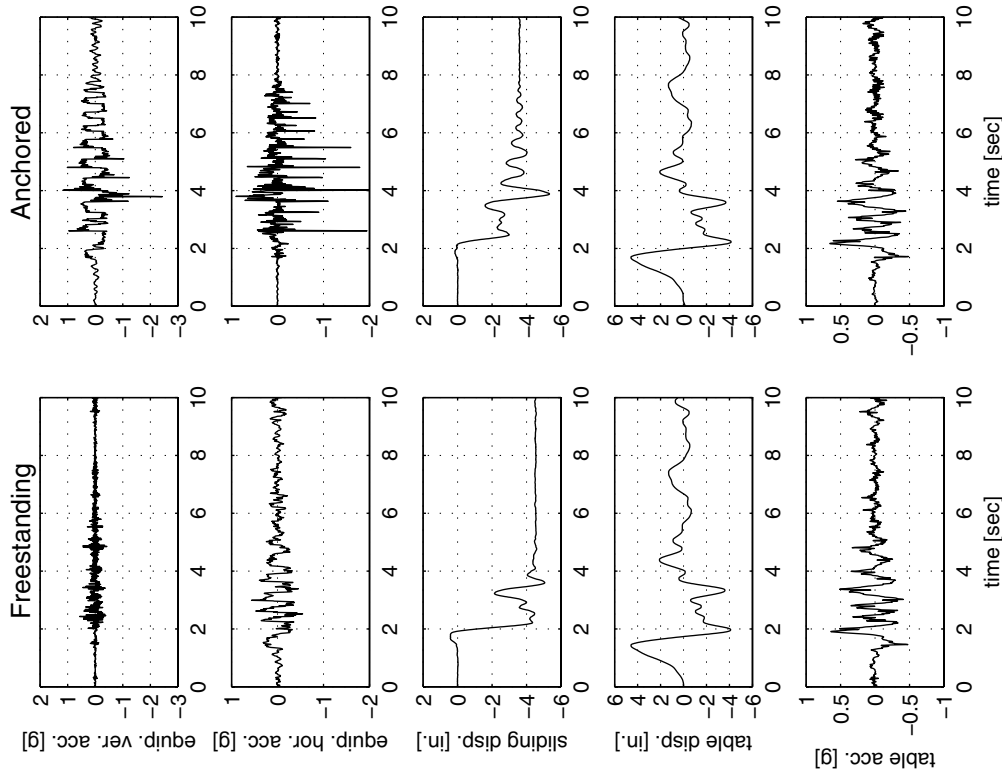
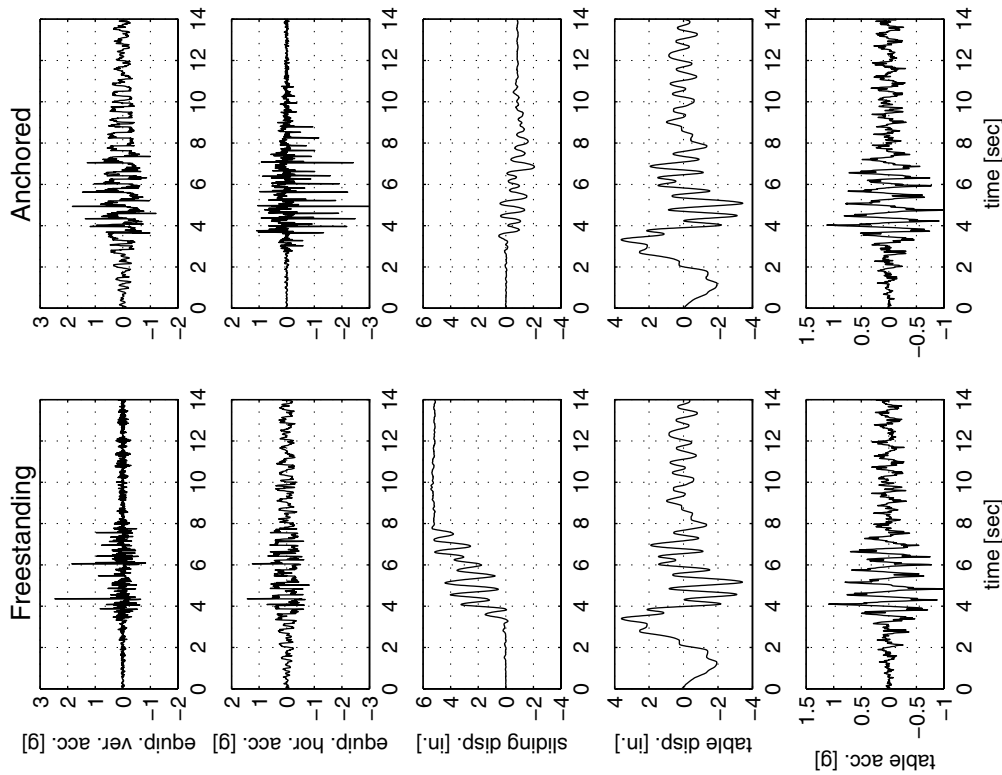


Figure 9.7 Shake table test results of the freestanding and anchored (cross-chained) Kelvinator refrigerator subjected to the Gavilan College FN (10% in 50 yrs) ground motion recorded during the 1989 Loma Prieta, California, earthquake (left) and to its corresponding UC Science Building 6th floor motion (right).

equipment: Kelvinator refrigerator (cross-chained)
 motion: Tottori, Kofu FN Ground (10% in 50 yrs)



equipment: Kelvinator refrigerator (cross-chained)
 motion: Tottori, Kofu FN 6th Floor (10% in 50 yrs)

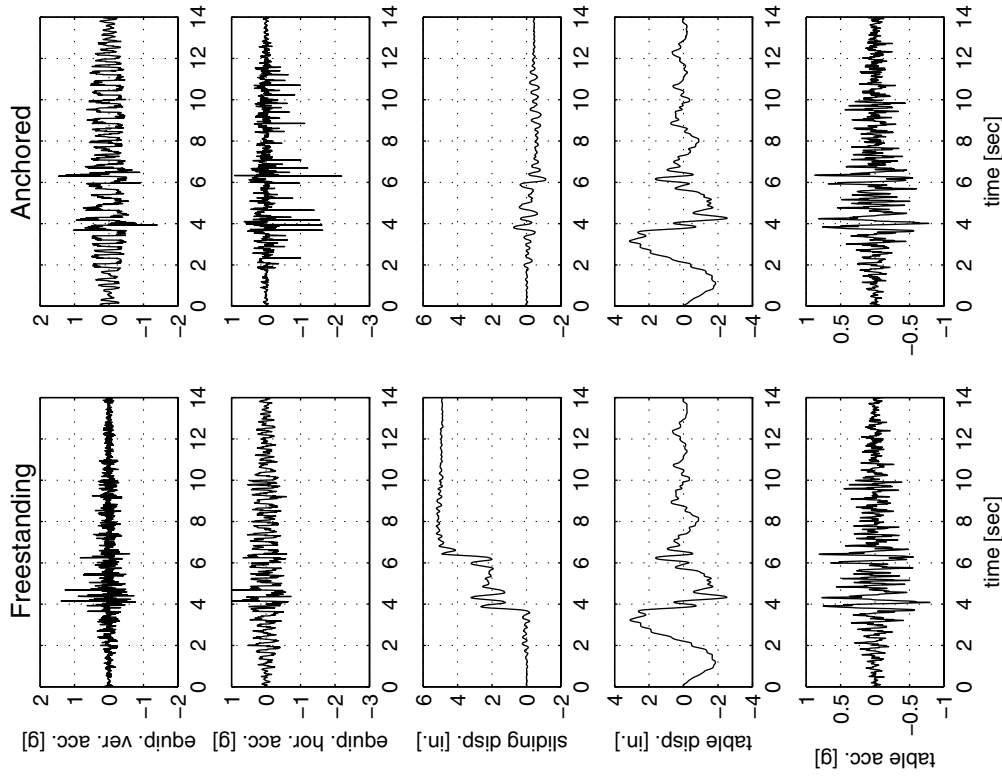
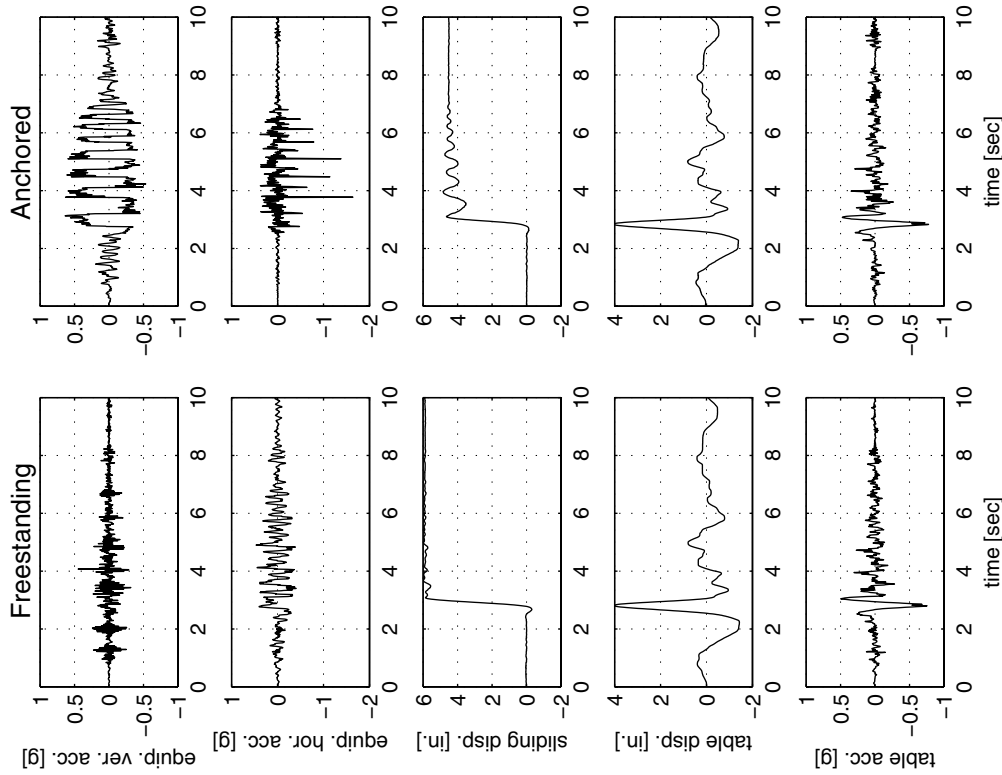


Figure 9.8 Shake table test results of the freestanding and anchored (cross-chained) Kelvinator refrigerator subjected to the Kofu FN (10% in 50 years) ground motion recorded during the 2000 Tottori, Japan, earthquake (left) and to its corresponding UC Science Building 6th floor motion (right).

equipment: Kelvinator refrigerator (straight-chained)
 motion: Aigion, OTE FP



equipment: Kelvinator refrigerator (straight-chained)
 motion: Coyote Lake, Gilroy Array #6 FN

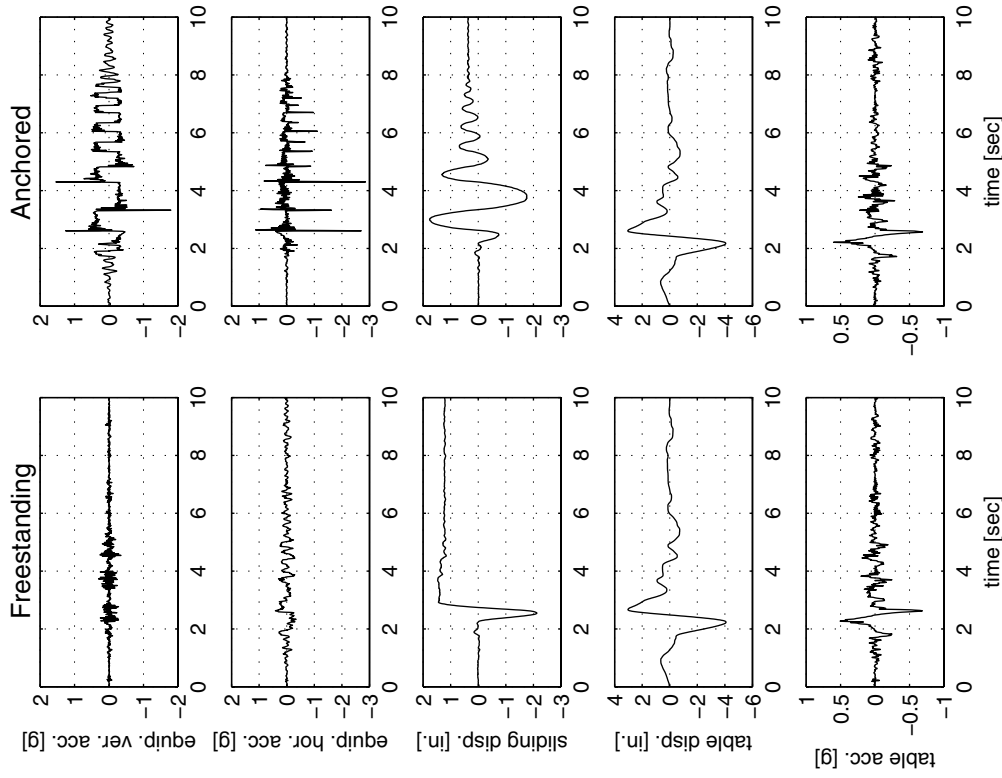
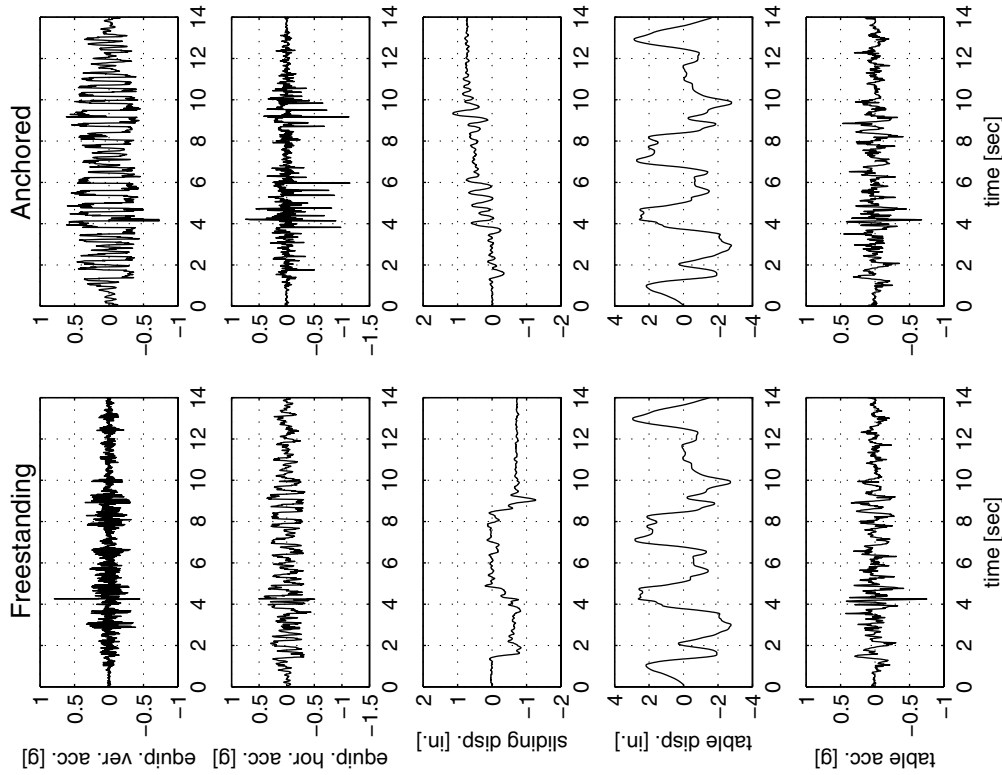


Figure 9.9 Shake table test results of the freestanding and anchored (straight-chained) Kelvinator refrigerator subjected to OTE FP motion recorded during the 1995 Aigion, Greece, earthquake (left) and to the Gilroy Array #6 FN motion recorded during the 1979 Coyote Lake, California, earthquake (right).

equipment: Kelvinator refrigerator (straight-chained)
 motion: Parkfield, Cholome Array #8 FN Ground (50% in 50 yrs)



equipment: Kelvinator refrigerator (straight-chained)
 motion: Parkfield, Cholome Array #8 FN 6th Floor (50% in 50 yrs)

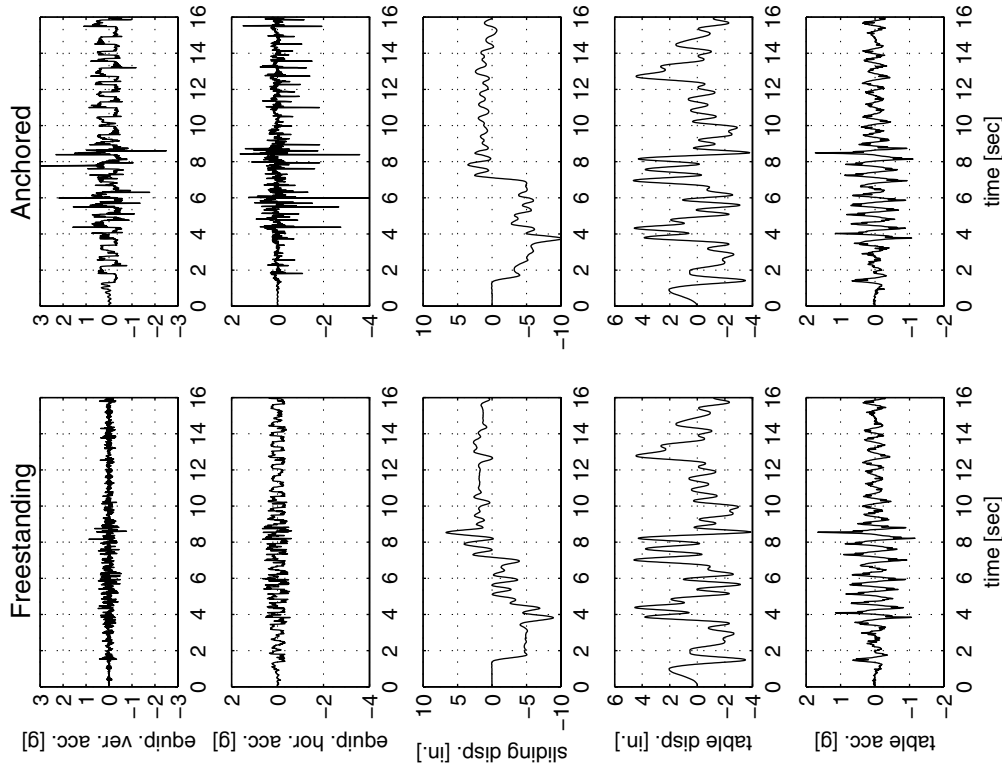
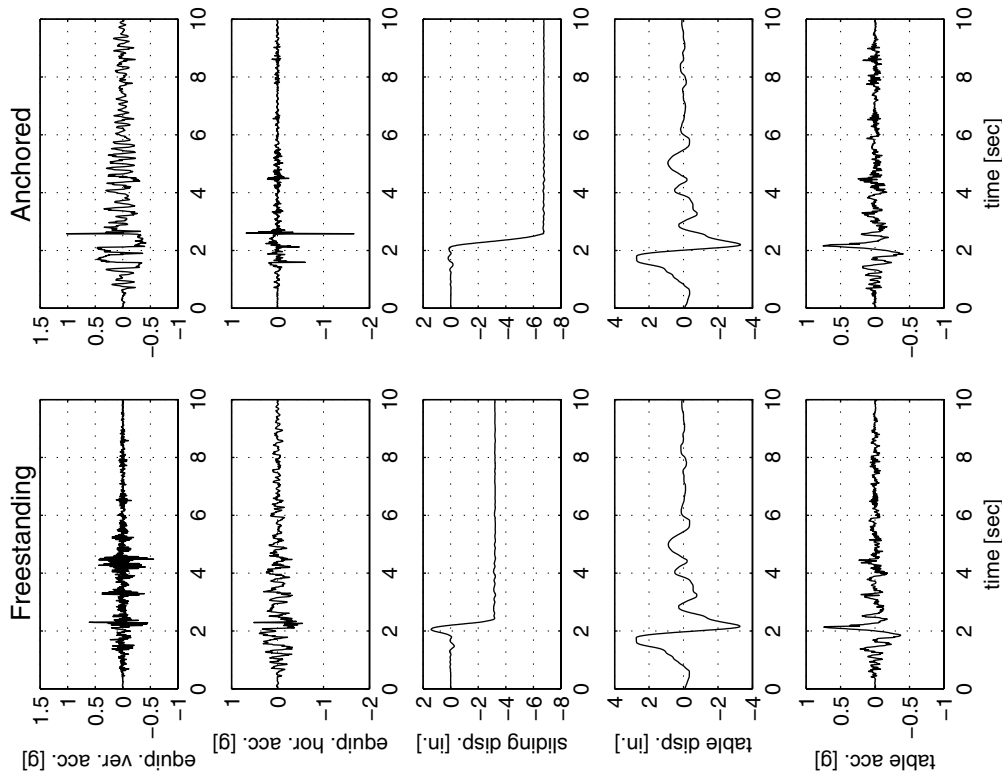


Figure 9.10 Shake table test results of the freestanding and anchored (straight-chained) Kelvinator refrigerator subjected to the Cholome Array #8 FN (50% in 50 years) ground motion recorded during the 1966 Parkfield, California, earthquake (left) and to its corresponding UC Science Building 6th floor motion (right).

equipment: Kelvinator refrigerator (straight-chained)
 motion: Coyote Lake, Gilroy Array #6 FN Ground (50% in 50 yrs)



equipment: Kelvinator refrigerator (straight-chained)
 motion: Coyote Lake, Gilroy Array #6 FN 6th Floor (50% in 50 yrs)

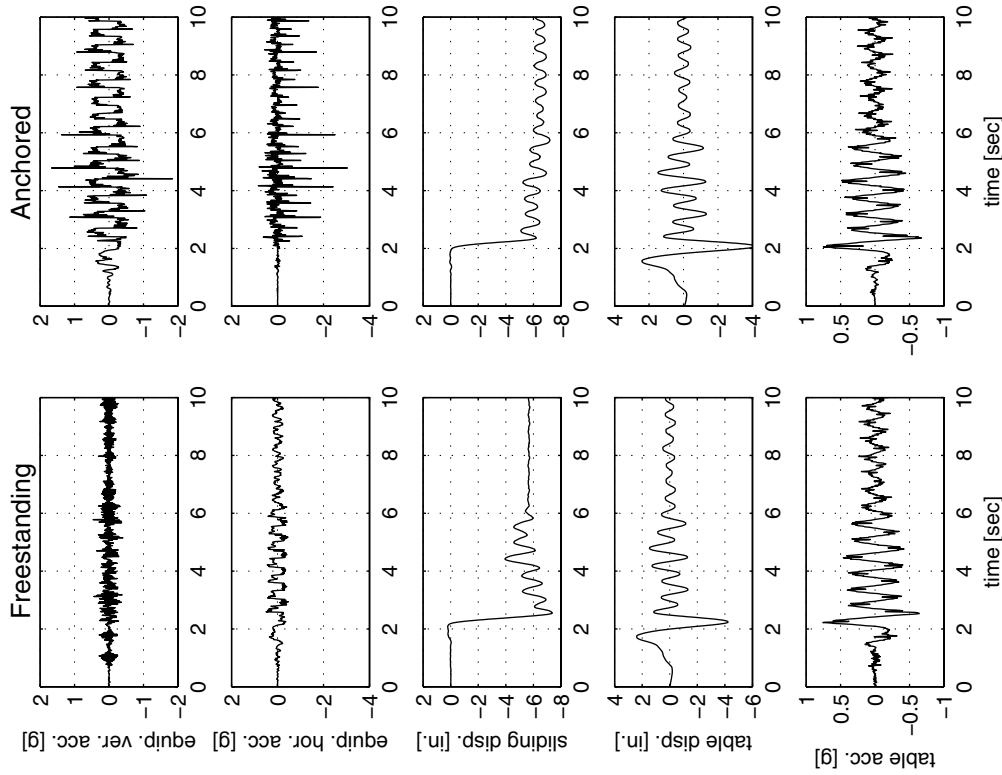
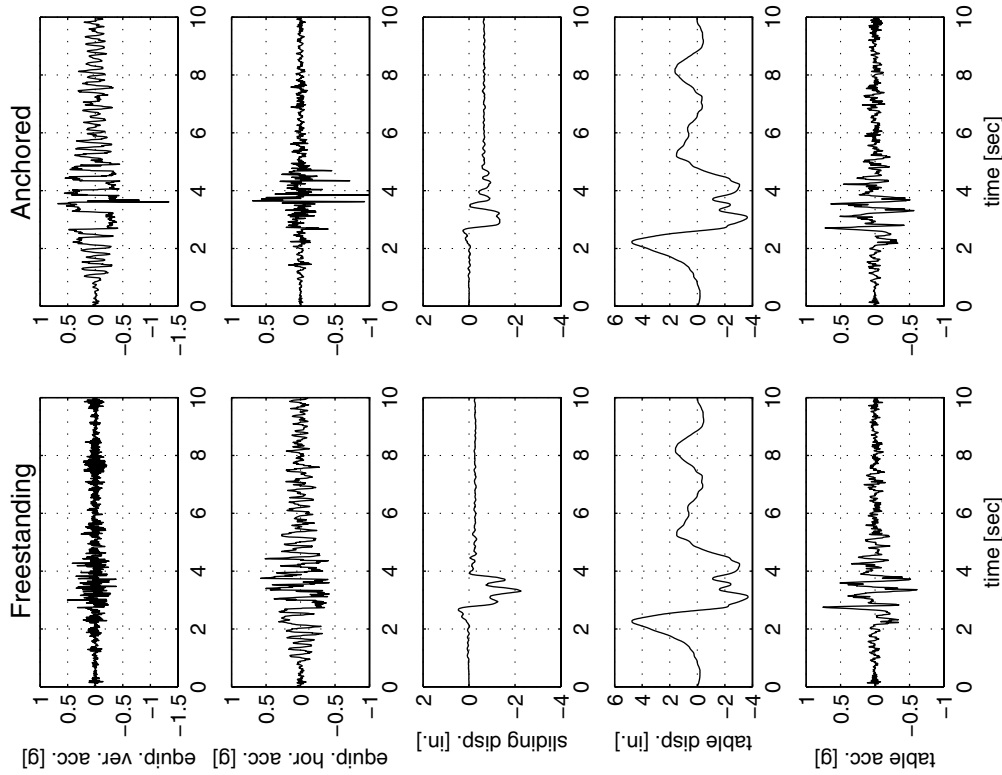


Figure 9.11 Shake table test results of the freestanding and anchored (straight-chained) Kelvinator refrigerator subjected to the Gilroy Array #6 FN (50% in 50 years) ground motion recorded during the 1979 Coyote Lake, California, earthquake (left) and to its corresponding UC Science Building 6th floor motion (right).

equipment: Kelvinator refrigerator (straight-chained)
 motion: Loma Prieta, Gavilan College FN Ground (10% in 50 yrs)



equipment: Kelvinator refrigerator (straight-chained)
 motion: Loma Prieta, Gavilan College FN 6th Floor (10% in 50 yrs)

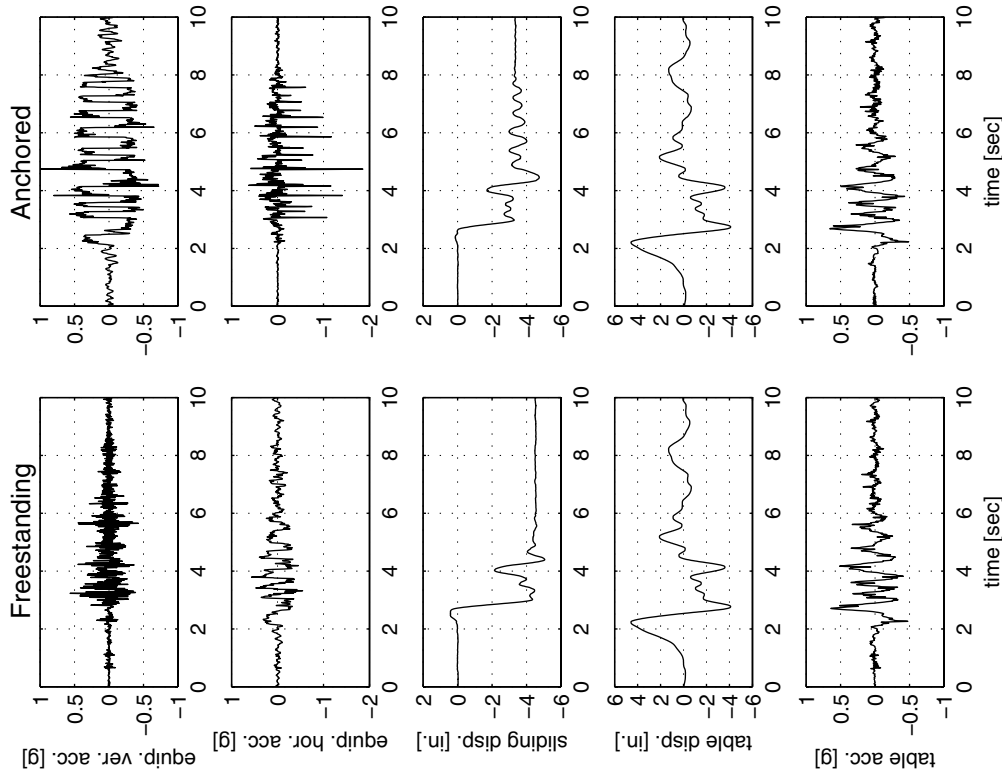
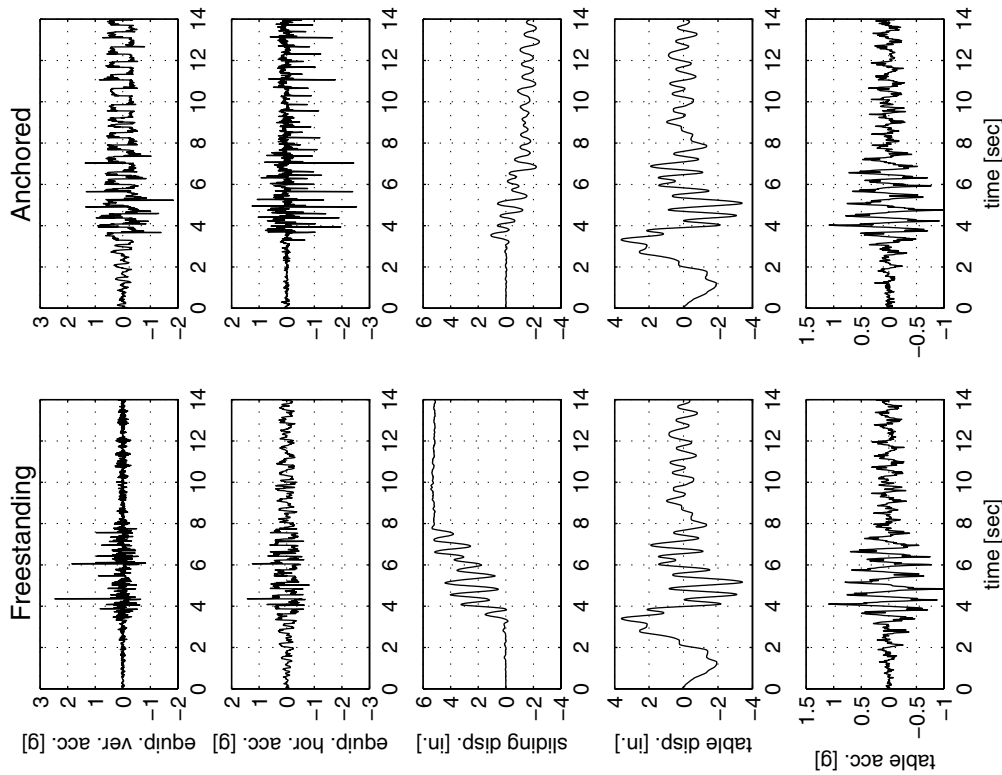


Figure 9.12 Shake table test results of the freestanding and anchored (straight-chained) Kelvinator refrigerator subjected to the Gavilan College FN (10% in 50 yrs) ground motion recorded during the 1989 Loma Prieta, California, earthquake (left) and to its corresponding UC Science Building 6th floor motion (right).

equipment: Kelvinator refrigerator (straight-chained)
 motion: Tottori, Kofu FN Ground (10% in 50 yrs)



equipment: Kelvinator refrigerator (straight-chained)
 motion: Tottori, Kofu FN 6th Floor (10% in 50 yrs)

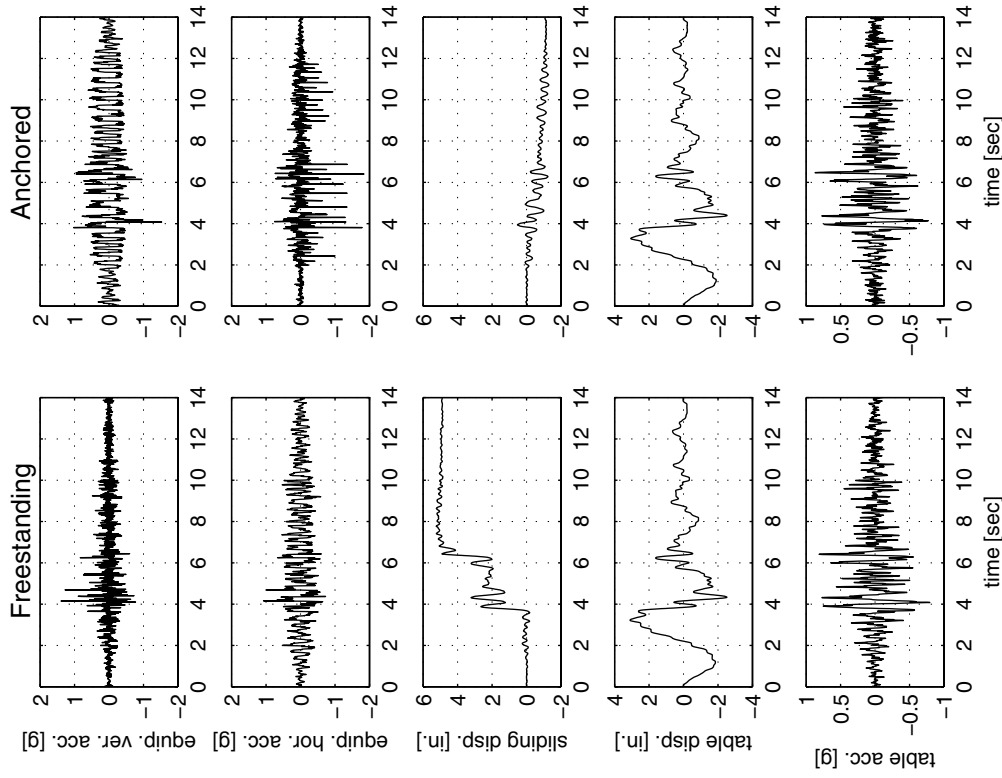
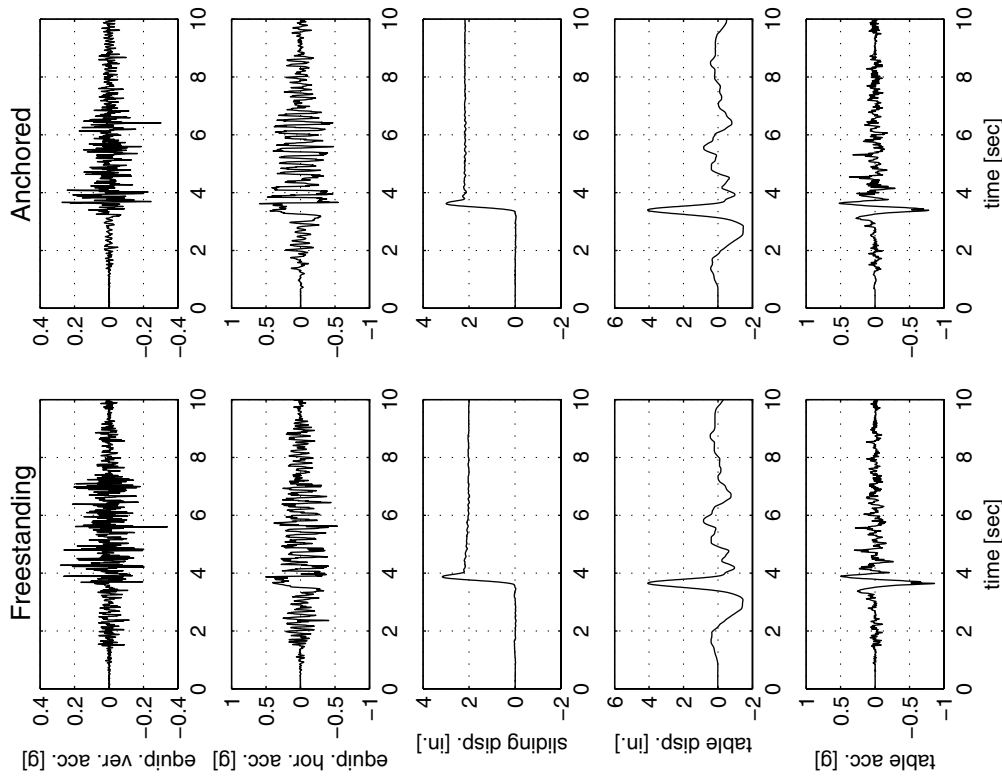


Figure 9.13 Shake table test results of the freestanding and anchored (straight-chained) Kelvinator refrigerator subjected to the Kofu FN (10% in 50 yrs) ground motion recorded during the 2000 Tottori, Japan, earthquake (left) and to its corresponding UC Science Building 6th floor motion (right).

equipment: ASP refrigerator
 motion: Aigion, OTE FP



equipment: ASP refrigerator
 motion: Coyote Lake, Gilroy Array #6 FN

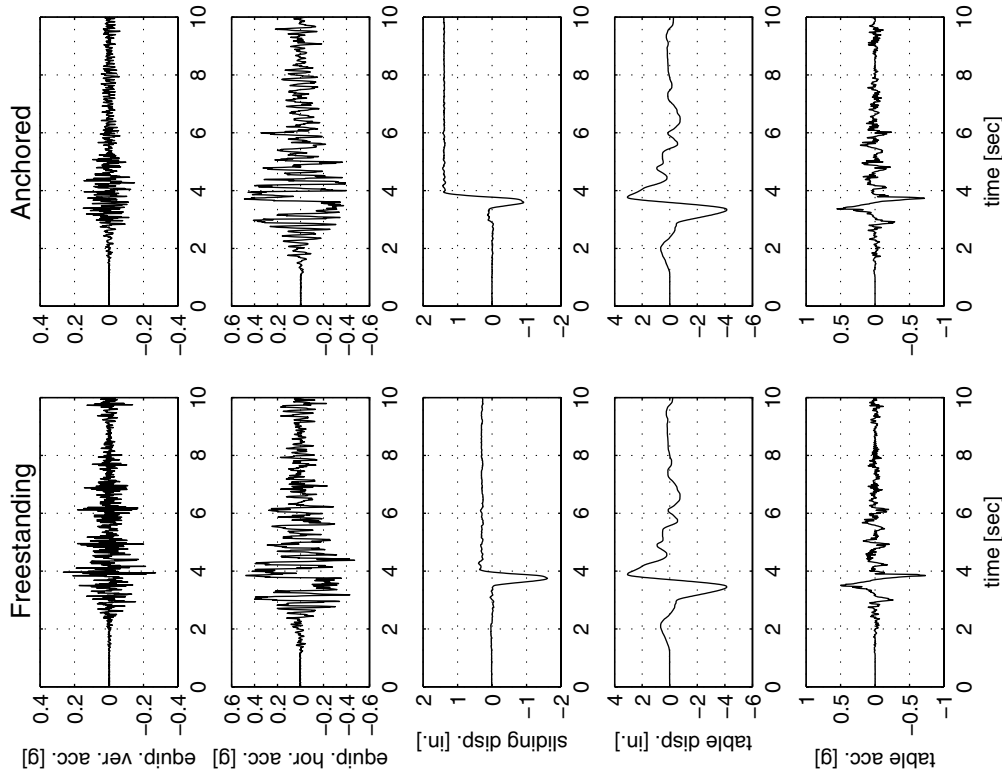


Figure 9.14 Shake table test results of the freestanding and anchored (cross-chained) ASP refrigerator subjected to OTE FP motion recorded during the 1995 Aigion, Greece, earthquake (left) and to the Gilroy Array #6 FN motion recorded during the 1979 Coyote Lake, California, earthquake (right).

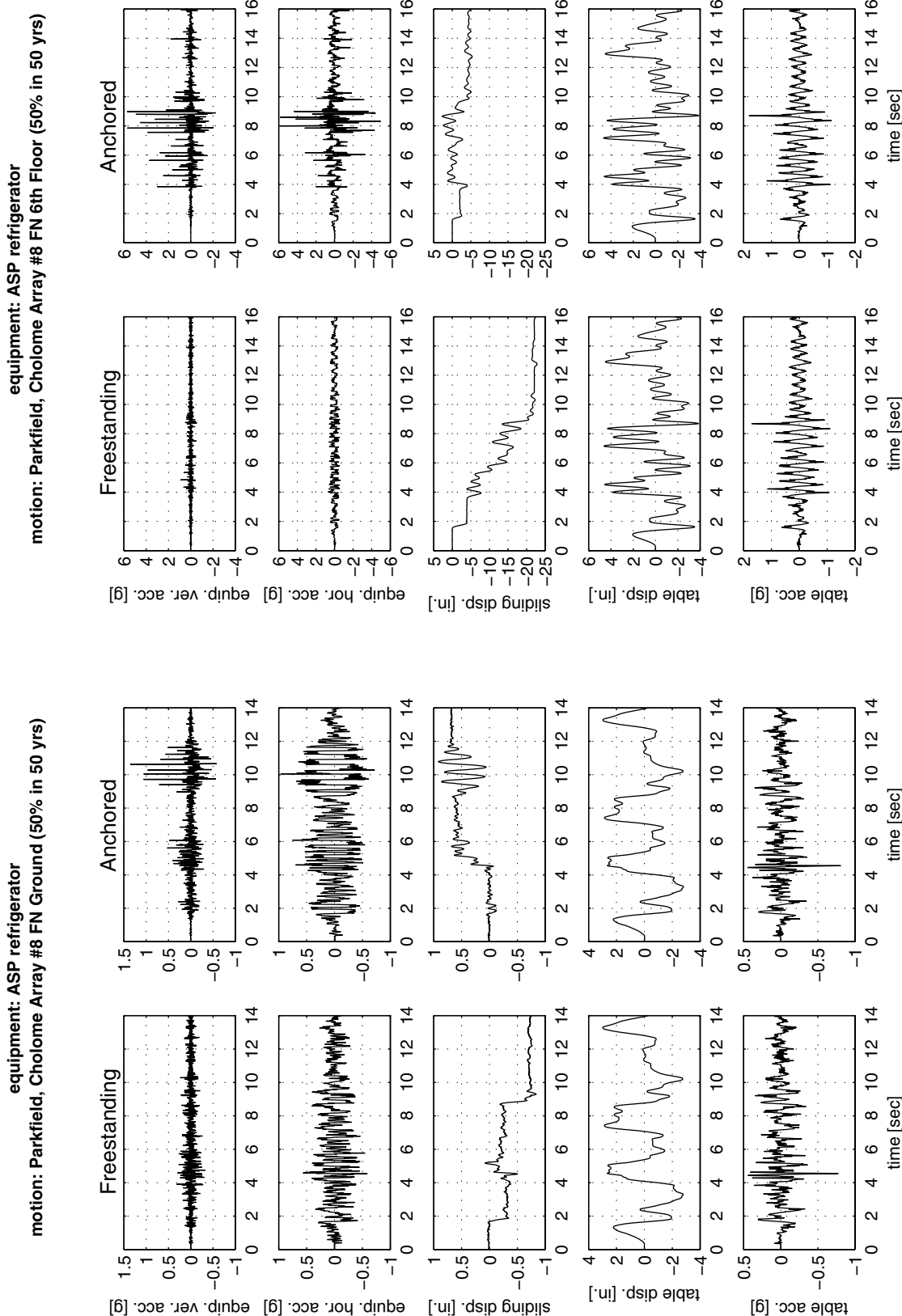
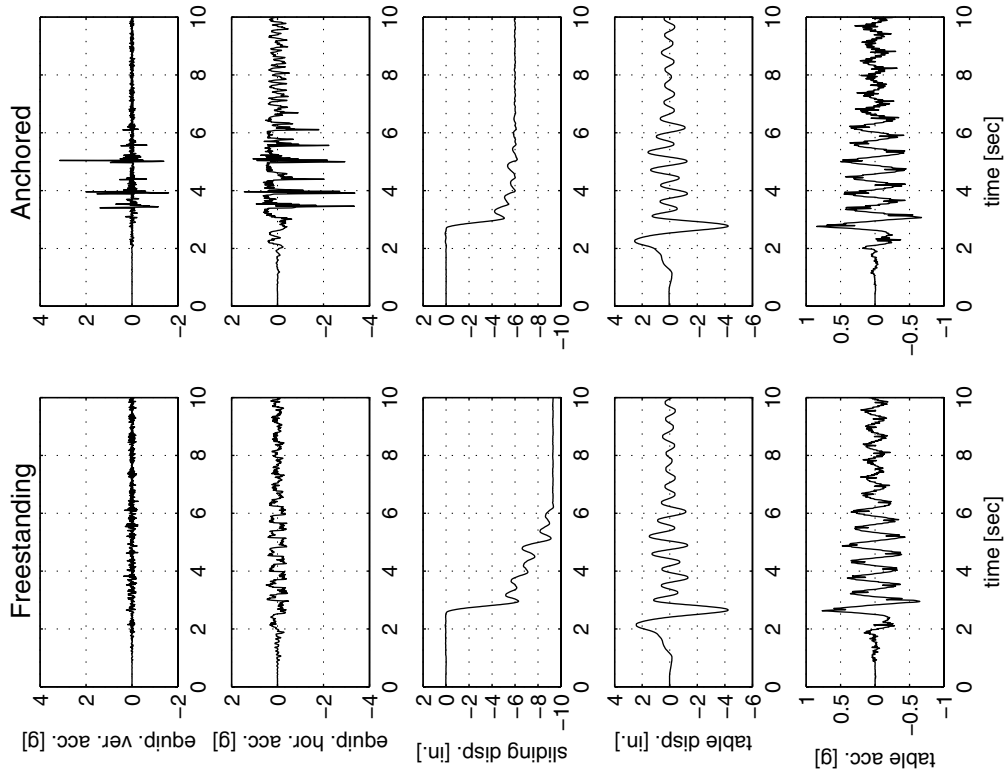


Figure 9.15 Shake table test results of the freestanding and anchored (cross-chained) ASP refrigerator subjected to the Cholome Array #8 FN (50% in 50 years) ground motion recorded during the 1966 Parkfield, California, earthquake (left) and to its corresponding UC Science Building 6th floor motion (right).

equipment: ASP refrigerator
 motion: Coyote Lake, Gilroy Array #6 FN 6th Floor (50% in 50 yrs)



equipment: ASP refrigerator
 motion: Coyote Lake, Gilroy Array #6 FN Ground (50% in 50 yrs)

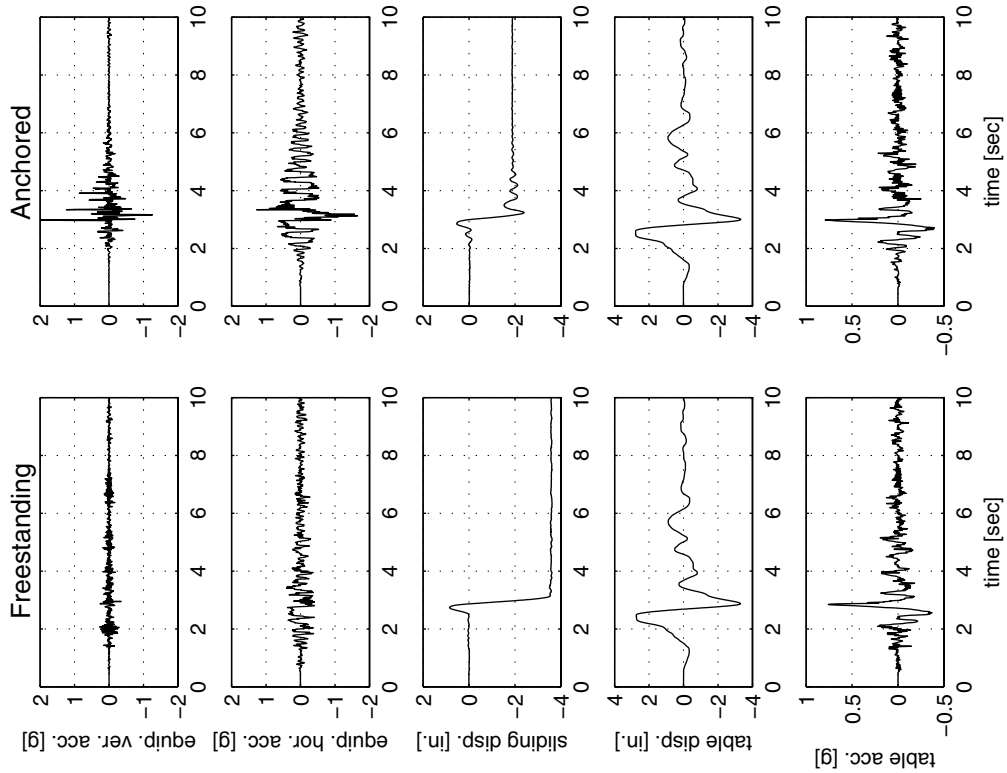
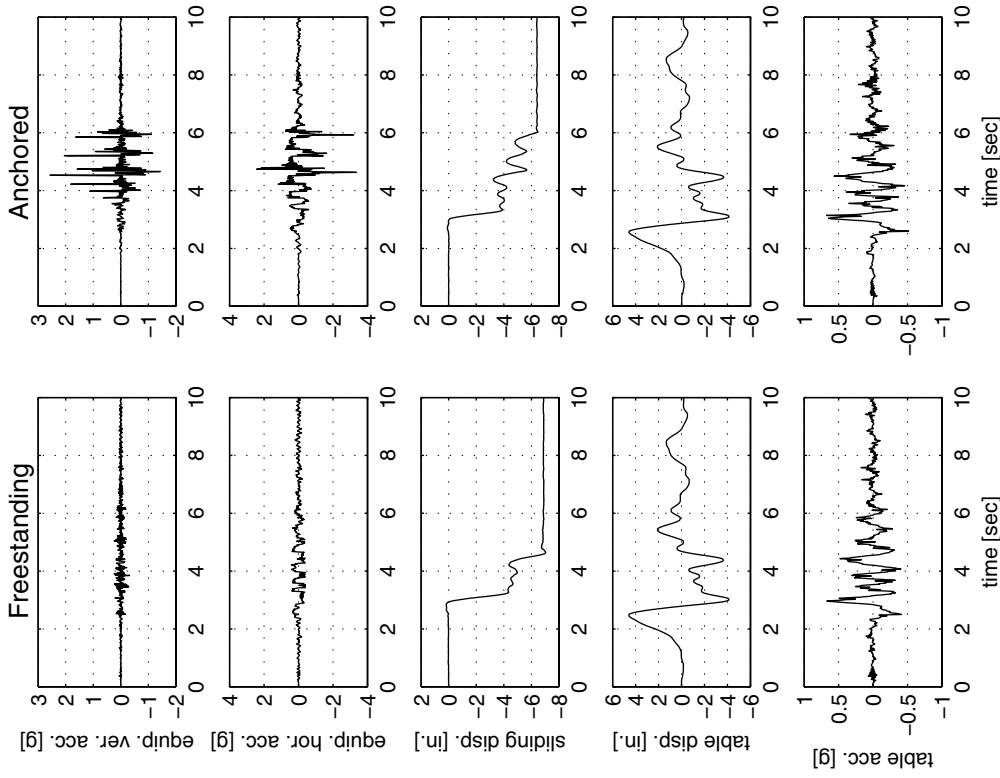


Figure 9.16 Shake table test results of the freestanding and anchored (cross-chained) ASP refrigerator subjected to the Gilroy Array #6 FN (50% in 50 yrs) ground motion recorded during the 1979 Coyote Lake, California, earthquake (left) and to its corresponding UC Science Building 6th floor motion (right).

equipment: ASP refrigerator
 motion: Loma Prieta, Gavilan College FN 6th Floor (10% in 50 yrs)



equipment: ASP refrigerator
 motion: Loma Prieta, Gavilan College FN Ground (10% in 50 yrs)

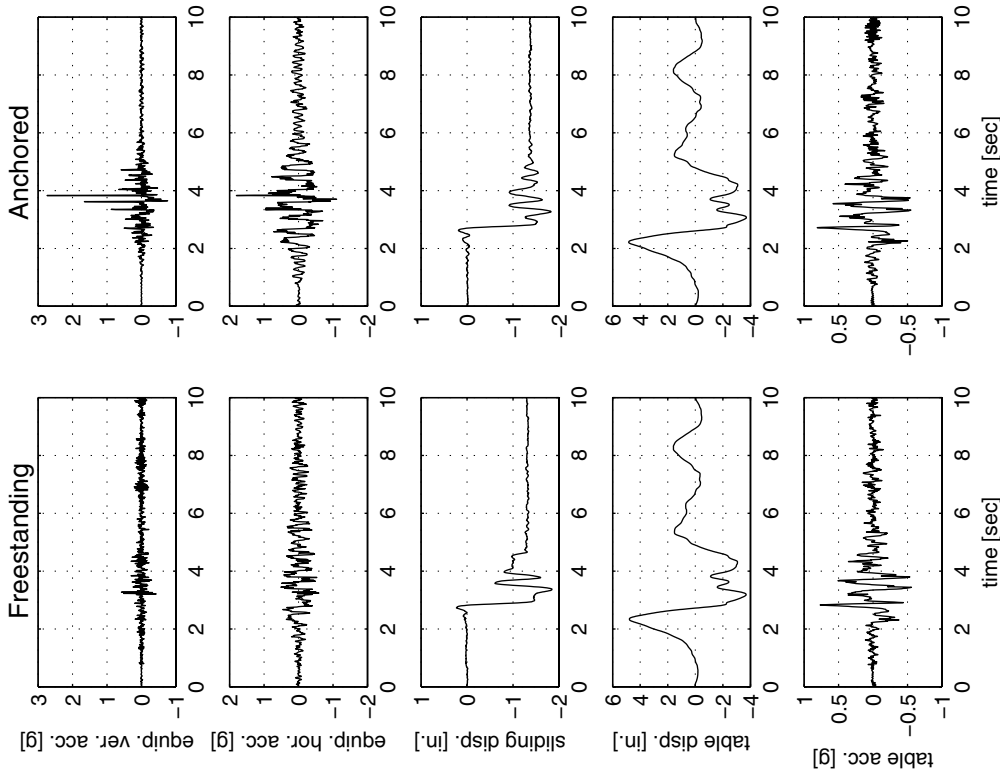
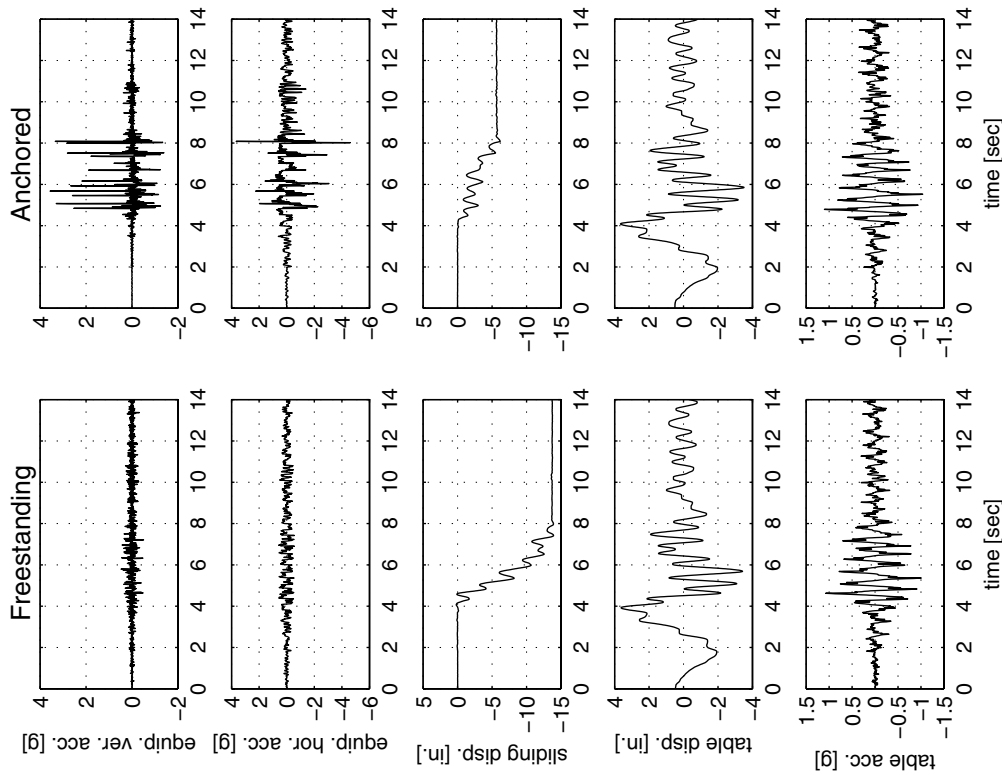


Figure 9.17 Shake table test results of the freestanding and anchored (cross-chained) ASP refrigerator subjected to the Gavilan College FN (10% in 50 years) ground motion recorded during the 1989 Loma Prieta, California, earthquake (left) and to its corresponding UC Science Building 6th floor motion (right).

equipment: ASP refrigerator
 motion: Tottori, Kofu FN Ground (10% in 50 yrs)



equipment: ASP refrigerator
 motion: Tottori, Kofu FN 6th Floor (10% in 50 yrs)

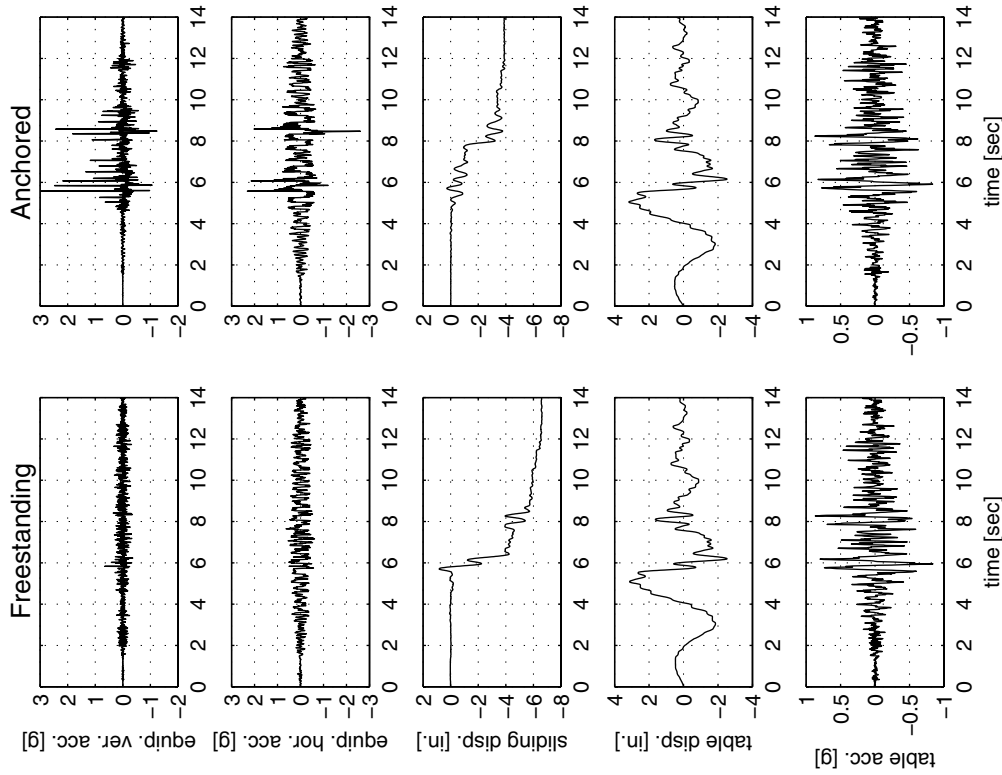


Figure 9.18 Shake table test results of the freestanding and anchored (cross-chained) ASP refrigerator subjected to the Kofu FN (10% in 50 years) ground motion recorded during the 2000 Tottori, Japan, earthquake (left) and to its corresponding UC Science Building 6th floor motion (right).

10 Conclusions

In this study, a comprehensive experimental program investigating the seismic response of free-standing and anchored laboratory equipment located in the UC Science Building laboratories within several floor levels was undertaken. The study followed the approach of performance-based earthquake engineering (PBEE) as it is proposed by the PEER Center.

The mechanical properties of the contact interface between the equipment of interest and the laboratory floors was examined. Slow-pull tests provided load-displacement curves which exhibited a pre-sliding elasticity which depended on the flexural resistance of the equipment legs, a peak value when sliding initiates, and subsequently a relatively constant friction force during sliding. Two idealized two-parameter mechanical contact models were then constructed; one was an elastoplastic model defined by the yield displacement, u_y (the displacement when sliding commences), and the friction coefficient, $\mu = \mu_s = \mu_k$; the other was the classical Coulomb friction model where a static friction coefficient, μ_s , and a kinetic friction coefficient, μ_k , were used.

In the sequel, experimental results of shake table tests on the freestanding equipment subjected to ground and floor motions of 50% and 10% in 50 years hazard levels were presented. For the equipment tested, although there was some rocking observed (particularly for the FORMA incubator), sliding was the predominant mode of response, with sliding displacements reaching up to 2 ft. The experimental results were then used to calibrate and validate numerical simulation models. Numerical simulation studies with *MATLAB* (2002) on the sliding response of the equipment using the elastoplastic model with the values of the friction coefficient μ extracted from the slow-pull tests yielded results that were in fair agreement with the experimental data. The predicted response of the equipment was appreciably improved when reduced values of their friction coefficients were used. Numerical simulation studies with *Working Model* (2000) using the Coulomb friction model also provided fair results that were considerably improved when the values of μ_s and μ_k were reduced.

In accordance with the PEER methodology, the intensity measure $IM = PTA / \mu g - 1$ and (random) engineering demand parameter $\Delta = U_{max} \omega_p^2 / PTA$ were identified. The results of the shake table tests were then used to test the hypothesized lognormal distribution of the random variable Δ and to arrive at simple linear relationships for the mean $\bar{\Delta}$ and standard deviation σ_{Δ} in terms of the IM . Fragility curves, which give the probability that the EDP will exceed a specified threshold C as a function of the IM were generated, and an example was presented to illustrate how the fragility curves can be used.

Due to displacement limitations of the shake table, experiments could be performed only for lower to medium hazard levels on the equipment. However, shake table tests for which stronger motions (2% in 50 years hazard level) were applied were done on quarter-scale wooden models of the equipment. This was achieved by halving the time-scale of the acceleration record input. The interface friction coefficient for the wooden models was higher ($\mu = 0.68$) than for the full scale equipment, and therefore the models were more prone to overturn. The results obtained were used to confirm the software *Working Model's* ability to capture well the overturning potential for equipment. With gained confidence on *Working Model's* all-around capabilities, the software was then used to analyze the response of equipment subjected to 2% in 50 years hazard level motions. The results were used in the aforementioned procedure for the 50% and 10% in 50 years motions: obtain relationships for $\bar{\Delta}$ and σ_{Δ} in terms of the IM , and generate fragility curves for various thresholds C .

Shake table experiments performed on the restrained equipment showed that the type of connection typically used to restrain the equipment suffered minimal damage. The experiments revealed large spikes in the equipment acceleration histories. It was concluded that the peak equipment accelerations recorded are significantly larger than those recorded during the free-standing equipment tests; in several occasions 7 or more times larger. Such high accelerations may pose a threat to the sensitive contents of laboratory equipment.

REFERENCES

- Barenblatt, G. I. 1996. *Scaling, Self-Similarity, and Intermediate Asymptotics*. Cambridge, UK: Cambridge University Press.
- Casey, J. 1995. "On the Advantages of a Geometrical Viewpoint in the Derivation of Lagrange's Equations for a Rigid Continuum." *Journal of Applied Mechanics and Physics (ZAMP)*. 46: S805-S847.
- Choi, B., and C. C. D. Tung. 2002. "Estimating Sliding Displacement of an Unanchored Body Subjected to Earthquake Excitation." *Earthquake Spectra*. 18(4): 601-613.
- Comerio, M. C. 2000. *The Economic Benefits of a Disaster Resistant University*. Report WP #2000-02. Berkeley, California: Institute of Urban and Regional Development, University of California.
- Comerio, M. C. (editor). 2004. *PEER Testbed Study on a Laboratory Building: Exercising Seismic Performance Assessment*. Report PEER 2005/12. Berkeley, California: Pacific Earthquake Engineering Research Center, University of California.
- Comerio, M. C., and J. C. Stallmeyer. 2002. *Nonstructural Loss Estimation: The UC Berkeley Case Study*. Peer Report 2002/01. Berkeley, California: Pacific Earthquake Engineering Research Center, University of California.
- Comerio, M. C. 2003. *Seismic Protection of Laboratory Contents: The U. C. Berkeley Science Building Case Study*. Report WP #2003-02. Berkeley, California: Institute of Urban and Regional Development, University of California.
- Crow, E. L., and K. Shimizu (editors). 1988. *Lognormal Distributions*. New York: Marcel Dekker.
- Daniel, W. W. 1990. *Applied Nonparametric Statistics*. 2nd ed. Boston, Massachusetts: PWS-KENT.
- Greenwood, D. T. 1977. *Classical Dynamics*. Englewood Cliffs, New Jersey: Prentice-Hall.
- Hogan, S. J. 1989. "On the Dynamics of Rigid Block Motion under Harmonic Forcing." *Proceedings of the Royal Society of London*. Series A. 425: 441-476.
- Housner, G. W. 1963. "The Behavior of Inverted Pendulum Structures during Earthquakes." *Bulletin of the Seismological Society of America*. 53(2): 404-417.
- Jacobsen, L. S., and R. S. Ayre. 1958. *Engineering Vibrations, with Applications to Structures and Machinery*. New York: McGraw-Hill.

Konstantinidis, D., and N. Makris. 2003. "Experimental and Analytical Results on the Seismic Response of Slender Laboratory Equipment." *Proceedings of the ATC-29-2 Seminar on Seismic Design, Performance, and Retrofit of Nonstructural Components in Critical Facilities*. Newport Beach, California, October 23-24, 2003. Redwood City, California

Konstantinidis, D., and N. Makris. 2005. "Seismic Response Analysis of Multidrum Classical Columns." *Earthquake Engineering and Structural Dynamics*. 34(10): 1243-1270.

Lee, T.-H., and K. M. Mosalam. 2002. Personal Correspondence.

Lee, T.-H., and K. M. Mosalam. 2005. "Seismic Demand Sensitivity of Reinforced Concrete Shear-Wall Building Using FOSM Method." *Earthquake Engineering and Structural Dynamics*. 34(14): 1719-1736.

Lopez Garcia, D., and T. T. Soong. 2003(a). "Sliding Fragility of Block-Type Non-Structural Components. Part 1: Unrestrained Components." *Earthquake Engineering and Structural Dynamics*. 32: 111-129.

Lopez Garcia, D., and T. T. Soong. 2003(b). "Sliding Fragility of Block-Type Non-Structural Components. Part 2: Restrained Components." *Earthquake Engineering and Structural Dynamics*. 32: 131-149.

Makris, N. 1997. "Rigidity-Plasticity-Viscosity: Can Electrorheological Dampers Protect Base-Isolated Structures from Near-Source Ground Motions?" *Earthquake Engineering and Structural Dynamics*. 26(5): 571-591.

Makris, N., and C. J. Black. 2003. *Dimensional Analysis of Inelastic Structures Subjected to Near-Fault Ground Motions*. Report EERC 2003-05. Berkeley, California: Earthquake Engineering Research Center, University of California.

Makris, N., and C. J. Black. 2004(a). "Dimensional Analysis of Rigid-Plastic and Elastoplastic Structures under Pulse-Type Excitations." *Journal of Engineering Mechanics (ASCE)*. 130(9): 1006-1019.

Makris, N., and C. J. Black. 2004(b). "Dimensional Analysis of Bilinear Oscillators under Pulse-Type Excitations." *Journal of Engineering Mechanics (ASCE)*. 130(9): 1019-1031.

Makris, N., and S.-P. Chang. 2000. "Effects of Viscous, Viscoplastic and Friction Damping on the Response of Seismic Isolation Structures." *Earthquake Engineering and Structural Dynamics*. 29(1): 85-107.

Makris, N., and D. Konstantinidis. 2003(a). "The Rocking Spectrum and the Limitations of Practical Design Methodologies." *Earthquake Engineering and Structural Dynamics*. 32(2): 265-289.

Makris, N., and D. Konstantinidis. 2003(b). "The Rocking Spectrum, Existing Design Guidelines, and a Scale Invariance." *Proceedings of the Fédération Internationale du Béton 2003 Symposium*. Athens, Greece.

Makris, N., and Y. Roussos. 2000. "Rocking Response of Rigid Blocks under Near-Source Ground Motions." *Géotechnique*. 50(3): 243-262.

MATLAB. 2002. *High-Performance Language Software for Technical Computation*. Natick, Massachusetts: The MathWorks, Inc.

Mavroeidis, G. P., and A.S. Papageorgiou. 2003. "A Mathematical Representation of Near-Fault Ground Motions." *Bulletin of the Seismological Society of America*. 93(3): 1099-1131.

McKenna, F., and G. L. Fenves. 2001. *OpenSees Manual*. Pacific Earthquake Engineering Research Center. <http://opensees.berkeley.edu>.

Newmark, N. M. 1965. "Effects of Earthquakes on Dams and Embankments." Fifth Rankine Lecture. *Géotechnique*. 15: 139-160.

O'Reilly, O. M. 2003. *Lecture Notes on the Dynamics of Particles and Rigid Bodies*. Berkeley, California: Department of Mechanical Engineering, University of California.

Pompei, A., A. Scalia, and M. A. Sumbatyan. 1998. "Dynamics of Rigid Block due to Horizontal Ground Acceleration." *Journal of Engineering Mechanics (ASCE)*. 124(7): 713-717.

Porter, K. A. 2003. "An Overview of PEER's Performance-Based Earthquake Engineering Methodology." *Proceedings of the Ninth International Conference on Applications of Statistics and Probability in Civil Engineering (ICASP9)*. San Francisco, California. Civil Engineering Risk and Reliability Association (CERRA).

Scalia, A., and M. A. Sumbatyan. 1996. "Slide Rotation of Rigid Bodies Subjected to a Horizontal Ground Motion." *Earthquake Engineering and Structural Dynamics*. 25(10): 1139-1149.

Scheaffer, R. L., and J. T. McClave. 1995. *Probability and Statistics for Engineers*. 4th ed. Belmont, California: Duxbury Press.

Shenton, H. W. III. 1996. "Criteria for Initiation of Slide, Rock, and Slide-Rock Rigid-Body Modes." *Journal of Engineering Mechanics (ASCE)*. 122(7): 690-693.

Somerville, P. 2001. "Ground Motion Time Histories for the UC Lab Building." PEER Testbed Project. Berkeley, California: Pacific Earthquake Engineering Research Center, University of California.

Taniguchi, T. 2002. "Non-Linear Response Analyses of Rectangular Rigid Bodies Subjected to Horizontal and Vertical Ground Motion." *Earthquake Engineering and Structural Dynamics*. 31(8): 1481-1500.

University of California, Berkeley. 1997. *Preliminary Seismic Evaluation*. Berkeley, California: Planning, Design and Construction, University of California.

Veletsos, A. S., N. M. Newmark, and C. V. Chelepati. 1965. "Deformation Spectra for Elastic and Elastoplastic Systems Subjected to Ground Shock and Earthquake Motions." *Proceedings of the 3rd World Conference on Earthquake Engineering*. Wellington, New Zealand, Vol. 2.

Wen, Y. K. 1975. "Approximate Method for Nonlinear Random Vibration." *Journal of Engineering Mechanics Division (ASCE)*. 101(EM4): 389-401.

Wen, Y. K. 1976. "Method for Random Vibration of Hysteretic Systems." *Journal of Engineering Mechanics Division (ASCE)*. 102(EM2): 249-263.

Working Model™. 2000. *User's Manual*. San Mateo, California: MSC Software Corporation.

Yim, S. C. S., A. K. Chopra, and J. Penzien. 1980. "Rocking Response of Rigid Blocks to Earthquakes." *Earthquake Engineering and Structural Dynamics*. 8(6): 565-587.

Younis, C., and G. Tadjbakhsh. 1984. "Response of Sliding Rigid Structure to Base Excitation." *Journal of Engineering Mechanics (ASCE)*. 110(3): 417-432.

Zhang, J., and N. Makris. 2001. "Rocking Response of Free-Standing Blocks under Cycloidal Pulses." *Journal of Engineering Mechanics (ASCE)*. 127(5): 473-483.

INDEX

A

acceleration spikes, *see* equipment
anchoring, *see* chains
angular momentum, conservation of, 84
angular velocity, 80
ASP, *see* equipment types
Ayre, R. S., 57

B

Barenblatt, G. I., 62
Black, C. J., 56, 62, 99
Bouc-Wen model, 87
Buckingham's Pi Theorem, 62

C

capacity, 75, 139
Casey, J., 81
catastrophe, 1
center of rotation, 78
chains, 1, 141
Chang, S.-P., 56, 58
characteristic length scale, *see also* pulse approximation, 56
Chelepati, C. V., 57
Chopra, A. K., 1, 82
coefficient of determination, 64, 135
coefficient of kinetic friction 55
coefficient of kinetic friction, 12, 64, 67, 86, 103, 163
coefficient of restitution, 82, 84, 91
coefficient of static friction, 12, 55, 86, 103, 163
Comerio, M. C., 2, 3, 4, 169
condition for sustaining rocking, 85–86
configuration manifold, 80, 88
corotational basis, 78
Coulomb friction model, 12, 24, 56, 91, 163
cross-chained, 141, 144
Crow, E. L., 67, 137

D

damage analysis, 2
Damage Measure, *DM*, 2
Damage Variable, *DV*, 2
Daniel, W. W., 69, 137
DCDT, 78
dimensional analysis, 61, 99
dimensionless Pi products, 62
dissipation mechanisms, 85

E

elastoplastic model, 12, 56, 163
energy lost during impact, 82, 90
Engineering Demand Parameter, *EDP*, 2, 5, 60–64, 67, 135, 164
equations of motion
 pure rocking, 81
 pure sliding, 86, 87
 slide-rocking, 88, 89
equipment
 acceleration spikes, 1, 164
 contents, 1
 locations, 1
 response modes, 1, 78
 types, 5, 9

F

Fenves, G. L., 8
floors, 12
FORMA, *see* equipment types
fragility curves
 10% and 50% in 50 years, 5, 71–75
 2% in 50 years, 5, 139
 example, 75
fragility, 71, 139
frequency parameter, 9
friction tests
 on equipment, 12–18, 163
 on wooden blocks, 99, 163

G

goodness of fit, 68, 137
Greenwood, D. T., 80

H

Hayward fault, 3, 7
hazard analysis, 2
hazard level, 5, 7, 21, 133, 163
hazardous agents, 3
Hogan, S. J., 82
holonomic constraints, 80, 88
hospitals, 3
Housner, G. W., 12, 81, 84

I

impact, inelasticity of, 84
impulse-based collision model, 93
inertia tensor, 80
initial conditions, 9
Intensity Measure, *IM*, 2, 5, 60, 135, 164

J

Jacobsen, L. S., 57

K

Kelvinator, *see* equipment types
kinetic energy
 pure rocking, 80
 slide-rocking, 88
Kolmogorov-Smirnov test, 68, 137
König decomposition, 80
Konstantinidis, D., 1, 12, 62, 99
Kutta-Merson method, 93

L

Lagrangian, *see* equations of motion
Lee, T.-H., 7, 8
load-displacement curve, 12, 104
lognormal distribution
 cumulative distribution function, 67
 probability distribution function, 67
loss analysis, 2

M

Makris, N., 1, 12, 56, 57, 58, 62, 82, 85, 86, 95, 99
mass matrix, 90
master node, 93
MATLAB, 56, 62, 78, 82, 87, 90, 93, 95, 163
McClave, J. T., 64, 68
McKenna, F., 8
mean of the EDP, 64, 67, 135
mock wall, 141
Mosalam, K. M., 7, 8
motion
 Aigion
 OTE FP, 24, 26, 31, 38, 46, 57, 147, 148, 153, 158
 Chi-Chi
 TCU052NS, 93
 Coyote Lake
 Gilroy Array #6 FN, 24, 27, 28, 29, 32, 33, 39, 40, 41, 47, 48, 49, 57, 147, 148, 150, 153, 155, 158, 160
 Loma Prieta
 Corralitos FP, 104
 Gavilan College FN, 30, 34, 35, 36, 42, 43, 50, 51, 56, 151, 156, 161
 Gilroy Historic Bldg. FN, 104
 Los Gatos PC FP, 103
 Northridge
 Rinaldi 228, 93
 Parkfield
 Cholome Array #6 FN, 141, 149, 154, 159
 Tottori
 Kofu FN, 37, 44, 45, 52, 53, 58, 152, 157, 162
multivaluedness, 95

N

NEHRP soil classification, 7
Newmark, N. M., 57, 61, 95

O

O'Reilly, O. M., 81

OpenSees, 8
overlap tolerance, 93
overturning acceleration spectrum, 95

P

PBEE, 1, 163
Peak Equipment Acceleration, *PEA*, 144
Peak Ground Acceleration, *PGA*, 2, 56
Peak Ground Displacement, *PGD*, 2
Peak Table Acceleration, *PTA*, 56, 61
PEER methodology, 1–3, 163, 164
Penzien, J., 1, 82
phase angle of Type-C pulse, 58
planar slide-rocking, 88–91
plane rotations, 21
Pompei, A., 85, 89
Porter, K. A., 2, 3
pre-yielding elasticity, 24
Probability of Exceedence, *POE*, 2, 7
pulse approximation
 rectangular, 61
 Type-A, 57
 Type-B, 57
 Type-C, 58

R

reaction force, 81, 85, 86, 89
regression analysis, 55, 64, 67, 135
research funding, 3
research laboratories, 3
rigidity of equipment, 78
rocking
 generalized force
 pure rocking, 81
 slide-rocking, 89
 pure-planar, 78–86
 undesirable response, 1
 velocity of center of mass
 pure rocking, 80
 slide-rocking, 88
Roussos, Y., 1, 56, 58, 82
Runge-Kutta method, 93

S

sample size, 69, 137
Scalia, A., 78, 85, 89
Scheaffer, R. L., 64, 68
seismic hazard, 2, 7
shake table tests
 anchored, 144–147
 freestanding, 5, 8, 9, 18, 55, 64
 on wooden blocks, 99
Shenton, H. W. III., 78, 82, 85
Shimizu, K., 67, 137
signum function, 80
similarity, 61
sliding
 excessive displacements, 1
 pure-planar, 86–87
Somerville, P., 7
standard deviation, 64, 67, 135
standard normal distribution, 68, 137
state vector, 82, 87, 90
stockiness, 9
straight-chained, 141, 144
strike-slip, *see* Hayward fault, 7
structural analysis, 2, 7–8
structural system, 3
Sumbatyan, M. A., 78, 85, 89

T

Tadjbakhsh, G., 95
Taniguchi, T., 88

U

UC Science testbed, 2, 3
UCB, 3

V

Veletsos, A. S., 57

W

Wen, Y. K., 87
wire transducers, 22
wooden blocks, 99
Working Model

validation

 pure sliding, 95

 slide-rocking, 97

Working Model validation

 pure rocking, 93

Working Model, 18, 56, 67, 78, 91, 95, 103,
133, 163

Y

yield displacement, 12, 87, 163

yielding mechanism, 12

Yim, S. C. S., 1, 82

Younis, C., 95

Z

Zhang, J., 85, 86, 95

PEER REPORTS

PEER reports are available from the National Information Service for Earthquake Engineering (NISEE). To order PEER reports, please contact the Pacific Earthquake Engineering Research Center, 1301 South 46th Street, Richmond, California 94804-4698. Tel.: (510) 231-9468; Fax: (510) 231-9 461.

- PEER 2005/11** *Van Nuys Hotel Building Testbed Report: Exercising Seismic Performance Assessment.* Helmut Krawinkler, editor. October 2005.
- PEER 2005/10** *First NEES/E-Defense Workshop on Collapse Simulation of Reinforced Concrete Building Structures.* September 2005.
- PEER 2005/07** *Experimental and Analytical Studies on the Seismic Response of Freestanding and Anchored Laboratory Equipment.* Dimitrios Konstantinidis and Nicos Makris. January 2005.
- PEER 2005/06** *Global Collapse of Frame Structures under Seismic Excitations.* Luis F. Ibarra and Helmut Krawinkler. September 2005.
- PEER 2005/01** *Empirical Characterization of Site Conditions on Strong Ground Motion.* Jonathan P. Stewart, Yoojoong Choi, and Robert W. Graves. June 2005.
- PEER 2004/09** *Electrical Substation Equipment Interaction: Experimental Rigid Conductor Studies.* Christopher Stearns and André Filiatrault. February 2005.
- PEER 2004/08** *Seismic Qualification and Fragility Testing of Line Break 550-kV Disconnect Switches.* Shakhzod M. Takhirov, Gregory L. Fenves, and Eric Fujisaki. January 2005.
- PEER 2004/07** *Ground Motions for Earthquake Simulator Qualification of Electrical Substation Equipment.* Shakhzod M. Takhirov, Gregory L. Fenves, Eric Fujisaki, and Don Clyde. January 2005.
- PEER 2004/06** *Performance-Based Regulation and Regulatory Regimes.* Peter J. May and Chris Koski. September 2004.
- PEER 2004/05** *Performance-Based Seismic Design Concepts and Implementation: Proceedings of an International Workshop.* Peter Fajfar and Helmut Krawinkler, editors. September 2004.
- PEER 2004/04** *Seismic Performance of an Instrumented Tilt-up Wall Building.* James C. Anderson and Vitelmo V. Bertero. July 2004.
- PEER 2004/03** *Evaluation and Application of Concrete Tilt-up Assessment Methodologies.* Timothy Graf and James O. Malley. October 2004.
- PEER 2004/02** *Analytical Investigations of New Methods for Reducing Residual Displacements of Reinforced Concrete Bridge Columns.* Junichi Sakai and Stephen A. Mahin. August 2004.
- PEER 2004/01** *Seismic Performance of Masonry Buildings and Design Implications.* Kerri Anne Taeko Tokoro, James C. Anderson, and Vitelmo V. Bertero. February 2004.
- PEER 2003/18** *Performance Models for Flexural Damage in Reinforced Concrete Columns.* Michael Berry and Marc Eberhard. August 2003.
- PEER 2003/17** *Predicting Earthquake Damage in Older Reinforced Concrete Beam-Column Joints.* Catherine Pagni and Laura Lowes. October 2004.
- PEER 2003/16** *Seismic Demands for Performance-Based Design of Bridges.* Kevin Mackie and Božidar Stojadinovic. August 2003.
- PEER 2003/15** *Seismic Demands for Nondeteriorating Frame Structures and Their Dependence on Ground Motions.* Ricardo Antonio Medina and Helmut Krawinkler. May 2004.
- PEER 2003/14** *Finite Element Reliability and Sensitivity Methods for Performance-Based Earthquake Engineering.* Terje Haukaas and Armen Der Kiureghian. April 2004.
- PEER 2003/13** *Effects of Connection Hysteretic Degradation on the Seismic Behavior of Steel Moment-Resisting Frames.* Janise E. Rodgers and Stephen A. Mahin. March 2004.
- PEER 2003/12** *Implementation Manual for the Seismic Protection of Laboratory Contents: Format and Case Studies.* William T. Holmes and Mary C. Comerio. October 2003.

- PEER 2003/11** *Fifth U.S.-Japan Workshop on Performance-Based Earthquake Engineering Methodology for Reinforced Concrete Building Structures.* February 2004.
- PEER 2003/10** *A Beam-Column Joint Model for Simulating the Earthquake Response of Reinforced Concrete Frames.* Laura N. Lowes, Nilanjan Mitra, and Arash Altoontash. February 2004.
- PEER 2003/09** *Sequencing Repairs after an Earthquake: An Economic Approach.* Marco Casari and Simon J. Wilkie. April 2004.
- PEER 2003/08** *A Technical Framework for Probability-Based Demand and Capacity Factor Design (DCFD) Seismic Formats.* Fatemeh Jalayer and C. Allin Cornell. November 2003.
- PEER 2003/07** *Uncertainty Specification and Propagation for Loss Estimation Using FOSM Methods.* Jack W. Baker and C. Allin Cornell. September 2003.
- PEER 2003/06** *Performance of Circular Reinforced Concrete Bridge Columns under Bidirectional Earthquake Loading.* Mahmoud M. Hachem, Stephen A. Mahin, and Jack P. Moehle. February 2003.
- PEER 2003/05** *Response Assessment for Building-Specific Loss Estimation.* Eduardo Miranda and Shahram Taghavi. September 2003.
- PEER 2003/04** *Experimental Assessment of Columns with Short Lap Splices Subjected to Cyclic Loads.* Murat Melek, John W. Wallace, and Joel Conte. April 2003.
- PEER 2003/03** *Probabilistic Response Assessment for Building-Specific Loss Estimation.* Eduardo Miranda and Hesameddin Aslani. September 2003.
- PEER 2003/02** *Software Framework for Collaborative Development of Nonlinear Dynamic Analysis Program.* Jun Peng and Kincho H. Law. September 2003.
- PEER 2003/01** *Shake Table Tests and Analytical Studies on the Gravity Load Collapse of Reinforced Concrete Frames.* Kenneth John Elwood and Jack P. Moehle. November 2003.
- PEER 2002/24** *Performance of Beam to Column Bridge Joints Subjected to a Large Velocity Pulse.* Natalie Gibson, André Filiatrault, and Scott A. Ashford. April 2002.
- PEER 2002/23** *Effects of Large Velocity Pulses on Reinforced Concrete Bridge Columns.* Greg L. Orozco and Scott A. Ashford. April 2002.
- PEER 2002/22** *Characterization of Large Velocity Pulses for Laboratory Testing.* Kenneth E. Cox and Scott A. Ashford. April 2002.
- PEER 2002/21** *Fourth U.S.-Japan Workshop on Performance-Based Earthquake Engineering Methodology for Reinforced Concrete Building Structures.* December 2002.
- PEER 2002/20** *Barriers to Adoption and Implementation of PBEE Innovations.* Peter J. May. August 2002.
- PEER 2002/19** *Economic-Engineered Integrated Models for Earthquakes: Socioeconomic Impacts.* Peter Gordon, James E. Moore II, and Harry W. Richardson. July 2002.
- PEER 2002/18** *Assessment of Reinforced Concrete Building Exterior Joints with Substandard Details.* Chris P. Pantelides, Jon Hansen, Justin Nadauld, and Lawrence D. Reaveley. May 2002.
- PEER 2002/17** *Structural Characterization and Seismic Response Analysis of a Highway Overcrossing Equipped with Elastomeric Bearings and Fluid Dampers: A Case Study.* Nicos Makris and Jian Zhang. November 2002.
- PEER 2002/16** *Estimation of Uncertainty in Geotechnical Properties for Performance-Based Earthquake Engineering.* Allen L. Jones, Steven L. Kramer, and Pedro Arduino. December 2002.
- PEER 2002/15** *Seismic Behavior of Bridge Columns Subjected to Various Loading Patterns.* Asadollah Esmaeily-Gh. and Yan Xiao. December 2002.
- PEER 2002/14** *Inelastic Seismic Response of Extended Pile Shaft Supported Bridge Structures.* T.C. Hutchinson, R.W. Boulanger, Y.H. Chai, and I.M. Idriss. December 2002.
- PEER 2002/13** *Probabilistic Models and Fragility Estimates for Bridge Components and Systems.* Paolo Gardoni, Armen Der Kiureghian, and Khalid M. Mosalam. June 2002.
- PEER 2002/12** *Effects of Fault Dip and Slip Rake on Near-Source Ground Motions: Why Chi-Chi Was a Relatively Mild M7.6 Earthquake.* Brad T. Aagaard, John F. Hall, and Thomas H. Heaton. December 2002.

- PEER 2002/11** *Analytical and Experimental Study of Fiber-Reinforced Strip Isolators.* James M. Kelly and Shakhzod M. Takhirov. September 2002.
- PEER 2002/10** *Centrifuge Modeling of Settlement and Lateral Spreading with Comparisons to Numerical Analyses.* Sivapalan Gajan and Bruce L. Kutter. January 2003.
- PEER 2002/09** *Documentation and Analysis of Field Case Histories of Seismic Compression during the 1994 Northridge, California, Earthquake.* Jonathan P. Stewart, Patrick M. Smith, Daniel H. Whang, and Jonathan D. Bray. October 2002.
- PEER 2002/08** *Component Testing, Stability Analysis and Characterization of Buckling-Restrained Unbonded Braces™.* Cameron Black, Nicos Makris, and Ian Aiken. September 2002.
- PEER 2002/07** *Seismic Performance of Pile-Wharf Connections.* Charles W. Roeder, Robert Graff, Jennifer Soderstrom, and Jun Han Yoo. December 2001.
- PEER 2002/06** *The Use of Benefit-Cost Analysis for Evaluation of Performance-Based Earthquake Engineering Decisions.* Richard O. Zerbe and Anthony Falit-Baiamonte. September 2001.
- PEER 2002/05** *Guidelines, Specifications, and Seismic Performance Characterization of Nonstructural Building Components and Equipment.* André Filiatrault, Constantin Christopoulos, and Christopher Stearns. September 2001.
- PEER 2002/04** *Consortium of Organizations for Strong-Motion Observation Systems and the Pacific Earthquake Engineering Research Center Lifelines Program: Invited Workshop on Archiving and Web Dissemination of Geotechnical Data, 4–5 October 2001.* September 2002.
- PEER 2002/03** *Investigation of Sensitivity of Building Loss Estimates to Major Uncertain Variables for the Van Nuys Testbed.* Keith A. Porter, James L. Beck, and Rustem V. Shaikhutdinov. August 2002.
- PEER 2002/02** *The Third U.S.-Japan Workshop on Performance-Based Earthquake Engineering Methodology for Reinforced Concrete Building Structures.* July 2002.
- PEER 2002/01** *Nonstructural Loss Estimation: The UC Berkeley Case Study.* Mary C. Comerio and John C. Stallmeyer. December 2001.
- PEER 2001/16** *Statistics of SDF-System Estimate of Roof Displacement for Pushover Analysis of Buildings.* Anil K. Chopra, Rakesh K. Goel, and Chatpan Chintanapakdee. December 2001.
- PEER 2001/15** *Damage to Bridges during the 2001 Nisqually Earthquake.* R. Tyler Ranf, Marc O. Eberhard, and Michael P. Berry. November 2001.
- PEER 2001/14** *Rocking Response of Equipment Anchored to a Base Foundation.* Nicos Makris and Cameron J. Black. September 2001.
- PEER 2001/13** *Modeling Soil Liquefaction Hazards for Performance-Based Earthquake Engineering.* Steven L. Kramer and Ahmed-W. Elgamal. February 2001.
- PEER 2001/12** *Development of Geotechnical Capabilities in OpenSees.* Boris Jeremi . September 2001.
- PEER 2001/11** *Analytical and Experimental Study of Fiber-Reinforced Elastomeric Isolators.* James M. Kelly and Shakhzod M. Takhirov. September 2001.
- PEER 2001/10** *Amplification Factors for Spectral Acceleration in Active Regions.* Jonathan P. Stewart, Andrew H. Liu, Yoojoong Choi, and Mehmet B. Baturay. December 2001.
- PEER 2001/09** *Ground Motion Evaluation Procedures for Performance-Based Design.* Jonathan P. Stewart, Shyh-Jeng Chiou, Jonathan D. Bray, Robert W. Graves, Paul G. Somerville, and Norman A. Abrahamson. September 2001.
- PEER 2001/08** *Experimental and Computational Evaluation of Reinforced Concrete Bridge Beam-Column Connections for Seismic Performance.* Clay J. Naito, Jack P. Moehle, and Khalid M. Mosalam. November 2001.
- PEER 2001/07** *The Rocking Spectrum and the Shortcomings of Design Guidelines.* Nicos Makris and Dimitrios Konstantinidis. August 2001.
- PEER 2001/06** *Development of an Electrical Substation Equipment Performance Database for Evaluation of Equipment Fragilities.* Thalia Agnanos. April 1999.
- PEER 2001/05** *Stiffness Analysis of Fiber-Reinforced Elastomeric Isolators.* Hsiang-Chuan Tsai and James M. Kelly. May 2001.

- PEER 2001/04** *Organizational and Societal Considerations for Performance-Based Earthquake Engineering.* Peter J. May. April 2001.
- PEER 2001/03** *A Modal Pushover Analysis Procedure to Estimate Seismic Demands for Buildings: Theory and Preliminary Evaluation.* Anil K. Chopra and Rakesh K. Goel. January 2001.
- PEER 2001/02** *Seismic Response Analysis of Highway Overcrossings Including Soil-Structure Interaction.* Jian Zhang and Nicos Makris. March 2001.
- PEER 2001/01** *Experimental Study of Large Seismic Steel Beam-to-Column Connections.* Egor P. Popov and Shakhzod M. Takhirov. November 2000.
- PEER 2000/10** *The Second U.S.-Japan Workshop on Performance-Based Earthquake Engineering Methodology for Reinforced Concrete Building Structures.* March 2000.
- PEER 2000/09** *Structural Engineering Reconnaissance of the August 17, 1999 Earthquake: Kocaeli (Izmit), Turkey.* Halil Sezen, Kenneth J. Elwood, Andrew S. Whittaker, Khalid Mosalam, John J. Wallace, and John F. Stanton. December 2000.
- PEER 2000/08** *Behavior of Reinforced Concrete Bridge Columns Having Varying Aspect Ratios and Varying Lengths of Confinement.* Anthony J. Calderone, Dawn E. Lehman, and Jack P. Moehle. January 2001.
- PEER 2000/07** *Cover-Plate and Flange-Plate Reinforced Steel Moment-Resisting Connections.* Taejin Kim, Andrew S. Whittaker, Amir S. Gilani, Vitelmo V. Bertero, and Shakhzod M. Takhirov. September 2000.
- PEER 2000/06** *Seismic Evaluation and Analysis of 230-kV Disconnect Switches.* Amir S. J. Gilani, Andrew S. Whittaker, Gregory L. Fenves, Chun-Hao Chen, Henry Ho, and Eric Fujisaki. July 2000.
- PEER 2000/05** *Performance-Based Evaluation of Exterior Reinforced Concrete Building Joints for Seismic Excitation.* Chandra Clyde, Chris P. Pantelides, and Lawrence D. Reaveley. July 2000.
- PEER 2000/04** *An Evaluation of Seismic Energy Demand: An Attenuation Approach.* Chung-Che Chou and Chia-Ming Uang. July 1999.
- PEER 2000/03** *Framing Earthquake Retrofitting Decisions: The Case of Hillside Homes in Los Angeles.* Detlof von Winterfeldt, Nels Roselund, and Alicia Kitsuse. March 2000.
- PEER 2000/02** *U.S.-Japan Workshop on the Effects of Near-Field Earthquake Shaking.* Andrew Whittaker, ed. July 2000.
- PEER 2000/01** *Further Studies on Seismic Interaction in Interconnected Electrical Substation Equipment.* Armen Der Kiureghian, Kee-Jeung Hong, and Jerome L. Sackman. November 1999.
- PEER 1999/14** *Seismic Evaluation and Retrofit of 230-kV Porcelain Transformer Bushings.* Amir S. Gilani, Andrew S. Whittaker, Gregory L. Fenves, and Eric Fujisaki. December 1999.
- PEER 1999/13** *Building Vulnerability Studies: Modeling and Evaluation of Tilt-up and Steel Reinforced Concrete Buildings.* John W. Wallace, Jonathan P. Stewart, and Andrew S. Whittaker, editors. December 1999.
- PEER 1999/12** *Rehabilitation of Nonductile RC Frame Building Using Encasement Plates and Energy-Dissipating Devices.* Mehrdad Sasani, Vitelmo V. Bertero, James C. Anderson. December 1999.
- PEER 1999/11** *Performance Evaluation Database for Concrete Bridge Components and Systems under Simulated Seismic Loads.* Yael D. Hose and Frieder Seible. November 1999.
- PEER 1999/10** *U.S.-Japan Workshop on Performance-Based Earthquake Engineering Methodology for Reinforced Concrete Building Structures.* December 1999.
- PEER 1999/09** *Performance Improvement of Long Period Building Structures Subjected to Severe Pulse-Type Ground Motions.* James C. Anderson, Vitelmo V. Bertero, and Raul Bertero. October 1999.
- PEER 1999/08** *Envelopes for Seismic Response Vectors.* Charles Menun and Armen Der Kiureghian. July 1999.
- PEER 1999/07** *Documentation of Strengths and Weaknesses of Current Computer Analysis Methods for Seismic Performance of Reinforced Concrete Members.* William F. Cofer. November 1999.
- PEER 1999/06** *Rocking Response and Overturning of Anchored Equipment under Seismic Excitations.* Nicos Makris and Jian Zhang. November 1999.
- PEER 1999/05** *Seismic Evaluation of 550 kV Porcelain Transformer Bushings.* Amir S. Gilani, Andrew S. Whittaker, Gregory L. Fenves, and Eric Fujisaki. October 1999.

- PEER 1999/04** *Adoption and Enforcement of Earthquake Risk-Reduction Measures.* Peter J. May, Raymond J. Burby, T. Jens Feeley, and Robert Wood.
- PEER 1999/03** *Task 3 Characterization of Site Response General Site Categories.* Adrian Rodriguez-Marek, Jonathan D. Bray, and Norman Abrahamson. February 1999.
- PEER 1999/02** *Capacity-Demand-Diagram Methods for Estimating Seismic Deformation of Inelastic Structures: SDF Systems.* Anil K. Chopra and Rakesh Goel. April 1999.
- PEER 1999/01** *Interaction in Interconnected Electrical Substation Equipment Subjected to Earthquake Ground Motions.* Armen Der Kiureghian, Jerome L. Sackman, and Kee-Jeung Hong. February 1999.
- PEER 1998/08** *Behavior and Failure Analysis of a Multiple-Frame Highway Bridge in the 1994 Northridge Earthquake.* Gregory L. Fenves and Michael Ellery. December 1998.
- PEER 1998/07** *Empirical Evaluation of Inertial Soil-Structure Interaction Effects.* Jonathan P. Stewart, Raymond B. Seed, and Gregory L. Fenves. November 1998.
- PEER 1998/06** *Effect of Damping Mechanisms on the Response of Seismic Isolated Structures.* Nicos Makris and Shih-Po Chang. November 1998.
- PEER 1998/05** *Rocking Response and Overturning of Equipment under Horizontal Pulse-Type Motions.* Nicos Makris and Yiannis Roussos. October 1998.
- PEER 1998/04** *Pacific Earthquake Engineering Research Invitational Workshop Proceedings, May 14–15, 1998: Defining the Links between Planning, Policy Analysis, Economics and Earthquake Engineering.* Mary Comerio and Peter Gordon. September 1998.
- PEER 1998/03** *Repair/Upgrade Procedures for Welded Beam to Column Connections.* James C. Anderson and Xiaojing Duan. May 1998.
- PEER 1998/02** *Seismic Evaluation of 196 kV Porcelain Transformer Bushings.* Amir S. Gilani, Juan W. Chavez, Gregory L. Fenves, and Andrew S. Whittaker. May 1998.
- PEER 1998/01** *Seismic Performance of Well-Confined Concrete Bridge Columns.* Dawn E. Lehman and Jack P. Moehle. December 2000.